UNIVERSITY OF CALIFORNIA SAN DIEGO

From Molecules to Wafer-Scale: Total Fabrication of Plasmonic Platform from the Bottom-up

A Dissertation submitted in partial satisfaction of the requirements
for the degree Doctor of Philosophy

in

Materials Science and Engineering

by

Yuan Zeng

Committee in charge:

Professor Andrea R. Tao, Chair
Professor Prabhakar R. Bandaru
Professor Zheng Chen
Professor Zhaowei Liu
Professor Donald J. Sirbuly

2022

This dissertation of Yuan Zeng is approved, and it is acceptable in quality and form for publication on microfilm and electronically:

University of California San Diego

2022

EPIGRAPH

“Yesterday is history, tomorrow is a mystery, but today is a gift. That’s why it is called the present” - Bil Keane (and Kung Fu Panda)

TABLE OF CONTENTS

LIST OF FIGURES

LIST OF TABLES

LIST OF ABBREVIATIONS

SERS	Surface Enhanced Raman Spectroscopy
mSERS	Metasurface Enhanced Raman Spectroscopy
LSPR	Localized Surface Plasmon Resonance
EM Field	Electromagnetic Field
EF	Enhancement Factor
AgNC	Silver Nanocubes
CuS	Copper (II) Sulfide
SHG	Second Harmonic Generation
NOM	Nanoparticle on Metal
PBDE	Polybrominated Diphenyl Ether
PDMS	Polydimethylsiloxane
HMDS	Hexamethyldisilazane
BT (PhSH)	Benzenethiol (Thiophenol)
2D Materials	Two-dimensional Materials
NIL	Nanoimprint Lithography
SCIL	Substrate Conformal Imprint Lithography

ACKNOWLEDGEMENTS

I would like to thank my advisor Professor Andrea Tao. In the past six and half years, she always gave me the suggestions and support, to improve my abilities and skills in critical thinking, project organization, experimental designing, and scientific writing. Also, Professor Tao gave me the enough freedom to explore the projects and directions that I interested in and make me keep passion in my research.

I would like to thank Dr. Whitney Bryks, Dr. Suwen Hsu, Dr. Matthew Rozin, Dr. Tyler Dill, and Dr. Andrea Rodarte for teaching me knowledges and lab skills when I joined in Tao group. I also would like to thank current Tao group members and all my collaborators in Professor Zhaowei Liu's group, Professor Zheng Chen's group, Professor David Fenning's group, and Professor Kesong Yang's group. The collaborated research with all you guys is so exciting.

Finally, I would like to thank my parents, Jiuyu Zeng and Li Peng, for being supportive to my choices and decisions in the past 30 years (actually, 29.5 years). Also, I would like to thank my aunts, Xiufeng and Xiuping for their care in my childhood.

Chapter 2, in full, is a reprint of the material as it appears in Chemistry of Materials 33.1 (2020): 117-125. Yuan Zeng, Paul Hyunggyu Joo, Kesong Yang, and Andrea R. Tao. The dissertation author was the primary investigator and author of this paper.

Chapter 3, in full, is a reprint of the material as it appears in Advanced Functional Materials 28.51 (2018): 1803019. Yuan Zeng[‡], Haoliang Qian[‡], Matthew J. Rozin[‡], Zhaowei Liu, and Andrea R. Tao ([‡] Equal contribution). The dissertation author was the primary investigator and author of this paper.

Chapter 4, in full, is a reprint of the material as it appears in an under reviewed manuscript for ACS Applied Materials & Interfaces. Yuan Zeng, Riddhi Ananth, Tyler J. Dill, Andrea Rodarte, Matthew J. Rozin, Nathan Bradshaw, Eric R. Brown, and Andrea R. Tao. The dissertation author

was the primary investigator and author of this paper.

Chapter 5, in full, is currently being prepared for submission for publication of the materials by Yuan Zeng, Riddhi Ananth, Wade Shipley, and Andrea R. Tao*. The dissertation author was the primary investigator and author of this paper.

Chapter 6, in part (Figure 1,2,3,4,6), is currently being prepared for submission for publication of the materials by Yuan Zeng[‡], Steven Bopp[‡], Tod Pascal, Zhaowei Liu* and Andrea R. Tao*. The dissertation author was the primary investigator and author of this paper

Chapter 6, in part (Figure 5), is currently being prepared for submission for publication of the materials by Steven Bopp[‡], Yuan Zeng[‡], Tod Pascal, Andrea R. Tao* and Zhaowei Liu*. The dissertation author was the co-author of this paper.

Chapter 7, in full, is currently being prepared for submission for publication of the materials by Yuan Zeng, Andrea L. Rodarte, Tyler J. Dill, and Andrea R. Tao* (The dissertation author was the primary investigator and author of this paper)

VITA

2014	Bachelor of Science in Materials Science and Engineering. University of Arizona
2015	Teaching Assistant. Department of NanoEngineering. University of California San Diego
2015-2022	Graduate Researcher. University of California San Diego
2016	Master of Science in Materials Science and Engineering, University of California San Diego
2018-2020	Teaching Assistant. Department of NanoEngineering. University of California San Diego
2021	Nanoimprint Lithography Intern. Engineered Optics, Office of the CTO at Applied Materials
2022	Doctor of Philosophy in Materials Science and Engineering, University of California, San Diego
2022	Senior Process Engineer in ASM America Inc.

PUBLICATIONS

Yuan Zeng[‡], Haoliang Qian[‡], Matthew J. Rozin[‡], Zhaowei Liu, and Andrea R. Tao*. "Enhanced Second Harmonic Generation in Double-Resonance Colloidal Metasurfaces." Advanced Functional Materials 28, no. 51 (2018): 1803019.

Yuan Zeng, Paul Hyunggyu Joo, Kesong Yang, and Andrea R. Tao*. "Computation-Motivated Design of Ternary Plasmonic Copper Chalcogenide Nanocrystals." Chemistry of Materials 33, no. 1 (2020): 117-125.

Yuan Zeng, Riddhi Ananth, Tyler J. Dill, Andrea Rodarte, Matthew J. Rozin, Nathan Bradshaw, Eric R. Brown, and Andrea R. Tao*. "Metasurface-Enhanced Raman Spectroscopy (mSERS) for Oriented Molecular Sensing." **(Submitted)**

Yuan Zeng, Riddhi Ananth, Wade Shipley, and Andrea R. Tao*. "Rapid Raman Detection of PBDEs in Water Using a Colloidal Metasurface" **(In Preparation)**

Yuan Zeng, Andrea L. Rodarte, Tyler J. Dill, and Andrea R. Tao*. "Probing Raman Enhancement for a Colloidal Metasurface in the Quantum Regime." **(In Preparation)**

Yuan Zeng[‡]**,** Steven Bopp[‡], Zhaowei Liu, Tod Pascal and Andrea R. Tao*. "Metasurface Enhanced Raman Spectroscopy (mSERS) for Two-dimensional Materials Wafer-Scale Characterization" **(In Preparation)**

Steven Bopp[‡], **Yuan Zeng**[‡]**,** Tod Pascal, Andrea R. Tao*, Zhaowei Liu*. "Optical and Structural Properties of Trans-dimensional TiN: a Joint Experiment and Theoretical Study" **(In Preparation)**

‡ These authors contributed equally

* Corresponding author

ABSTRACT OF THE DISSERTATION

Bottom-Up Total Fabrication: From Molecule to Wafer-Scale Plasmonic Devices

by

Yuan Zeng

Doctor of Philosophy in Materials Science and Engineering

University of California San Diego, 2022

Professor Andrea R. Tao

Localized surface plasmon resonance (LSPR) is a collective oscillation of electrons at the interface of metallic nanostructures or metal-dielectric interface. At the resonance frequency, light-matter interaction results in a coherent coupling between surface conduction electrons and incident light, generating an enhanced electromagnetic (EM) field at the plasmonic nanostructure surface. Taking advantage of this EM field enhancement, plasmonic nanostructures have been widely used in nonlinear optics, chemical sensing, biomedical imaging, and photocatalysis. However, due to the requirement for precisely controlled size, shape, and orientation, most of these plasmonic nanostructures have been fabricated with top-down methods; the major challenge has been industrial-scale production of plasmonic devices.

In this work, I have developed a four-step bottom-up total fabrication process for cost-effective and wafer-scale fabrication of plasmonic platforms. First, we used wet chemistry methods to synthesize (1) plasmonic noble metal nanocrystals with a tunable size and shape, and (2) plasmonic semiconductor nanocrystals with a tunable composition, resonance frequency, and bandgap. Next, we used self-assembly methods to group multiple plasmonic components together and build a submicron-scale meta-atom. Owing to nanometer-scale separation between plasmonic components, there was a strong plasmon coupling effect within the artificial building blocks of metasurface (named as meta-atoms) that resulted in two orders of magnitude in near-field enhancement. Then we used a micro-fabrication method, such as Langmuir-Blodgett film, a soft imprint, etc., to build a wafer-scale plasmonic device that consists of billions of repeating meta-atoms. Finally, we used surface chemistry to functionalize the surface of plasmonic devices and then used these plasmonic devices for different applications, including optical second harmonic generation, water pollutant molecules sensing, and wafer-scale 2D materials characterization.

Chapter 1

An Introduction to the Total Fabrication and Plasmonic Devices

Yuan Zeng[1,2]

[1]Department of NanoEngineering, University of California, San Diego, 9500 Gilman Drive MC 0448, La Jolla, California 92093-0448

[2]Materials Science and Engineering, University of California, San Diego, 9500 Gilman Drive, La Jolla, California 92093-0448

1.1 Total Fabrication from the Bottom-up.

Nanotechnology is the manipulation of matter on the nanometer-scale to produce new structures, materials, and devices. In nanotechnology, the engineering and manufacturing of materials are developed by two general strategies: a top-down approach and a bottom-up approach.[1] The top-down approach, through patterning and etching, is a subtractive process where bulk materials are removed to produce features with controlled size and shape. The bottom-up approach, through supramolecular chemistry and self-assembly, is an additive process where atoms and molecules are used to build up the desired objects. In the past half-century, people spent tremendous efforts to make top-down approaches get smaller feature size to increase the efficiency and make bottom-up approach get large device area to decrease the cost (Figure 1.1a).[2] Recently, significant progress has been made in both avenues. Using a top-down approach, IBM announced a 2-nm chip technology which has a 45% higher performance or 75% lower energy use than 7-nm node chips.[3] For the bottom-up approach, researchers in the University of Chicago developed a micron-scale all-inorganic supercrystal which is strongly electronically coupled.[4] However, owing to significant challenges, such as impurities and defects induced local aggregation and thermodynamical stability induced domain size limitation, in scaling-up from micron-scale to centimeter-scale, industrial production with bottom-up approaches has not been well-developed yet. To overcome challenges in industrial production of wafer-scale platforms, I have integrated self-assembly methods with microfabrication techniques and developed a novel nanoengineering process, called the “Total Fabrication”. In organic chemistry, total synthesis is one of the most important topics because it is the complete chemical synthesis of a complex molecule, from simple and commercially available precursors.[5,6] Similarly, bottom-up total fabrication is a complete nanoengineering fabrication of wafer-scale devices, from simple and commercially available precursors. Figure 1.1b shows the schematic[7] of bottom-up total fabrication. First, commercially available precursors and wet chemistry methods are used to synthesis 10 – 100 nm scale nanocrystals. Secondly, self-assembly method is used to assemble

nanocrystals into sub-micron scale meta-atoms. Then, microfabrication processes are used to group billions of meta-atoms into wafer-scale platforms. Finally, surface modification is used to functionalize platform surface and these platforms are used for different technological applications, such as optical second harmonic generation (SHG), Surface Enhancement Raman Spectroscopy

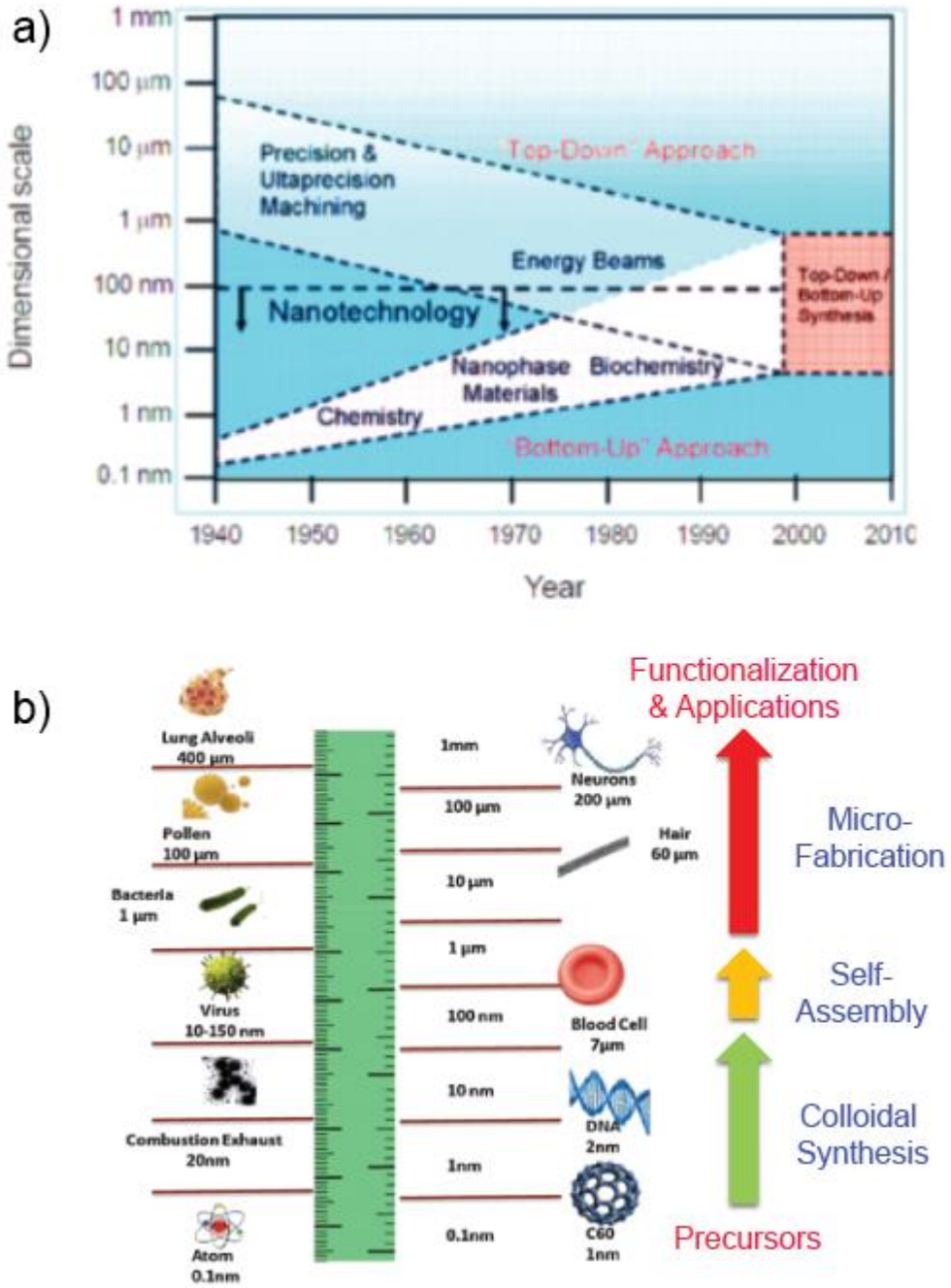

Figure 1.1 | Total Fabrication from the bottom-up. (a) Progress of bottom-up approach and top-down approach. Reproduced with permission from ref 2 (b) Schematic of Bottom-up total fabrication. Reproduced and modified with permission from ref 7

(SERS) sensor and wafer-scale two-dimensional materials characterization, via device level engineering.

1.2 Localized Surface Plasmon Resonance (LSPR) and Plasmonic Materials.

Localized Surface Plasmon Resonance (LSPR) is a collective free carrier oscillation on the confined surface of noble metal nanostructures.[8] At the resonance frequency, incident electromagnetic (EM) wave excites LSPR and results a significant increased extinction cross-section (σ_{ext}), which is related to the complex materials dielectric function as follow:

$$\sigma_{ext} \sim \frac{\varepsilon_2}{(\varepsilon_1 + 2\varepsilon_m)^2 + {\varepsilon_2}^2}$$

Where ε_1 is the real part of dielectric function, ε_2 is the imaginary part of dielectric function and ε_m is the dielectric constant of the medium.[9] Because the real part of the dielectric function describes the polarizability of metal and the imaginary part of dielectric function describes the probability of photon absorption through one electron excitation, metals with small ε_2 (Au, Ag, Cu) have good plasmonic properties and widely used in plasmonic applications.[10] In addition to metal, degenerately doped compound semiconductors, such as copper chalcogenide[11,12] and transition metal oxide[13] also been developed for plasmonic applications. Owing to large carrier density (10^{23}/cm^3) in metal and relative low carrier density (10^{21} to 10^{22}/cm^3) in semiconductor, the LSPR wavelength of plasmonic metal is located in visible range and the LSPR wavelength of plasmonic semiconductor is located NIR wavelength.[14] Moreover, because noble metal nanostructures have minimized electron oscillation damping and dephasing, the quality factor[15] and optical enhancement is optimized.[16] Compare with noble metals, plasmonic semiconductors have lower quality factor and less optical enhancement. However, owing to great composition tunability in compound semiconductor[17], plasmonic semiconductors have higher degree of freedom in tuning plasmonic properties and enable more applications in the future.

1.3 Plasmon Coupling and Optical Applications

1.3.1 Plasmon Coupling

Taking the advantages of near-field enhancement, electromagnetic hotspots are generated at the surface of nanostructure and result more than one order of magnitude local field enhancement inside the hotspots.[18] In most cases, the resonance frequency and hotspot strength only dependent on size, shape, orientation, and composition of nanostructure. However, when we have two or more plasmonic nanostructures in a system, the LSPR of individual nanostructure hybridize with each other and cause a new phenomenon called “plasmon coupling” occurs.[19] At large interparticle distances (4 to 7 particles separation), far-field coupling is observed in experiment and results a slightly shift in the scattering spectra.[20] At small interparticle distances, near-field coupling becomes more dominant, resulting in a large shift in far-field spectra and a large enhancement in near-field.[21] This extremely strong local field enhancement enables different optical applications, including optical second harmonic generation and Surface Enhanced Raman Spectroscopy (SERS).

1.3.2 Second Harmonic Generation (SHG)

Second Harmonic Generation is a nonlinear optical process that two photons with the same energy interact with a nonlinear material, combine with each other, and generate a new photon with twice the energy of incident photons. Because SHG originates from light matter interactions with nano-centrosymmetric crystal lattice, bulk materials with large nonlinear susceptibility and long optical path are required. In the past decade, people realized that conventional optical components rely on light propagation over large distances have significant challenges in microdevice fabrication. Therefore, development on flat and ultrathin optical components is focused recently.[22,23] However, owing to reduced nonlinear interaction length, SHG supported by flat optics has much lower efficiency than conventional nonlinear crystal and limits the nonlinear optical applications of flat optics. To overcome this challenge, double resonance

plasmonic nanostructures have been developed to enhance both excitation and emission process of SHG, and result in an orders of magnitude enhancement in SHG efficiency.[24,25]

1.3.3 Surface Enhanced Raman Spectroscopy (SERS)

Raman scattering is an inelastic scattering of photons by the material. Typically, the incident photons interact with the chemical bonds, excite the bond vibrations and transfer energy to the bond vibrational modes. Owing to energy loss during energy transfer, the Raman scattering photons have lower energy than incident photons. Therefore, by measuring the energy difference between incident photons and Raman scattering photons, we are able to calculate the bond vibrational energy indirectly. However, different from elastic Rayleigh scattering which efficiency is about 10^{-3} to 10^{-4}, Raman scattering efficiency is more than 4 orders magnitude lower and causes a significant challenge in detecting Raman scattering photons. To overcome this challenge, Van Duyne's group used rough surface from silver electrode to enhance the Raman scattering and significantly increase the efficiency. This new technique is called Surface Enhanced Raman Spectroscopy (SERS).[26] After more than three decades of research and development, the enhancement factor of SERS has been improved to 10^{10} to 10^{11} and capable for single molecule level detection.[27,28] To explain the SERS phenomenon, both electromagnetic theory and chemical theory have been proposed. In chemical theory, there is a high intensity charge transfer from metal surface to the adsorbing molecules, results in a huge enhancement of Raman scattering intensity.[29] In electromagnetic theory, LSPR magnifies the incident light intensity and create hotspots on nanostructure surface. Because both excitation and emission process have been enhanced as E^2, the total SERS signal is enhanced as E^4.[30]

1.4 Organization of Chapters

This dissertation is organized by the procedure of bottom-up total fabrication. As we introduced in section 1.1, bottom-up total fabrication includes four steps. In the first stage, we used wet chemistry method to synthesize 10 – 100 nm scale nanocrystals. In the second stage,

we used self-assembly methods to fabricate sub-micron scale meta-atoms. In the third stage, we used microfabrication methods to fabricate wafer-scale plasmonic devices. In the fourth stage, we used surface chemistry to functionalize the devices and then used them for different applications.

Chapter 2 is dedicated to the first stage of bottom-up total fabrication. It involves calculated electronic and optical properties of $CuSe_xS_{1-x}$ alloy, experimental synthesis of $CuSe_xS_{1-x}$ alloy, measured bandgap and LSPR of as-synthesized $CuSe_xS_{1-x}$ alloy.

Chapter 3 is dedicated to the second stage of bottom-up total fabrication. It involves Langmuir film preparation, designing and fabrication of first generation colloidal metasurface. Also, we performed a systematic study on the metasurface resonance modes and build-up a double resonance SHG device based on this colloidal metasurface

Chapter 4 is dedicated to the second stage of bottom-up total fabrication. It involves more deep understanding of first generation colloidal metasurface, including meta-atom density dependent study, molecular orientation dependent study and a demonstration of sensor design.

Chapter 5 is dedicated to the third and fourth stage of bottom-up total fabrication. It involves design of new microfabrication process and fabrication of second generation colloidal metasurface. Also, we designed a rapid sensor for polybrominated diphenyl ether (PBDE) molecules based on the second generation colloidal metasurface.

Chapter 6 is dedicated to the third stage of bottom-up total fabrication. It involves the design of wafer-scale characterization platform based on second generation colloidal metasurface. Also, we performed a systematic study and demonstrated this platform can be used to characterize different properties of 2-D materials.

Chapter 7 is dedicated to the fourth stage of bottom-up total fabrication. It involves surface functionalization with different alkanethiol and the critical chain length for quantum effects. Also, we did a fundamental study on the observed quantum effects and studied the relationship between quantum effects and near-field strength and SERS intensity.

References

(1) Farokhzad, O. C.; Langer, R. Impact of Nanotechnology on Drug Delivery. *ACS Nano* **2009**, *3* (1), 16–20. https://doi.org/10.1021/NN900002M/ASSET/IMAGES/MEDIUM/NN-2009-00002M_0003.GIF.

(2) Ingenia - Nanotechnology: big prospects for small engineering https://www.ingenia.org.uk/ingenia/issue-9/nanotechnology-big-prospects-for-small-engineering (accessed Jun 2, 2022).

(3) IBM Unveils World's First 2 Nanometer Chip Technology, Opening a New Frontier for Semiconductors - May 6, 2021 https://newsroom.ibm.com/2021-05-06-IBM-Unveils-Worlds-First-2-Nanometer-Chip-Technology,-Opening-a-New-Frontier-for-Semiconductors (accessed May 6, 2022).

(4) Coropceanu, I.; Janke, E. M.; Portner, J.; Haubold, D.; Nguyen, T. D.; Das, A.; Tanner, C. P. N.; Utterback, J. K.; Teitelbaum, S. W.; Hudson, ¸ Margaret H.; Sarma, N. A.; Hinkle, A. M.; Tassone, C. J.; Eychmüller, A.; Limmer, D. T.; Olvera de la Cruz, M.; Ginsberg, N. S.; Talapin, D. V. Self-Assembly of Nanocrystals into Strongly Electronically Coupled All-Inorganic Supercrystals. *Science (80-.).* **2022**, *375* (6587), 1422–1426. https://doi.org/10.1126/SCIENCE.ABM6753/SUPPL_FILE/SCIENCE.ABM6753_SM.PDF.

(5) Nicolaou, K. C.; Vourloumis, D.; Winssinger, N.; Baran, P. S. The Art and Science of Total Synthesis at the Dawn of the Twenty-First Century**. https://doi.org/10.1002/(SICI)1521-3773(20000103)39:1.

(6) Nicolaou, K. C.; Sorensen, E. J. (Erik J. . Classics in Total Synthesis I : Targets, Strategies, Methods. **1996**, 798.

(7) Kang, J.; Sangwan, V. K.; Wood, J. D.; Hersam, M. C. Solution-Based Processing of Monodisperse Two-Dimensional Nanomaterials. *Acc. Chem. Res.* **2017**, *50* (4), 943–951. https://doi.org/10.1021/ACS.ACCOUNTS.6B00643/ASSET/IMAGES/LARGE/AR-2016-006436_0007.JPEG.

(8) Mayer, K. M.; Hafner, J. H. Localized Surface Plasmon Resonance Sensors. *Chem. Rev.* **2011**, *111* (6), 3828–3857. https://doi.org/10.1021/CR100313V/ASSET/IMAGES/CR-2010-00313V_M029.GIF.

(9) Stiles, P. L.; Dieringer, J. A.; Shah, N. C.; Van Duyne, R. P. Surface-Enhanced Raman Spectroscopy. *http://dx.doi.org/10.1146/annurev.anchem.1.031207.112814* **2008**, *1* (1), 601–626. https://doi.org/10.1146/ANNUREV.ANCHEM.1.031207.112814.

(10) Aslam, U.; Rao, V. G.; Chavez, S.; Linic, S. Catalytic Conversion of Solar to Chemical Energy on Plasmonic Metal Nanostructures. *Nat. Catal. 2018 19* **2018**, *1* (9), 656–665. https://doi.org/10.1038/s41929-018-0138-x.

(11) Hsu, S. W.; On, K.; Tao, A. R. Localized Surface Plasmon Resonances of Anisotropic Semiconductor Nanocrystals. *J. Am. Chem. Soc.* **2011**, *133* (47), 19072–19075. https://doi.org/10.1021/ja2089876.

(12) Hsu, S.-W.; Bryks, W.; Tao, A. R. Effects of Carrier Density and Shape on the Localized Surface Plasmon Resonances of Cu 2−x S Nanodisks Other Examples of Anisotropic Cu 2 S Nanostructures with Large. *Chem. Mater* **2012**, *24*, 10. https://doi.org/10.1021/cm302363x.

(13) Manthiram, K.; Alivisatos, A. P. Tunable Localized Surface Plasmon Resonances in Tungsten Oxide Nanocrystals. *J. Am. Chem. Soc.* **2012**, *134* (9), 3995–3998. https://doi.org/10.1021/JA211363W/SUPPL_FILE/JA211363W_SI_001.PDF.

(14) Luther, J. M.; Jain, P. K.; Ewers, T.; Alivisatos, A. P. Localized Surface Plasmon Resonances Arising from Free Carriers in Doped Quantum Dots. *Nat. Mater.* **2011**, *10*. https://doi.org/10.1038/NMAT3004.

(15) Kristensen, A.; Yang, J. K. W.; Bozhevolnyi, S. I.; Link, S.; Nordlander, P.; Halas, N. J.; Mortensen, N. A. Plasmonic Colour Generation. *Nat. Rev. Mater. 2016 21* **2016**, *2* (1), 1–14. https://doi.org/10.1038/natrevmats.2016.88.

(16) Jain, P. K.; El-Sayed, M. A. Plasmonic Coupling in Noble Metal Nanostructures. *Chem. Phys. Lett.* **2010**, *487* (4–6), 153–164. https://doi.org/10.1016/J.CPLETT.2010.01.062.

(17) Peidong Yang, C. Z. N.; Dou, L.; Yang, P. Bandgap Engineering in Semiconductor Alloy Nanomaterials with Widely Tunable Compositions. *Nat. Rev. Mater. 2017 212* **2017**, *2* (12), 1–14. https://doi.org/10.1038/natrevmats.2017.70.

(18) Kelly, K. L.; Coronado, E.; Zhao, L. L.; Schatz, G. C. The Optical Properties of Metal Nanoparticles: The Influence of Size, Shape, and Dielectric Environment. *J. Phys. Chem. B* **2003**, *107* (3), 668–677. https://doi.org/10.1021/JP026731Y/ASSET/IMAGES/LARGE/JP026731YF00014.JPEG.

(19) Zhang, Y.; Zhen, Y. R.; Neumann, O.; Day, J. K.; Nordlander, P.; Halas, N. J. Coherent Anti-Stokes Raman Scattering with Single-Molecule Sensitivity Using a Plasmonic Fano Resonance. *Nat. Commun. 2014 51* **2014**, *5* (1), 1–7. https://doi.org/10.1038/ncomms5424.

(20) Fromm, D. P.; Sundaramurthy, A.; James Schuck, P.; Kino, G.; Moerner, W. E. Gap-Dependent Optical Coupling of Single "Bowtie" Nanoantennas Resonant in the Visible. *Nano Lett.* **2004**, *4* (5), 957–961. https://doi.org/10.1021/NL049951R/ASSET/IMAGES/MEDIUM/NL049951RN00001.GIF.

(21) Tabor, C.; Murali, R.; Mahmoud; El-Sayed, M. A. On the Use of Plasmonic Nanoparticle Pairs as a Plasmon Ruler: The Dependence of the near-Field Dipole Plasmon Coupling on Nanoparticle Size and Shape. *J. Phys. Chem. A* **2009**, *113* (10), 1946–1953. https://doi.org/10.1021/JP807904S/SUPPL_FILE/JP807904S_SI_001.PDF.

(22) Chen, W. T.; Zhu, A. Y.; Capasso, F. Flat Optics with Dispersion-Engineered Metasurfaces. *Nat. Rev. Mater. 2020 58* **2020**, *5* (8), 604–620. https://doi.org/10.1038/s41578-020-0203-3.

(23) Yu, N.; Capasso, F. Flat Optics with Designer Metasurfaces. *Nat. Mater. 2014 132* **2014**, *13* (2), 139–150. https://doi.org/10.1038/nmat3839.

(24) Park, S.; Hahn, J. W.; Lee, J. Y. Doubly Resonant Metallic Nanostructure for High Conversion Efficiency of Second Harmonic Generation. *Opt. Express* **2012**, *20* (5), 4856. https://doi.org/10.1364/OE.20.004856.

(25) Thyagarajan, K.; Rivier, S.; Lovera, A.; Martin, O. J. F. Enhanced Second-Harmonic Generation from Double Resonant Plasmonic Antennae. *Opt. Express* **2012**, *20* (12), 12860. https://doi.org/10.1364/OE.20.012860.

(26) Jeanmaire, D. L.; Van Duyne, R. P. Surface Raman Spectroelectrochemistry: Part I. Heterocyclic, Aromatic, and Aliphatic Amines Adsorbed on the Anodized Silver Electrode. *J. Electroanal. Chem. Interfacial Electrochem.* **1977**, *84* (1), 1–20. https://doi.org/10.1016/S0022-0728(77)80224-6.

(27) Blackie, E. J.; Le Ru, E. C.; Etchegoin, P. G. Single-Molecule Surface-Enhanced Raman Spectroscopy of Nonresonant Molecules. *J. Am. Chem. Soc.* **2009**, *131* (40), 14466–14472. https://doi.org/10.1021/JA905319W/ASSET/IMAGES/MEDIUM/JA-2009-05319W_0006.GIF.

(28) Le Ru, E. C.; Blackie, E.; Meyer, M.; Etchegoint, P. G. Surface Enhanced Raman Scattering Enhancement Factors: A Comprehensive Study. *J. Phys. Chem. C* **2007**, *111* (37), 13794–13803. https://doi.org/10.1021/JP0687908/SUPPL_FILE/JP0687908SI20070717_104641.PDF.

(29) Tsuneda, T.; Iwasa, T.; Taketsugu, T. Roles of Silver Nanoclusters in Surface-Enhanced Raman Spectroscopy. *J. Chem. Phys.* **2019**, *151* (9), 094102. https://doi.org/10.1063/1.5111944.

(30) Moskovits, M. Surface-Enhanced Raman Spectroscopy: A Brief Perspective. *Surface-Enhanced Raman Scatt.* **2006**, 1–17. https://doi.org/10.1007/3-540-33567-6_1.

Chapter 2

Computation-Motivated Design of Ternary Plasmonic Copper Chalcogenide Nanocrystals

Yuan Zeng[1,2], Paul H. Joo[2], Kesong Yang[1,2], Andrea R. Tao[1,2*]

[1]Department of NanoEngineering, University of California, San Diego, 9500 Gilman Drive MC 0448, La Jolla, California 92093-0448

[2]Materials Science and Engineering, University of California, San Diego, 9500 Gilman Drive, La Jolla, California 92093

*Email: atao@eng.ucsd.edu

Introduction

Copper (II) sulfide (CuS, covellite) is a highly self-doped p-type semiconductor[1] with free carrier densities on the order of 10^{22} cm^{-3} [2] that exhibit a strong LSPR at 1150 nm (1.08 eV) and a direct bandgap of 2.4 eV [3] at room temperature. The LSPR feature provides strong NIR absorption and use in potential applications, ranging from photothermal therapy[4], drug delivery, therapeutics, cancel cell diagnostic[5] to photoacoustic imaging[6]. In addition, because its optical bandgap energy is approximately twice that of the dipolar LSPR, CuS nanoparticles can be used as a platform for studying nonlinear optical phenomena[8] including plasmon-enhanced two-photon emission[7] and exciton-plasmon coupling.[9] To achieve higher efficiencies in these optical processes and to realize processes that rely on exciton-plasmon coupling, the ability to tune the LSPR and bandgap energies (i) relative to each other and (ii) over a wide energy range is desired.

Strategies to tune LSPR energy typically focus on changing parameters such as carrier density, nanoparticle size, or nanoparticle shape. Based on the free electron model, LSPR energy is expected to scale exponentially with carrier concentration.[10] For example, an increase in carrier density accomplished via cation doping in an n-type semiconductor (e.g., 10% Sn in indium oxide)[11] or anion doping in p-type semiconductor (e.g., 2.3% Se in CuS)[7] can increase LSPR energy by 20%. For CuS, tuning carrier concentration is limited by the stability of the crystal phase; for the $Cu_{2-x}S$ system, the carrier concentration of CuS represents the upper limit for self-doping via Cu vacancies. Further, while LSPR energy tuning through nanoparticle size[12] and shape[13–15] is well-studied for Ag and Au nanoparticles, the lower carrier concentrations exhibited by copper chalcogenides (10^{21}-10^{22} cm^{-3}) limits LSPR excitation to below 1.38 eV (~900 nm) regardless of nanoparticle geometry.[16]

A complementary strategy is to tune the energy of the optical bandgap associated with CuS nanoparticles. Alloying is a well-known strategy in the semiconductor industry for bandgap engineering[17,18], where the bandgap of an alloyed material is manipulated by controlling the stoichiometry of the constituent components. Alloying has been demonstrated as particularly

useful for mixed chalcogen systems such as $CdSe_xTe_{1-x}$ and $ZnSe_xTe_{1-x}$. According to Vegard's Law[19], the bandgap of an alloy with consituents A and B can be expressed as:

$$E_{g,AB} = xE_{g,A} + (1-x)E_{g,B} - bx(1-x)$$

where $E_{g,AB}$ is the alloy bandgap, $E_{g,A}$ is the bandgap of material A, $E_{g,B}$ is the bandgap of material B, and *x* is the molar fraction of constituent A.[20] The bowing parameter, *b*, is included to correct for nonlinear relationships between alloy bandgap and molar fraction[21], which is particularly pronounced in mixed chalcogens. In these alloys, *b* is typically high because of strong competition between different anions in charge trapping and charge loss, resulting in a large variation of the charge distribution across the different metal-chalcogen bonds and a significant valence-band offset.

For plasmonic CuS nanoparticles, alloying with CuSe (klockmannite) to generate a ternary $CuSe_xS_{1-x}$ semiconductor alloy (where $0 \leq x \leq 1$) has the potential to tune the optical bandgap adequately without significantly altering free carrier densities, and thus, the characteristic LSPR energies of the nanoparticles. CuSe is a semiconductor with a direct bandgap in the range of 1.66-1.75 eV[22] and is known to possess a similar crystal structure (hexagonal,P63/mmc) and carrier density as CuS. Owing to the large size difference between different chalcogen atoms, one major challenge in forming mixed micron-scale (> 1000 nm) chalcogenide compounds is the large lattice mismatch between different chalcogenide compounds (e.g. a 5% size difference between S atoms and Se atoms) which can break structure under thermal stress. However, alloyed semiconductor nanomaterials (< 40 nm) respond to dissimilar expansion elastically, result in a much larger tolerance for atomic bond misfit and thus provide more opportunities for growing new alloy compositions.[23,24]

To-date, efforts have demonstrated limited success with both bandgap tuning and retaining the desired plasmonic properties in $CuSe_xS_{1-x}$ alloys. Xu et al. reported the synthesis of

$CuSe_xS_{1-x}$ alloys with tunable composition by co-reacting Cu ions with controlled ratios of S and Se precursors.[25] However, the reactivity difference between the respective chalcogen precursors at low reaction temperatures (~90°C) resulted in a large polydispersity of both size and shape of the $CuSe_xS_{1-x}$ nanocrystals. Co-reaction methods that promote epitaxial growth/deposition tend to require higher temperatures during the nucleation and growth process, yielding more polydisperse nanocrystals.[26–28] Ion exchange is an alternative method to co-reaction that achieves more monodisperse samples of alloyed nanocrystals. While cation exchange is a widely used method in metal chalcogenide alloy synthesis[29–32], anion exchange typically requires longer reaction times and higher reaction temperatures since exchange must occur between species with large ionic radii and lower mobilities.[33,34] A commonly observed structure from the anion exchange of metal chalcogenide nanostructures are hollow morphologies corresponding to the Kirkendall effect.[35] These hollow structures result from the discrepancy in diffusion rate between outward transport and inward diffusion during anion exchange. Faster outward transport produces inner vacancies that are progressively generated during nanocrystal synthesis.[36] More recently, Lim et al. reported a promising strategy for anion exchange that avoids formation of these hollow structures using an anion extracting reagent to facilitate the exchange process. They successfully transformed solid oxide (Fe_3O_4 , ZnO, MnO) nanoparticles to their solid sulfide counterparts using a complexed extracting agent that contains oxophilic and nucleophilic functional groups.[37]

Here, we report a method to synthesize solid $CuSe_xS_{1-x}$ nanodisks using an anion exchange protocol starting with a CuS nanodisk, which serves as an initial template or seed for alloy formation. This method overcomes the challenges of co-reacting S- and Se-based precursors, producing plasmonic nanodisks with tunable alloy compositions where Se atomic percentage is controlled by varying reaction time. First-principles density functional theory (DFT) is used to understand how the optical and plasmonic properties of such nanostructures is affected by alloy composition. The ability to use DFT calculations to provide predictions on the plasmonic

properties of a given nanostructure is advantageous because it does not require *a priori* knowledge of a material's composition- and wavelength-dependent bulk dielectric function, which can be difficult to obtain experimentally. This allows us to probe new alloy compositions, such as $CuSe_xS_{1-x}$, which have the potential to support strong LSPRs but for which clear structure-optical function relationships do not exist. Our experimental results from the anion exchange process are then compared against DFT results. The ability to tune both optical bandgap and LSPRs via alloy composition is potentially enabling for the study of light-matter interactions these plasmonic semiconductor nanostructures.[9]

Experimental Methods

DFT Computation. First-principles density functional theory (DFT) calculations were performed using the Vienna Ab initio Simulation Package (VASP).[38] The projector-Augmented Wave (PAW) potential was employed for the electron-ion interactions treatment[39] and the Generalized Gradient Approximation (GGA) parameterized by Perdew-Burke-Ernzerhof (PBE) was used for the electron exchange-correlation functional.[40] The cut-off energy was set to 400 eV and 5 x 5 x 2 k-point meshed centered at Γ point was used. The cell parameters and all the atoms were relaxed until all components of the residual forces became less than 0.01 eV Å-1 and the tolerance of convergence for the self-consistent-field iteration was set to 10-5 eV.

Chemicals. Oleylamine (70%, technical grade), Oleic acid (90%, technical grade), Sulfur (100 mesh particle size, reagent grade) were purchased from Sigma-Aldrich.1-Octadecene (90%), Selenium (99.999%, metal basis) were purchased from Fisher Scientific. Copper (II) nitrate, hemipentahydrate (>98%, ACS reagent) was purchased from VWR International, LLC. All reagents were used as purchased.

Preparation of CuS templates. This synthesis protocol was modified from Brandon C. Marin et al.[7] that 464 mg Copper (II) nitrate, hemipentahydrate, 5 mL Oleylamine, 15 mL 1-Octadecene was mixed in a 100 mL round bottom flask (RBF) and sonicated till fully disperse (0.1 M Cu precursor). 100 mg Sulfur powder was added into the Cu precursor solution and heated in 160 °C silicone oil bath for 35 minutes. After reaction completed and cooled down to room temperature, 20 mL ethanol was added and centrifuged at 3K rpm for 7.5 min. The precipitation was dispersed in chloroform/ethanol mixture, centrifuged at 3K for 15 min, and repeat once. Finally, the washed nanocrystals were dispersed in 6 mL chloroform for later use.

Preparation of 0.2 M Se-oleate precursor. This synthesis protocol was modified from Xin Liu et al.[41] that 474 mg (6mmol) selenium and 30 mL oleic acid was mixed in a 100 mL RBF, sonicated 5 min, degassed at room temperature for 1 hour and filled with nitrogen gas. Then, the RBF was heated in a 220 °C aluminum heating mantle for 8 hours, until all Se powder dissolved (transparent orange color solution). Finally, the as-made Se-oleate precursor was cooled in air for 20 min, transferred to glass vial (5mL in each vial) and stored for later use. When Se-oleate precursor cooled down to room temperature, it was solidified and has yellowish color. For the synthesis batches named as 0.1M Se and 0.15M Se in Figure 4, the only variable is amount of selenium added into oleic acid. Instead of 474 mg selenium, we added 355.5 mg selenium to prepare 0.15M Se-oleate and 237 mg selenium to prepare 0.1M Se-oleate.

Synthesis $CuSe_xS_{1-x}$ with anion exchange method. 3 mL oleylamine, 9 mL 1-Octadecene, 1 mL CuS (in chloroform) was added in 50 mL RBF, degassed at room temperature for 30 min and filled with nitrogen. To remove excess chloroform and make reaction temperature approach to equilibrium, the mixture was pre-heated in 160 °C silicone oil bath for 15 min. During the pre-heating process, 5 mL solid Se-oleate was placed in 80 °C oven for melting. When reaction started (0 min), 5 mL Se-oleate was injected into the 50 mL RBF and keep varied time, from 10 min to 240 min and cooled in air when reaction completed. To remove excess precursor

and capping ligand, 20 mL ethanol was added to as-made nanocrystals and centrifuged at 3K for 7.5 min to precipitate down nanocrystals. These nanocrystals were washed with 1:2 ratio chloroform: ethanol for three times and dispersed in 4 mL chloroform for later use.

Characterization: TEM samples were prepared by dissolving as-made nanocrystals in chloroform and drop-casted on air-water interface, then transferred to 200 mesh Carbon-film Cu grid by dip-coating method. The TEM images were obtained with FEI Tecnai G2 Sphera with a 200kV LaB_6 filament and Gatan Ultrascan 1000 UHS CCD camera. SEM and Raman samples were prepared by drop-casting ~ 50 uL as-made nanocrystals to 0.5 cm X 0.5 cm ethanol washed silicon wafer substrate. EDS results were obtained with Philips XL30 ESEM with an Oxford EDS detector. Raman results were obtained with Renishaw inVia confocal Raman microscope, the setting we used is 514 nm excitation, 2400 grating, 10 seconds exposure time, 10% power and 10 accumulations. XRD samples were prepared by drop-casting ~ 90 uL as-made nanocrystals on zero background single crystal silicon substrate. XRD pattern was obtained with Bruker D8 Advanced XRD and scan setup is 1 second dwell time and 0.04° step size. UV-VIS spectra were obtained with PerkinElmer Lambda-1050 UV-vis-NIR spectrophotometer (three-detector module), we used standard quartz cuvette with 1 cm path length and scan setup is wavelength range from 300 nm to 2000 nm and 1 nm step size.

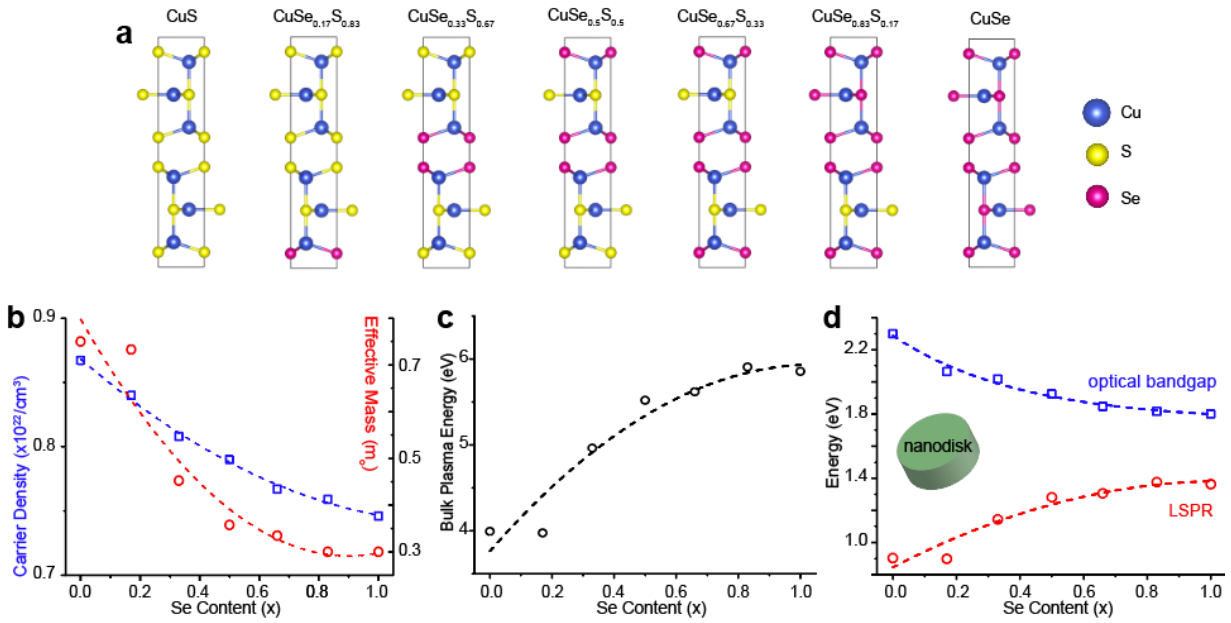

Figure 2.1 | DFT simulation results probing the fundamental materials properties of various $CuSe_xS_{1-x}$ alloys. (a) Representative schematics of the various $CuSe_xS_{1-x}$ unit cells used in DFT models for different Se concentrations. High-throughput algorithms are used to probe all possible non-equivalent unit cell structures. (b) Calculated carrier density (blue) and effective mass (red) of $CuSe_xS_{1-x}$ alloys as a function of Se content. (c) Predicted values of bulk plasma frequency based on DFT-obtained values in (b). (d) Predicted optical bandgap energy (blue) for $CuSe_xS_{1-x}$ alloys and LSPR energy (red) for $CuSe_xS_{1-x}$ nanodisks as a function of Se content.

To understand the influence of Se content (herein defined as the total atomic ratio, x= [Se]/[S+Se]) on the fundamental electronic and optical properties of $CuSe_xS_{1-x}$, we investigated carrier density, effective mass, and bandgap of alloys with varying composition using DFT calculations. (For details on these calculations, see Experimental Section) Geometrical representations of the unit cells used to model the various compositions of $CuSe_xS_{1-x}$ (with $0.17 \leq x \leq 0.83$) are shown in Figure 2.1a. In principle, there are multiple structures for the alloyed $CuSe_xS_{1-x}$ system at any given x, which are differentiated by the different occupation sites of Se atoms. For each x, we calculated the total energy for all the possible non-equivalent structural models using high-throughput first-principles calculations and studied the formation probability for each model based on the Boltzmann distribution.[42] Figure 2.1 shows the $CuSe_xS_{1-x}$ structure model (unit cell) with the highest formation probability at each value of x. Figure 2.1b shows the

calculated carrier density (blue line) and effective mass (red line) for $CuSe_xS_{1-x}$ as a function of *x*. The weighted average carrier density and the hole effective mass were calculated by considering all the non-equivalent structural models with their room-temperature formation probability at each value of *x*. As Se content increases from *x* =0 to *x*=1, the carrier density decreases 14% from 0.867×10^{22} cm^{-3} to 0.746×10^{22} cm^{-3}. Our calculations indicate that this decrease is primarily attributed to physical lattice expansion and that the number of carriers per unit cell does not change significantly. Since Se possesses a larger atomic radius than S, the calculated unit cell volume for CuSe is 11.6% larger than CuS because of large Cu-Se bond. This atomic "misfit" also induces a structural distortion in the $CuSe_xS_{1-x}$ cell between $0.33<x<1$. We also observe that the hole effective mass decreases by 60% from 0.75 to 0.3 as Se content is increased, attributed to the more diffuse 4p orbitals of the Se atom compared to the 3p orbitals of the S atom. The valence band of CuSe is mainly composed of Se 4p orbitals, whereas the valence band of CuS is mainly composed of S 3p orbitals, as confirmed from our DFT calculations. The more diffuse 4p orbitals lead to more dispersive valence bands and thus result in a lower hole effective mass. Using these data generated from DFT calculations, we calculated the bulk plasma energy of $CuSe_xS_{1-x}$ as a function of Se content,[10] as shown in Figure 2.1c. The bulk plasma energy increases nonlinearly with Se content from 3.99 eV at *x*=0 to 5.86 eV a at *x*=1. These values are comparable with experimental and simulated CuS bulk plasma energies (near 4.5 eV[43]), indicating that our computational model is reliable for predicting these core materials parameters.

Table 2.1 | DFT-derived LSPR Energy. (a) Plasmon frequency (ω_p) is calculated with following equation: $\omega_p = \sqrt{\frac{Ne^2}{m^*\epsilon_0}}$, where ω_p = plasmon frequency, n = carrier density, e = elementary charge, m = electron mass and ϵ_0 = permittivity of free space (b) LSPR frequency (ω_{sp}) is calculated with following e[43,44]: $\omega_{sp} = \sqrt{\frac{{\omega_p}^2}{1-\varepsilon_{r,2}} - \gamma^2}$, where $1 - \varepsilon_{r,2}$= 20.51 (calculated with parameters from 21 nm diameter, 5 nm thickness CuS nanodisk[43]) and γ=0.3.

Se content	Carrier density ($\times 10^{+21}$ cm^{-3})	Hole effective mass (m_0)	plasmon frequency ($\times 10^{+15}$ rad/s)	bulk plasma energy (eV)	LSPR Energy (eV)
0	10.1	0.75	6.55	4.31	0.903
0.17	9.674	0.73	6.48	4.27	0.893
0.33	9.485	0.45	8.17	5.38	1.15
0.50	9.382	0.36	9.14	6.02	1.29
0.66	9.129	0.33	9.32	6.13	1.32
0.83	8.953	0.30	9.75	6.41	1.38
1	8.841	0.30	9.68	6.37	1.38

These DFT-derived parameters can be used to provide a general roadmap for the synthesis of ternary $CuSe_xS_{1-x}$ semiconductor nanocrystals whose optical bandgap can be tuned relative to the LSPR energy. The LSPR energy of $CuSe_xS_{1-x}$ nanoparticles can be calculated using the DFT-derived bulk plasma energy. For $CuSe_xS_{1-x}$ nanodisks, the frequency of the longitudinal dipolar LSPR can be approximated using Mie theory[44] and by inputting a shape factor for a nanodisk aspect-ratio of 5. (Table 2.1). The corresponding energy of the dipolar LSPR can then be compared against the optical bandgap energies derived from DFT calculations, as shown in Figure 2.1d. As Se content increases from *x*=0 to *x*=1, the calculated LSPR energy (red circles) increases from 0.83 eV to 1.26 eV. The optical bandgap (blue squares) decreases from 2.3 eV at *x*=0 (the E_g for CuS) to 1.8 eV at *x*=1 (the E_g for CuSe) and can be fit to Vegard's law to obtain a bowing parameter of *b*=0.51. It should be noted that first-principles calculation methods intrinsically underestimate the value of the bandgap.[45–47] However, the observed bowing parameter is consistent with the expected competition between S and Se anions for trapped charges[21] and charge redistribution associated with a change in bond strain.[48] The predicted values are also in agreement with previous observations for $CuSe_xS_{1-x}$ synthesized by a co-reaction method.[25] These data suggest the possibility of $CuSe_xS_{1-x}$ compositions where the optical

bandgap and LSPR energies differ by only a few tenths of an eV, sufficient for weak to moderate plasmon-exciton coupling.

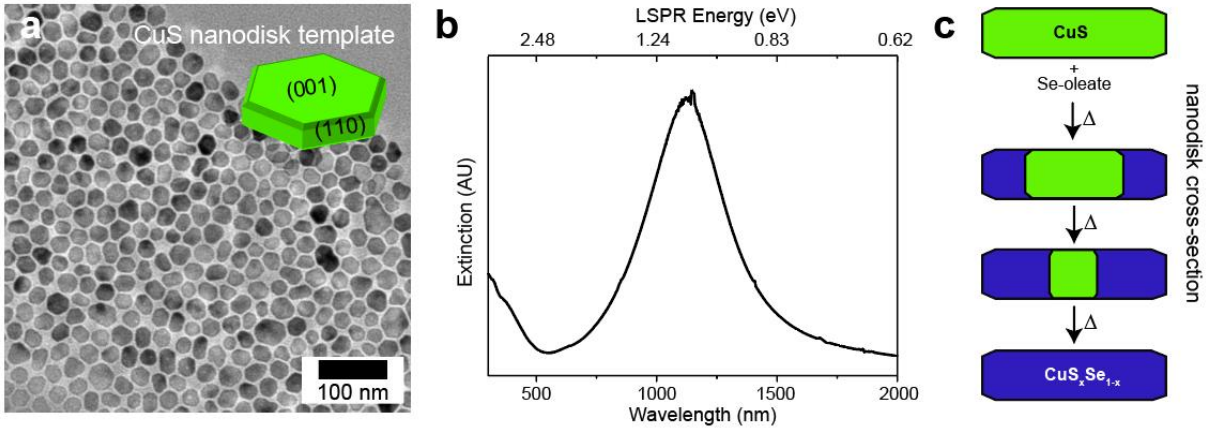

Figure 2.2 | CuS nanodisk templates. a) TEM image of as-synthesized CuS nanodisks, which show faceting due to stabilization of the (110) crystal face during nucleation and growth. b) UV-VIS spectrum of colloidal CuS nanodisks dispersed in $CHCl_3$ showing the characteristic dipolar, longitudinal LSPR mode. c) Schematic of the anion-exchange reaction for the CuS nanodisk, showing the displacement of S atoms in CuS (green) by Se to form a $CuSe_xS_{1-x}$ phase (blue). Influx of the Se atoms occurs at the (110) side facets of the nanodisk, which are less protected by oleate/oleylamine capping ligands than the (001) basal planes.

To experimentally realize these ternary semiconductor nanocrystals, we designed a two-step anion exchange reaction that utilizes a CuS nanodisk as the starting template (Details provided in the Methods section). In the first step, CuS nanodisks were prepared by reacting sulfur powder and $Cu(NO_3)\cdot 2.5H_2O$ at 160°C in a mixture of 1-octadecene and oleylamine for 35 min, according to a previously published protocol.[7] The as-made CuS nanodisks have an average diameter of 24.6 nm and an aspect ratio of 3.6, as confirmed by electron microscopy (Figure 2.2a). Figure 2.2b shows an optical absorption spectrum for a CuS nanodisk dispersion with characteristic peaks at 468 nm (2.65 eV) attributed to the optical bandgap and at 1145 nm $\pm$ 20 nm (1.08 eV $\pm$ 0.02 eV) attributed to the longitudinal, dipolar LSPR mode. In the second step, the as-made CuS nanodisks were used as templates for anion exchange employing a Se-oleate complex as the Se source. The Se-oleate precursor was prepared by reacting Se powder in oleic acid at 220°C under nitrogen.[41] The Se content of the nanocrystals can be tuned by controlling the anion exchange time, shown schematically in Figure 2.2c. Given the crystallographically flat

basal facets of the CuS nanodisk and strong oleylamine adsorption on these facets, S/Se ion exchange is expected to occur primarily at the nanodisk edges, resulting in an anisotropic and laterally directed exchange process.[49,50]

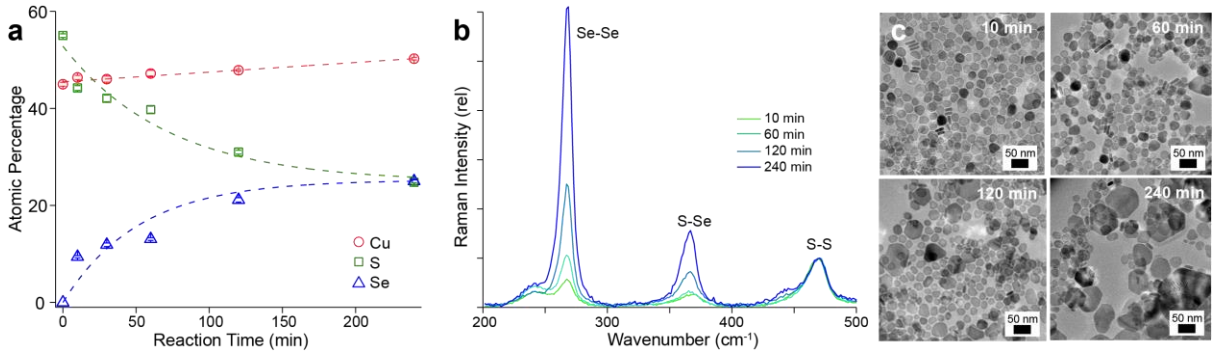

Figure 2.3 | Characterizing the anion exchange process. a) Plot of the time-dependent atomic percentages of Cu (red), S (green), and Se (blue) of the $CuSe_xS_{1-x}$ alloy nanodisks during the reaction, as measured by EDS. b) Raman spectra obtained at various reaction times in the low wavenumber range show chalcogen vibrational modes indicative of alloy formation. Peak intensities are normalized relative to the intensity of the S-S stretch peak within each spectrum. c) TEM images of the resulting nanodisks at varying times during the anion exchange reaction, showing a change in the nanodisk size distribution at later reaction times.

The resulting $CuSe_xS_{1-x}$ nanocrystals were characterized by energy-dispersive X-ray spectroscopy (EDS), Raman spectroscopy, and transmission electron microscopy (TEM). EDS results clearly indicate that Se atoms displace S atoms with throughout the anion exchange reaction while retaining the 1:1 metal-to-chalcogen stoichiometry. (Figure 2.3a). As the anion exchange progresses from 10 min to 240 min, the Cu atomic percentage increases by 11.7% from 44.97% to 50.25%, which indicates a decrease in Cu vacancies and the absence of Cu-rich impurity phases, such as $Cu_2Se_xS_{1-x}$ alloys, in the ternary nanocrystals. The Se atomic percentage increases exponentially (from 9.4% to 25%) while the S atomic percentage decreases exponentially (from 44.2% to 24.8%) over the same reaction period and with equal rates. This corresponds to an overall stoichiometry change from $CuSe_{0.18}S_{82}$ at 10 min to $CuSe_{0.50}Se_{0.50}$ at 240 min, and the reaction kinetics fit well to a second-order model. (Appendix A, A1) Figure 2.3b shows Raman spectra of the different $CuSe_xS_{1-x}$ products as a function of anion exchange time, with specific attention given to the S-S stretching band (442-470 cm^{-1}), the Se-Se stretching band

(260-274 cm^{-1}), and the Se-S stretching band (365-380 cm^{-1}). For comparison across these different alloy products, all spectra were normalized relative to the intensity of the S-S stretching band. As anion exchange progresses from 10 min to 240 min, both the Se-Se and S-Se bands increase in intensity, confirming the formation of a ternary $CuSe_xS_{1-x}$ alloy.[25] Figure 2.3c shows TEM images of the $CuSe_xS_{1-x}$ nanocrystals with respect to reaction time, showing that the nanodisks maintain their shape and display no evidence of phase segregation. While average nanodisk diameter stays constant at 24 nm ±2 nm, the size distribution of the nanodisks increases significantly with reaction time, as given by the increase in the standard deviation of average diameter from ±3.2 at 10 min to ±7.3 at 240 min. This is seen in the appearance of larger nanoplates after 120 min. This increase in size dispersity is attributed to Ostwald ripening, as observed in the synthesis of other metal chalcogenide nanocrystals (e.g. PbS quantum dots) in the presence of oleylamine. Oleylamine is hypothesized to react with unpassivated surface atoms, leading to nanocrystal etching and an increase in nanoparticle size distribution.[51] However, because CuS nanodisks adopt a preferential growth direction normal to the <001> direction[52], nanodisk thickness remains fairly constant at 7.3 ± 0.8 nm during the anion exchange process. Thus, a significant change in the transverse dipolar LSPR mode due to an increase in polydispersity is not expected.

Interestingly, the ternary $CuSe_xS_{1-x}$ nanodisks are quite different from the hollow nanocrystals observed for other anion exchange reactions. For example, when S anions are used to displace O anions using ZnO or Cu_2O nanocrystal templates, spherical shells form due to the well-known Kirkendall effect.[53–56] In these reactions, hollow morphologies result from fast anion diffusion from the nanocrystal core. In our system, no evidence of hollow structures are observed, likely due to the small size mismatch between S^{2-} and Se^{2-} anions (an 8% mismatch) versus S^{2-} and O^{2-} anions (a 35% size mismatch). As a result, the difference in anion diffusivity between S^{2-} and Se^{2-} is expected to be negligible. Another contribution to the formation of solid ternary

$CuSe_xS_{1-x}$ nanodisks is that anion exchange may occur preferentially at the CuS/$CuSe_xS_{1-x}$ interface rather than at the $CuSe_xS_{1-x}$/solution interface. This may be due to strong ligand-surface interactions that more effectively passivate the nanocrystal surface.[57]

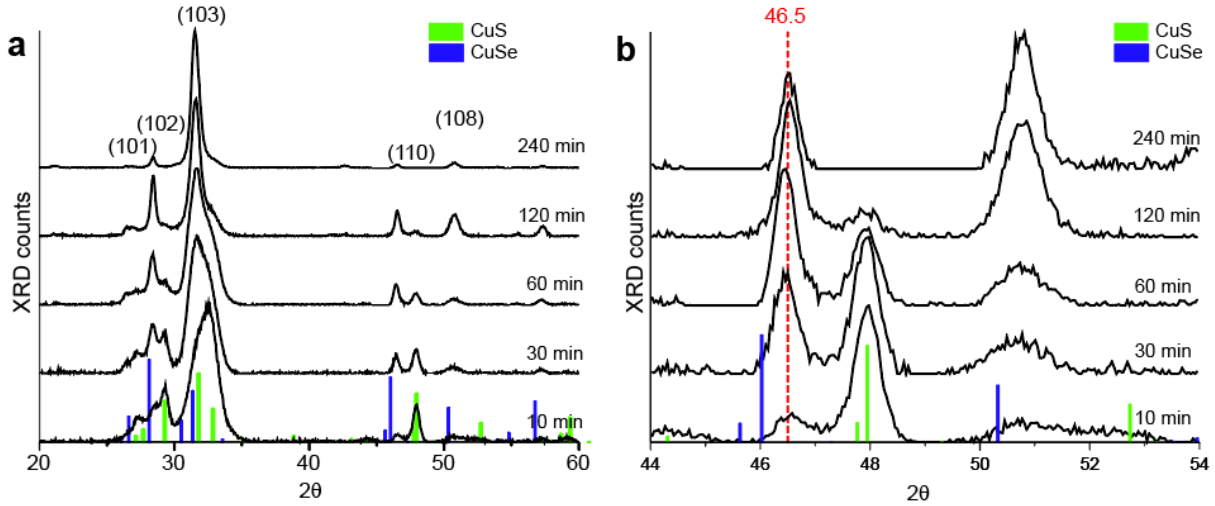

Figure 2.4 | XRD analysis of ternary phase nanodisks. a) XRD pattern (from 20° to 60°) for as-made nanodisks at different anion exchange times. (b) Close-up of XRD peaks corresponding to the (110) plane, with the 2θ=47.95° peak (green) corresponding to (110) in CuS reference pattern [JCPDS Data File No.-04-004-8687] and 2θ=46° (blue) corresponding to (110) in CuSe reference pattern [JCPDS Data File No.-00-020-1020]. The peak at 2θ=46.5 (red) corresponds to the ternary $CuSe_xS_{1-x}$ alloy.

To gain further insight into the nanodisk morphology, we carried out X-ray diffraction (XRD) analysis of the ternary alloy products. Figure 2.4a shows XRD pattern (from 2θ = 20-60°) as a function of anion exchange time. As the reaction proceeds from 10 to 240 min, the covellite CuS peaks (green bars) gradually decrease and a new set of peaks appear, which are attributed to a $CuSe_xS_{1-x}$ alloy because they lie at a smaller inter-plane distance than CuSe (blue bar) and a larger inter-plane distance than CuS. This confirms the formation of a CuS/$CuSe_xS_{1-x}$ heterostructure that is composed of a $CuSe_xS_{1-x}$ alloyed shell and a shrinking CuS core. As reaction time increases to 240 min, the relative intensity of the alloy (103) peak increases dramatically and becomes dominant in the XRD pattern, which indicates a significant morphology change that form large nanoplates. Figure 2.4b shows a close-up of the XRD pattern between 44-54°. The peak at 48.0° corresponds to CuS (110) and the peak at 46.5° corresponds to the (110) plane of the $CuSe_xS_{1-x}$ alloy. As anion exchange progresses, the $CuSe_xS_{1-x}$ peak stays at a

constant 2θ, indicating that the composition of the $CuSe_xS_{1-x}$ alloy does not change during the reaction. However, the relative intensity of the $CuSe_xS_{1-x}$ (110) peak increases, consistent with a shrinking CuS core. After 240 min of anion exchange, the CuS (110) peak completely disappears, indicating that the anion exchange reaction has run to completion and that a homogenous $CuSe_xS_{1-x}$ nanodisk should be the final end-product.

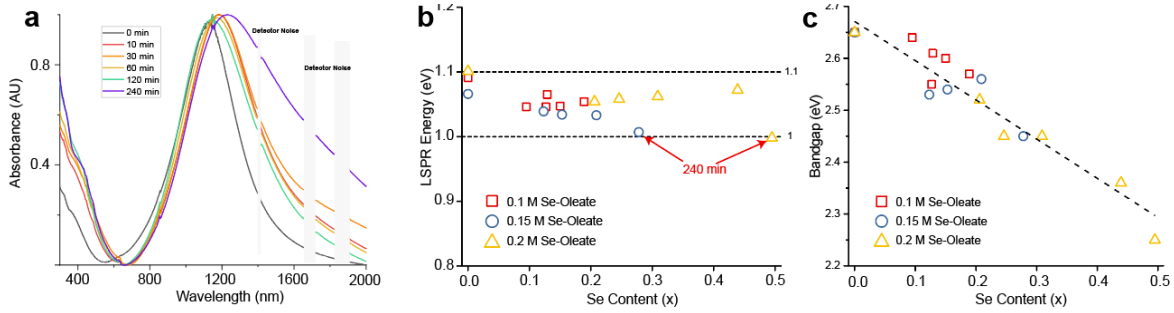

Figure 2.5 | Optical characterization of ternary phase plasmonic nanodisks. a) UV-Vis spectra of colloidal nanodisk dispersions for different anion exchange reaction times. b) Peak LSPR energies plotted as a function of anion exchange reaction times for reactions run with different Se-oleate concentrations. (c) Measured optical bandgap energies plotted as a function of anion exchange reaction times for reactions run with different Se-oleate concentrations.

Finally, we characterized the optical properties of the resulting alloyed $CuSe_xS_{1-x}$ nanodisks by UV-VIS absorption spectroscopy. Figure 2.5a shows absorption spectra for $CuSe_xS_{1-x}$ nanodisks with different anion exchange times. As anion exchange progresses from 0 min to 240 min, the full width at half maximum (FWHM) of the peak corresponding to LSPR excitation increases from 282 nm to 717 nm and LSPR wavelength experiences a slightly red shift from 1126 nm to 1242 nm. The observed LSPR broadening can be attributed to the increase in size dispersity, variant amount of alloy between nanocrystals (Appendix A, A2) and the formation of larger nanoplates after 120 min. To account for this ensemble effect, which varies across a reaction batch, we carried out anion exchange at various reaction times using three different Se-oleate concentrations (0.1 M, 0.15 M, and 0.2 M Se-oleate) to achieve a range of nanodisks with varying Se content. Figure 2.5b shows that the dipolar LSPR energy lies within a 0.1 eV (~10%) energy range when Se content is increased from 0 to 0.5. This is discrepant from our DFT-derived

calculations (Figure 2.1d), which predict LSPR energy to increase with Se content. Instead, we observe nearly constant (~0.05 eV) LSPR energy for the alloyed nanodisks with increasing Se content, which consistent with observations by Manna et al. in a similar $Cu_{2-x}Se_yS_{1-y}$ system[58]. The outliers to this are alloyed nanodisks obtained after a 240 min reaction time with high (> 0.15 M) Se-oleate concentrations (indicated by red arrows), which we attribute to the formation of larger nanoplates as confirmed by TEM.

This negligible change in LSPR energy is at odds with our observations from our DFT results, which suggest that that LSPR should blueshift. There are three potential mechanisms not included in our DFT calculation can cause this deviation. The first possibility is that the anion exchange process results in a decrease in free carriers in the alloy, which cancels out the effect of the increasing Se content. This is supported by our observation that there is an 11.7% increase in Cu content during anion exchange. (Figure 2.3a) This significant increase in Cu content suggests that anion exchange may promote a decrease in Cu vacancies and subsequent decrease in the number of free carriers (holes). As second possibility is that the surface of the alloyed nanocrystals may interact with adsorbates that modulate free carrier density. For example, our DFT models no not account for the presence of chemisorbed oleic acid, which has been reported to contribute to a decrease in hole carrier density for Cu chalcogenide nanostructures.[59] However, we carried out post-synthetic modification of the CuS nanocrystals (with oleic acid, oleylamine, and 1-dodecanethiol) that shows changing the adsorbed species on the nanodisk surfaces lead to a negligible redshift (0.02 eV) in LSPR (Appendix A, A3). A third possibility is that the dielectric constant in our calculations for LSPR energy do not take into account variable Se content. However, this is not likely to play a large role given that the CuS dielectric constant (3.8 to 4.4)[60] in the relevant wavelength range is very close to the CuSe dielectric constant (3.756)[61]

Figure 2.5c plots the measured bandgap energies of the alloyed nanodisks as a function of Se content, showing a clear linear relationship. As Se content increases from x=0 to x=0.5, the

bandgap energy can be directly tuned from 2.66 eV to 2.26 eV, respectively. This linear relationship is different from previous experiments using a co-reaction method[25] and our simulation results in which the nonlinear relationship (i.e. bowing) between bandgap energy and Se content was observed. Because the thickness of the nanodisks do not change significantly during anion exchange and the nanodisk diameter is one order of magnitude larger than the exciton Bohr radius (3-5 nm) of Cu_xS,[62,63] we do not expect that quantum confinement effects to play a significant role in bandgap tuning. Rather, we believe this difference originates from the biphasic morphology of our nanodisk, which consists of an alloyed shell and an inner CuS core. Se content increases as the thickness of the alloy shell increases; however, the composition of the alloy remains constant. In contrast, our simulation results assume that the nanodisks adopt a homogeneous alloyed nanostructure, where increasing Se content is obtained by increasing the value of *x* in the $CuSe_xS_{1-x}$ alloy. It is likely that the heterogeneous $CuSe_xS_{1-x}$/CuS core-shell nanodisks are able to relax bond strain and charge redistribution through the introduction of an interface, resulting in a nearly zero bowing parameter.

Conclusion

Overall, this work uses both DFT calculations and chemical synthesis to study the electrical and optical properties of alloyed $CuSe_xS_{1-x}$ nanocrystals. Using first-principles electronic structure calculations, we built a homogeneous $CuSe_xS_{1-x}$ model and calculated carrier density, carrier effective mass, and plasma energy with respect to Se content. Our calculations show the potential for wide range tunability in both LSPR energy and optical bandgap, indicating that these alloyed nanomaterials are good candidates for exciton-plasmon coupling. Motivated by these results, we designed a novel anion exchange protocol that utilizes CuS nanodisks as a template for the synthesis of $CuSe_xS_{1-x}$ nanocrystals. The synthesized nanocrystals exhibit a bandgap that is tunable from 2.66 eV to 2.26 eV by changing Se content between $0<x<0.5$, whereas LSPR

energy remains relatively unchanged. Future efforts will explore how exotic chalcogen compositions can be used to close the exciton-LSPR energy gap, including the exploration of CuTe alloys, given that CuTe has an even smaller direct bandgap (1.1 to 1.5 eV)[64] than CuSe. Discrepancies between our DFT and experimental results are attributed to two factors: (i) the difference in nanocrystal structure (homogenous alloy in our DFT calculations vs. a heterogeneous core-shell structure in experiments) and (ii) an increase in Cu content that modulates free carrier concentrations in the synthesized alloyed nanodisks. As a result, the synthesized nanodisks have a larger exciton-plasmon energy gap than we predicted in our DFT-based calculations. These discrepancies point to the ever-present need for rational alloyed nanocrystal synthesis, both for the accurate validation of DFT models that can lead to predictive materials design and for achieving the tight compositional and morphological control required for enabling strong light-matter interactions such as exciton-plasmon coupling.

Acknowledgments

The authors would like to thank the NanoEngineering Research facility (NE-MRC), Nano3 facility of SDNI (NSF ECCS # 2025752) and Cryo-EM facility at University of California, San Diego for the use of their facility.

ART acknowledges National Science Foundation under award number CHE-1807891.

KY acknowledges the American Chemical Society Petroleum Research Fund under award number 55481-DNI6 and National Science Foundation under award number ACI-1550404. This work used the Extreme Science and Engineering Discovery Environment (XSEDE), which is supported by National Science Foundation grant number ACI-1548562.

Chapter 2, in full, is a reprint of the material as it appears in Chemistry of Materials 33.1 (2020): 117-125. Yuan Zeng, Paul Hyunggyu Joo, Kesong Yang, and Andrea R. Tao. The dissertation author was the primary investigator and author of this paper.

References

(1) Luther, J. M.; Jain, P. K.; Ewers, T.; Alivisatos, A. P. Localized Surface Plasmon Resonances Arising from Free Carriers in Doped Quantum Dots. *Nat. Mater.* **2011**, *10*. https://doi.org/10.1038/NMAT3004.

(2) Hsu, S. W.; Ngo, C.; Tao, A. R. Tunable and Directional Plasmonic Coupling within Semiconductor Nanodisk Assemblies. *Nano Lett.* **2014**, *14* (5), 2372–2380. https://doi.org/10.1021/nl404777h.

(3) . F. I. E.; . M. N. N.; . R. U. O. Optical Properties of CuS Thin Films Deposited by Chemical Bath Deposition Technique and Their Applications. *Trends Appl. Sci. Res.* **2006**, *1* (5), 467–476. https://doi.org/10.3923/tasr.2006.467.476.

(4) Huang, X.; El-Sayed, I. H.; Qian, W.; El-Sayed, M. A. Cancer Cell Imaging and Photothermal Therapy in the Near-Infrared Region by Using Gold Nanorods. *J. Am. Chem. Soc.* **2006**, *128* (6), 2115–2120. https://doi.org/10.1021/ja057254a.

(5) Wang, L. Synthetic Methods of CuS Nanoparticles and Their Applications for Imaging and Cancer Therapy. *RSC Adv.* **2016**, *6* (86), 82596–82615. https://doi.org/10.1039/c6ra18355g.

(6) Wang, J.; Hsu, S.; Gonzalez-Pech, N.; Jhunjhunwala, A.; Chen, F.; Hariri, A.; Grassian, V.; Tao, A.; Jokerst, J. V. Copper Sulfide Nanodisks and Nanoprisms for Photoacoustic Ovarian Tumor Imaging. *Part. Part. Syst. Charact.* **2019**, *36* (8), 1900171. https://doi.org/10.1002/ppsc.201900171.

(7) Marin, B. C.; Hsu, S.-W.; Chen, L.; Lo, A.; Zwissler, D. W.; Liu, Z.; Tao, A. R. Plasmon-Enhanced Two-Photon Absorption in Photoluminescent Semiconductor Nanocrystals. *ACS Photonics* **2016**, *3* (4), 526–531. https://doi.org/10.1021/acsphotonics.6b00037.

(8) Hong, G.; Diao, S.; Chang, J.; Antaris, A. L.; Chen, C.; Zhang, B.; Zhao, S.; Atochin, D. N.; Huang, P. L.; Andreasson, K. I.; et al. Through-Skull Fluorescence Imaging of the Brain in a New near-Infrared Window. *Nat. Photonics* **2014**, *8* (9), 723–730. https://doi.org/10.1038/nphoton.2014.166.

(9) Han, S. K.; Gu, C.; Zhao, S.; Xu, S.; Gong, M.; Li, Z.; Yu, S. H. Precursor Triggering Synthesis of Self-Coupled Sulfide Polymorphs with Enhanced Photoelectrochemical Properties. *J. Am. Chem. Soc.* **2016**, *138* (39), 12913–12919. https://doi.org/10.1021/jacs.6b06609.

(10) Jain, P. K.; El-Sayed, M. A.; El-Sayed, M. A. Plasmonic Coupling in Noble Metal Nanostructures. *Chem. Phys. Lett.* **2010**, *487*, 153–164. https://doi.org/10.1016/j.cplett.2010.01.062.

(11) Kanehara, M.; Koike, H.; Yoshinaga, T.; Teranishi, T. Indium Tin Oxide Nanoparticles with Compositionally Tunable Surface Plasmon Resonance Frequencies in the Near-IR Region. *J. Am. Chem. Soc.* **2009**, *131* (49), 17736–17737. https://doi.org/10.1021/ja9064415.

(12) Steinigeweg, D.; Schlücker, S. Monodispersity and Size Control in the Synthesis of 20–100 Nm Quasi-Spherical Silver Nanoparticles by Citrate and Ascorbic Acid Reduction in Glycerol–Water Mixtures. *Chem. Commun.* **2012**, *48* (69), 8682. https://doi.org/10.1039/c2cc33850e.

(13) Kriegel, I.; Rodríguez-Ferná Ndez, J.; Wisnet, A.; Zhang, H.; Waurisch, C.; Eychmü, A.; Dubavik, A.; Govorov, A. O.; Feldmann, J. Shedding Light on Vacancy-Doped Copper Chalcogenides: Shape-Controlled Synthesis, Optical Properties, and Modeling of Copper Telluride Nanocrystals with Near-Infrared Plasmon Resonances. ACS Nano 7.5 (**2013**): 4367-4377 https://doi.org/10.1021/nn400894d.

(14) Mock, J. J.; Barbic, M.; Smith, D. R.; Schultz, D. A.; Schultz, S. Shape Effects in Plasmon Resonance of Individual Colloidal Silver Nanoparticles. *J. Chem. Phys.* **2002**, *116* (15), 6755–6759. https://doi.org/10.1063/1.1462610.

(15) Orendorff, C. J.; Sau, T. K.; Murphy, C. J. Shape-Dependent Plasmon-Resonant Gold Nanoparticles. *Small* **2006**, *2* (5), 636–639. https://doi.org/10.1002/smll.200500299.

(16) Liu, X.; Swihart, M. T. Heavily-Doped Colloidal Semiconductor and Metal Oxide Nanocrystals: An Emerging New Class of Plasmonic Nanomaterials. *Chemical Society Reviews*. Royal Society of Chemistry May 13, 2014, pp 3908–3920. https://doi.org/10.1039/c3cs60417a.

(17) Pan, A.; Liu, R.; Sun, M.; Ning, C.-Z. Quaternary Alloy Semiconductor Nanobelts with Bandgap Spanning the Entire Visible Spectrum. *J. Am. Chem. Soc.* **2009**, *131* (27), 9502–9503. https://doi.org/10.1021/ja904137m.

(18) Pan, D.; Weng, D.; Wang, X.; Xiao, Q.; Chen, W.; Xu, C.; Yang, Z.; Lu, Y. Alloyed Semiconductor Nanocrystals with Broad Tunable Band Gaps. *Chem. Commun.* **2009**, *0* (28), 4221. https://doi.org/10.1039/b905151a.

(19) Vegard, Lars. Die konstitution der mischkristalle und die raumfüllung der atome. Zeitschrift für Physik 5.1 **(1921)**: 17-26. https://doi.org/10.1007/BF01349680

(20) Swafford, L. A.; Weigand, L. A.; Bowers, M. J.; McBride, J. R.; Rapaport, J. L.; Watt, T. L.; Dixit, S. K.; Feldman, L. C.; Rosenthal, S. J. Homogeneously Alloyed CdSxSe1-x Nanocrystals: Synthesis, Characterization, and Composition/Size-Dependent Band Gap. *J. Am. Chem. Soc.* **2006**, *128* (37), 12299–12306. https://doi.org/10.1021/ja063939e.

(21) Tit, N.; Obaidat, I. M.; Alawadhi, H. Origins of Bandgap Bowing in Compound-Semiconductor Common-Cation Ternary Alloys. *J. Phys. Condens. Matter* **2009**, *21* (7), 075802. https://doi.org/10.1088/0953-8984/21/7/075802.

(22) Gu, Y.; Su, Y.; Chen, D.; Geng, H.; Li, Z.; Zhang, L.; Zhang, Y. Hydrothermal Synthesis of Hexagonal CuSe Nanoflakes with Excellent Sunlight-Driven Photocatalytic Activity. *CrystEngComm* **2014**, *16* (39), 9185–9190. https://doi.org/10.1039/C4CE01470G.

(23) Peidong Yang, C. Z. N.; Dou, L.; Yang, P. Bandgap Engineering in Semiconductor Alloy Nanomaterials with Widely Tunable Compositions. *Nature Reviews Materials*. 2017. https://doi.org/10.1038/natrevmats.2017.70.

(24) Glas, F. Critical Dimensions for the Plastic Relaxation of Strained Axial Heterostructures in

Free-Standing Nanowires. *Phys. Rev. B - Condens. Matter Mater. Phys.* **2006**, *74* (12). https://doi.org/10.1103/PhysRevB.74.121302.

(25) Xu, J.; Yang, X.; Yang, Q.-D.; Huang, X.; Tang, Y.; Zhang, W.; Lee, C.-S. Controllable Synthesis of Bandgap-Tunable CuS_xSe_{1-x} Nanoplate Alloys. *Chem. - An Asian J.* **2015**, *10* (7), 1490–1495. https://doi.org/10.1002/asia.201500156.

(26) Beberwyck, B. J.; Alivisatos, A. P. Ion Exchange Synthesis of III-V Nanocrystals. *J. Am. Chem. Soc.* **2012**, *134* (49), 19977–19980. https://doi.org/10.1021/ja309416c.

(27) Heath, J. R.; Shiang, J. J. Covalency in Semiconductor Quantum Dots. *Chem. Soc. Rev.* **1998**, *27* (1), 65–71. https://doi.org/10.1039/a827065z.

(28) Nozik, A. J.; Mićić, O. I. Colloidal Quantum Dots of III-V Semiconductors. *MRS Bull.* **1998**, *23* (2), 24–30. https://doi.org/10.1557/S0883769400031237.

(29) Van Der Stam, W.; Berends, A. C.; De Mello Donega, C. Prospects of Colloidal Copper Chalcogenide Nanocrystals. *ChemPhysChem*. Wiley-VCH Verlag March 3, 2016, pp 559–581. https://doi.org/10.1002/cphc.201500976.

(30) Li, H.; Brescia, R.; Povia, M.; Prato, M.; Bertoni, G.; Manna, L.; Moreels, I. Synthesis of Uniform Disk-Shaped Copper Telluride Nanocrystals and Cation Exchange to Cadmium Telluride Quantum Disks with Stable Red Emission. *J. Am. Chem. Soc.* **2013**, *135* (33), 12270–12278. https://doi.org/10.1021/ja404694k.

(31) Ha, D. H.; Caldwell, A. H.; Ward, M. J.; Honrao, S.; Mathew, K.; Hovden, R.; Koker, M. K. A.; Muller, D. A.; Hennig, R. G.; Robinson, R. D. Solid-Solid Phase Transformations Induced through Cation Exchange and Strain in 2D Heterostructured Copper Sulfide Nanocrystals. *Nano Lett.* **2014**, *14* (12), 7090–7099. https://doi.org/10.1021/nl5035607.

(32) Lesnyak, V.; George, C.; Genovese, A.; Prato, M.; Casu, A.; Ayyappan, S.; Scarpellini, A.; Manna, L. Alloyed Copper Chalcogenide Nanoplatelets via Partial Cation Exchange Reactions. *ACS Nano* **2014**, *8* (8), 8407–8418. https://doi.org/10.1021/nn502906z.

(33) Cho, G.; Park, Y.; Hong, Y. K.; Ha, D. H. Ion Exchange: An Advanced Synthetic Method for Complex Nanoparticles. *Nano Convergence*. Korea Nano Technology Research Society December 1, 2019, pp 1–17. https://doi.org/10.1186/s40580-019-0187-0.

(34) Anderson, B. D.; Tracy, J. B. Nanoparticle Conversion Chemistry: Kirkendall Effect, Galvanic Exchange, and Anion Exchange. *Nanoscale*. Royal Society of Chemistry November 7, 2014, pp 12195–12216. https://doi.org/10.1039/c4nr02025a.

(35) Zhao, W.; Zhang, C.; Geng, F.; Zhuo, S.; Zhang, B. Nanoporous Hollow Transition Metal Chalcogenide Nanosheets Synthesized via the Anion-Exchange Reaction of Metal Hydroxides with Chalcogenide Ions. *ACS Nano* **2014**, *8* (10), 10909–10919. https://doi.org/10.1021/nn504755x.

(36) Hou, L.; Hua, H.; Bao, R.; Chen, Z.; Yang, C.; Zhu, S.; Pang, G.; Tong, L.; Yuan, C.; Zhang, X. Anion-Exchange Formation of Hollow $NiCo_2S_4$ Nanoboxes from Mesocrystalline Nickel Cobalt Carbonate Nanocubes towards Enhanced Pseudocapacitive Properties. *Chempluschem* **2016**, *81* (6), 557–563. https://doi.org/10.1002/cplu.201600175.

(37) Lim, Y.; Lee, C. H.; Jun, C. H.; Kim, K.; Cheon, J. Morphology-Conserving Non-Kirkendall Anion Exchange of Metal Oxide Nanocrystals. *J. Am. Chem. Soc.* **2020**, *142* (20), 9130–9134. https://doi.org/10.1021/jacs.0c03230.

(38) Kresse, G.; Furthmüller, J. Efficient Iterative Schemes for *Ab Initio* Total-Energy Calculations Using a Plane-Wave Basis Set. *Phys. Rev. B* **1996**, *54* (16), 11169–11186. https://doi.org/10.1103/PhysRevB.54.11169.

(39) Blöchl, P. E. Projector Augmented-Wave Method. *Phys. Rev. B* **1994**, *50* (24), 17953–17979. https://doi.org/10.1103/PhysRevB.50.17953.

(40) Perdew, J. P.; Burke, K.; Ernzerhof, M. Generalized Gradient Approximation Made Simple. *Phys. Rev. Lett.* **1996**, *77* (18), 3865–3868. https://doi.org/10.1103/PhysRevLett.77.3865.

(41) Liu, X.; Wang, X.; Swihart, M. T. Cu $_{2-x}$ S $_{1-y}$ Se $_{y}$ Alloy Nanocrystals with Broadly Tunable Near-Infrared Localized Surface Plasmon Resonance. *Chem. Mater.* **2013**, *25* (21), 4402–4408. https://doi.org/10.1021/cm402848k.

(42) Yang, K.; Oses, C.; Curtarolo, S. Modeling Off-Stoichiometry Materials with a High-Throughput Ab-Initio Approach. *Chem. Mater.* **2016**, *28* (18), 6484–6492. https://doi.org/10.1021/acs.chemmater.6b01449.

(43) Xie, Y.; Carbone, L.; Nobile, C.; Grillo, V.; D'Agostino, S.; Della Sala, F.; Giannini, C.; Altamura, D.; Oelsner, C.; Kryschi, C.; et al. Metallic-like Stoichiometric Copper Sulfide Nanocrystals: Phase- and Shape-Selective Synthesis, near-Infrared Surface Plasmon Resonance Properties, and Their Modeling. *ACS Nano* **2013**, *7* (8), 7352–7369. https://doi.org/10.1021/nn403035s.

(44) Hsu, S.-W.; On, K.; Tao, A. R. Localized Surface Plasmon Resonances of Anisotropic Semiconductor Nanocrystals. *J. Am. Chem. Soc.* **2011**, *133* (47), 19072–19075. https://doi.org/10.1021/ja2089876.

(45) Zamulko, S.; Berland, K.; Persson, C. Optical Properties of Cu 2 ZnSn(S x Se 1- x) 4 by First-Principles Calculations. *Phys. status solidi* **2018**, *215* (17), 1700945. https://doi.org/10.1002/pssa.201700945.

(46) Brik, M. G. First-Principles Study of the Electronic and Optical Properties of CuXS 2 (X = Al, Ga, In) and AgGaS 2 Ternary Compounds. *J. Phys. Condens. Matter* **2009**, *21* (48), 485502. https://doi.org/10.1088/0953-8984/21/48/485502.

(47) Khan, M.; Lan, Z.; Zeng, Y. Analysis of Indium Oxidation State on the Electronic Structure and Optical Properties of TiO2. *Materials (Basel).* **2018**, *11* (6), 952. https://doi.org/10.3390/ma11060952.

(48) Eberhart, M. E.; Clougherty, D. P.; MacLaren, J. M. Bonding-Property Relationships in Interrnetallic Alloys. *J. Mater. Res.* **1993**, *8* (3), 438–448. https://doi.org/10.1557/JMR.1993.0438.

(49) Mu, L.; Wang, F.; Sadtler, B.; Loomis, R. A.; Buhro, W. E. Influence of the Nanoscale Kirkendall Effect on the Morphology of Copper Indium Disulfide Nanoplatelets Synthesized by Ion Exchange. *ACS Nano* **2015**, *9* (7), 7419–7428. https://doi.org/10.1021/acsnano.5b02427.

(50) De Trizio, L.; Gaspari, R.; Bertoni, G.; Kriegel, I.; Moretti, L.; Scotognella, F.; Maserati, L.; Zhang, Y.; Messina, G. C.; Prato, M.; et al. Cu $_{3-x}$ P Nanocrystals as a Material Platform for Near-Infrared Plasmonics and Cation Exchange Reactions. *Chem. Mater.* **2015**, *27* (3), 1120–1128. https://doi.org/10.1021/cm5044792.

(51) Zhao, H.; Wang, D.; Chaker, M.; Ma, D. Effect of Different Types of Surface Ligands on the Structure and Optical Property of Water-Soluble PbS Quantum Dots Encapsulated by

Amphiphilic Polymers. *J. Phys. Chem. C* **2011**, *115* (5), 1620–1626. https://doi.org/10.1021/jp109282m.

(52) Du, Y.; Yin, Z.; Zhu, J.; Huang, X.; Wu, X. J.; Zeng, Z.; Yan, Q.; Zhang, H. A General Method for the Large-Scale Synthesis of Uniform Ultrathin Metal Sulphide Nanocrystals. *Nat. Commun.* **2012**, *3* (1), 1–7. https://doi.org/10.1038/ncomms2181.

(53) Park, J.; Zheng, H.; Jun, Y. W.; Alivisatos, A. P. Hetero-Epitaxial Anion Exchange Yields Single-Crystalline Hollow Nanoparticles. *J. Am. Chem. Soc.* **2009**, *131* (39), 13943–13945. https://doi.org/10.1021/ja905732q.

(54) Xu, H.; Wang, W.; Zhu, W.; Zhou, L. Synthesis of Octahedral CuS Nanocages via a Solid-Liquid Reaction. *Nanotechnology* **2006**, *17* (15), 3649–3654. https://doi.org/10.1088/0957-4484/17/15/005.

(55) Chen, G.; Niu, M.; Cui, L.; Bao, F.; Zhou, L.; Wang, Y. Facile Synthesis and Formation Mechanism of Metal Chalcogenides Hollow Nanoparticles. *J. Phys. Chem. C* **2009**, *113* (18), 7522–7525. https://doi.org/10.1021/jp9012834.

(56) Zhu, H.; Wang, J.; Wu, D. Fast Synthesis, Formation Mechanism, and Control of Shell Thickness of CuS Hollow Spheres. *Inorg. Chem.* **2009**, *48* (15), 7099–7104. https://doi.org/10.1021/ic900201p.

(57) Cabot, A.; Ibáñez, M.; Guardia, P.; Alivisatos, A. P. Reaction Regimes on the Synthesis of Hollow Particles by the Kirkendall Effect. *J. Am. Chem. Soc.* **2009**, *131* (32), 11326–11328. https://doi.org/10.1021/ja903751p.

(58) Dilena, E.; Dorfs, D.; George, C.; Miszta, K.; Povia, M.; Genovese, A.; Casu, A.; Prato, M.; Manna, L. Colloidal Cu2-x(SySe1-y) Alloy Nanocrystals with Controllable Crystal Phase: Synthesis, Plasmonic Properties, Cation Exchange and Electrochemical Lithiation. *J. Mater. Chem.* **2012**, *22* (26), 13023–13031. https://doi.org/10.1039/c2jm30788j.

(59) Liu, X.; Wang, X.; Zhou, B.; Law, W.-C.; Cartwright, A. N.; Swihart, M. T. Size-Controlled Synthesis of Cu $_{2-x}$ E (E = S, Se) Nanocrystals with Strong Tunable Near-Infrared Localized Surface Plasmon Resonance and High Conductivity in Thin Films. *Adv. Funct. Mater.* **2013**, *23* (10), 1256–1264. https://doi.org/10.1002/adfm.201202061.

(60) Liu, L.; Zhong, H.; Bai, Z.; Zhang, T.; Fu, W.; Shi, L.; Xie, H.; Deng, L.; Zou, B. Controllable Transformation from Rhombohedral Cu1.8S Nanocrystals to Hexagonal CuS Clusters: Phase- and Composition-Dependent Plasmonic Properties. *Chem. Mater.* **2013**, *25* (23), 4828–4834. https://doi.org/10.1021/cm403420u.

(61) Thirumavalavan, S.; Mani, K.; Sagadevan, S. Investigation of the Structural, Optical and Electrical Properties of Copper Selenide Thin Films. *Mater. Res.* **2015**, *18* (5), 1000–1007. https://doi.org/10.1590/1516-1439.039215.

(62) Zhao, Y.; Pan, H.; Lou, Y.; Qiu, X.; Zhu, J.; Burda, C. Plasmonic Cu 2-XS Nanocrystals: Optical and Structural Properties of Copper-Deficient Copper(I) Sulfides. *J. Am. Chem. Soc.* **2009**, *131* (12), 4253–4261. https://doi.org/10.1021/ja805655b.

(63) Suárez, J. A.; Plata, J. J.; Márquez, A. M.; Sanz, J. F. Effects of the Capping Ligands, Linkers and Oxide Surface on the Electron Injection Mechanism of Copper Sulfide Quantum Dot-Sensitized Solar Cells. Phys. Chem. Chem. Phys. **2017**, 19 (22), 14580–14587. https://doi.org/10.1039/c7cp01076a.

(64) Li, W.; Zamani, R.; Rivera Gil, P.; Pelaz, B.; Ibáñez, M.; Cadavid, D.; Shavel, A.; Alvarez-

Puebla, R. A.; Parak, W. J.; Arbiol, J.; et al. CuTe Nanocrystals: Shape and Size Control, Plasmonic Properties, and Use as SERS Probes and Photothermal Agents. *J. Am. Chem. Soc.* **2013**, *135* (19), 7098–7101. https://doi.org/10.1021/ja401428e.

Chapter 3

Enhanced Second Harmonic Generation in Colloidal Metasurfaces

Yuan Zeng[1,3,‡] Haoliang Qian[2,‡] Matthew J. Rozin[1,3,‡] Zhaowei Liu[2,3] and Andrea R. Tao[1,3*]

([‡] Equal contribution)

[1]Department of NanoEngineering, University of California, San Diego, 9500 Gilman Drive MC 0448, La Jolla, California 92093-0448

[2]Department of Electrical and Computer Engineering, University of California, San Diego, 9500 Gilman Drive, La Jolla, California 92093

[3]Materials Science and Engineering, University of California, San Diego, 9500 Gilman Drive, La Jolla, California 92093

[‡]These authors contributed equally to this work.
*Email: atao@eng.ucsd.edu

Introduction

Metallic nanostructures that support surface plasmons have been demonstrated to exhibit a wide range of nonlinear optical phenomena,[1,2] including enhanced second harmonic generation (SHG).[3–5] SHG is a nonlinear wave-mixing process where two incident photons at the same fundamental wavelength (λ_{FW}) combine to produce a single, higher energy photon at the second harmonic ($\lambda_{SH}=\lambda_{FW}/2$) wavelength. In bulk materials that possess a large nonlinear susceptibility[6] (χ^2) such as β-barium borate and lithium niobate, SHG stems from light-matter interactions with a non-centrosymmetric crystal lattice. SHG is also supported by under-coordinated surface structures due to centrosymmetric break-down.[7–11] A major drawback with using surface-generated SHG, however, is a reduced nonlinear interaction length. Enhanced SHG overcomes this by taking advantage of metal surfaces that support the excitation of surface plasmon resonances (SPRs)[12,13] that can serve to enhance the near-field intensity[14–16] at either the fundamental or the second harmonic wavelengths.[2,17,18] However, it is difficult to match both optical excitation and emission by a structure that exhibits only a single plasmon resonance.

Double resonance nanostructures can be designed to support two different types of optical modes (e.g. a Fabry-Perot-like resonance mode and a SPR mode),[19] similar types of resonance modes with different polarizations,[20] two separate optical components that each supports a resonance mode,[17,21–23] or multi-resonances structure with either multiple components or branches.[24–29] The ability of these double resonance structures to maximize re-emission into the far-field is highly promising for the development of nonlinear light sources. However, the majority of these designs require components that possess complex nanostructured architectures and precise control of the resonance frequencies, which determined by the size,[30] shape[31,32] and orientation[33] of metal nanostructures. As a result, nanostructured metasurfaces supporting SHG have predominantly relied on direct-write or lithography-based nanofabrication techniques,[17,19,22,34,35] limiting the ability to generate large-scale arrays for light emission. While suitable for building proof-of-concept structures, such fabrication processes are not amenable to nanomanufacturing considerations such as scalability, throughput, and cost.

Plasmonic metasurfaces have the potential to serve as effective platforms for enhanced SHG because they can be designed to exhibit a double resonance effect, with near-field enhancement occurring at both the fundamental and the second harmonic wavelengths. Here, we present a highly scalable, bottom-up approach to fabricating plasmonic metasurfaces for SHG and light emission. Colloidal nanocrystals assembled into periodic arrays serve as the foundation for ultrathin nonlinear optical metasurfaces that absorb in the near-infrared (IR) and emit in the visible. We observe SHG from a nanocube-on-metal structure similar to those first reported by Moreau *et al.*[36] Rozin *et al.* previously demonstrated that colloidal metasurfaces are capable of supporting multiple, spectrally separated but spatially overlapping plasmon resonances that induce strongly enhanced optical fields.[37] Such colloidal metasurfaces are particularly advantageous for enhanced SHG platforms because the parameters that affect field enhancement at the fundamental and second harmonic frequencies can be independently tuned.

Experimental Methods

Gold Substrate Fabrication. Au Substrates are fabricated through Sputtering (using Denton Discovery 18 Sputter System). 500 um thick, 1 cm by 1 cm size glass substrates were washed with ethanol, piranha solution, DI water and dryied with Nitrogen stream. The sputtering RF bias is used to clean the substrate for 40 seconds, and follows with Cr (400 W, 5 second) and Au film (300 W, 115 second) sputtering with the Ar gas pressure as 2.4 mTorr.

AgNC Synthesis. AgNCs are synthesized via a polyol synthesis described before[38,39]. We add $CuCl_2$, $AgNO_3$, 1,5-pentanediol in a glass vial and dissolve through sonication. In a separate glass vial, we dissolved PVP (MW=55000) in 1,5-pentanediol. Then we add 10mL 1,5-pentanediol in a 50mL Round Bottom Flask, heat up to 193 degrees and inject the precursors into the hot solution. The synthesized AgNCs are vaccum-filtered (using 650 nm, 450 nm and 220 nm pore size Millipore Durapore membranes) to reduce the polydispersity. The filtered AgNCs are centrifuged in ethanol to remove excess PVP and re-dispersed in 15 mL ethanol for later using.

Metasurface Fabrication. Take 3 mL AgNCs (stored in ethanol), add 17 mL ethanol and centrifuge at 3400 RPMs for 15 minutes, re-disperse in 10 mL ethanol and centrifuge at 3400 RPMs for 15 minutes. Then add 1 mL $CHCl_3$ and sonicate to fully dispersed. Fill a glass petri dish with DI water, add AgNCs (in $CHCl_3$) drop by drop to the petri dish. More drops added, the higher AgNCs film density we achieved. After making the AgNCs film, wait about 1 hour and transfer the AgNCs film to the Au substrates by simply dipping into the petri dish.

SHG Measurement With Confocal Microscope (Figure 3b, c). We use back-scattering mode of Leica SP5 Confocal/MultiPhoton System (Leica Upright Microscope; 0.75NA 20x dry objective; Leica GaAsP hybrid PMT detector). A tunable Ti-Sapphire laser was used as the excitation source with approximately 100 femtosecond pulse width, 80 MHz repetition rate, and tunable emission from 690–1040 nm.

SHG Measurement With Picosecond Photon Detection Series. We use picosecond photon detection series for all SHG measurements except for Figure 3b,c because it has well-calibrated counts to photon number conversion efficiency, for accurate measurement of SHG emission power. The excitation laser source is MaiTai HP (100fs Pulse Width and 80MHz Repetition Rate, 690 nm to 1040 nm tunable wavelength); the objective lens is 20x with 0.45NA; microscope is Olympus IX81; detector is Horiba PM, Picosecond Photon Detection Series.

We chose excitation wavelength from 750 nm to 1040 nm, with 50 nm increment (with the exception of a 40 nm increment between last two data point). For each individual measurement, excitation wavelength and laser power are constant, we carried out an emission scan using a monochromator starting at 300 nm and with a 2 nm bandwidth, 2 nm increments, and a 1 second dwell time (unless otherwise noted). Then we calculated the total counts from ($\frac{\lambda_{Excitation}}{2}$ – 5) nm to ($\frac{\lambda_{Excitation}}{2}$ + 5) nm because the bandwidth of laser is roughly 10 nm. System detection efficiency at different wavelengths is calibrated with standard nonlinear crystal, we use the system detection

efficiency to covert measured counts to SHG photon numbers, and then calculate the SHG power. Excitation power at fundamental wavelength is measured with Vega P/N 7Z01560 Power Meter.

Results and Discussion

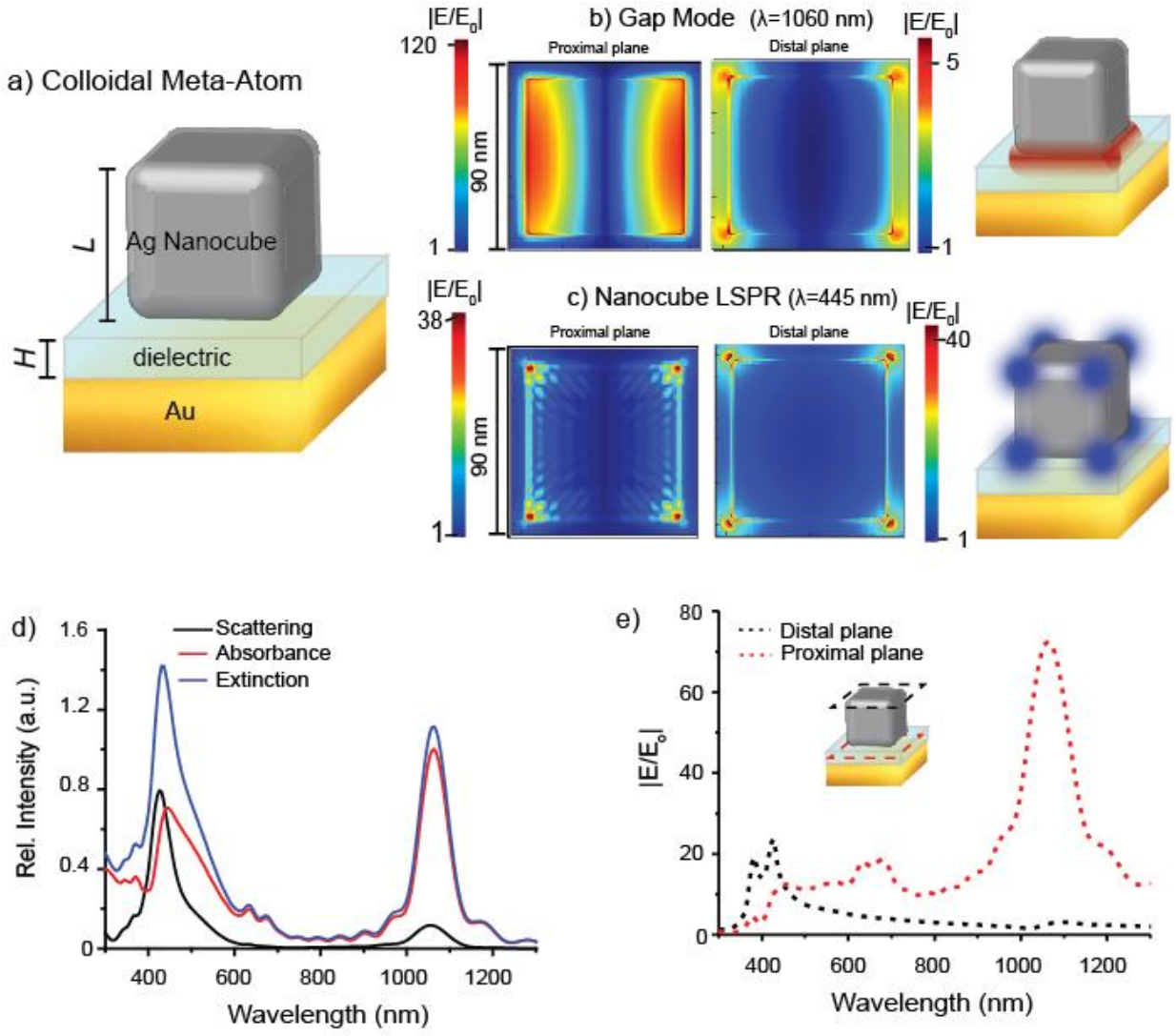

Figure 3.1 | Schematic and simulated metasurface near-field distributions: (a) schematic of single meta-atom (90 nm cube, 10 nm radius of curvature on the corners, 3 nm dielectric layer), L is cube size and H is gap height, **(b)** Electric field distributions on distal plane, proximal plane, and schematic of hotspots at fundamental wavelengths **(c)** Electric field distributions on distal plane, proximal plane, and schematic of hotspots at second harmonic wavelengths. **(d)** Far-field scattering, absorbance, and calculated extinction spectra for the metasurface. **(e)** Local electric field intensity in the cavity (proximal) and on the AgNC top surface (distal plane) as a function of incident wavelength, inset is schematic of distal plane and proximal plane.

A schematic of the metasurface geometry is shown in Figure 3.1a. Ag nanocubes

deposited onto a metal backplane forms a metal-dielectric-metal interface that serves as the structural repeat unit, or meta-atom, of the SHG metasurface. Near-field enhancement at the fundamental frequency is largely dictated by the thickness of the polymer space layer due to a gap mode that results from capacitive coupling between the nanocube and the Au backplane. This gap mode (Figure 3.1b) is largely dependent on both spacer layer thickness (which determines gap height) and cube size (which determines gap size). Field enhancement at the second harmonic frequency stems from a localized surface plasmon resonance (LSPR) associated with the Ag nanocube (Figure 3.1c), and is thus primarily dictated by the size of the Ag cube. This cube mode is highly dependent on cube size, but independent on spacer layer thickness. Thus, control over the structural parameters of the colloidal metasurface allow for orthogonal control over near-field enhancement at the fundamental and second harmonic frequencies.

First, we carried out full–wave electrodynamic simulations (Lumerical FDTD Solutions) to investigate how the LSPRs of the nanocube and coupled nanocube-film architecture influence SHG enhancement. The local electric-field enhancement ($|E/E_0|$) distribution for a cross-section located in the nanocube-film gap, 0.5 nm below Ag nanocube bottom surface (proximal plane) is shown in Figure 3.1b,c. Figure 3.1d plots the simulated far-field scattering (black), absorbance (red), and the calculated extinction (blue) of the metasurface. The fundamental gap mode (λ=1060 nm) is a source of strong optical absorption and moderate scattering. Absorptions associated with confinement of the gap mode are observed at the edges of the nanocube, and are present in the simulated absorbance as oscillations in the absorbance intensity at wavelengths just above and below the fundamental mode. The absorption and scattering peaks located between 400 nm to 700 nm in the simulated spectra are consistent with “isolated” LSPR modes of the Ag nanocube.[40] The broad feature at λ=500 nm corresponds to the first order dipole mode of the Ag nanocube, whereas the peak located near λ=420 nm originates from the quadrupole and other higher-order LSPRs.[41] However, the field enhancement induced by the quadrupole mode is dominant over the

enhancement induced by dipole modes at the SHG wavelength.[42] The field enhancement distribution for a cross-section taken just above (0.5 nm) the top surface of the Ag nanocube (distal plane) and a cross-section taken inside the gap (proximal plane) is shown in Figure 3.1e. Thus, the nanocube metasurface exhibits a clear double SPR resonance: the gap mode responsible for enhanced absorption, and the nanocube LSPR responsible for emission. From the simulation of near-field distribution, we assigned the gap mode at the fundamental wavelength as a dipole mode that stems from coupling between the Ag nanocube and Au substrate. Thus, field enhancement is consistent with SHG selection rules,[43,44] where the excitation of a SH quadrupole mode results from combined photons that stem from a dipole mode at the fundamental wavelength.[45] The spatial mode overlap that occurs inside the metasurface gap between the fundamental mode and SH mode is likely a major contributor to increasing the efficiency of the SHG process.[20]

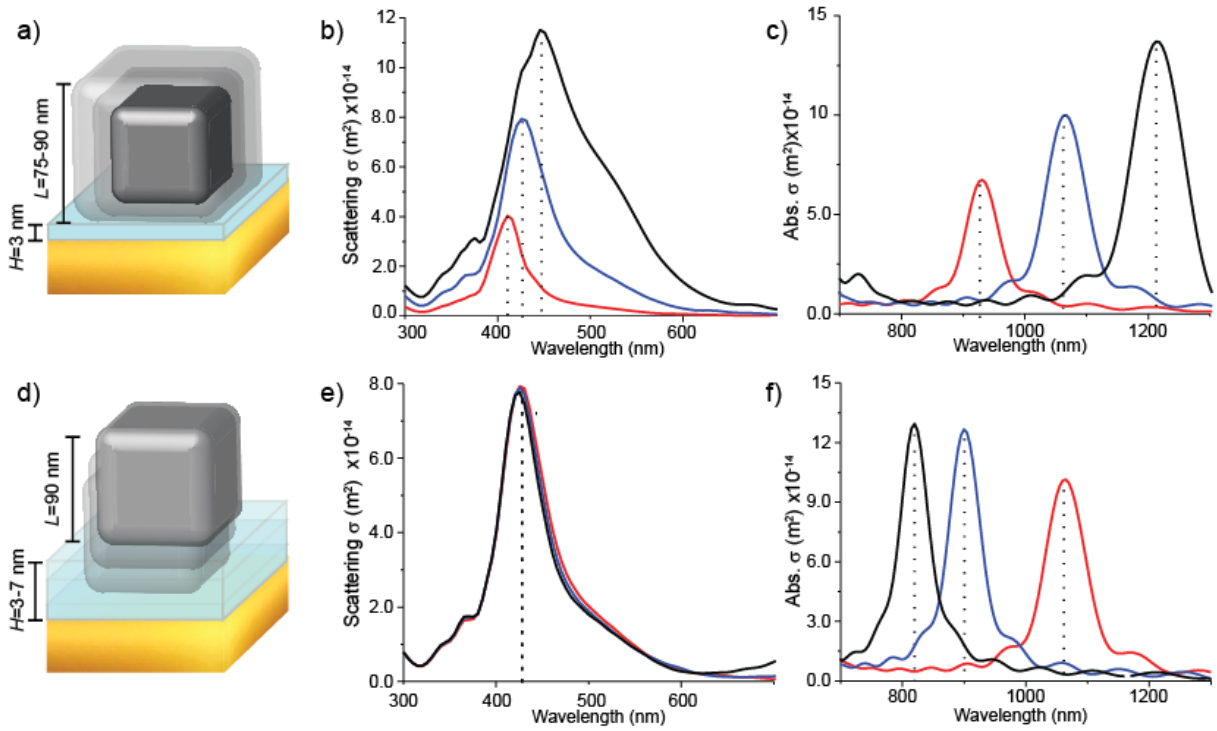

Figure 3.2 | Simulation, dependence of gap height and cube size: (a) Schematic of Meta-atom made by different size of cube. **(b)(c)** Scattering and absorption Cross-section of metasurfaces with constant (3 nm) gap size and varied cube size (Red is 75 nm, blue is 90 nm, black is 105 nm). **(d)** Schematic of Meta-atom made by different thickness of dielectric layer. **(e, f)** Scattering and absorption Cross-section of metasurfaces with constant (90 nm) cube size and varied gap size (red is= 3 nm, blue = 5 nm, black = 7 nm).

To investigate whether these two resonances can be independently tuned, we used FDTD simulations to investigate metasurface dependence on nanocube size and gap height. Figure 3.2 shows the resulting NIR absorption and visible scattering spectra obtained for three colloidal metasurfaces composed of: (i) different cube sizes a constant gap of H= 3 nm; and (ii) different gap heights and a constant cube edge length *L*=90 nm. The strong scattering peak in the visible range red-shifts significantly with increasing nanocube size, from λ= 410 nm for *L*=75 nm to λ= 448 nm for *L*=105 nm. However, optical scattering remains constant at λ=428 nm for all three gap heights, confirming that field enhancement near λ_{SH} is completely independent of H. The strong NIR absorption response is dependent on both cube size and gap height. For increasing cube size from *L*=75 nm to *L*=105 nm, the absorption peak red-shifts by 286 nm due to an increase in the optical cavity size. For increasing gap height from *H*=3 nm to *H*=7 nm, the absorption peak blue-shifts 243 nm due to weaker coupling between the nanocube and Au substrate.

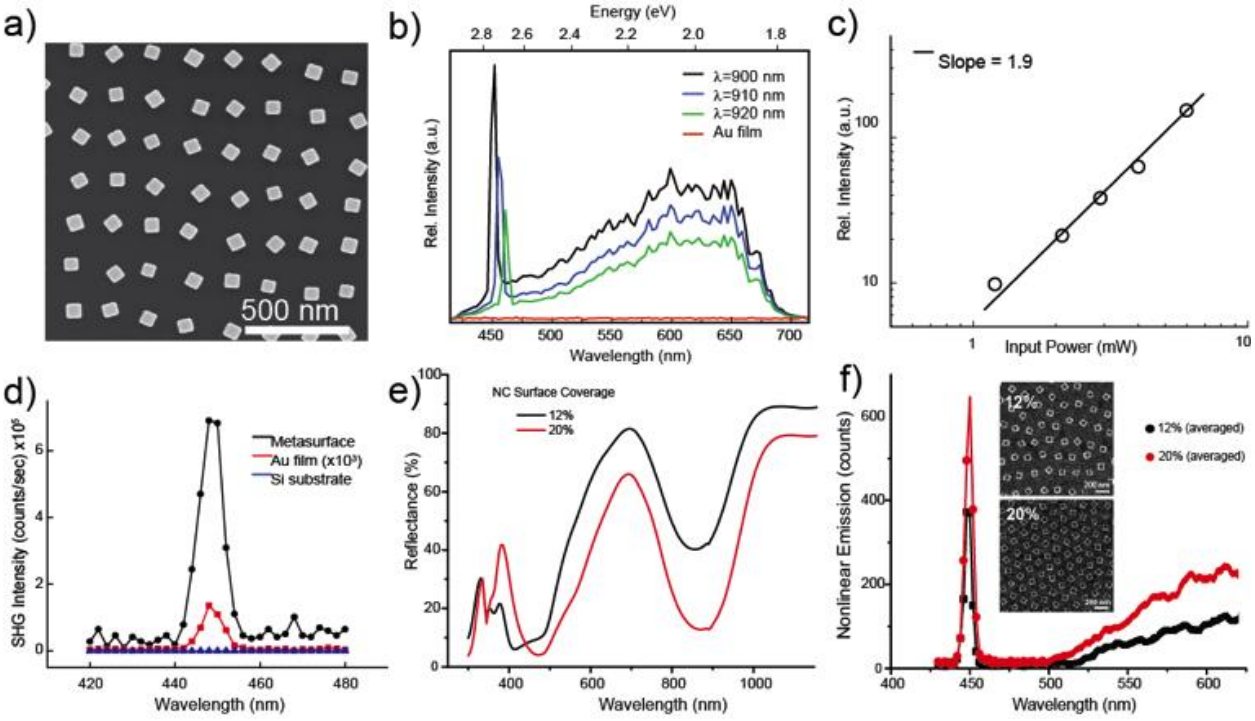

Figure 3.3 | Wavelength, power and density dependence of metasurface Second Harmonic Generation (a) SEM image of nanocube metasurface displaying well-spaced NC array. **(b)** Nonlinear emission spectra from a colloidal metasurface with a fundamental gap mode at 900 nm showing λ_{FW}-dependent SHG. (Corresponding reflectance spectra in Appendix B, B1) **(c)** SHG power dependence, showing SHG is a 2nd-order NLO process. **(d)** Metasurface second harmonic enhancement factor. **(e)** Reflectance spectra of Ag nanocube metasurfaces. **(f)** Nonlinear emission spectra (measured with Picosecond Photon Detection Series). Showing SHG at λ_{SH}=450 nm, inset is SEM images of two metasurfaces with different density. **(a-c),(d-f)** used two different batches of metasurfaces

To fabricate the metasurfaces, colloidal Ag nanocubes were synthesized according to a modified polyol reaction, described in detail elsewhere[39] and deposited onto a supported 50-nm Au film using Langmuir-Blodgett deposition.[46] (Details in Methods Section) Each nanocube is encapsulated in a thin (<2 nm) polymer shell, providing a nanoscale spacer layer that insulates the Ag nanocube from the underlying Au film. Figure 3.3a shows a (top-down) SEM image of a metasurface fabricated with nanocubes possessing an average edge length of 89±4 nm. The nanocube array has an average nanocube center-to-center spacing of 224±45 nm, and a nanocube purity of >98% (particle defect rate of <2%). Nanocube density and spacing can be controlled during the deposition process. A typical nonlinear optical emission spectrum for the nanocube metasurface is shown in Figure 3.3b (black), excited with a scanning, normal incidence pulse train at λ_{FW}=900 nm. During excitation at the fundamental wavelength, light-matter interactions

of the plasmonic structure (at the gap mode resonance) can convert the far-field E_{xy} component of the normal incident light to a near-field E_z component.[47] Plasmon excitation also promotes the interaction of the near-field with the zzz component of the second-order susceptibility tensor, which is strongly localized near the bottom facet of the AgNCs (inside the metasurface gap). Owing to the surface centrosymmetry broken at these metasurface junctions[43] along z-direction, only zzz component of the second-order susceptibility tensor is non-vanished, therefore, a significant near-field z-polarized coherent SHG response can be generated inside the particle-substrate gaps. The narrow SHG peak is prominent in the emission spectrum at precisely λ_{SH}=450 nm. The other prominent feature is the expansive range of cathedral-like peaks throughout the visible spectrum from 450 nm to 700 nm, which we attribute to multi-photon photoluminescence; their investigation is outside the primary scope of the present work and has been reported elsewhere.[48] For comparison, the nonlinear emission from a pristine Au thin-film (*sans* nanocubes) is shown with an identical illumination configuration, revealing a relatively flat and featureless spectrum (Figure 3.3b red).

The nonlinear emission spectra were also recorded for optical excitation at λ_{FW} = 900, 910, and 920 nm (Figure 3.3b). Each spectrum exhibits a narrow second harmonic peak (FWHM<6 nm) whose position follows a strict $\lambda_{FW}/2$ dependence. Unlike this SHG peak, the broad signal attributed to multiphoton emission does not exhibit a spectral shift with varying incident wavelengths. Figure 3.3c shows a log-log plot of the intensity of the second harmonic peak with respect to the input power for excitation at λ_{FW}=900 nm. Peak intensity was found to increase with a nonlinearity order of approximately 1.9, confirms the optical signal we measured originate from second order nonlinear process.

In order to compare the performance of our colloidal metasurface to other SPR-based SHG platforms,[19] we calculated the SHG enhancement factor (EF). Here, we define the SHG EF as the ratio of metasurface SHG power *(P_{MS})* to the SHG power of a pristine Au thin-film *(P_{Au}),* consistent with other studies.[49] Figure 3.3d plots the SHG emission intensity for both the colloidal metasurface, a 75 nm Au thin-film, and a 500 μm-thick Si substrate, normalized to accommodate

for pump power. Here, the metasurface was fabricated with Ag nanocubes (average size=87.5 ± 3.8 nm) deposited at a surface density of 12.1%, and onto an underlying Au thin-film that is 75 nm thick. For an excitation power of 3.80 mW at λ_{FW}=900 nm, we measured the power of the SHG signal to be P_{MS} = 2.20×10^{-13} W. Because the unenhanced SHG signal from the bare Au film is much weaker, a higher pump power was required to detect the SHG. Using an excitation power of 264.75 mW at λ_{FW}=900 nm, we measured the SHG power from the Au film to be P_{Au} = 7.00×10^{-14} W (equivalent to 1.45×10^{-17} W at 3.80 mW incident power). This gives a metasurface SHG enhancement factor of EF_{MS} = 1.52×10^{4}. In addition, we did a comparison with AgNCs on a bare Si substrate. Since there is no coupling between the AgNCs and Si, this structure serves as a single resonance structure that only exhibits a nanocube mode resonance and field enhancement at the SHG emission wavelength. As a result, the SHG efficiency of the colloidal AgNC metasurface fabricated on Au (double resonance structure) is one order of magnitude higher than AgNCs on silicon (single resonance structure). (Appendix B, B2)"

We then compared the SHG efficiencies of two colloidal metasurfaces fabricated with different nanocube densities (12% and 20%) and all other parameters the same. Figure 3.3e shows their near-normal specular reflectance spectra. The large dip in reflectance centered at 875 nm corresponds to the fundamental gap resonance. The spectral positions of the fundamental gap mode for both metasurfaces are similar, indicating that there is minimal interaction between the Ag nanocubes in-plane and that both metasurfaces operate within the weak interparticle coupling limit.[37] The only significant difference between the far-field response of each metasurface is the marked decrease in reflectance for the higher nanocube density. To calculate the SHG efficiency of each metasurface, we define efficiency as the ratio of the fundamental beam power to the metasurface SHG power:

$$\boldsymbol{\eta_{SHG}} = \frac{P_{FW}}{P_{MS}}$$

For a colloidal metasurface with a 12% nanocube density excited with P_{FW} = 3.80×10^{-3} W, we

measured SHG efficiency to be $\eta_{SHG}=(4.87 \pm 0.28)\times10^{-11}$, whereas for the 20% density metasurface the efficiency is $\eta_{SHG}=(8.29 \pm 1.23)\times10^{-11}$. This 67% increase in the density of meta-atoms covering the surface leads to a 70% increase in SHG efficiency (Figure 3.3f), indicates the far-field emission we collected is incoherent SHG. During emission process, near-field E_z component at fundamental frequency been converted to near-field coherent z-polarized SHG signal which confined inside junction. Then, through cube mode plasmonic resonance (at SHG frequency), near-field SHG signal emits out from junction and become incoherent far-field SHG due to the plasmonic resonance lifetime. Furthermore, owing to the aperiodic macroscopic pattern, the far-field SHG signal from different junctions has interference with poor phase matching in spatial, therefore, the overall far-field SHG signal is incoherent [50] which propagate off-(z)axis, and collected by the aperture of the objective.

The highest efficiencies we measured were $\eta_{SHG}=5.36\times10^{-9}$ (Appendix B, B3) with 15.6 GW/cm^2 peak excitation intensity (λ_{FW}=800 nm, 0.2 s dwell time) and $\eta_{SHG}=1.2\times10^{-9}$ from the same metasurface with a longer 1 s dwell time. This decrease in efficiency indicates some materials degradation of the colloidal metasurface under extended laser illumination, potentially from either oxidation of Ag or nanocrystal reshaping due to photothermal effects.[51–53] In comparison, previous reports for bowtie apertures made by lithography exhibit $\eta_{SHG}=6.33\times10^{-9}$ under 0.8 GW/cm^2,[19] and comparably $\eta_{SHG}=1.23\times10^{-8}$ under 1.61 GW/cm^2 for ultrasmooth antennas.[20] While our colloidal metasurfaces exhibit lower SHG emission efficiencies, they possess much larger device areas with the potential for high meta-atom densities and wafer-scale fabrication. (See Appendix B, B4 for a detailed comparison)

Tunability of the colloidal metasurface structure also enables further investigation of the double resonance effect. SHG enhancement is proportional to $f(\lambda_{SH})^2 \cdot f(\lambda_{FW})^4$ where f is field strength.[54] Thus, the near-field enhancement at λ_{FW} is expected to dominate the observed SHG signal in our double-resonance structure. In a double-resonance structure, energy transfer from mode coupling (η_{rad}) has also been shown to be a crucial factor in determining SHG efficiency.[21]

To investigate the relative importance of near-field enhancement versus mode coupling, we fabricated two colloidal metasurfaces that exhibit the same nanocube LSPR modes but possess different gap resonance wavelengths at λ=890 nm (labeled M890) and λ=1020 nm (labeled M1020).

Figure 3.4a,b shows the SHG excitation spectrum, which is a plot of the SHG intensity for varying fundamental excitation wavelengths between λ_{FW}=750–1050 nm. Data points were obtained in 50 nm increments and normalized to the incident intensity (10 GW/ cm^2) (Appendix B, B5) and detector efficiency. The data points are fit with two overlapped Gaussian functions (Appendix B, B6) to identify SHG maxima. In Figure 4a, a maximum in SHG signal intensity for M890 is obtained at λ_{FW}=815 nm excitation, with a secondary SHG peak obtained at λ_{FW}=884 nm and a weak but non-zero SHG signal at λ_{FW}>1000 nm. Figure 4b, shows the SHG excitation scan for M1020, where a peak in SHG emission occurs at λ_{FW}=1029 nm, another peak located at λ_{FW}=875 nm. Figure 3.4c,d shows the reflectance and absorbance for M890 and M1020, respectively. For M890, the optical resonances of the metasurface are designed to possess good overlap with λ_{FW} and λ_{SH}. For M1020, the LSPR modes of the metasurface are designed to possess poor overlap with either λ_{FW} or λ_{SH}. Figure 4e,f shows the expected SHG enhancement factors and radiation efficiencies for each metasurface. Experimental absorbance and reflectance spectra in Figure 4c,d were used to calculate the relative SHG enhancement factor $f(\lambda_{SH})^2 \cdot f(\lambda_{FW})^4$ (Appendix B, B7). To validate these results, we performed Finite Element Method simulations to obtain the wavelength dependent radiation efficiency (blue line). These results were obtained by adding 28 dipoles sources at the hotspots inside gap (Appendix B, B8), this radiation efficiency corresponds to conversion of near-field SHG to far-field SHG. The radiation efficiency includes several factors, including coupling between the near-field SHG quadrupole mode and the far-field SHG dipole mode.

For M890 (Figure 3.4e), the SHG enhancement factor peak (black) at λ_{FW}=825

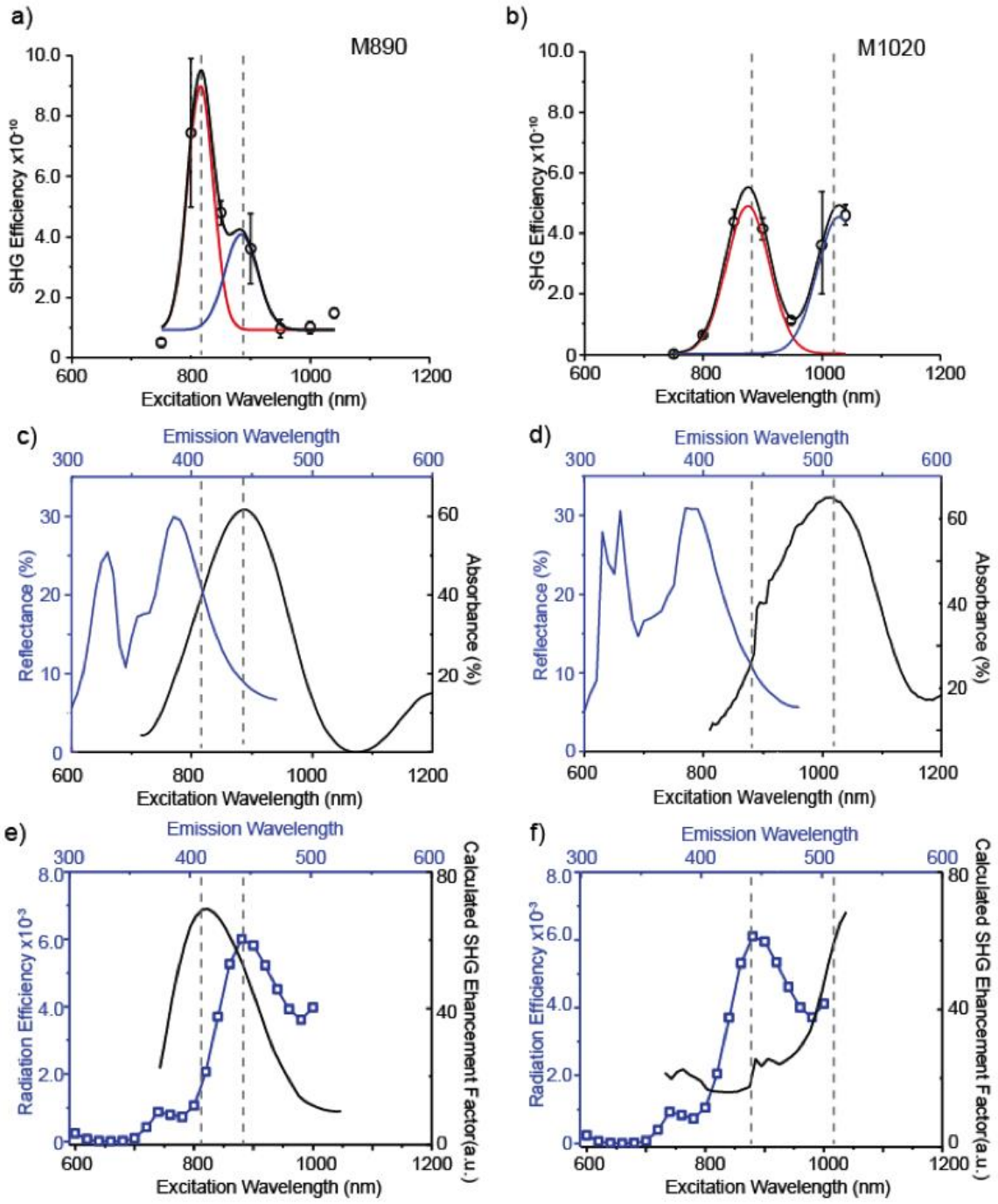

Figure 3.4 Linear and nonlinear optical metasurface response. Excitation wavelength dependent SHG efficiency of M890 **(a)** and M1020 **(b)**, respectively, black dots are measured data points, red and blue curve are Gaussian function curve fitting. All SHG efficiency data is normalized to excitation intensity of 10 GW/cm^2. Experimental reflectance and absorbance spectra for metasurfaces with fundamental gap-modes centered at 890 nm **(c)**, and 1020 nm **(d)**. blue curve is reflectance measurement at emission wavelength (top axis) and black curve is absorption measurement at excitation wavelength (bottom axis). Wavelength dependent radiation efficiency (blue curve) and calculated enhancement $f(\lambda_{SH})^2 \cdot f(\lambda_{FW})^4$ (black curve) of M890 **(e)** and M1020 **(f)**, respectively.

nm is consistent with strong SHG efficiency peak at λ_{FW}=815 nm, and the radiation efficiency peak (blue) at λ_{FW}=880 nm is consistent with the secondary SHG efficiency peak at 884 nm. For M1020 (Figure 3.4f), the SHG enhancement factor peak (black) at 1040 nm is consistent with peak in SHG emission (black) at λ_{FW}=1029 nm, and the maximum radiation efficiency (blue) at λ_{FW}=880 nm is consistent with another SHG efficiency peak at λ_{FW}=875 nm. To confirm the peak identification and analysis, we fabricate another metasurface with 920 nm gap mode resonance (M920) and perform excitation scan with 25 nm data interval (Appendix B, B9). Our experimental data shows M920 has two SHG efficiency peaks, one peak at 825 nm consists with enhancement factor peak, another peak at 875 nm consists with radiation efficiency peak, and both peaks can be fitted with gaussian function. As a result, we find that SHG is proportional to both SHG enhancement factor and radiation efficiency ($f(\lambda_{SH})^2 \cdot f(\lambda_{FW})^4 \cdot \eta_{rad}$).

Conclusion

Overall, this work demonstrates the scalable fabrication of colloidal metasurfaces for enhanced SHG platforms utilizing a double resonance structure. We use these platforms to explore the mechanism for enhanced SHG, and determine that both near field enhancement and mode coupling are critical parameters. By tuning meta-atom size, density, and arrangement, the field enhancement associated with both nonlinear absorption and linear scattering processes can be precisely controlled. Given the ability to synthesize metal nanocrystal with a wide variety of shapes and materials, it may be possible to greatly increase SHG efficiencies of these platforms and extend SPR-based enhancement to other nonlinear optical conversion processes. The tunability of the colloidal device structure also provides a convenient strategy for designing SHG platforms with different working frequencies, with the potential for creating hybrid structures with multiple working frequencies on a single platform. Also, owing to plasmonic resonance lifetime and poor phase matching in spatial, the far-field SHG signal we measured is incoherent. In the future, with proper design of the periodic colloidal metasurface by using surface functionalized

AgNCs, it is possible to generate far-field spatial-coherent SHG from colloidal metasurface. Such metasurface will enable the phase and polarization control for the further functionalization in the integrated nonlinear optics.

Acknowledgments

The authors would like to thank the UCSD School of Medicine Microscopy Core for the use of their facility and acknowledge its supporting grant, NS047101 and NSF Awards CHE-1807891. We also would like to thank the Nano3 facility at Calit2 for the use of their facility.

Chapter 3, in full, is a reprint of the material as it appears in Advanced Functional Materials 28.51 (2018): 1803019. Yuan Zeng[‡], Haoliang Qian[‡], Matthew J. Rozin[‡], Zhaowei Liu, and Andrea R. Tao. ([‡] Equal contribution). The dissertation author was the primary investigator and author of this paper.

References

(1) Kauranen, M.; Zayats, A. V. Nonlinear Plasmonics. **2012**. https://doi.org/10.1038/NPHOTON.2012.244.

(2) Butet, J.; Brevet, P.-F.; Martin, O. J. F. Optical Second Harmonic Generation in Plasmonic Nanostructures: From Fundamental Principles to Advanced Applications. *ACS Nano* **2015**, *9* (11), 10545–10562. https://doi.org/10.1021/acsnano.5b04373.

(3) Butet, J.; Duboisset, J.; Bachelier, G.; Russier-Antoine, I.; Benichou, E.; Jonin, C.; Brevet, P.-F. Optical Second Harmonic Generation of Single Metallic Nanoparticles Embedded in a Homogeneous Medium. *Nano Lett.* **2010**, *10* (5), 1717–1721. https://doi.org/10.1021/nl1000949.

(4) Zhang, Y.; Grady, N. K.; Ayala-Orozco, C.; Halas, N. J. Three-Dimensional Nanostructures as Highly Efficient Generators of Second Harmonic Light. *Nano Lett.* **2011**, *11* (12), 5519–5523. https://doi.org/10.1021/nl2033602.

(5) Czaplicki, R.; Husu, H.; Siikanen, R.; Mäkitalo, J.; Kauranen, M.; Laukkanen, J.; Lehtolahti, J.; Kuittinen, M. Enhancement of Second-Harmonic Generation from Metal Nanoparticles by Passive Elements. *Phys. Rev. Lett.* **2013**, *110* (9), 093902. https://doi.org/10.1103/PhysRevLett.110.093902.

(6) Boyd, R. W.; Boyd, R. W. Chapter 1 – The Nonlinear Optical Susceptibility. In *Nonlinear*

Optics; 2008; pp 1–67. https://doi.org/10.1016/B978-0-12-369470-6.00001-0.

(7) Jha, S. S. Theory of Optical Harmonic Generation at a Metal Surface. *Phys. Rev.* **1965**, *140* (6A), A2020–A2030. https://doi.org/10.1103/PhysRev.140.A2020.

(8) Bloembergen, N.; Chang, R. K.; Jha, S. S.; Lee, C. H. Optical Second-Harmonic Generation in Reflection from Media with Inversion Symmetry. *Phys. Rev.* **1968**, *174* (3), 813–822. https://doi.org/10.1103/PhysRev.174.813.

(9) Wang, F. X.; Rodríguez, F. J.; Albers, W. M.; Ahorinta, R.; Sipe, J. E.; Kauranen, M. Surface and Bulk Contributions to the Second-Order Nonlinear Optical Response of a Gold Film. *Phys. Rev. B* **2009**, *80* (23), 233402. https://doi.org/10.1103/PhysRevB.80.233402.

(10) Bachelier, G.; Butet, J.; Russier-Antoine, I.; Jonin, C.; Benichou, E.; Brevet, P.-F. Origin of Optical Second-Harmonic Generation in Spherical Gold Nanoparticles: Local Surface and Nonlocal Bulk Contributions. *Phys. Rev. B* **2010**, *82* (23), 235403. https://doi.org/10.1103/PhysRevB.82.235403.

(11) Ciracì, C.; Poutrina, E.; Scalora, M.; Smith, D. R. Second-Harmonic Generation in Metallic Nanoparticles: Clarification of the Role of the Surface. *Phys. Rev. B* **2012**, *86* (11), 115451. https://doi.org/10.1103/PhysRevB.86.115451.

(12) Pu, Y.; Grange, R.; Hsieh, C.-L.; Psaltis, D. Nonlinear Optical Properties of Core-Shell Nanocavities for Enhanced Second-Harmonic Generation. *Phys. Rev. Lett.* **2010**, *104* (20), 207402. https://doi.org/10.1103/PhysRevLett.104.207402.

(13) Zhang, Y.; Manjavacas, A.; Hogan, N. J.; Zhou, L.; Ayala-Orozco, C.; Dong, L.; Day, J. K.; Nordlander, P.; Halas, N. J. Toward Surface Plasmon-Enhanced Optical Parametric Amplification (SPOPA) with Engineered Nanoparticles: A Nanoscale Tunable Infrared Source. *Nano Lett.* **2016**, *16* (5), 3373–3378. https://doi.org/10.1021/acs.nanolett.6b01095.

(14) Mühlschlegel, P.; Eisler, H.-J.; Martin, O. J. F.; Hecht, B.; Pohl, D. W. Resonant Optical Antennas. *Science (80-.).* **2005**, *308* (5728).

(15) Chen, C. K.; Heinz, T. F.; Ricard, D.; Shen, Y. R. Surface-Enhanced Second-Harmonic Generation and Raman Scattering. *Phys. Rev. B* **1983**, *27* (4), 1965–1979. https://doi.org/10.1103/PhysRevB.27.1965.

(16) Bouhelier, A.; Beversluis, M.; Hartschuh, A.; Novotny, L. Near-Field Second-Harmonic Generation Induced by Local Field Enhancement. *Phys. Rev. Lett.* **2003**, *90* (1), 013903. https://doi.org/10.1103/PhysRevLett.90.013903.

(17) Thyagarajan, K.; Rivier, S.; Lovera, A.; Martin, O. J. F. Enhanced Second-Harmonic Generation from Double Resonant Plasmonic Antennae. *Opt. Express* **2012**, *20* (12), 12860. https://doi.org/10.1364/OE.20.012860.

(18) Linnenbank, H.; Grynko, Y.; Förstner, J.; Linden, S. Second Harmonic Generation Spectroscopy on Hybrid Plasmonic/Dielectric Nanoantennas. *Light Sci. Appl.* **2016**, *5* (1), e16013. https://doi.org/10.1038/lsa.2016.13.

(19) Park, S.; Hahn, J. W.; Lee, J. Y. Doubly Resonant Metallic Nanostructure for High

Conversion Efficiency of Second Harmonic Generation. *Opt. Express* **2012**, *20* (5), 4856. https://doi.org/10.1364/OE.20.004856.

(20) Celebrano, M.; Wu, X.; Baselli, M.; Großmann, S.; Biagioni, P.; Locatelli, A.; De Angelis, C.; Cerullo, G.; Osellame, R.; Hecht, B.; Duò, L.; Ciccacci, F.; Finazzi, M. Mode Matching in Multiresonant Plasmonic Nanoantennas for Enhanced Second Harmonic Generation. *Nat. Nanotechnol.* **2015**, *10* (5), 412–417. https://doi.org/10.1038/nnano.2015.69.

(21) Yang, K. Y.; Butet, J.; Yan, C.; Bernasconi, G. D.; Martin, O. J. F. Enhancement Mechanisms of the Second Harmonic Generation from Double Resonant Aluminum Nanostructures. *ACS Photonics* **2017**, *4* (6), 1522–1530. https://doi.org/10.1021/acsphotonics.7b00288.

(22) Weber, N.; Protte, M.; Walter, F.; Georgi, P.; Zentgraf, T.; Meier, C. Double Resonant Plasmonic Nanoantennas for Efficient Second Harmonic Generation in Zinc Oxide. *Phys. Rev. B* **2017**, *95* (20), 205307. https://doi.org/10.1103/PhysRevB.95.205307.

(23) Harutyunyan, H.; Volpe, G.; Quidant, R.; Novotny, L. Enhancing the Nonlinear Optical Response Using Multifrequency Gold-Nanowire Antennas. *Phys. Rev. Lett.* **2012**, *108* (21), 217403. https://doi.org/10.1103/PhysRevLett.108.217403.

(24) Aouani, H.; Navarro-Cia, M.; Rahmani, M.; Sidiropoulos, T. P. H.; Hong, M.; Oulton, R. F.; Maier, S. A. Multiresonant Broadband Optical Antennas As Efficient Tunable Nanosources of Second Harmonic Light. *Nano Lett.* **2012**, *12* (9), 4997–5002. https://doi.org/10.1021/nl302665m.

(25) Liu, S.-D.; Leong, E. S. P.; Li, G.-C.; Hou, Y.; Deng, J.; Teng, J. H.; Ong, H. C.; Lei, D. Y. Polarization-Independent Multiple Fano Resonances in Plasmonic Nonamers for Multimode-Matching Enhanced Multiband Second-Harmonic Generation. *ACS Nano* **2016**, *10* (1), 1442–1453. https://doi.org/10.1021/acsnano.5b06956.

(26) Thyagarajan, K.; Butet, J.; Martin, O. J. F. Augmenting Second Harmonic Generation Using Fano Resonances in Plasmonic Systems. *Nano Lett.* **2013**, *13* (4), 1847–1851. https://doi.org/10.1021/nl400636z.

(27) Gennaro, S. D.; Rahmani, M.; Giannini, V.; Aouani, H.; Sidiropoulos, T. P. H.; Navarro-Cía, M.; Maier, S. A.; Oulton, R. F. The Interplay of Symmetry and Scattering Phase in Second Harmonic Generation from Gold Nanoantennas. *Nano Lett.* **2016**, *16* (8), 5278–5285. https://doi.org/10.1021/acs.nanolett.6b02485.

(28) Butet, J.; Martin, O. J. F. Fano Resonances in the Nonlinear Optical Response of Coupled Plasmonic Nanostructures. *Opt. Express* **2014**, *22* (24), 29693. https://doi.org/10.1364/OE.22.029693.

(29) Navarro-Cia, M.; Maier, S. A. Broad-Band Near-Infrared Plasmonic Nanoantennas for Higher Harmonic Generation. *ACS Nano* **2012**, *6* (4), 3537–3544. https://doi.org/10.1021/nn300565x.

(30) Lyon, L. A.; Pen, D. J.; Natan, M. J. Surface Plasmon Resonance of Au Colloid-Modified Au Films : Particle Size Dependence. **1999**, 5826–5831.

(31) Orendorff, C. J.; Sau, T. K.; Murphy, C. J. Shape-Dependent Plasmon-Resonant Gold Nanoparticles. *Small* **2006**, *2* (5), 636–639. https://doi.org/10.1002/smll.200500299.

(32) Mock, J. J.; Barbic, M.; Smith, D. R.; Schultz, D. A.; Schultz, S. Shape Effects in Plasmon Resonance of Individual Colloidal Silver Nanoparticles. *J. Chem. Phys.* **2002**, *116* (15), 6755–6759. https://doi.org/10.1063/1.1462610.

(33) Funston, A. M.; Novo, C.; Davis, T. J.; Mulvaney, P. Plasmon Coupling of Gold Nanorods at Short Distances and in Different Geometries. *Nano Lett.* **2009**, *9* (4), 1651–1658. https://doi.org/10.1021/nl900034v.

(34) Airola, M.; Liu, Y.; Blair, S. Second-Harmonic Generation from an Array of Sub-Wavelength Metal Apertures. *J. Opt. A* **2005**, *7* (2), S118–S123. https://doi.org/10.1088/1464-4258/7/2/016.

(35) Lee, D.; Yoon, S. Effect of Nanogap Curvature on SERS: A Finite-Difference Time-Domain Study. *J. Phys. Chem. C* **2016**, *120* (37), 20642–20650. https://doi.org/10.1021/acs.jpcc.6b01453.

(36) Moreau, A.; Ciracì, C.; Mock, J. J.; Hill, R. T.; Wang, Q.; Wiley, B. J.; Chilkoti, A.; Smith, D. R. Controlled-Reflectance Surfaces with Film-Coupled Colloidal Nanoantennas. *Nature* **2012**, *492* (7427), 86–89. https://doi.org/10.1038/nature11615.

(37) Rozin, M. J.; Rosen, D. A.; Dill, T. J.; Tao, A. R. Colloidal Metasurfaces Displaying Near-Ideal and Tunable Light Absorbance in the Infrared. *Nat. Commun.* **2015**, *6*, 7325. https://doi.org/10.1038/ncomms8325.

(38) Dill, T. J.; Rozin, M. J.; Palani, S.; Tao, A. R. Colloidal Nanoantennas for Hyperspectral Chemical Mapping. *ACS Nano* **2016**, *10* (8), 7523–7531. https://doi.org/10.1021/acsnano.6b02403.

(39) Sun, Y.; Xia, Y. Shape-Controlled Synthesis of Gold and Silver Nanoparticles. *Sci. (Washington, DC, United States)* **2002**, *298* (5601), 2176–2179. https://doi.org/10.1126/science.1077229.

(40) McLellan, J. M.; Li, Z. Y.; Siekkinen, A. R.; Xia, Y. The SERS Activity of a Supported Ag Nanocube Strongly Depends on Its Orientation Relative to Laser Polarization. *Nano Lett.* **2007**, *7* (4), 1013–1017. https://doi.org/10.1021/nl070157q.

(41) Nicoletti, O.; de la Peña, F.; Leary, R. K.; Holland, D. J.; Ducati, C.; Midgley, P. a. Three-Dimensional Imaging of Localized Surface Plasmon Resonances of Metal Nanoparticles. *Nature* **2013**, *502* (7469), 80–84. https://doi.org/10.1038/nature12469.

(42) Zhou, F.; Li, Z.-Y.; Liu, Y.; Xia, Y. Quantitative Analysis of Dipole and Quadrupole Excitation in the Surface Plasmon Resonance of Metal Nanoparticles. *J. Phys. Chem. C* **2008**, *112* (51), 20233–20240. https://doi.org/10.1021/jp807075f.

(43) Dadap, J. I.; Shan, J.; Eisenthal, K. B.; Heinz, T. F. Second-Harmonic Rayleigh Scattering from a Sphere of Centrosymmetric Material. *Phys. Rev. Lett.* **1999**, *83* (20), 4045–4048. https://doi.org/10.1103/PhysRevLett.83.4045.

(44) Butet, J.; Bachelier, G.; Russier-Antoine, I.; Jonin, C.; Benichou, E.; Brevet, P. F. Interference between Selected Dipoles and Octupoles in the Optical Second-Harmonic Generation from Spherical Gold Nanoparticles. *Phys. Rev. Lett.* **2010**, *105* (7), 1–4. https://doi.org/10.1103/PhysRevLett.105.077401.

(45) Butet, J.; Russier-Antoine, I.; Jonin, C.; Lascoux, N.; Benichou, E.; Brevet, P. F. Sensing with Multipolar Second Harmonic Generation from Spherical Metallic Nanoparticles. *Nano Lett.* **2012**, *12* (3), 1697–1701. https://doi.org/10.1021/nl300203u.

(46) Petty, M. C. *Langmuir-Blodgett Films : An Introduction*; Cambridge University Press, 1996.

(47) Lee, J.; Tymchenko, M.; Argyropoulos, C.; Chen, P.-Y.; Lu, F.; Demmerle, F.; Boehm, G.; Amann, M.-C.; Alù, A.; Belkin, M. A. Giant Nonlinear Response from Plasmonic Metasurfaces Coupled to Intersubband Transitions. *Nature* **2014**, *511* (7507), 65–69. https://doi.org/10.1038/nature13455.

(48) Demichel, O.; Petit, M.; Viarbitskaya, S.; M??jard, R.; De Fornel, F.; Hertz, E.; Billard, F.; Bouhelier, A.; Cluzel, B. Dynamics, Efficiency, and Energy Distribution of Nonlinear Plasmon-Assisted Generation of Hot Carriers. *ACS Photonics* **2016**, *3* (5), 791–795. https://doi.org/10.1021/acsphotonics.5b00726.

(49) Lassiter, J. B.; Chen, X.; Liu, X.; Ciracì, C.; Hoang, T. B.; Larouche, S.; Oh, S. H.; Mikkelsen, M. H.; Smith, D. R. Third-Harmonic Generation Enhancement by Film-Coupled Plasmonic Stripe Resonators. *ACS Photonics* **2014**, *1* (11), 1212–1217. https://doi.org/10.1021/ph500276v.

(50) Mamonov, E. A.; Murzina, T. V.; Kolmychek, I. A.; Maydykovsky, A. I.; Valev, V. K.; Silhanek, A. V.; Ponizovskaya, E.; Bratkovsky, A.; Verbiest, T.; Moshchalkov, V. V.; Aktsipetrov, O. A. Coherent and Incoherent Second Harmonic Generation in Planar G-Shaped Nanostructures. *Opt. Lett.* **2011**, *36* (18), 3681. https://doi.org/10.1364/OL.36.003681.

(51) Stephan Link, †; Zhong L. Wang, ‡ and; Mostafa A. El-Sayed*, †. How Does a Gold Nanorod Melt?#. **2000**. https://doi.org/10.1021/JP0011701.

(52) Tong, L.; Cobley, C. M.; Chen, J.; Xia, Y.; Cheng, J.-X. Bright Three-Photon Luminescence from Gold/Silver Alloyed Nanostructures for Bioimaging with Negligible Photothermal Toxicity. *Angew. Chemie Int. Ed.* **2010**, *49* (20), 3485–3488. https://doi.org/10.1002/anie.201000440.

(53) Petrova, H.; Perez Juste, J.; Pastoriza-Santos, I.; Hartland, G. V.; Liz-Marzán, L. M.; Mulvaney, P.; Penisson, J. M.; Bourret, A. On the Temperature Stability of Gold Nanorods: Comparison between Thermal and Ultrafast Laser-Induced Heating. *Phys. Chem. Chem. Phys.* **2006**, *8* (7), 814–821. https://doi.org/10.1039/B514644E.

(54) Ding, S.-J.; Nan, F.; Yang, D.-J.; Zhong, Y.-T.; Hao, Z.-H.; Wang, Q.-Q. Tunable Plasmon Resonance and Enhanced Second Harmonic Generation and Upconverted Fluorescence of Hemispheric-like Silver Core/Shell Islands. *Nanoscale* **2015**, *7* (38), 15798–15805. https://doi.org/10.1039/C5NR03627E.

Chapter 4

Metasurface-Enhanced Raman Spectroscopy (mSERS) for Oriented Molecular Sensing

Yuan Zeng[1,2], Riddhi Ananth[3], Tyler J. Dill[1], Andrea Rodarte[1], Matthew J. Rozin[1,2], Nathan Bradshaw[1], Eric R. Brown[1], and Andrea R. Tao[1,2,3*]

[1]Department of NanoEngineering, University of California, San Diego, 9500 Gilman Drive MC 0448, La Jolla, California 92093-0448

[2]Materials Science and Engineering, University of California, San Diego, 9500 Gilman Drive, La Jolla, California 92093

[3] Department of Chemistry & Biochemistry, University of California, San Diego, 9500 Gilman Drive, La Jolla, California 92093

*Email: atao@eng.ucsd.edu

Introduction

Surface-enhanced Raman spectroscopy (SERS) is a well-developed surface-sensitive technique that relies on large enhancements — with a theoretical enhancement factor up to 10^{13} and most experimental enhancement factors measuring between 10^{7} to 10^{11} [1,2] —of Raman scattering signals from chemisorbed or physiosorbed molecules near a metal surface.[3,4] The enhancement mechanism is mainly explained by two phenomena associated with electromagnetic and chemical charge transfer effects. In the first, the excitation of localized surface plasmon resonances (LSPRs) supports nanoscale localization of the electromagnetic near-field (i.e. the formation of hotspots), where enhancement factor is approximately proportional to the fourth power of this near-field intensity.[4–6] In the second mechanism, intermolecular charge transfer, charge transfer between a metallic surface and adsorbed molecules produces enhancements in Raman scattering due to resonance effects between the excitation of light and various electronic processes.[7–9] Decades of effort have been dedicated toward understanding and optimizing these two mechanisms for maximizing SERS signals for applications such as single-molecule sensing[10,11] and biomedical imaging.[12]

While SERS performed on rough metal surfaces has been used as a platform to provide signal enhancement for over forty years,[13] such substrates provide low hotspot uniformity, poor optical tunability in operation wavelength, and low surface sensitivities due to poor near-field confinement. In response, the past two decades has seen incredible growth of SERS substrates based on aggregated nanoparticles (NPs) that generate large field confinement due to plasmonic coupling between closely spaced NPs.[10,14–17] While aggregated NPs can provide large SERS signals and can provide a means toward large-scale fabrication of SERS platforms, the large sample-to-sample variation of these materials inherently limits the ability to perform quantitative SERS analysis of analyte concentration. For example, prior work measuring the distribution of SERS intensities for molecules adsorbed to a closed-packed Ag NP film showed that “cold” sites contain 61% of analyte molecules and that 24% of the total observed SERS signal is given by less than 0.007% of the total analyte molecules located in hotspots with anomalously highest

enhancement factors.[18] This heterogeneity in signal collection over a single SERS substate creates challenges in utilizing these NP-based platforms for calculating sensing metrics such as limit of detection (LOD), where a clear dependence between SERS signal and molecular concentration must be established. In addition, the nanogaps responsible for hotspot formation in these NP aggregates are characterized by random orientations and morphologies, which limits the optimization of charge transfer processes that depend highly on molecular orientation within a nanogap.

In more recent years, the design of SERS platforms has focused on metallic substrates that utilize coupling between individual plasmonic NPs and metal films, such as nanoscale patch antenna (NPA) structures and metasurfaces comprised of nanoparticles deposited on top of metal substrates.[19,20] Yi et al. drop-casted a colloidal mixture of Rhodamine 6G (R6G) and Ag nanocubes (AgNCs) onto a polymer coated silver thin film and achieved 10^{-11} M limit of detection for R6G molecules.[21] Marshall et al. used a spin coating method to deposit Ag nanospheres (AgNS) on a polymer-coated Ag thin-film.[22,23] The relative SERS intensity depends on the molecular orientation relative to the local electric field because SERS intensity is proportional to $\cos^2(\theta)$, where θ is the angle between the local electric field and Raman tensor directions.[24] By modeling molecular geometry and local field directions in density functional theory calculations, they were able to calculate the molecular orientation of a trapped analyte. However, to avoid interparticle coupling stemming from disordered aggregation, both NPA structures typically have a very low surface density of NPs, precluding many of these SERS platforms from being employed in SERS mapping and quantitative analysis of large-scale analytes (e.g. molecular monolayers or two-dimensional materials).

To address these challenges with molecular orientation and large-scale SERS mapping, we fabricated colloidal metasurfaces using a previously published method[25] using AgNCs that are deposited onto a flat metal film.[26–28] The resulting metasurface-based surface-enhanced Raman spectroscopy (mSERS) substrate possess a “nanocube-on-metal” (NOM) type structure and

operate by confining light to a resonant optical gap,[27] where a molecular analyte is trapped. Advantageously, Raman enhancement can be generated from a large cross-sectional area (>20% of the total substrate area) of the mSERS substrate,[26] which allows for sampling a broad range of different analytes without necessitating specific binding chemistries. Here, we characterize these mSERS substrates and the design parameters that dictate mSERS detection capabilities at low analyte concentrations, such as nanocrystal density, illumination wavelength, near-field polarization, and molecular analyte orientation. As a demonstration, we carry out sensing experiments for an emerging organic pollutant in drinking water, Bis (4-bromophenyl) ether (BDE-15) that is expected to possess highly anisotropic molecular orientations when adsorbed onto a surface. We measure the quantitative LOD for BDE-15 in aqueous solutions to compare to other SERS-based PBDE sensors.[29]

Experimental Methods

Materials. Ethanethiol (97%), Thiophenol (97%) were purchased from Sigma-Aldrich. Pyrene (in solution), SPEX CertiPrep (1.2 mL, 1000 µg / mL) was purchased from Fisher scientific. Pyrene (powder) was purchased from Spectrum Chemical. Bis(4-bromophenyyl) ether (BDE-15), 99% was purchased from Alfa Aesar. Monolayer graphene on pre-diced Au substrate (1cm x 1 cm) was ordered from Grolltex, Inc. All materials were used as purchased.

Gold Substrate Fabrication. Au thin-film substrates were fabricated through Sputter Deposition (using Denton Discovery 18 Sputter System). 100mm diameter, 500 µm thick P type doped wafer (University wafer) was cleaned with isopropanol and cleanroom cloth. The sputtering RF bias is used to clean the substrate for 20 seconds and followed with 10 seconds Cr (400 W) and 120 seconds Au (300 W) sputtering with the Ar gas pressure as 2.4 mTorr. Then the wafer was diced into 1cm x 1cm size for later use.

BT SAM Substrate Fabrication. Au thin-film substrates were washed with ethanol, piranha solution (60 seconds), DI water and dried with compressed air. Then the washed substrates were incubated in 1mL, 10% BT solution (in Ethanol) for 3 hours, rinsed 8 times with ethanol thoroughly, dried under compressed air and kept in a fume hood overnight (about 16 hours).

Pyrene SAM Substrate Fabrication. 2mL, 5 μg / mL pyrene solution (in chloroform) was deposited dropwise onto a deionized water (18 MΩ) subphase in KSV Nima KN2001 Langmuir-Blodgett trough. Then the Teflon barriers were compressed at 4 mm / min speed until the end and achieved 10mN ± 1mN surface pressure (surface area is about 30 cm^2). Pre-cleaned Au thin-film substrate was mechanically dipped into the air-water interface quickly, placed vertically on paper towel and dried in air.

Ag nanocubes (AgNCs) Preparation. Ag Nanocubes were synthesized via a polyol method published elsewhere.[30] $AgNO_3$ is reduced in a solution of pentanediol, $CuCl_2$, and polyvinylpyrrolidone (PVP) (M_w=55,000). PVP serves as a selective capping agent that controls nanocube nucleation and growth. The reaction was allowed to proceed until the resulting colloidal dispersion turned an opaque yellow-green color. To remove excess reactants, the nanocube dispersion product was centrifuged (2700 rpm for 10 min) using a Thermo Scientific CL2 Centrifuge, and the resulting precipitate was redispersed and diluted in an ethanol and water mixture, and then vacuum-filtered (Millipore Durapore membranes, with 0.65 μm, 0.45 μm, then 0.22 μm pore sizes) to remove any larger, unwanted particles.

Metasurface Fabrication. To prepare the AgNCs for Langmuir-Schaefer deposition, a nanocube dispersion is washed by centrifugation and the precipitate is dispersed in EtOH. This process was repeated three times before finally dispersing the precipitate in chloroform. AgNC films were fabricated using a KSV Nima KN2001 Langmuir-Blodgett trough, as previously described.[31] The AgNC solution was deposited drop-wise onto a deionized water (18 MΩ) subphase. The film formed at the air-water interface was allowed to equilibrate for 30 min. The Ag

nanocube film was isothermally compressed to a desired surface density before being transferred to the Au or functionalized Au substrates via mechanical dipping.

PBDE mSERS Sensor Fabrication. Pre-cleaned Au thin-film substrate was incubated in 1mL, 1% Ethanethiol solution (in Ethanol) for 3 hours. Washed with Ethanol 5 times and dried under compressed air. Then the substrates were held in a glass vial with 10 mL BDE-15 DI water solution (prepared by diluting 0.1mM BDE-15 ethanol solution with DI water), stirring at 500 RPMs and keep 3 hours. Because the surface is hydrophobic, there was no water residue left on the Au thin-film substrate with the BDE-15 molecules. Then AgNCs were deposited on the thin-film with the method introduced before.

mSERS measurements. All Raman spectra were obtained using a Renishaw inVia confocal Raman microscope. Measurements were taken at powers < 1 mW to prevent laser induced damage. 785 nm illumination was provided by a Renishaw 300 mW diode laser. 633 nm illumination was provided by a Renishaw 17mW HeNe laser. 514, 488, and 457 nm illumination was provided by a Modu-Laser 50 mW Ar+ Ion laser. All spectra were collected through a 50x, 0.75 NA objective.

FDTD Simulations & Simulated EF. Electromagnetic modeling was performed with Lumerical FDTD Solutions. AgNCs (Palik dielectric data) were modeled in 90 nm cube size, 10 nm radius of curvature on the corners with an underlying 75 nm Au thin-film. A 6 nm dielectric layer with n = 1.4 was added to reflect the analyte layer positioned within the plasmon volume. Incident light was injected normal to the substrate and polarized parallel to the (100) faces of the AgNC. A 1 nm global mesh was used; to improve accuracy, the mesh size was reduced in the gap region to 0.5 nm. The electric field profiles were calculated in the plane of the Au thin film, 1 nm offset from the surface. An average EF for the mSERS substrate is calculated by summing $|E/E_o|^4$ at each pixel (1x1 nm) and normalizing to the cross-sectional area of each nanocubes. This calculation was carried out at discrete wavelengths over the visible range.

Results and Discussion

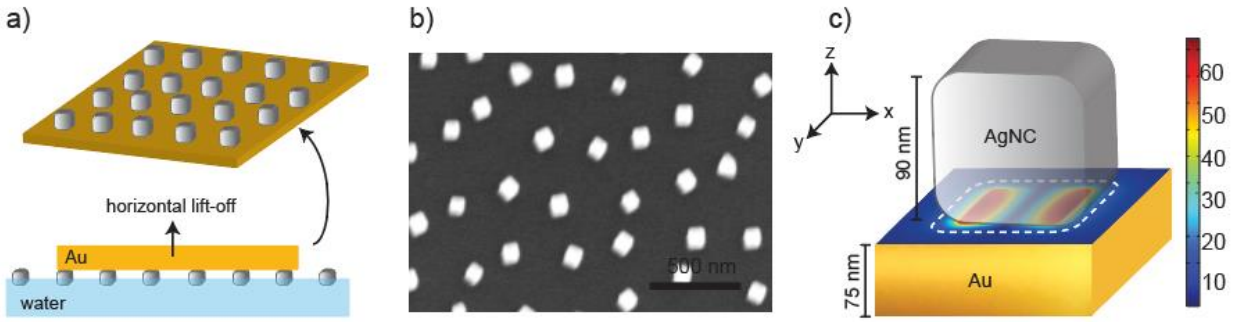

Figure 4.1 | Fabrication of the mSERS platform: (a) Schematic of the colloidal metasurface via deposition of AgNCs onto a flat Au film. **(b)** Top-down SEM image of the resulting metasurface showing well-spaced AgNCs (90 nm in edge length). **(c)** Schematic of a single nanocube-on-metal (NOM) meta-atom and the location of the electromagnetic hotspot inside the meta-atom gap. The color map shows FDTD simulation results indicating the overall electric field strength associated with the optical gap. For the excitation plane wave, propagation direction is along the z-axis and polarization is along the x-axis.

A schematic of the fabrication process for our NOM metasurface is shown in Figure 4.1a, depicting how Langmuir-Schaefer deposition is used to generate the layered metallic structure.[28] Briefly, Ag nanocubes (AgNCs) are dispersed in chloroform, drop-casted onto an air-water interface to form a floating AgNC monolayer, and isothermally compressed with a mechanical barrier until a target AgNC density within the monolayer is reached. Here, we aim for a target AgNC density range of 5-30% surface coverage, which avoids the formation of AgNC clusters or close-packing within the monolayer. The AgNC monolayer is then transferred to an Au thin-film by horizontal dip-coating. This bottom-up assembly technique allows us to form a NOM metasurface with controlled AgNC densities in the range of 11-65 AgNCs / μm^2 such that the AgNCs that behave as well-separated optical meta-atoms (Fig. 4.1b). Figure 4.1c shows a finite-difference time-domain (FDTD) model and electromagnetic heat map for a single meta-atom consisting of AgNCs (edge length=90 nm, edge/corner radius of curvature=10 nm) and a 95 nm thick Au thin-film (Appendix C, C1), separated by a dielectric gap of 6 nm. In this model, the dielectric gap is modeled to approximate the polymer layer that serves as the capping agent in the AgNC synthesis and is retained on the AgNC surface. Strong capacitive coupling between the AgNC and Au thin-film in this meta-atom produces an electromagnetic hot-spot located inside the dielectric gap that gives rise to a 70-fold near-field enhancement (E/E_0) within the optical gap at the resonant

wavelength of 847 nm (Appendix C, C2). This heat map includes both the in-plane polarized electric field components (E_x, E_y) and the out-of-plane polarized electric field component E_z, with the highest intensity near-field generated from the E_z component.

First, we investigated how meta-atom density affects mSERS intensity. We selected the widely used Raman analyte benzenethiol (BT) [32–34] as a SERS benchmark for our analysis because it is known to form an oriented, uniform self-assembled monolayer (SAM) on metal surfaces[35] and because the SERS fingerprint of BT adsorbed on a metal surface is identical to that of free BT molecules in solution.[36] We deposited AgNCs (edge length=91 ± 4 nm) on a BT functionalized Au thin-film with an AgNC density estimated by SEM at the following surface coverages: 6%, 16%, 17%, 27%, 32%, 43%, and 65%. Figure 4.2a shows averaged mSERS

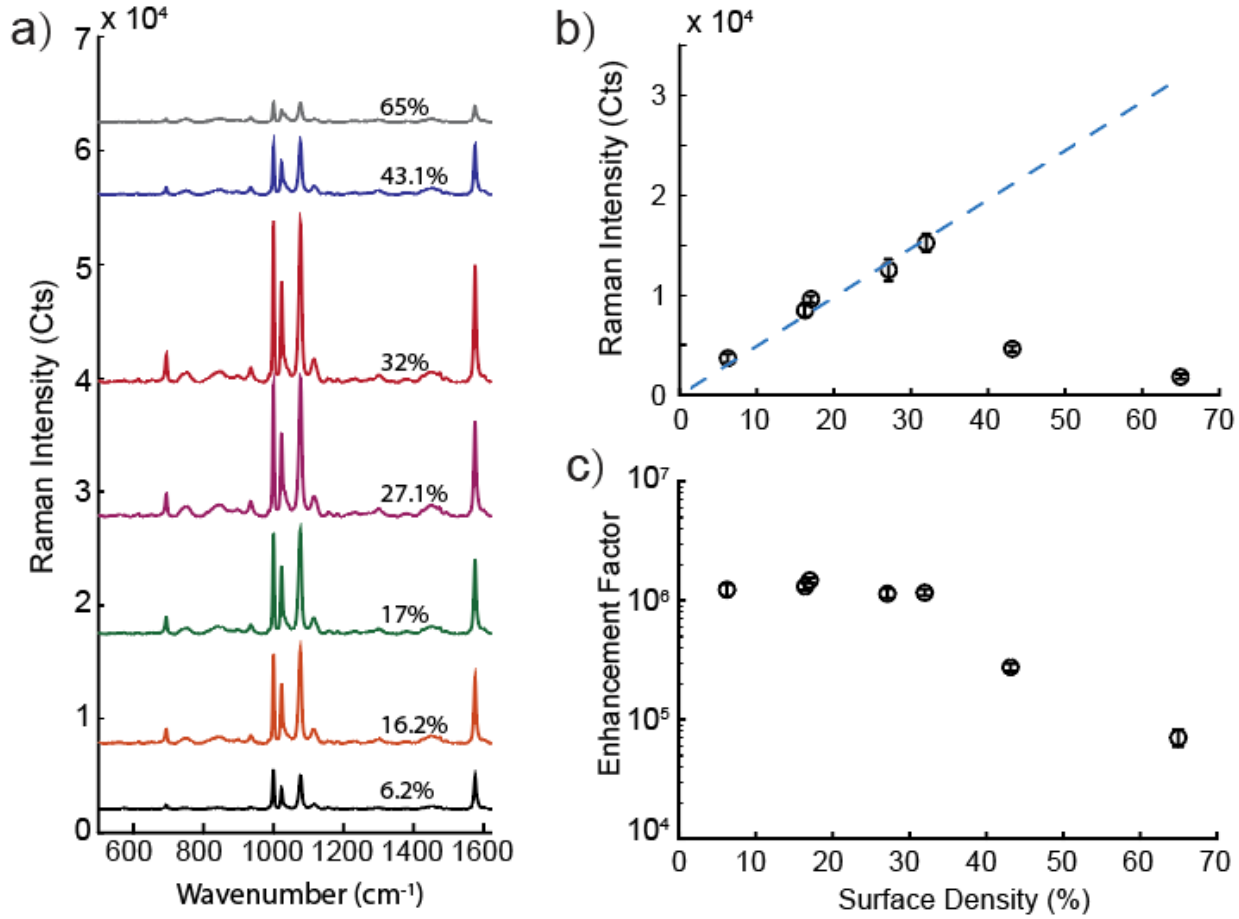

Figure 4.2 | mSERS intensity and enhancement factor: (a) Raman Spectra for BT collected using our mSERS platform as a function of increasing meta-atom density. **(b)** Raman intensity of the 1023 cm^{-1} vibrational mode of BT as a function of meta-atom density. **(c)** Calculated meta-atom density dependent enhancement factor (EF) showing a falloff as AgNCs begin to aggregate at higher surface densities.

spectra for these various surface coverages, where each spectral point is an average of 100 points collected over the metasurface. The peaks at 999 cm^{-1} and 1076 cm^{-1} correspond to the $\beta_{CCC}(a_1)$ vibrational mode, the peak at 1023 cm^{-1} corresponds to $\beta_{CH}(a_1)$ vibrational mode and the peak at 1575 cm^{-1} corresponds to C=C ring stretch mode.[37,38] As coverage density increases from 6% to 32%, the mSERS intensity of all the peaks gradually increases. However, when coverage density increases above 32%, the mSERS intensity starts to decrease. We plotted the intensity of the $\beta_{CH}(a_1)$ vibrational mode (1023 cm^{-1}) for each coverage density (Figure 4.2b). As coverage density increases from 6% to 32%, the SERS intensity increases linearly (R^2 = 0.96) from 1950 to 9492 counts. At 43% and 65% coverage density, the average cluster size is 2 AgNCs and 56 aggregated AgNCs, respectively, resulting in a significant decrease in SERS intensity to 3015 and 1150 counts, respectively. Figure 4.2c shows the calculated change in SERS enhancement factor (EF) using the procedure reported by Zhang et al.[39] As coverage density increases from 6% to 32%, the EF stays constant at 10^6, indicating that near-field intensity is independent of coverage density when meta-atoms are well spaced. However, when coverage density increases from 32% to 65%, the EF decreases by more than one order of magnitude. This EF decrease is attributed to interparticle coupling between neighboring AgNCs, which causes a redshift of the optical resonance and causes the metasurface to move off-resonance and significant decrease in E/E_0 at our laser wavelength (785 nm) (Appendix C, C3).[28]

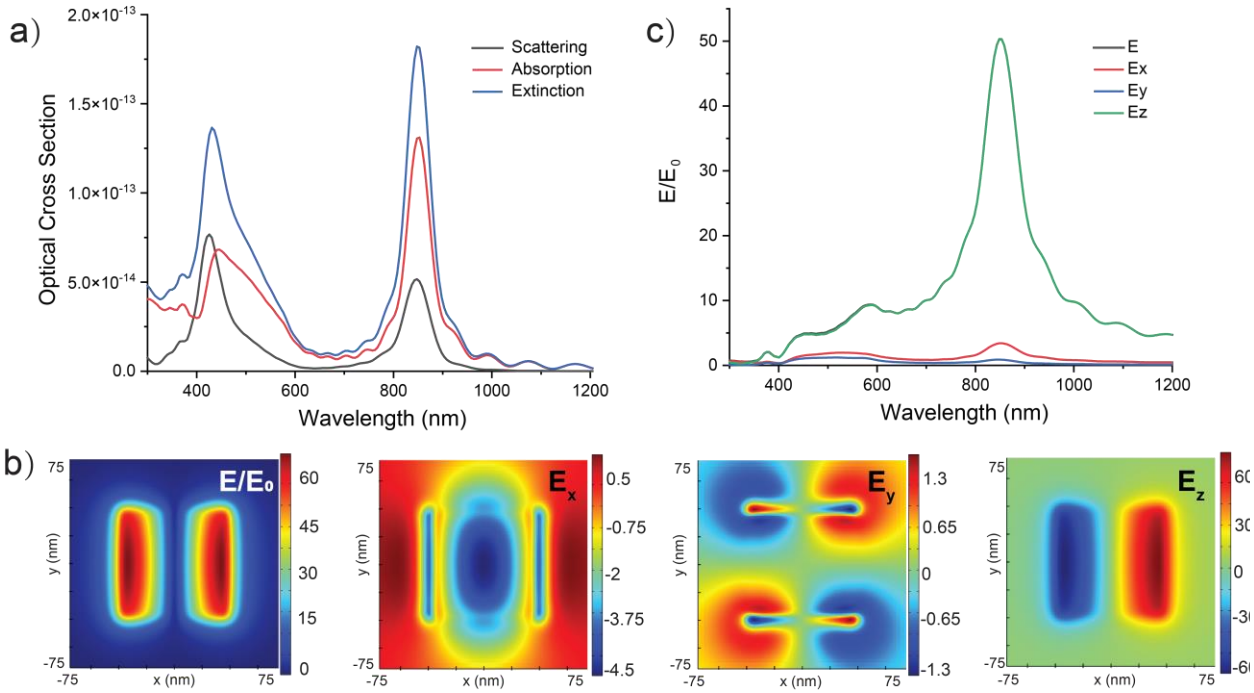

Figure 4.3 | Simulated far-field spectra, near-field distributions, and EFs: a) Simulated optical scattering (black), absorption (red) and extinction spectra (blue). b) Color map showing the simulated electric field distribution for different polarizations at the nanogap resonance. From left to right: E/E_0, x-polarized E-field, y-polarized E-field, and z-polarized E-field. For the excitation plane wave, propagation direction is along the z-axis and polarization is along the x-axis. (c) Wavelength-dependent E-field with different polarizations. The black line (E/E_0) overlaps significantly with the green line and is not visible in this plot

Because SERS enhancement is known to exhibit a strong polarization dependence that is dictated by the geometries of the metal nanostructures used as substrates,[40–42] we carried out a wavelength-dependent simulation of both in-plane (E_x, E_y) and out-of-plane (E_z) components of the near-field to calculate the theoretical contribution of each component to the mSERS enhancement factor in Fig. 4.2c. Figure 4.3a shows a simulated far-field spectra of our NOM metasurface (Appendix C, C4). At 425 nm, there is a large scattering cross-section peak and a broad absorption cross-section peak originating from a cube mode resonance.[27] At 847 nm, the gap mode resonance results in a strong absorption cross-section and moderate scattering cross-section, which can provide enhancement for both excitation and emission processes of mSERS. Figure 4.3b shows a color map of the electric field distribution for illumination at the gap mode resonance wavelength, 847 nm. This on-resonance gap mode is a dipolar mode with a maximum enhancement of E/E_0 =71. Also, this gap mode resonance is highly polarized. The E_x component

of near-field enhancement is 4.5, the E_y component is 1.3 and the E_z component is 66, indicating that the out-of-plane (E_z) polarized electric-field is dominant in our metasurface. We then integrated the electric field strength over the hot spot area for each wavelength, as plotted in Figure 4.3c. At the gap mode resonance (847 nm), the E_z component is more than 2 orders of magnitude higher than the E_x and E_y components. At the cube mode resonance (425 nm), this NOM structure has a large scattering cross-section, but the near-field enhancement is much weaker than the gap mode resonance.

The large out-of-plane component of the near-field suggests that molecular orientation is likely to play a large role in determining the Raman EF of our NOM metasurface when detecting analytes that are highly anisotropic and that adopt preferred orientations within the optical gap. To better quantify the relationship between molecular analyte orientation and the EF of our NOM metasurface, we characterized our mSERS response using two different analytes that adopt different orientations within the NOM gap: BT and pyrene. Figure 4.4a shows a schematic of these two analyte orientations. Owing to π-π interactions between aromatic rings, BT molecules preferentially orientate normal to the metal surface and self-organize in this manner [43]. On the other hand, because the transition dipoles of pyrene are in-plane polarized, pyrene molecules preferentially orient parallel to the metal surface.[44] Figure 4.4b shows a comparison of the Raman spectra obtained for isotropic BT molecules dispersed in ethanol (black line), the bare NOM metasurface prior to BT exposure (blue line), and the NOM metasurface after exposure to BT (red

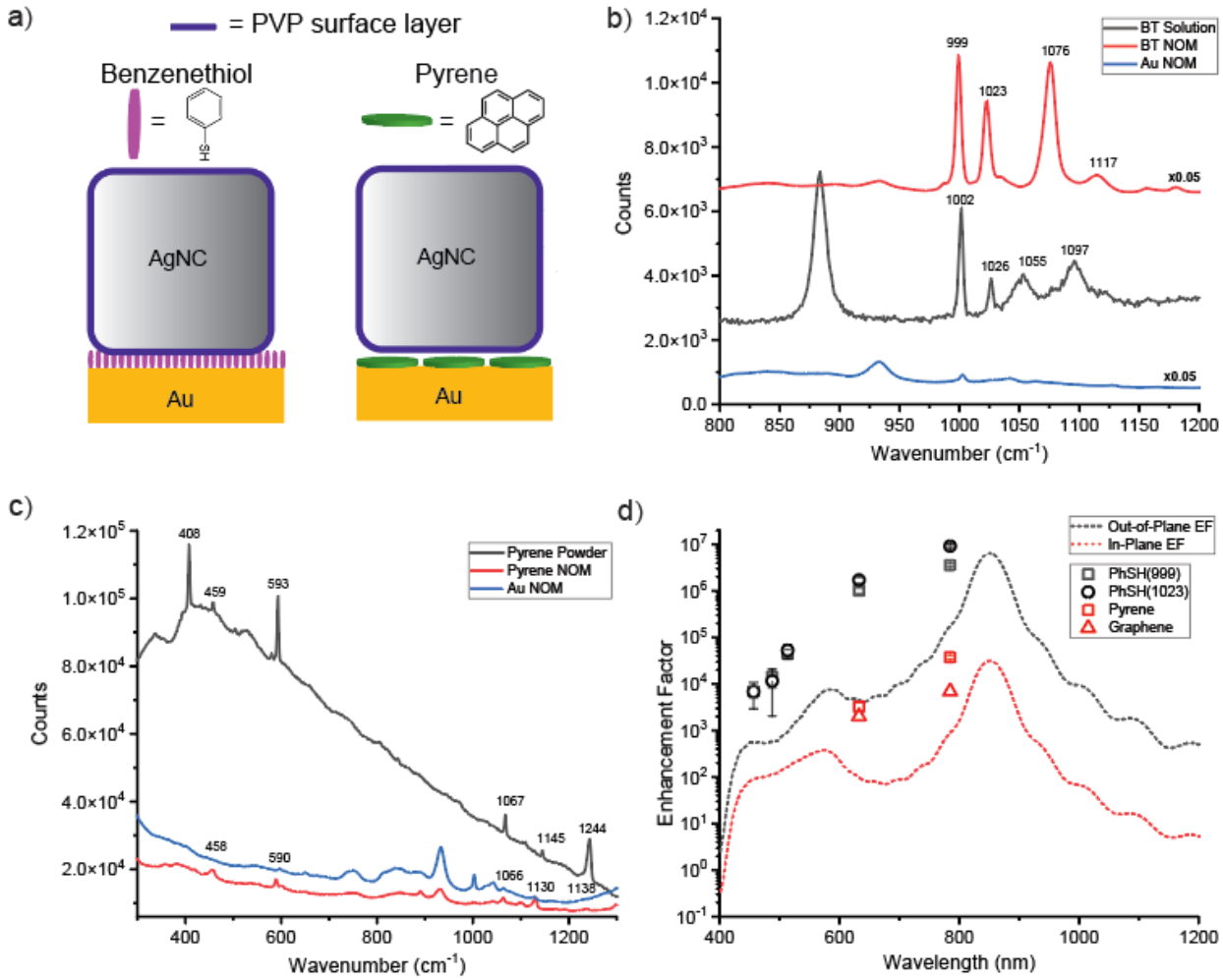

Figure 4.4 | Schematic and wavelength dependent EF of molecule analyst: (a) Schematic of meta-atom with BT molecules (left) and pyrene molecules (right) in gap. **(b)** Raman spectra of BT-NOM under 785 nm excitation (black is free BT molecules in Ethanol, red is BT metasurface and blue is metasurface without BT). **(c)** Raman spectra of pyrene metasurface under 785 nm excitation (black is pyrene powder on Au thin-film, red is pyrene metasurface and blue is metasurface without pyrene). **(d)** wavelength dependent EF for BT metasurface (black square is BT vibrational mode at 999 cm^{-1}, black circle = 1023 cm^{-1}), pyrene metasurface (red square = 590 cm^{-1}) and graphene metasurface (red triangle = 2593 cm^{-1}).

line). The BT-NOM exhibits peaks corresponding to the $\beta_{CCC}(a_1)$ vibrational mode at 999 cm^{-1}, $\beta_{CH}(a_1)$ vibrational mode at 1023 cm^{-1} and $\beta_{CCC}(a_1)$ vibrational mode at 1076 cm^{-1}. Compared to the Raman spectra of free BT molecules, the vibrational modes at 999 cm^{-1} and 1023 cm^{-1} are redshifted ~3 cm^{-1} which is attributed to surface adsorption. However, the vibrational mode at 1076 cm^{-1} is redshifted ~15 cm^{-1},which overlaps with the ethanol C-H rocking mode at 1096 cm^{-1}.[37,45] In addition, the peak at 884 cm^{-1} can be assigned to the ethanol C-C stretching mode and the peak at 1055 cm^{-1} corresponds to the ethanol C-O stretching mode (Appendix C, C5).[45] The weak modes in the Au NOM reference spectrum originate from trace amounts of PVP molecules

that remain grafted on the AgNC surface.[46] Figure 4.4c shows the Raman spectra of pyrene molecule dispersed in ethanol solution (black line) and pyrene adsorbed to the NOM metasurface (red line). Because pyrene is an excimer with strong fluorescence, pyrene solution has a broad band background centered around 450 cm^{-1}.[47,48] The Raman peaks at 408 cm^{-1}, 458 cm^{-1} and 593 cm^{-1} correspond to skeletal stretching modes, the peaks at 1067 cm^{-1} and 1145 cm^{-1} correspond to C-H in-plane bending and the peak at 1244 cm^{-1} corresponds to C-C stretching/C-H in-plane bending.[49] Compared with pyrene solution, the pyrene NOM signature only has two detectable peaks at 458 cm^{-1} and 593 cm^{-1}. The pyrene band at 408 cm^{-1} is notably weaker when adsorbed to the NOM, which is likely due to charge transfer with the Au thin-film. This is also supported by the observed fluorescence quenching in the pyrene-NOM spectrum.

We then calculated EF using the fourth-power approximation where EF = $(E/E_0)^4$ where E/E_0 is the local electric field.[4,5]. Because our NOM metasurface has a polarized E-field which dominated by E_z and because our surface analytes are highly oriented, we modified this fourth-power equation with an additional dipole moment term, as follows:[22]

$$G = \frac{|E(\omega_0)|^2}{|E_0(\omega_0)|^2}\left(\frac{\left|\hat{E}\cdot\hat{\mu}\right|^2}{\left|\widehat{E_0}\cdot\hat{\mu}\right|^2}\right)\frac{\rho(\omega_1)}{\rho_0(\omega_1)} = G_{ex}\cdot S_{\mu}\cdot G_{em}$$

Where E_0 is the incident electric field, E is the electric field at molecule location, ω_0 is incident frequency, ω_1 is scattering frequency, $\widehat{E_0}$ and $\hat{E}$ correspond to polarization direction of incident electric field and electric field at the molecule location, $\hat{\mu}$ corresponds to the oriented molecular dipole, and ρ corresponds to optical density. Because both $\hat{E}$ and $\hat{\mu}$ have x-, y-, and z-components, $\left|\hat{E}\cdot\hat{\mu}\right|^2$ can be rewritten as $(E_x\mu_x)^2 + (E_y\mu_y)^2 + (E_z\mu_z)^2$ where $(E_x\mu_x)^2 + (E_y\mu_y)^2$ is an in-plane term and $(E_z\mu_z)^2$ is an out-of-plane term.

Figure 4.4d shows the calculated and experimental wavelength-dependent Raman EFs

for the BT-NOM and pyrene-NOM samples (Appendix C, C6, C7, C8, and C11). Calculated EFs are obtained from the FDTD-simulated near-field strengths for the out-of-plane (E_z, black dashed line) and in-plane (E_{xy}, red dashed line) polarized components. At resonance, the in-plane oriented dipole moments are enhanced by more than 4-orders of magnitude and the out-of-plane oriented dipole moments are enhanced by more than 6-orders of magnitude. Experimental EFs were obtained by measuring mSERS intensities for the BT-NOM and pyrene-NOM at five different Raman excitation wavelengths: 457 nm, 488 nm, 514 nm, 633 nm and 785 nm. We then used the strongest Raman bands (the 999 cm^{-1} and 1023 cm^{-1} peaks for BT and the 593 cm^{-1} peak for pyrene) to calculate the experimental EFs. In the BT-NOM, the experimental EFs are one order of magnitude higher than the calculated EFs at 457 nm, 488 nm, 514 nm and 785 nm. This is attributed to chemical contributions[50–52] to SERS enhancement. At 633 nm excitation, the experimental EF is more than two orders of magnitude higher than calculated EF. This large overperformance likely originates from two factors: i) partially on-resonance meta-atoms in our metasurface due to the size distribution of AgNCs, and ii) the areal distribution of hotspots inside NOM junctions. Also, we observed that the EF of the $\beta_{CH}(a_1)$ vibrational mode (1023 cm^{-1}) is 2.58-fold larger than the EF of the $\beta_{CCC}(a_1)$ vibrational mode (999 cm^{-1}) at resonance. This difference in EF originates from the difference in dipole moment orientation, given that $\beta_{CH}(a_1)$ has larger μ_z component than $\beta_{CCC}(a_1)$. At off-resonance wavelengths, near-field enhancement does not play a dominant role and there is no difference between these two EFs for $\beta_{CH}(a_1)$ and $\beta_{CCC}(a_1)$.

In the pyrene-NOM, we only have two data points at 633 nm and 785 nm because pyrene has a lower Raman scattering cross-section and its experimental EF at 457 nm, 488 nm and 514 nm is lower than our instrumental detection limit (around 10^3). The theoretical EF is calculated using the in-plane polarized near-field (red dashes). Overall, the experimental EF of the pyrene-NOM is more than two orders of magnitude lower than the experimental EF of the BT-NOM, indicating that pyrene molecules are enhanced by the relative weakly in-plane polarized near-

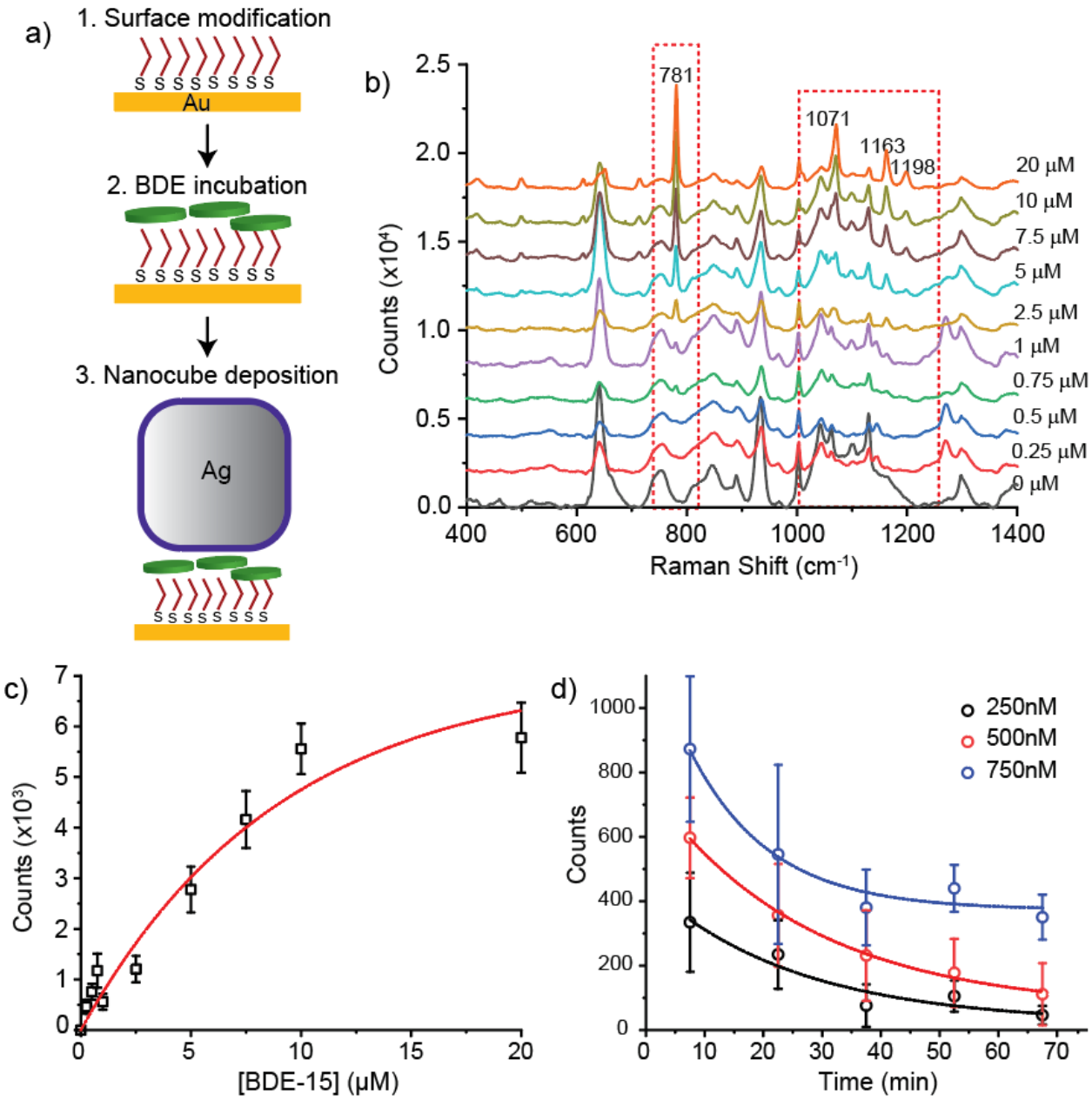

Figure 4.5 | Schematic of PBDE mSERS sensor fabrication and Raman spectra of PBDE metasurface: (a) Schematic of PBDE mSERS fabrication. (b) mSERS spectra of metasurface sensor incubated in different BDE-15 concentration (c) Concentration-dependent and (d) post-fabrication time-dependent Raman intensity of BDE-15 collected at 781cm^{-1}.

field. Similar to BT-NOM, pyrene-NOM also exhibits a discrepancy of ~10 between experimental data and simulations. To confirm weaker enhancement on in-plane orientated bonds, we replaced pyrene molecules with monolayer graphene (Graphene-NOM) and the experimental EF is consistent with the calculated EF at 785 nm excitation. At 633 nm, there is a small overestimation in experimental EF owing to heterogeneities in AgNC size and areal distribution of NOM

junctions.[53] The experimental EF of pyrene NOM is slightly higher than Graphene-NOM at 785 nm because trace amounts of misaligned pyrene molecules due to molecular aggregation possess an out-of-plane orientation and, thus, a large μ_z.

Because our NOM structure provides an EF greater than four orders of magnitude for flat aromatic hydrocarbon molecules such as pyrene, it suggests that such a sensor platform might perform exceptionally well for in detecting hazardous analytes with similar planar molecular structures, such as BDEs. To demonstrate, we prepared a BDE mSERS sensor using the fabrication method shown in Figure 4.5a. First, a piranha-cleaned Au thin-film was functionalized with ethanethiol and incubated in a 1 μM BDE-15 solution. BDE-15 molecules spontaneously physisorb to the functionalized Au thin-film due to poor solubility of BDE-15 in water and due to attractive hydrophobic interactions between BDE-15 molecules and the alkyl chains of ethanethiol. Following this incubation, we transferred AgNCs to the functionalized Au thin-film via Langmuir-Schaefer deposition, trapping the physisorbed BDE-15 molecules inside a NOM junction. Because our NOM structure has highest EF at 785 nm, our BDE-15 SERS measurement was carried out using 785 nm laser. mSERS spectra were obtained by generating a Raman map with automated collection using a programmed x-y stage. Each mSERS spectrum obtained is the averaged lineshape from 49 different collection points (a 7x7 array) across the mSERS substrate. This averaging allows us to obtain highly reproducible mSERS signatures over thousands of meta-atoms. Figure 4.5b shows the mSERS spectra of our BDE sensor incubated at different BDE-15 concentrations. The peak at 781 cm^{-1} corresponds to the β(C-H) mode, the peak at 1071 cm^{-1} corresponds to the υ(C-Br), ring stretch mode, and the peaks at 1163 cm^{-1} and 1198 cm^{-1} correspond to the υ_s(C-O), β(C-H) modes.[54] Although the peaks at 781 cm^{-1}, 1071 cm^{-1} and 1163 cm^{-1} have similar intensities in the BDE-15 powder reference spectrum (Appendix C, C9), the peak at 781 cm^{-1} has a higher relative intensity in our BDE mSERS sensor owing to stronger

enhancement of the β(C-H) mode. This is attributed to symmetry-breaking upon BDE-15 adsorption to the mSERS substrate and the larger μ_z component in β(C-H) dipole moment. At concentrations from 0 μM to 0.25 μM, no BDE-15 peak is apparent in the mSERS spectra because the BDE-15 concentration is lower than the limit of detection (LOD) of the platform. Above 0.25 μM, the peak intensity of the β(C-H) mode (781 cm^{-1}) gradually increases with concentration; however, owing to strong background noise (1000 cm^{-1} to 1200 cm^{-1}) from polyvinylpyrrolidone (PVP) on the AgNCs, the peaks at 1071 cm^{-1} and 1163 cm^{-1} are not detectable at concentrations below 2.5 μM. As BDE-15 concentration is increased to above 2.5 μM, three BDE-15 vibrational modes appear at 781 cm^{-1}, 1071 cm^{-1} and 1163 cm^{-1}. This is consistent with the BDE-15 powder spectrum, although the peak maxima are slightly shifted by ~5 cm^{-1}.

Moving forward, we chose to analyze the response of the 781 cm^{-1} peak (β C-H mode) for quantitative BDE-15 analysis, aligned with previous studies.[29] Figure 4.5c shows the plot of mSERS intensity vs. BDE-15 concentration, it has a linear relation below 5 μM and decreases above 5 μM. This decreased detection at higher concentration ranges is indicative of: i) saturation of surface binding sites on Au substrate, ii) increased thickness in the adsorbed BDE-15 layer, which results in a larger gap distance and weaker near-field enhancement, and iii) increased surface roughness due to adsorbed BDE-15 causing a decrease in AgNC density. We performed a time-dependent study of the response of the BDE sensor to probe how robust the mSERS signal is. We observed a decrease in mSERS intensity with time, as plotted in Figure 4.5d which displays Raman counts at various times after AgNC transfer. At 7.5 min, 0.25 μM sensor has 334 counts, 0.5 μM sensor has 597 counts and 0.75 μM sensor has 873 counts. As post-fabrication time increases from 7.5 min to 67.5 min, the Raman intensity decreases exponentially to 46 counts, 111 counts and 350 counts, respectively. We attribute this exponential decay to molecular diffusion of analytes inside the nanogap, which has been previously observed[23,55,56] and likely to occur

given that the mSERS hotspot is located less than 10 nm away from the edge of the nanogap. While this molecular diffusion potentially results in an underestimation of the LOD for our mSERS sensor, it provides added challenges in carrying out in-line quantitative analysis due to this time-dependent Raman signal, which will depend on both analyte diffusion timescales and the kinetics of analyte adsorption.

Conclusion

Overall, we show that a colloidal NOM metasurface with a strong gap mode resonance can serve as a valuable platform for chemical detection based on mSERS. Both FDTD simulations and experimental results confirm that the strong out-of-plane polarized near-field plays the dominant role in mSERS enhancement, providing ~10^7 enhancement for the out-of-plane and ~10^5 enhancement for the in-plane aligned aromatic molecules observed in this study. Because vibrational modes with different dipole moment orientations provide vastly different mSERS signal intensities, this platform provides the ability to study molecular orientation and local order/orientation of 2D materials and thin-films. As a chemical sensor for aromatic BDE-15 analytes, we achieved quantitative and reproducible measurements at low-level concentrations with a LOD of 0.25 μM. Although our metasurface has relative low maximum EF (10^7), the large hotspot area of the AgNC meta-atom provides sampling over many more molecules and leads to a comparable LOD as other SERS-based BDE sensors that rely on only a few, high-performing hotspots. In the future, by decreasing meta-atom gap distance and precise engineering of the metasurface resonance frequency, the EF of this mSERS platform has the potential to exhibit even lower LODs in chemical sensing. Future work will focus on how such mSERS platforms can be utilized for in situ or in-line chemical sensing, where directional diffusion of physiosorbed molecules inside the gap will be addressed, in addition to improving mSERS performance and signal stability.

Acknowledgements

The authors would like to thank Nano3 and the San Diego Nanotechnology Infrastructure (NSF Award ECCS-2025752), the UC San Diego MRSEC (NSF Award DMR-2011924), and the NanoEngineering MRC for use of their equipment and facilities, and Dr. Aliaksandr Zaretski in Grolltex, inc. for graphene sample fabrication. This work was supported by NSF Awards CHE-1807891 and DMR-2011924.

Chapter 4, in full, is a reprint of the material as it appears in an under reviewed manuscript for ACS Applied Materials & Interfaces. Yuan Zeng, Riddhi Ananth, Tyler J. Dill, Andrea Rodarte, Matthew J. Rozin, Nathan Bradshaw, Eric R. Brown, and Andrea R. Tao. The dissertation author was the primary investigator and author of this paper

References

(1) Lee, D.; Yoon, S. Effect of Nanogap Curvature on SERS: A Finite-Difference Time-Domain Study. *J. Phys. Chem. C* **2016**, *120* (37), 20642–20650. https://doi.org/10.1021/acs.jpcc.6b01453.

(2) Le Ru, E. C.; Blackie, E.; Meyer, M.; Etchegoint, P. G. Surface Enhanced Raman Scattering Enhancement Factors: A Comprehensive Study. *J. Phys. Chem. C* **2007**, *111* (37), 13794–13803. https://doi.org/10.1021/jp0687908.

(3) Jeanmaire, D. L.; Van Duyne, R. P. Surface Raman Spectroelectrochemistry. Part I. Heterocyclic, Aromatic, and Aliphatic Amines Adsorbed on the Anodized Silver Electrode. *J. Electroanal. Chem.* **1977**, *84* (1), 1–20. https://doi.org/10.1016/S0022-0728(77)80224-6.

(4) Sharma, B.; Frontiera, R. R.; Henry, A. I.; Ringe, E.; Van Duyne, R. P. SERS: Materials, Applications, and the Future. *Materials Today*. Elsevier January 1, 2012, pp 16–25. https://doi.org/10.1016/S1369-7021(12)70017-2.

(5) Stiles, P. L.; Dieringer, J. A.; Shah, N. C.; Van Duyne, R. P. Surface-Enhanced Raman Spectroscopy. *Annu. Rev. Anal. Chem.* **2008**, *1* (1), 601–626. https://doi.org/10.1146/annurev.anchem.1.031207.112814.

(6) Schatz, G. C.; Young, M. A.; Duyne, R. P. Electromagnetic Mechanism of SERS. In *Surface-Enhanced Raman Scattering*; Springer Berlin Heidelberg, 2006; pp 19–45. https://doi.org/10.1007/3-540-33567-6_2.

(7) Wang, Y.; Ji, W.; Sui, H.; Kitahama, Y.; Ruan, W.; Ozaki, Y.; Zhao, B. Exploring the Effect of Intermolecular H-Bonding: A Study on Charge-Transfer Contribution to Surface-Enhanced Raman Scattering of p-Mercaptobenzoic Acid. *J. Phys. Chem. C* **2014**, *118* (19),

10191–10197. https://doi.org/10.1021/jp5025284.

(8) Liu, S.; Wan, S.; Chen, M.; Sun, M. Theoretical Study on SERRS of Rhodamine 6G Adsorbed on Ag2 Cluster: Chemical Mechanism via Intermolecular or Intramolecular Charge Transfer. *J. Raman Spectrosc.* **2008**, *39* (9), 1170–1177. https://doi.org/10.1002/jrs.1958.

(9) Ling, X.; Moura, L. G.; Pimenta, M. A.; Zhang, J. Charge-Transfer Mechanism in Graphene-Enhanced Raman Scattering. *J. Phys. Chem. C* **2012**, *116* (47), 25112–25118. https://doi.org/10.1021/jp3088447.

(10) Lim, D. K.; Jeon, K. S.; Kim, H. M.; Nam, J. M.; Suh, Y. D. Nanogap-Engineerable Raman-Active Nanodumbbells for Single-Molecule Detection. *Nat. Mater.* **2010**, *9* (1), 60–67. https://doi.org/10.1038/nmat2596.

(11) Blackie, E. J.; Le Ru, E. C.; Etchegoin, P. G. Single-Molecule Surface-Enhanced Raman Spectroscopy of Nonresonant Molecules. *J. Am. Chem. Soc.* **2009**, *131* (40), 14466–14472. https://doi.org/10.1021/ja905319w.

(12) Kong, K. V.; Lam, Z.; Goh, W. D.; Leong, W. K.; Olivo, M. Metal Carbonyl-Gold Nanoparticle Conjugates for Live-Cell SERS Imaging. *Angew. Chemie - Int. Ed.* **2012**, *51* (39), 9796–9799. https://doi.org/10.1002/anie.201204349.

(13) Fleischmann, M.; Hendra, P. J.; McQuillan, A. J. Raman Spectra of Pyridine Adsorbed at a Silver Electrode. *Chem. Phys. Lett.* **1974**, *26* (2), 163–166. https://doi.org/10.1016/0009-2614(74)85388-1.

(14) Yokota, Y.; Ueno, K.; Misawa, H. Essential Nanogap Effects on Surface-Enhanced Raman Scattering Signals from Closely Spaced Gold Nanoparticles. *Chem. Commun.* **2011**, *47* (12), 3505–3507. https://doi.org/10.1039/c0cc05320a.

(15) Hu, C.; Shen, J.; Yan, J.; Zhong, J.; Qin, W.; Liu, R.; Aldalbahi, A.; Zuo, X.; Song, S.; Fan, C.; He, D. Highly Narrow Nanogap-Containing Au@Au Core - Shell SERS Nanoparticles: Size-Dependent Raman Enhancement and Applications in Cancer Cell Imaging. *Nanoscale* **2016**, *8* (4), 2090–2096. https://doi.org/10.1039/c5nr06919j.

(16) Mun, C. W.; Linh, V. T. N.; Kwon, J. D.; Jung, H. S.; Kim, D. H.; Park, S. G. Highly Sensitive and Selective Nanogap-Enhanced SERS Sensing Platform. *Nanomaterials* **2019**, *9* (4), 619. https://doi.org/10.3390/nano9040619.

(17) Li, J.; Zhu, Z.; Zhu, B.; Ma, Y.; Lin, B.; Liu, R.; Song, Y.; Lin, H.; Tu, S.; Yang, C. Surface-Enhanced Raman Scattering Active Plasmonic Nanoparticles with Ultrasmall Interior Nanogap for Multiplex Quantitative Detection and Cancer Cell Imaging. *Anal. Chem.* **2016**, *88* (15), 7828–7836. https://doi.org/10.1021/acs.analchem.6b01867.

(18) Fang, Y.; Seong, N. H.; Dlott, D. D. Measurement of the Distribution of Site Enhancements in Surface-Enhanced Raman Scattering. *Science (80-.).* **2008**, *321* (5887), 388–392. https://doi.org/10.1126/science.1159499.

(19) Akselrod, G. M.; Argyropoulos, C.; Hoang, T. B.; Ciracì, C.; Fang, C.; Huang, J.; Smith, D. R.; Mikkelsen, M. H. Probing the Mechanisms of Large Purcell Enhancement in Plasmonic

Nanoantennas. *Nat. Photonics 2014 811* **2014**, *8* (11), 835–840. https://doi.org/10.1038/nphoton.2014.228.

(20) Benz, F.; Tserkezis, C.; Herrmann, L. O.; De Nijs, B.; Sanders, A.; Sigle, D. O.; Pukenas, L.; Evans, S. D.; Aizpurua, J.; Baumberg, J. J. Nanooptics of Molecular-Shunted Plasmonic Nanojunctions. *Nano Lett.* **2015**, *15* (1), 669–674. https://doi.org/10.1021/nl5041786.

(21) Yi, M.; Zhang, D.; Wang, P.; Jiao, X.; Blair, S.; Wen, X.; Fu, Q.; Lu, Y.; Ming, H. Plasmonic Interaction Between Silver Nano-Cubes and a Silver Ground Plane Studied by Surface-Enhanced Raman Scattering. https://doi.org/10.1007/s11468-011-9230-7.

(22) Marshall, A. R. L.; Stokes, J.; Viscomi, F. N.; Proctor, J. E.; Gierschner, J.; Bouillard, J. S. G.; Adawi, A. M. Determining Molecular Orientation: Via Single Molecule SERS in a Plasmonic Nano-Gap. *Nanoscale* **2017**, *9* (44), 17415–17421. https://doi.org/10.1039/c7nr05107g.

(23) Marshall, A. R. L.; Roberts, M.; Gierschner, J.; Bouillard, J.-S. G.; Adawi, A. M. Probing the Molecular Orientation of a Single Conjugated Polymer via Nanogap SERS. *ACS Appl. Polym. Mater.* **2019**, *1* (5), 1175–1180. https://doi.org/10.1021/acsapm.9b00180.

(24) Li-Jun Wan, †,§; Mimi Terashima, ‡; Hiroyuki Noda, ‡ and; Masatoshi Osawa*, †. Molecular Orientation and Ordered Structure of Benzenethiol Adsorbed on Gold(111). *J. Phys. Chem. B* **2000**, *104* (15), 3563–3569. https://doi.org/10.1021/JP993328R.

(25) Moreau, A.; Ciracì, C.; Mock, J. J.; Smith, D. R.; Hill, R. T.; Chilkoti, A.; Wang, Q.; Wiley, B. J. Controlled-Reflectance Surfaces with Film-Coupled Colloidal Nanoantennas. *Nature*. Nature Publishing Group December 5, 2012, pp 86–89. https://doi.org/10.1038/nature11615.

(26) Dill, T. J.; Rozin, M. J.; Brown, E. R.; Palani, S.; Tao, A. R. Investigating the Effect of Ag Nanocube Polydispersity on Gap-Mode SERS Enhancement Factors. *Analyst* **2016**, *141* (12), 3916–3924. https://doi.org/10.1039/c6an00212a.

(27) Zeng, Y.; Qian, H.; Rozin, M. J.; Liu, Z.; Tao, A. R. Enhanced Second Harmonic Generation in Double-Resonance Colloidal Metasurfaces. *Adv. Funct. Mater.* **2018**, *28* (51), 1803019. https://doi.org/10.1002/adfm.201803019.

(28) Rozin, M. J.; Rosen, D. A.; Dill, T. J.; Tao, A. R. Colloidal Metasurfaces Displaying Near-Ideal and Tunable Light Absorbance in the Infrared. *Nat. Commun.* **2015**, *6* (1), 1–7. https://doi.org/10.1038/ncomms8325.

(29) Jiang, X.; Lai, Y.; Wang, W.; Jiang, W.; Zhan, J. Surface-Enhanced Raman Spectroscopy Detection of Polybrominated Diphenylethers Using a Portable Raman Spectrometer. *Talanta* **2013**, *116*, 14–17. https://doi.org/10.1016/j.talanta.2013.04.056.

(30) Sun, Y.; Xia, Y. Shape-Controlled Synthesis of Gold and Silver Nanoparticles. *Science (80-.).* **2002**, *298* (5601), 2176–2179. https://doi.org/10.1126/science.1077229.

(31) Tao, A.; Sinsermsuksakul, P.; Yang, P. Tunable Plasmonic Lattices of Silver Nanocrystals. *Nat. Nanotechnol.* **2007**, *2* (7), 435–440. https://doi.org/10.1038/nnano.2007.189.

(32) Bell, S. E. J.; Charron, G.; Cortés, E.; Kneipp, J.; Chapelle, M. L.; Langer, J.; Procházka, M.; Tran, V.; Schlücker, S. Towards Reliable and Quantitative Surface-Enhanced Raman Scattering (SERS): From Key Parameters to Good Analytical Practice. *Angew. Chemie Int. Ed.* **2020**, *59* (14), 5454–5462. https://doi.org/10.1002/anie.201908154.

(33) Le-The, H.; Lozeman, J. J. A.; Lafuente, M.; Muñoz, P.; Bomer, J. G.; Duy-Tong, H.; Berenschot, E.; Van Den Berg, A.; Tas, N. R.; Odijk, M.; Eijkel, J. C. T. Wafer-Scale Fabrication of High-Quality Tunable Gold Nanogap Arrays for Surface-Enhanced Raman Scattering. *Nanoscale* **2019**, *11* (25), 12152–12160. https://doi.org/10.1039/c9nr02215e.

(34) Biggs, K. B.; Camden, J. P.; Anker, J. N.; Van Duyne, R. P. Surface-Enhanced Raman Spectroscopy of Benzenethiol Adsorbed from the Gas Phase onto Silver Film over Nanosphere Surfaces: Determination of the Sticking Probability and Detection Limit Time †. *J. Phys. Chem. A* **2009**, *113* (16), 4581–4586. https://doi.org/10.1021/jp8112649.

(35) Aggarwal, R. L.; Farrar, L. W.; Diebold, E. D.; Polla, D. L. Measurement of the Absolute Raman Scattering Cross Section of the 1584-Cm $^{-1}$ Band of Benzenethiol and the Surface-Enhanced Raman Scattering Cross Section Enhancement Factor for Femtosecond Laser-Nanostructured Substrates. *J. Raman Spectrosc.* **2009**, *40* (9), 1331–1333. https://doi.org/10.1002/jrs.2396.

(36) Kukushkin, V. I.; Kirpichev, V. E.; Morozova, E. N.; Solov'ev, V. V.; Fedotova, Y. V.; Kukushkin, I. V. Metastructures for the Giant Enhancement of Raman Scattering in the Near Infrared Spectral Range. *JETP Lett.* **2020**, *112* (1), 31–36. https://doi.org/10.1134/S0021364020130081.

(37) Kubo, A.; Gorup, L.; Toffano, L.; Amaral, L.; Rodrigues-Filho, E.; Mohan, H.; Aroca, R.; Camargo, E. Nanostructured Assemblies of Gold and Silver Nanoparticles for Plasmon Enhanced Spectroscopy Using Living Biotemplates. *Colloids and Interfaces* **2017**, *1* (1), 4. https://doi.org/10.3390/colloids1010004.

(38) Kim, J.; Oh, J.; Park, S.; Zafra, J. L.; Defrancisco, J. R.; Casanova, D.; Lim, M.; Tovar, J. D.; Casado, J.; Kim, D. Two-Electron Transfer Stabilized by Excited-State Aromatization. https://doi.org/10.1038/s41467-019-12986-w.

(39) Zhang, Q.; Li, X.; Ma, Q.; Zhang, Q.; Bai, H.; Yi, W.; Liu, J.; Han, J.; Xi, G. A Metallic Molybdenum Dioxide with High Stability for Surface Enhanced Raman Spectroscopy. *Nat. Commun.* **2017**, *8* (1), 1–9. https://doi.org/10.1038/ncomms14903.

(40) Theiss, J.; Pavaskar, P.; Echternach, P. M.; Muller, R. E.; Cronin, S. B. Plasmonic Nanoparticle Arrays with Nanometer Separation for High-Performance SERS Substrates. *Nano Lett.* **2010**, *10* (8), 2749–2754. https://doi.org/10.1021/nl904170g.

(41) Alexander, K. D.; Skinner, K.; Zhang, S.; Wei, H.; Lopez, R. Tunable SERS in Gold Nanorod Dimers through Strain Control on an Elastomeric Substrate. *Nano Lett.* **2010**, *10* (11), 4488–4493. https://doi.org/10.1021/nl1023172.

(42) Le Ru, E. C.; Meyer, M.; Blackie, E.; Etchegoin, P. G. Advanced Aspects of Electromagnetic SERS Enhancement Factors at a Hot Spot. *J. Raman Spectrosc.* **2008**, *39* (9), 1127–1134. https://doi.org/10.1002/jrs.1945.

(43) Frey, S.; Stadler, V.; Heister, K.; Eck, W.; Zharnikov, M.; Grunze, M.; Zeysing, B.; Terfort, A. Structure of Thioaromatic Self-Assembled Monolayers on Gold and Silver. *Langmuir* **2001**, *17* (8), 2408–2415. https://doi.org/10.1021/la001540c.

(44) Wistus, E.; Mukhtar, E.; Johansson, L. B. . A Conspicuous Orientation and Localization of Pyrene in Langmuir Lipid Monolayers. *Langmuir* **1996**, *12* (14), 3371–3373. https://doi.org/10.1021/la951095z.

(45) Noack, K.; Kiefer, J.; Leipertz, A. Concentration-Dependent Hydrogen-Bonding Effects on the Dimethyl Sulfoxide Vibrational Structure in the Presence of Water, Methanol, and Ethanol. *ChemPhysChem* **2010**, *11* (3), 630–637. https://doi.org/10.1002/cphc.200900691.

(46) Mao, H.; Feng, J.; Xiao, •; Can, M. •; • W.; Zhao, X. One-Dimensional Silver Nanowires Synthesized by Self-Seeding Polyol Process. https://doi.org/10.1007/s11051-012-0887-4.

(47) Sahoo, D.; Narayanaswami, V.; Kay, C. M.; Ryan, R. O. Pyrene Excimer Fluorescence: A Spatially Sensitive Probe to Monitor Lipid-Induced Helical Rearrangement of Apolipophorin III. *Biochemistry* **2000**, *39* (22), 6594–6601. https://doi.org/10.1021/bi992609m.

(48) Galarneau, A.; Lerner, D.; Ottaviani, M. F.; Di Renzo, F.; Fajula, F. EPR and UV-Visible Fluorescence Spectroscopic Evidences for Intermediate Phases during the Formation of Micelle-Templated Silicas. *Stud. Surf. Sci. Catal.* **1998**, *117*, 405–412. https://doi.org/10.1016/S0167-2991(98)81018-5.

(49) Xie, Y.; Wang, X.; Han, X.; Xue, X.; Ji, W.; Qi, Z.; Liu, J.; Zhao, B.; Ozaki, Y. Sensing of Polycyclic Aromatic Hydrocarbons with Cyclodextrin Inclusion Complexes on Silver Nanoparticles by Surface-Enhanced Raman Scattering. *Analyst* **2010**, *135* (6), 1389–1394. https://doi.org/10.1039/c0an00076k.

(50) Saikin, S. K.; Olivares-Amaya, R.; Rappoport, D.; Stopa, M.; Ala´n Aspuru-Guzik, A. On the Chemical Bonding Effects in the Raman Response: Benzenethiol Adsorbed on Silver Clusterswz. **2009**. https://doi.org/10.1039/b906885f.

(51) Lombardi, J. R.; Birke, R. L.; Lu, T.; Xu, J. Charge-Transfer Theory of Surface Enhanced Raman Spectroscopy: Herzberg-Teller Contributions. *J. Chem. Phys.* **1986**, *84* (8), 4174–4180. https://doi.org/10.1063/1.450037.

(52) Valley, N.; Greeneltch, N.; Van Duyne, R. P.; Schatz, G. C. A Look at the Origin and Magnitude of the Chemical Contribution to the Enhancement Mechanism of Surface-Enhanced Raman Spectroscopy (SERS): Theory and Experiment. *J. Phys. Chem. Lett.* **2013**, *4* (16), 2599–2604. https://doi.org/10.1021/jz4012383.

(53) Dill, T. J.; Rozin, M. J.; Brown, E. R.; Palani, S.; Tao, A. R. Investigating the Effect of Ag Nanocube Polydispersity on Gap-Mode SERS Enhancement Factors. *Analyst* **2016**, *141*, 3916. https://doi.org/10.1039/c6an00212a.

(54) Qiu, S.; Tan, X.; Wu, K.; Zhang, A.; Han, S.; Wang, L. Experimental and Theoretical Study on Molecular Structure and FT-IR, Raman, NMR Spectra of 4,4′-Dibromodiphenyl Ether. *Spectrochim. Acta - Part A Mol. Biomol. Spectrosc.* **2010**, *76* (5), 429–434. https://doi.org/10.1016/j.saa.2009.10.005.

(55) Schunack, M.; Linderoth, T. R.; Rosei, F.; Lægsgaard, E.; Stensgaard, I.; Besenbacher, F. Long Jumps in the Surface Diffusion of Large Molecules. *Phys. Rev. Lett.* **2002**, *88* (15), 156102. https://doi.org/10.1103/PhysRevLett.88.156102.

(56) Mahaffy, R.; Bhatia, R.; Garrison, B. J. Diffusion of a Butanethiolate Molecule on a Au{111} Surface. **1996**.

Chapter 5

Rapid Raman Detection of PBDEs in Water Using a Colloidal Metasurface

Yuan Zeng[1,2], Riddhi Ananth[3], Wade Shipley[1], and Andrea R. Tao[1,2,3*]

[1]Department of NanoEngineering, University of California, San Diego, 9500 Gilman Drive MC 0448, La Jolla, California 92093-0448

[2]Materials Science and Engineering, University of California, San Diego, 9500 Gilman Drive, La Jolla, California 92093

[3] Department of Chemistry & Biochemistry, University of California, San Diego, 9500 Gilman Drive, La Jolla, California 92093

*Email: atao@eng.ucsd.edu

Introduction

Waterborne diseases are a major public health concern and are attributed with an economic cost of ~1 billion dollars per year in United States.[1,2] Drinking water containing chemical contaminants related to pollutants, municipal and industrial discharges, and agricultural run-off have been linked to liver and kidney damage, cancer, and anomalous occurrences of birth defects. New contaminants are constantly emerging based on evolving urban, agricultural, industrial, recreational, and environmental practices. The ability to rapidly detect and identify these contaminants is imperative in ensuring drinking water quality and safety.

Optical platforms that are capable of rapid, high-sensitivity detection of water contaminants are highly desired because they have the potential to be deployed for continuous, online (e.g. real-time) water quality monitoring. This is especially desirable for water recycling and wastewater management, since contaminants can be introduced at any point in space/time within a water distribution system.[3] Deployment of multiple online sensors would allow accurate and early contaminant detection within these water distribution systems. Optical absorbance and emission spectroscopy methods are already employed for the online detection of dissolved organic matter (e.g. TOC), with the ability to determine total organic content down to a few mg/L.[4–6] However, detection of TOC is not contaminant specific and does not allow for accurate comparison against limit values set forth by agencies such as the World Health Organization. Analysis of specific contaminants is usually carried out offline using sample-based analysis methods. For example, trace organic contaminants[7] such pesticides and pharmaceuticals are typically analyzed by liquid chromatography-mass spectrometry (LC-MS) or electrospray ionization-MS[8] with quantification in the range of 0.006–0.208 μg/L.

Recently, surface-enhanced Raman spectroscopy (SERS) has emerged as an optical sensing modality that has the potential to detect trace chemical contaminants found in drinking

water.[9] Raman spectroscopy provides the vibrational fingerprint for a given analyte, enabling high-specificity for chemical detection without the use of molecular tags or labels. In addition, SERS platforms offer increased sensitivities and often required only a small volume of analyte with minimal preparation, making it a suitable technique for real-time water quality measurements. One such application is the detection of polydibrominated phenyl ethers (PBDEs), a common byproduct of recycled plastic waste that is of growing concern due to PBDE bioaccumulation. PBDEs are brominated flame retardants that were heavily used in consumer plastics and textiles from the 1970s until early 2000s and are present as multiple PBDE congeners; because PBDEs are blended in during formation and are not chemically bound to polymer substrates, PBDEs are migrating from consumer products into the environment.[1] Recent epidemiological studies have suggested that long-term exposure to PBDEs poses potential health risks such as hormone disruption, adverse neurobehavioral toxicity, and reproductive or developmental effects.[2,3] Typical concentrations of PBDEs in wastewater are found in the few ng/L range, as determined by liquid-liquid extractions from water samples followed by GC-MS analysis. SERS has been demonstrated as an alternative method in the detection of PBDEs. Jiang et al. used SERS to detect BDE-15 (4,4'-dibromodiphenyl ether) at concentrations between 250 μg/L (0.76 μM) to 5000 μg/L (15.24 μM) by a SERS platform prepared by decorating a hydrophobic substrate with Ag nanoparticle aggregates that trap PBDE molecules. Upon direct incubation with PBDE solutions, they demonstrated a detection limit of 120 μg/L (0.37 μM).[10] Jing et al. similarly fabricated a SERS platform by electrochemical deposition of hydrophobic Au nanostructures, achieving a Raman enhancement factor of 2.6×10^4 for BDE-15 and a detection limit of 2.6 nM.[11] Utilizing a SERS platform composed of a Cu/TiO_2 nanocomposite has also been demonstrated to provide both SERS enhancement for PBDE detection and debromination under mild conditions, enabling observation of the Br-C stretching mode at 1033 cm^{-1} due to analyte adsorption onto the SERS-active Cu nanoparticles.[12] However, the low concentrations and low water-solubility of PBDEs still present challenges to SERS detection, specifically in achieving appropriate limits of detection (<6

μg/m^3) for minimal risk level (MRL) established by the Agency for Toxic Substance and Disease Registry (ATSDR).[13] Also, owing to surface oxidation and potential contamination on metallic nanoparticles, all these SERS platforms need to be freshly prepared in wet lab just before the use, limit the detection speed, large scale fabrication and reproducibility in qualitative analysis.

To address these challenges in SERS sensing, we have developed a novel optical sensing platform by modifying nanoparticle-on-metal (NOM) optical metasurface fabrication[14–16]. Our SERS platform is composed of silver nanocube (AgNC) embedded PDMS film and a flat gold substrate, owing to the protection from PDMS (Polydimethylsiloxane), AgNCs are stable and clean for at least few months in ambient condition after embedding. For PBDE sensing, we simply incubated the pre-functionalized AgNC embedded PDMS film into PBDE solution and then attached to gold substrate to build up the sensor. As a demonstration, we carried out sensing experiments for the PBDE congener Bis (4-bromophenyl) ether (BDE-15) and our SERS platform has limit of detection (LOD) at 2.5 nM, quantitative detection ranges from 2.5 nM to 2.5 μM and rapid detection speed (< 20 min). Also, take the advantages of soft PDMS film, this SERS platform fabrication can scale up easily and cost-effectively.

Experimental Methods

Materials. Ethanethiol (97%), 1-Propanethiol (99%), 1-Butanethiol (99%) were purchased from Sigma-Aldrich. Methanethiol 1.2mL (S2433) was purchased from Fisher scientific. Bis(4-bromophenyyl) ether (BDE-15), 99% was purchased from Alfa Aesar. Sylgard 184 Silicon Elastomer was purchased Electron Microscopy Science.

Gold Substrate Fabrication. Au thin-film substrates were fabricated through Sputter Deposition (using Denton Discovery 18 Sputter System). 100mm diameter, 500 μm thick P type doped wafer (University wafer) was cleaned with isopropanol and cleanroom cloth. The sputtering

RF bias is used to clean the substrate for 20 seconds and followed with 10 seconds Cr (400 W) and 120 seconds Au (300 W) sputtering with the Ar gas pressure as 2.4 mTorr. Then the wafer was diced into 1cm x 1cm size for later use.

Ag nanocubes (AgNCs) Preparation. Ag Nanocubes were synthesized via a polyol method published elsewhere.[17] $AgNO_3$ is reduced in a solution of pentanediol, $CuCl_2$, and polyvinylpyrrolidone (PVP) (M_w=55,000). PVP serves as a selective capping agent that controls nanocube nucleation and growth. The reaction was allowed to proceed until the resulting colloidal dispersion turned an opaque yellow-green color. To remove excess reactants, the nanocube dispersion product was centrifuged (2700 rpm for 10 min) using a Thermo Scientific CL2 Centrifuge, and the resulting precipitate was redispersed and diluted in an ethanol and water mixture, and then vacuum-filtered (Millipore Durapore membranes, with 0.65 μm, 0.45 μm, then 0.22 μm pore sizes) to remove any larger, unwanted particles.

PDMS Embedded Metasurface Fabrication. AgNCs on silicon substrate was prepared by Langmuir-Blodgett deposition, as previously described. PDMS solution was prepared by mixing 10-part solution A and 1-part solution B of Sylgard 184, stirring 5 min, and degassing in vacuum desiccator for 30 min. We added few drops PDMS solution on the AgNCs supported by Si substrate and spin coated in 3 steps (500 RPMs for 15 sec, 2000 RPMs for 60 sec and 300 RPMs for 10 sec), followed by 20 hours curing at room temperature and 48 hours curing at 80°C.

PDMS Embedded Metasurface Functionalization. We cut the edges with blade and slowly lift off the AgNCs embedded PDMS film (plasmonic PDMS stamp) from the silicon substrate, turned over and attached to a clean silicon substrate. Then, the plasmonic PDMS stamp (supported with a silicon substrate) was incubated in 5mL alkanethiol ethanol solution (0.1%) for 3 hours and rinse 6 times with pure ethanol. This plasmonic PDMS stamp was covered with glass beaker and dried in ambient overnight.

PBDE mSERS Sensor Fabrication. BDE-15 water solution was prepared by diluting 0.1 mL BDE-15 stock solution in 9.9 mL DI water (Appendix D, D1). Pre-functionalized plasmonic PDMS

stamp was held in a glass vial with 10 mL BDE-15 water solution, stirring at 500 RPMs and keep 3 hours (In time dependent study, the incubation time is varied). Because the surface is hydrophobic, there was no water residue left on the plasmonic PDMS stamp after incubation. Then, plasmonic PDMS stamp was slowly removed from silicon substrate, turned over and attached to the Au substrate.

mSERS measurements. All Raman spectra were obtained using a Renishaw inVia confocal Raman microscope. Measurements were taken under 785 nm excitation with 2 seconds exposure, 10% excitation power (time dependent study used 5% excitation power) and 3 accumulations. 785 nm illumination was provided by a Renishaw 300 mW diode laser and spectra were collected through a 50x, 0.75 NA objective. For each sample, we randomly picked 5 different areas, mapping scanned 49 points in each area (245 points total) and calculate the average and standard deviation.

FDTD Simulations & Simulated EF. Electromagnetic modeling was performed with Lumerical FDTD Solutions. 90 nm AgNCs (Palik dielectric data) were modeled in 3 dimensions with an underlying 75 nm Au thin film. A 5 nm dielectric layer with n = 1.55 was added around AgNC to reflect PVP coating. Background refractive index was set to n = 1 in conventional NOM simulation and n = 1.43 in PDMS NOM. Incident light was injected normal to the substrate and polarized parallel to the (100) faces of the AgNC. A 1 nm global mesh was used. The electric field profiles were calculated in the plane parallel to Au thin film, distance to Au thin film is varied due to different gap location. An average EF for the mSERS substrate is calculated by summing $|E/E_o|^4$ at each pixel (1x1 nm) and normalizing to the cross-sectional area of each nanocubes. This calculation was carried out at discrete wavelengths over the visible range.

Results and Discussion

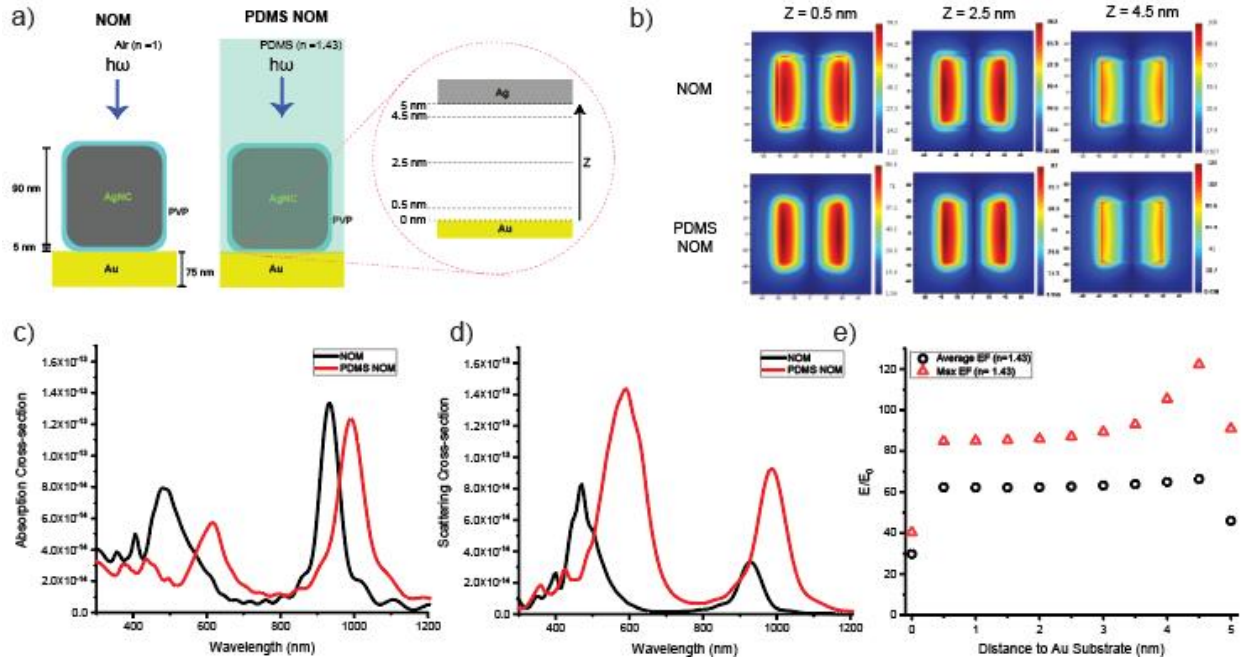

Figure 5.1 | Simulated far-field and near-field in PDMS metasurface. Schematic of nanocube-on-metal (NOM) meta-atom in air (conventional NOM, left) and embedded in PDMS (PDMS NOM, right). Simulated absorption spectra (solid) and scattering spectra (dashed) for conventional NOM (black) and PDMS NOM (red). (c) Near-field distribution at middle of the dielectric gap (left) and top of the dielectric gap (right). (d) Distance (to Au substrate) dependent near-field enhancement factor (circle represents average EF, triangle represents maximum EF, black represents conventional NOM and red represents PDMS NOM)

To get a fundamental insight of PDMS embedded metasurface (PDMS NOM), we performed full-wave electrodynamic FDTD simulation and make a comparison with conventional nanocubes on metal metasurface (NOM). Figure 5.1a shows a schematic of NOM meta-atom and PDMS NOM meta-atom. In NOM, the meta-atom is made by 90 nm silver nanocube (AgNC) with 10 nm radius of curvature on the corners, 5 nm thick PVP (Polyvinylpyrrolidone) layer around AgNC and 75 nm thick Au film. The PVP layer results a 5 nm dielectric nanojunction between AgNC and Au film. In PDMS NOM, we change the background refractive index from 1 (air) to 1.43 (PDMS) and all the other parameters are consistent with NOM. The insert figure shows location of near-field measurements (Z = 0 nm is gold surface and Z = 5 nm is AgNC bottom surface). Figure 5.1b shows the near-field distribution at different location of the dielectric nanojunction. To avoid interfacial effect from simulation, we use Z = 0.5 nm to represent bottom of nanojunction and Z = 4.5 nm to represent top of nanojunction. At the bottom of nanojunction (Z = 0.5 nm), the

near-field enhancement (E/E_0) is 79-fold in NOM and 85-fold in PDMS NOM. At the middle of nanojunction (Z = 2.5 nm), the near-field enhancement and hot spot distribution is nearly consistent with bottom of nanojunction. However, at the top of nanojunction (Z = 4.5 nm), E/E_0 increases significantly to 106-fold in NOM and 122-fold in PDMS NOM, and the hotspot is more confined to edge of AgNC, indicates a strong localization effect near the surface of AgNC. Figure 5.1c shows wavelength dependent absorption cross-section of NOM and PDMS NOM. In NOM, cube mode dipole resonance at 480 nm results a moderate absorption peak and gap mode resonance at 933 nm results a strong absorption peak. In PDMS NOM, owing to increased environment refractive index, the cube mode resonance red-shifted to 617 nm and the gap mode resonance red-shifted to 993 nm.[18] The maximum absorption cross-section in PDMS NOM (1.23 x 10^{-13} m^2) is only 8% smaller than NOM (1.34 x 10^{-13}). Figure 5.1d shows wavelength dependent scattering cross-section of NOM and PDMS NOM. At cube mode resonance, the scattering cross-section in PDMS NOM (1.44 x 10^{-13} m^2) is 74% larger than NOM (8.27 x 10^{-14} m^2). At gap mode resonance, PDMS NOM scattering cross-section is 9.26 x 10^{-14} m^2, 2.9-fold larger than NOM scattering cross-section (3.3x 10^{-14} m^2).

From this near-field and far-field analysis, PDMS NOM has the following advantages: i) larger near-field enhancement, ii) much larger scattering cross-section and iii) smaller mode volume due to higher refractive index[19,20]. Because both near-field enhancement and far-field scattering play a significant role in SERS, we believe PDMS NOM is a better platform for building SERS sensor. To find the optimized location for loading analyst molecules, we also performed gap location (Z) dependent study in PDMS NOM and shown in Figure 5.1e. At Z = 0 nm (Au surface) and Z = 5 nm (AgNC surface), large plasmon density on metal surface causes an electric-field screening effect[21] and results a relative weak near-field intensity. Between Z = 0.5 nm and Z = 4.5 nm, the average E/E_0 remains constant at 64($\pm$2)-fold. Different from average E/E0, maximum E/E_0 remains constant between Z = 0.5 nm and Z = 3 nm and increases exponentially from Z = 3 nm to Z = 4.5 nm. The largest maximum E/E_0 is obtained at Z = 4.5 nm, indicates the

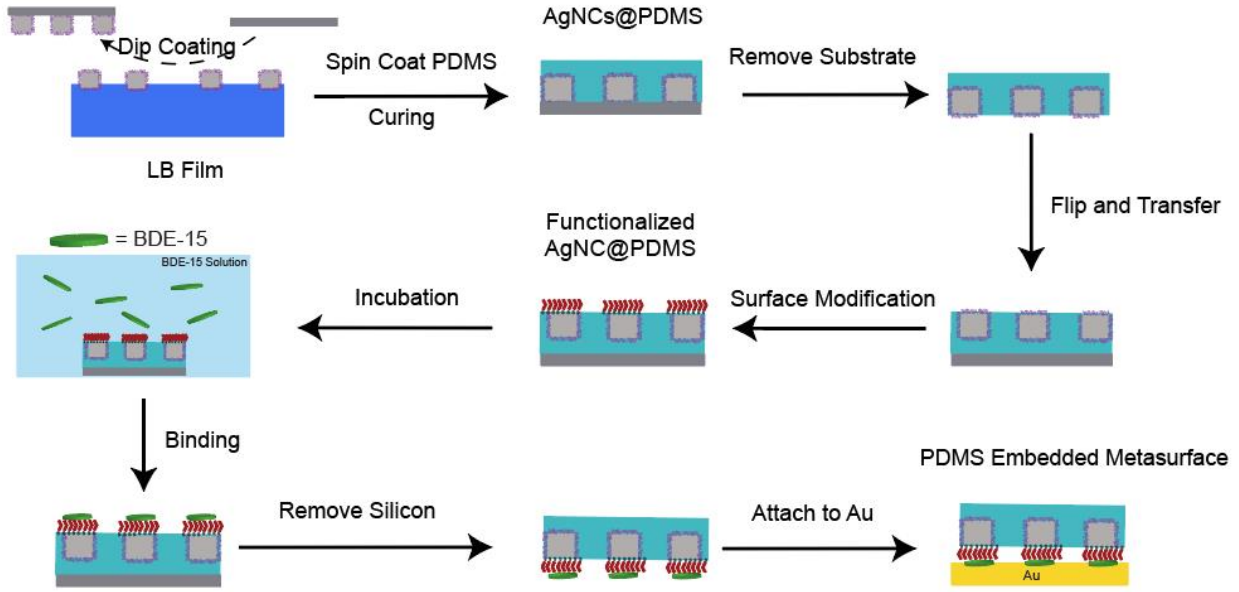

Figure 5.2 | Fabrication of plasmonic PDMS stamp, surface modification and PDMS mSERS sensor design.

optimized position for loading analyst molecules is 0.5 nm away from AgNC bottom surface because most of the SERS signals is given by a small fraction of hotspots with highest enhancement factor.[22]

To fabricate the PDMS embedded metasurface, we designed a novel fabrication protocol based on Langmuir-Blodgett (LB) deposition method[23] and soft imprint method[24] (Figure 5.2). Briefly, we transferred AgNCs Langmuir film to silicon substrate by dip-coating, followed by spin-coating of PDMS solution. After PDMS curing, we stripped plasmonic PDMS stamp from silicon substrate, turned it over and attached to a clean silicon substrate for alkanethiol surface functionalization, then alkanethiol functionalized plasmonic PDMS stamp was incubated in BDE-15 aqueous solution, owing to strong hydrophobic interaction with alkanethiol and low surface energy on PDMS, BDE-15 molecules were selectively bind to AgNCs surface. After incubation, we removed the silicon substrate and attached plasmonic PDMS stamp to a clean Au substrate, formed a PDMS mSERS sensor platform (PDMS NOM) that BDE-15 molecules were trapped inside the hotspot between AgNCs and Au film.

Figure 5.3a (left) shows photo images of Au thin film, NOM and PDMS NOM. Because

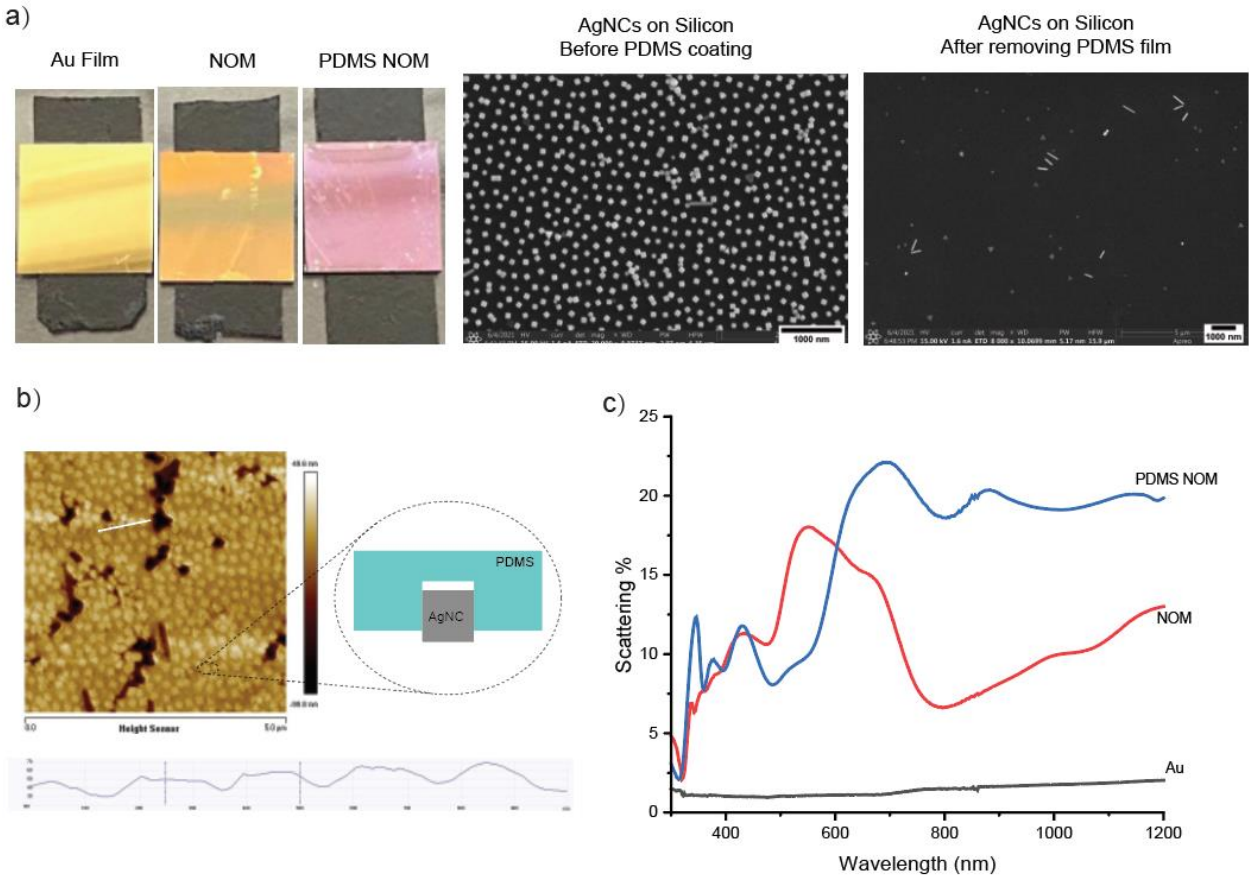

Figure 5.3 | Characterization of PDMS NOM. (a) Photo images of PDMS NOM (left), SEM image of LB deposited AgNCs on silicon before PDMS coating (middle) and silicon substrate after removing PDMS film (right). (b) AFM image of AgNCs embedded PDMS and height profile (bottom), Insert figure is schematic of AgNCs embedded PDMS after peeling off from silicon substrate (c) Scattering spectra of pristine Au substrate (black), conventional NOM metasurface (red) and PDMS embedded NOM metasurface (blue)

NOM has strong absorption around 800 nm due to strong gap mode resonance and PDMS NOM has strong scattering around 600 nm owing to larger dielectric constant, NOM has dark orange color and PDMS NOM has bright purple color. Figure 5.3a (middle) shows SEM image after AgNCs transferring to silicon substrate. The AgNCs LB film is dominant by well separated AgNCs which has minimized interparticle coupling, however, there are small number of aggregations and defect particles (rods, prisms etc.) in the LB film. After coating and removing PDMS film (Figure 5.3a (right)), most of the aggregations and defects are left on the silicon substrate because they have smaller surface to volume ratio than individual AgNCs and weaker interaction with PDMS film than the Van der Waals interaction with substrate. Therefore, compare to original AgNCs LB film, PDMS film has much less aggregations / defects and higher quality plasmon resonance

feature. Figure 5.3b shows AFM image of plasmonic PDMS stamp. Because aggregated AgNCs and large defects are left on silicon substrate, there are some vacancies left in the plasmonic PDMS stamp and the embedded particles are dominant by separated AgNCs. From the height measurement, all the AgNCs protrude out by about 20 nm, owing to Van der Waals interaction induced drag force during the peeling off process. Figure 5.3c shows far-field scattering spectra of Au film, NOM and PDMS NOM. NOM (red) has a broad scattering peak (18%) at 548 nm and another broad scattering peak in NIR range, the scattering at resonance wavelength (928 nm) is 8.6%. Owing to increased environment refractive index from 1 to 1.43, the scattering peak red shifts 140 nm to 688 nm in PDMS NOM (blue). Different from NOM, PDMS NOM has another scattering peak (20.4%) at 882 nm and nearly constant scattering intensity in NIR range. At the resonance frequency, NOM has 28.4% reflection, 8.6% scattering and 63% absorption and PDMS NOM has 4.3% reflection (85% decrease), 18.6% scattering (116.3% increase) and 77.1% absorption (22.4% increase). (Appendix D, D2) This is consistent with our simulation result in Figure 5.1b) that scattering cross-section increases significantly, and absorption cross-section changes slightly after PDMS embedding.

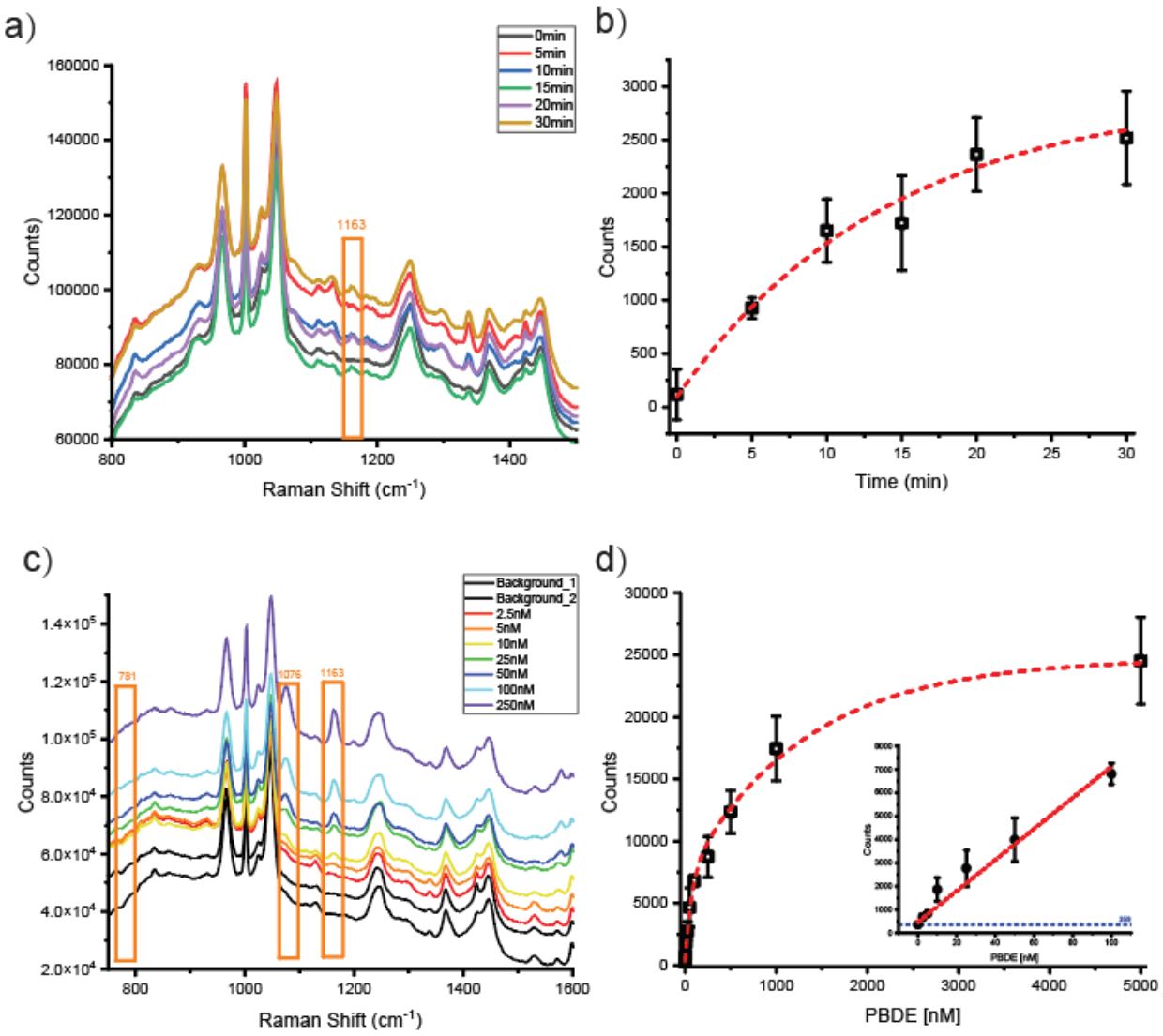

Figure 5.4 | Time dependent study and concentration dependent study on PDMS NOM. (a) SERS spectra of PDMS NOM sensor incubated in 250 nM BDE-15 for difference time. (b) Time dependent intensity of BDE-15 (vibrational mode at 1163 cm-1). (c) SERS spectra of PDMS NOM sensor incubated in different BDE-15 concentration. (d) Concentration dependent intensity of BDE-15, insert plot is linear relation between intensity and concentration at sub-100 nM range.

Because our PDMS NOM has stronger near-field enhancement, larger far-field scattering cross-section and excellent stability from PDMS protection, we used this platform to build a sensor for BDE-15 molecules detection. BDE-15 molecules have 3 major Raman peaks that β(C-H) mode at 779 cm^{-1}, υ(C-Br) ring stretch mode at 1076 cm^{-1} and υs (C-O), β(C-H) modes at 1167 cm^{-1}.[25] Owing to strong intensity and weak background noise at 1163 cm^{-1}, we used peak intensity at 1163 cm^{-1} for time dependent and concentration dependent study in Figure 5.4. First, we carried out a time dependent study at fixed concentration, 250 nM. Figure 5.4a shows the Raman spectra

after different incubation time in BDE-15 aqueous solution. There is only a background signal (336 counts) at 0 min and there is a 929 counts peak shows up at 5 min, corresponds to a signal to noise ratio of 2.76. As time increases from 5 min to 30 min, the peak intensity increases from 929 counts to 2521 counts, indicates more BDE-15 molecules binding on the surface. Figure 5.3b shows the plot of Raman intensity at 1163 cm^{-1} vs. incubation time. As time increases from 0 min to 30 min, the Raman intensity increases exponentially, and the saturation intensity is 2940 counts according to curve fitting (Appendix D, D3). It indicates that 31.6%, 56.2%, 80.5% and 85.8% BDE-15 molecules binding on the surface at 5 min, 10 min, 20 min and 30 min, respectively. Figure 5.4c shows the Raman spectra of PDMS NOM incubated at different BDE-15 concentrations. As concentration increases from 2.5 nM to 250 nM, the peak intensity at 1076 cm^{-1} and 1163 cm^{-1} gradually increased owing to more BDE-15 molecules physiosorbed on the surface. Figure 5.4d shows the plot of Raman intensity vs. PBDE concentration. As concentration increases from 2.5 nM to 5000 nM, the peak intensity at 1163 cm^{-1} increases exponentially from 686 counts to 24522 counts and stays constant, indicates a saturation concentration at 2.5 μM (Appendix D, D4) in PDMS NOM sensor. The insert figure shows linear relation between Raman intensity and BDE-15 concentration below 100 nM. The background noise is 359 counts (blue dashed line) and the signal to noise ratio is 1.93 at 2.5 nM, indicates the limit of detection (LOD) of our PDMS NOM sensor is comparable or better than previous PBDE sensors[10,11] and other aromatic molecule sensors[26].

Finally, we modified the AgNCs surface with different alkanethiols to study how surface functionalization affects the PBDE sensor performance. In this experiment, we used methanethiol (C_1SH), ethanethiol (C_2SH), 1-propanethiol (C_3SH) and 1-butanethiol (C_4SH) to functionalize the AgNCs embedded in PDMS film, then used them to fabricate the PDMS NOM sensors. Figure 5.5a shows the SERS spectra of PDMS sensor functionalized with different alkanethiols and incubated in 500 nM BDE-15 solution. As chain length (Cn) increases from 1 to 4, the peak intensity at 1076 cm-^{1} and 1163 cm-^{1} decreases dramatically from more than 10000 counts to

background noise level. Figure 5.5b shows the plot of Raman intensity at 1163 cm^{-1} vs. alkanethiol chain length. As C_n increases from 1 to 4, the peak intensity decreases exponentially from 14849 counts to 827 counts that C_1SH functionalized PDMS NOM (C_1SH PDMS NOM) has 18 times higher peak intensity than C_4SH functionalized PDMS NOM (PDMS NOM). Because C_4SH self-assembled monolayer (SAM) is 0.5 nm thicker[27] than C_1SH SAM and the enhancement factor difference between C_1SH PDMS NOM and C_4SH PDMS NOM is less than 2 times (Appendix D, D5), near-field does not play a significant role in the exponential decay. This chain length dependent exponential decay can originate from 3 possible reasons: i) more BDE-15 molecules binding on short alkanethiol functionalized PDMS NOM because short alkanethiol SAM is has weaker intermolecular interaction and lower packing density[28,29] ii) BDE-15 molecules binding on short alkanethiol functionalized NOM are more out-of-plane orientated and larger enhancement factor due to z-polarized near-field inside nanojunction[30], and iii) BDE-15 molecules binding on short alkanethiol functionalized NOM has smaller distance with AgNCs surface, results more efficient hot carrier transfer and larger charge-transfer enhancement[31]. Then, we prepared a reference sample consist of C_2SH functionalized Au thin film (served as binding sites) and PVP AgNCs (Figure 5.5c left). Owing to nearly identical lattice spacing between Au and Ag,[32] C_2SH SAM on Au thin-film and AgNCs in plasmonic PDMS stamp should be nearly consistent and BDE-15 molecules binding on surface should have same orientation and density. Figure 5.5d shows the Raman spectra of BDE-15 powder (black), BDE-15 binding on AgNCs (red) and BDE-15 binding on Au thin film (blue). Different from BDE-15 powder that has nearly consistent peak intensity at 780 cm^{-1}, 1076 cm^{-1}, and 1163 cm^{-1}, BDE-15 binding on Au film has larger peak intensity at 780 cm^{-1}, indicates a larger enhancement factor on β(C-H) mode. This observation is consistent with previous BDE-15 sensors that peak intensity at 780 cm^{-1} is higher or equivalent to

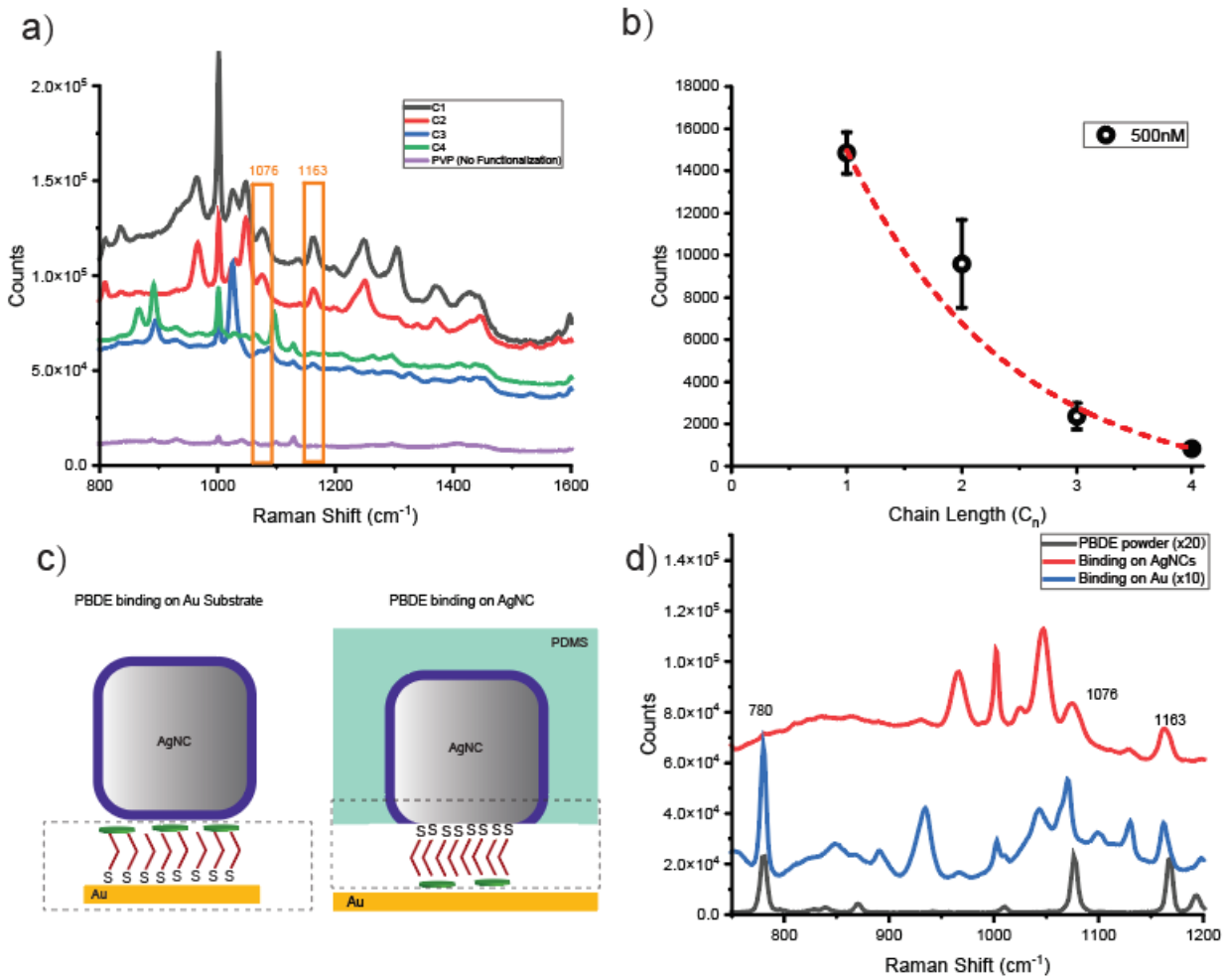

Figure 5.5 | Surface functionalization of PDMS NOM. SERS spectra of PDMS NOM functionalized with different alkanethiol and incubated in 500 nM PBDE solution. (b) Alkanethiol chain length dependent intensity of BDE-15 (c) schematic of BDE-15 molecules binding on alkanethiol functionalized Au thin-film (left) and BDE-15 molecules binding on alkanethiol functionalized AgNCs in plasmonic PDMS stamp (right). (d) Raman spectra of BDE-15 powder (black), BDE-15 molecules binding on Au thin film (blue) and BDE-15 molecules binding on AgNCs (red)

peak intensity at 1076 cm^{-1} and 1163 cm^{-1}.[10,11] However, when BDE-15 binding on AgNCs, peak intensity at 780 cm^{-1} is orders of magnitude lower than peak intensity at 1076 cm^{-1} and 1163 cm^{-1}. It means there is a selective excitation of vibrational mode, and BDE-15 orientation and density does not play a significant role. The most possible mechanism is hot carrier transfer from AgNCs to BDE-15 molecules. When BDE-15 binding on short alkanethiol functionalized AgNCs in plasmonic PDMS stamp, there is 0.5 nm separation between AgNCs and BDE-15 molecules. Because 0.5 nm is smaller than the electron tunneling distance[33–35], hot carriers generated from non-radiative Landau damping[36,37] can be injected into BDE-15 molecules and selectively excite

the vibrational mode.[38] When BDE-15 binding on Au film (reference sample), there is a few-nanometer thick PVP layer between BDE-15 and AgNCs surface, and the charge transfer is completely forbidden. In addition, because extended metal surface requires significantly higher light intensity compared with plasmonic metal nanoparticles[39], this charge transfer does not occur between Au film and BDE-15 molecules. This charge transfer mechanism also provides a reasonable explanation for chain length dependent decay in Figure 5.5b. As alkanethiol chain length (C_n) increases from 1 to 4, alkanethiol SAM thickness increase from 0.458 nm to 0.836 nm (Appendix D, D6) and electron tunneling efficiency decreases exponentially due to increased tunneling distance. It means both charge-transfer enhancement and electromagnetic enhancement play a significant role in our SERS platform.

Conclusion

Overall, we designed a SERS sensing platform based on PDMS embedded optical metasurface. Owing to increased dielectric constant from PDMS coating, this optical metasurface has stronger near-field enhancement and larger far-field scattering cross-section at resonance wavelength, resulting in a great improvement in Raman scattering. In our FDTD simulation, the average EF is nearly consistent inside the optical gap, however, owing to strong field localization at the AgNC surface, the maximum EF is located 0.5 nm below AgNC bottom surface. Then, we used this PDMS embedded metasurface to build up a sensor for PBDE congener Bis (4-bromophenyl) ether (BDE-15) detection. Take the advantages of increased optical cross-section and large maximum EF at the bottom surface of AgNCs, our SERS platform has a LOD at 2.5 nM and rapid detection speed that more than 80% binding at 20 min. Compare with previous SERS sensing platforms, our metasurface has lower LOD, faster detection speed, better reproducibility in qualitative analysis, and more importantly, no wet lab chemical processing is needed during the sensing procedure. Finally, we performed a systematic study and shown the importance of surface functionalization. In our experiment, methanethiol functionalized PDMS NOM has more than 1

orders magnitude stronger signal than 1-butanethiol functionalized PDMS NOM, probably due to hot carrier transfer between AgNCs and BDE-15 molecules which selectively excite the molecule vibrational mode. Therefore, we believe our novel SERS platform has a potential in other plasmonic applications, especially plasmonic catalysis.

Acknowledgements

The authors would like to thank Nano3 and the San Diego Nanotechnology Infrastructure (NSF Award ECCS-2025752), the UC San Diego MRSEC (NSF Award DMR-2011924), and the NanoEngineering MRC for use of their equipment and facilities. This work was supported by NSF Awards CHE-1807891 and DMR-2011924.

Chapter 5, in full, is currently being prepared for submission for publication of the materials by Yuan Zeng, Riddhi Ananth, Wade Shipley, and Andrea R. Tao*. The dissertation author was the primary investigator and author of this paper.

References:

(1) Ingerson-Mahar, M.; Reid, A. Microbes in Pipes: The Microbiology of the Water Distribution System. **2013**.

(2) Vacs Renwick, D.; Heinrich, A.; Weisman, R.; Arvanaghi, H.; Rotert, K. Potential Public Health Impacts of Deteriorating Distribution System Infrastructure. *J. Am. Water Works Assoc.* **2019**, *111* (2), 42–53. https://doi.org/10.1002/awwa.1235.

(3) Zulkifli, S. N.; Rahim, H. A.; Lau, W. J. Detection of Contaminants in Water Supply: A Review on State-of-the-Art Monitoring Technologies and Their Applications. *Sensors and Actuators, B: Chemical*. Elsevier B.V. February 1, 2018, pp 2657–2689. https://doi.org/10.1016/j.snb.2017.09.078.

(4) Matilainen, A.; Gjessing, E. T.; Lahtinen, T.; Hed, L.; Bhatnagar, A.; Sillanpää, M. An Overview of the Methods Used in the Characterisation of Natural Organic Matter (NOM) in Relation to Drinking Water Treatment. *Chemosphere*. Elsevier Ltd June 1, 2011, pp 1431–1442. https://doi.org/10.1016/j.chemosphere.2011.01.018.

(5) Bridgeman, J.; Bieroza, M.; Baker, A. The Application of Fluorescence Spectroscopy to Organic Matter Characterisation in Drinking Water Treatment. *Reviews in Environmental*

Science and Biotechnology. Springer September 12, 2011, pp 277–290. https://doi.org/10.1007/s11157-011-9243-x.

(6) Heibati, M.; Stedmon, C. A.; Stenroth, K.; Rauch, S.; Toljander, J.; Säve-Söderbergh, M.; Murphy, K. R. Assessment of Drinking Water Quality at the Tap Using Fluorescence Spectroscopy. *Water Res.* **2017**, *125*, 1–10. https://doi.org/10.1016/j.watres.2017.08.020.

(7) Development, O. of R. &. Detection of Contamination in Drinking Water Using Fluorescence and Light Absorption Based Online Sensors.

(8) Maldaner, L.; Jardim, I. C. S. F. Determination of Some Organic Contaminants in Water Samples by Solid-Phase Extraction and Liquid Chromatography-Tandem Mass Spectrometry. *Talanta* **2012**, *100*, 38–44. https://doi.org/10.1016/j.talanta.2012.08.006.

(9) Li, Z.; Deen, M.; Kumar, S.; Selvaganapathy, P. Raman Spectroscopy for In-Line Water Quality Monitoring—Instrumentation and Potential. *Sensors* **2014**, *14* (9), 17275–17303. https://doi.org/10.3390/s140917275.

(10) Jiang, X.; Lai, Y.; Wang, W.; Jiang, W.; Zhan, J. Surface-Enhanced Raman Spectroscopy Detection of Polybrominated Diphenylethers Using a Portable Raman Spectrometer. *Talanta* **2013**, *116*, 14–17. https://doi.org/10.1016/j.talanta.2013.04.056.

(11) Jing, L.; Shi, Y. E.; Cui, J.; Zhang, X.; Zhan, J. Hydrophobic Gold Nanostructures via Electrochemical Deposition for Sensitive SERS Detection of Persistent Toxic Substances. *RSC Adv.* **2015**, *5* (18), 13443–13450. https://doi.org/10.1039/c4ra14089c.

(12) Lei, M.; Guo, S.; Wang, Z.; Zhu, L.; Tang, H. Ultrarapid and Deep Debromination of Tetrabromodiphenyl Ether over Noble-Metal-Free Cu/TiO 2 Nanocomposites under Mild Conditions. *Environ. Sci. Technol* **2018**, *52*, 5. https://doi.org/10.1021/acs.est.8b03202.

(13) Environmental Protection Agency Federal Facilities Restoration, U.; Office, R. *Technical Fact Sheet – Polybrominated Diphenyl Ethers (PBDEs)*; 2017.

(14) Dill, T. J.; Rozin, M. J.; Brown, E. R.; Palani, S.; Tao, A. R. Investigating the Effect of Ag Nanocube Polydispersity on Gap-Mode SERS Enhancement Factors. *Analyst* **2016**, *141* (12), 3916–3924. https://doi.org/10.1039/c6an00212a.

(15) Zeng, Y.; Qian, H.; Rozin, M. J.; Liu, Z.; Tao, A. R. Enhanced Second Harmonic Generation in Double-Resonance Colloidal Metasurfaces. *Adv. Funct. Mater.* **2018**, *28* (51), 1803019. https://doi.org/10.1002/adfm.201803019.

(16) Rozin, M. J.; Rosen, D. A.; Dill, T. J.; Tao, A. R. Colloidal Metasurfaces Displaying Near-Ideal and Tunable Light Absorbance in the Infrared. *Nat. Commun.* **2015**, *6* (1), 1–7. https://doi.org/10.1038/ncomms8325.

(17) Sun, Y.; Xia, Y. Shape-Controlled Synthesis of Gold and Silver Nanoparticles. *Science (80-.).* **2002**, *298* (5601), 2176–2179. https://doi.org/10.1126/science.1077229.

(18) Mock, J. J.; Smith, D. R.; Schultz, S. Local Refractive Index Dependence of Plasmon Resonance Spectra from Individual Nanoparticles. **2003**. https://doi.org/10.1021/nl0340475.

(19) Shegai, T.; Antosiewicz, T. J.; Yang, Z.-J. Role of Material Loss and Mode Volume of Plasmonic Nanocavities for Strong Plasmon-Exciton Interactions. *Opt. Express, Vol. 24, Issue 18, pp. 20373-20381* **2016**, *24* (18), 20373–20381. https://doi.org/10.1364/OE.24.020373.

(20) Cuadra, J.; Baranov, D. G.; Wersäll, M.; Verre, R.; Antosiewicz, T. J.; Shegai, T. Observation of Tunable Charged Exciton Polaritons in Hybrid Monolayer WS2−Plasmonic Nanoantenna System. *Nano Lett.* **2018**, *18* (3), 1777–1785. https://doi.org/10.1021/ACS.NANOLETT.7B04965.

(21) Duan, C. G.; Velev, J. P.; Sabirianov, R. F.; Zhu, Z.; Chu, J.; Jaswal, S. S.; Tsymbal, E. Y. Surface Magnetoelectric Effect in Ferromagnetic Metal Films. *Phys. Rev. Lett.* **2008**, *101* (13), 137201. https://doi.org/10.1103/PHYSREVLETT.101.137201/FIGURES/4/MEDIUM.

(22) Fang, Y.; Seong, N. H.; Dlott, D. D. Measurement of the Distribution of Site Enhancements in Surface-Enhanced Raman Scattering. *Science (80-.).* **2008**, *321* (5887), 388–392. https://doi.org/10.1126/science.1159499.

(23) Paul, S.; Pearson, C.; Molloy, A.; Cousins, M. A.; Green, ⊥ M; Kolliopoulou, S.; Dimitrakis, P.; Normand, P.; Tsoukalas, D.; Petty, M. C. Langmuir−Blodgett Film Deposition of Metallic Nanoparticles and Their Application to Electronic Memory Structures. **2003**. https://doi.org/10.1021/nl034008t.

(24) Xia, Y.; Whitesides, G. M. SOFT LITHOGRAPHY. *http://dx.doi.org/10.1146/annurev.matsci.28.1.153* **2003**, *28* (1), 153–184. https://doi.org/10.1146/ANNUREV.MATSCI.28.1.153.

(25) Qiu, S.; Tan, X.; Wu, K.; Zhang, A.; Han, S.; Wang, L. Experimental and Theoretical Study on Molecular Structure and FT-IR, Raman, NMR Spectra of 4,4′-Dibromodiphenyl Ether. *Spectrochim. Acta Part A Mol. Biomol. Spectrosc.* **2010**, *76* (5), 429–434. https://doi.org/10.1016/J.SAA.2009.10.005.

(26) Renard, D.; Tian, S.; Ahmadivand, A.; Desantis, C. J.; Clark, B. D.; Nordlander, P.; Halas, N. J. Polydopamine-Stabilized Aluminum Nanocrystals: Aqueous Stability and Benzo[a]Pyrene Detection. *ACS Nano* **2019**, *13* (3), 3117–3124. https://doi.org/10.1021/ACSNANO.8B08445/SUPPL_FILE/NN8B08445_SI_001.PDF.

(27) Walczak, M. M.; Chung, C.; Stole, S. M.; Widrig, C. A.; Porter, M. D. Structure and Interfacial Properties of Spontaneously Adsorbed N-Alkanethiolate Monolayers on Evaporated Silver Surfaces. *J. Am. Chem. Soc* **1991**, *113*, 2370–2378.

(28) Singhana, B.; Jamison, A. C.; Hoang, J.; Lee, T. R. Self-Assembled Monolayer Films Derived from Tridentate Cyclohexyl Adsorbates with Alkyl Tailgroups of Increasing Chain Length. **2013**. https://doi.org/10.1021/la401899q.

(29) Ahn, Y.; Saha, J. K.; Schatz, G. C.; Jang, J.; Center, S. Molecular Dynamics Study of the Formation of a Self-Assembled Monolayer on Gold. *J. Phys. Chem. C* **2011**, *115*, 10668–10674. https://doi.org/10.1021/jp200447k.

(30) Marshall, A. R. L.; Stokes, J.; Viscomi, F. N.; Proctor, J. E.; Gierschner, J.; Bouillard, J. S. G.; Adawi, A. M. Determining Molecular Orientation: Via Single Molecule SERS in a

Plasmonic Nano-Gap. *Nanoscale* **2017**, *9* (44), 17415–17421. https://doi.org/10.1039/c7nr05107g.

(31) Zhao, L.; Jensen, L.; Schatz, G. C. Pyridine-Ag20 Cluster: A Model System for Studying Surface-Enhanced Raman Scattering. *J. Am. Chem. Soc.* **2006**, *128* (9), 2911–2919. https://doi.org/10.1021/JA0556326/SUPPL_FILE/JA0556326SI20050817_124420.PDF.

(32) Bent, S. F. Heads or Tails: Which Is More Important in Molecular Self-Assembly? *ACS Nano* **2007**, *1* (1), 10–12. https://doi.org/10.1021/NN700118K.

(33) Scholl, J. A.; García-Etxarri, A.; Koh, A. L.; Dionne, J. A. Observation of Quantum Tunneling between Two Plasmonic Nanoparticles. *Nano Lett.* **2013**, *13* (2), 564–569. https://doi.org/10.1021/nl304078v.

(34) Savage, K. J.; Hawkeye, M. M.; Esteban, R.; Borisov, A. G.; Aizpurua, J.; Baumberg, J. J. Revealing the Quantum Regime in Tunnelling Plasmonics. **2012**. https://doi.org/10.1038/nature11653.

(35) Esteban, R.; Borisov, A. G.; Nordlander, P.; Aizpurua, J. Bridging Quantum and Classical Plasmonics with a Quantum-Corrected Model. **2012**. https://doi.org/10.1038/ncomms1806.

(36) Li, X.; Xiao, D.; Zhang, Z. Landau Damping of Quantum Plasmons in Metal Nanostructures. *New J. Phys.* **2013**, *15* (15pp), 23011. https://doi.org/10.1088/1367-2630/15/2/023011.

(37) Brongersma, M. L.; Halas, N. J.; Nordlander, P. Plasmon-Induced Hot Carrier Science and Technology. *Nat. Nanotechnol. 2015 101* **2015**, *10* (1), 25–34. https://doi.org/10.1038/nnano.2014.311.

(38) Boerigter, C.; Campana, R.; Morabito, M.; Linic, S. Evidence and Implications of Direct Charge Excitation as the Dominant Mechanism in Plasmon-Mediated Photocatalysis. *Nat. Commun. 2015 71* **2016**, *7* (1), 1–9. https://doi.org/10.1038/ncomms10545.

(39) Aslam, U.; Rao, V. G.; Chavez, S.; Linic, S. Catalytic Conversion of Solar to Chemical Energy on Plasmonic Metal Nanostructures. *Nat. Catal. 2018 19* **2018**, *1* (9), 656–665. https://doi.org/10.1038/s41929-018-0138-x.

Chapter 6

Metasurface Enhancement Raman Spectroscopy (mSERS) for Two-dimensional Materials Wafer-Scale Characterization

Yuan Zeng[1,3‡], Steven Bopp[2‡], Tod Pascal[1,4], Zhaowei Liu[2,3*] and Andrea R. Tao[1,3*]

[1]Department of NanoEngineering, University of California, San Diego, 9500 Gilman Drive MC 0448, La Jolla, California 92093-0448

[2]Department of Electrical and Computer Engineering, University of California, San Diego, 9500 Gilman Drive, La Jolla, California 92093

[3]Materials Science and Engineering Program, University of California, San Diego, 9500 Gilman Drive, La Jolla, California 92093

[4]Department of Chemical Engineering, University of California, San Diego, 9500 Gilman Drive, La Jolla, California 92093

[‡]These authors contributed equally to this work.
*Email: atao@eng.ucsd.edu, zhaowei@ucsd.edu

Introduction

In the past 15 years, owing to special electronic, magnetic, mechanical, and thermal properties which never been observed in their 3D structure, graphene and related two-dimensional (2D) materials are focused by physicists, chemists, and engineers from different fields.[1,2] Different from conventional material, 2D materials are composed of one or a few atomic layers. The atoms within a layer are chemically bonded and no chemical bonds between each individual layers. The only interaction between atomic layers is van der Waals (vdW) interaction.[3] Take the advantages of unique physical and chemical properties, 2D materials have been well developed and widely used in catalysis[4], energy storage[5], optical devices[6,7], microelectronics[8,9], sensing[10], and superconducting[11]. For prove concept experiments on 2D materials, mechanical exfoliation is sufficient to produce micron-scale high-quality demonstration samples.[3] However, for industrial-scale production, the yield of mechanical exfoliation is orders magnitude lower and the cost is much higher than business expectation. An alternative strategy for industrial-scale production is solution-based (liquid phase) exfoliation.[12,13] Because electronic band structure of 2D materials is very sensitive to 2D materials thickness, the major drawbacks of solution-based processing are chemical induced defects and structural polydispersity induced heterogeneity in properties.[2]

To make a balance between 2D materials quality and fabrication scale, chemical vapor deposition and related thin-film deposition is the most promising strategy of 2D materials synthesis. In 2013, Future and Emerging Technologies program in European Union organized a large-scale scientific research project, called “Graphene Flagship”.[14] The main target of this project is translating 2D materials-based technologies from university laboratories to industrial environment and establishing an early prototype of cost-competitive production line.[15] Therefore, wafer-scale synthesis of single crystal 2D materials was focused by researchers around the world in the past decade and a significant progress was made recently.[16–18] Because defects and

impurities on substrate can lead to uncontrollable nucleation of 2D materials, full on-chip monitoring is required both within a single wafer and across wafers, to track unavoidable variations in 2D materials.[15] To characterize 2D materials morphology, optical imaging and Atomic Force Microscopy (AFM) are the most cost-efficient and widely used methods.[19,20] However, owing to limitation in contrast, these methods cannot characterize fundamental properties of 2D materials, such as chemical bonding and crystal structure. Surface Enhanced Raman Spectroscopy (SERS) is a great complementary technique because the vibrational modes in Raman spectra can provide detailed binding footprint in 2D materials. Soniya et. al. developed SERS characterization platform based on focused ion beam (FIB) nanofabrication and electron beam (E-beam) nanofabrication.[21] However, owing to expensive fabrication method, limited device size (tens of micron scale) and lack of reusability, this SERS platform cannot be integrated into industrial production line.

Here, inspired by PDMS assisted damage-free transfer mechanics of 2D materials[22], we integrated PDMS stamp fabrication from nanoimprint lithography (NIL)[23] with colloidal plasmonic metasurface[24], and developed a novel wafer-scale SERS platform, called plasmonic PDMS stamp, for 2D materials characterization. Because most 2D devices are fabrication with different types of 2D materials, we used graphene and h-BN heterostructure as the benchmark to demonstrate the ability of heterostructure characterization. Also, because 2D materials properties depend on both thickness[25] and structure, we used TiN as the benchmark to demonstrate the ability of monitoring thickness variation and phase transition. Owing to nearly consistent fabrication process and more than a decade industrial-scale application of NIL, we believe there is no significant barrier in scaling-up this characterization platform and integrating into current semiconductor industrial production line.

Experimental Methods

Materials. Sylgard 184 Silicon Elastomer was purchased Electron Microscopy Science. Graphene/h-BN heterostructure was ordered from the Grolltex Inc. TiN thin-films were grown and characterized by Steven, using the well-established protocol from his lab (Details in Appendix E, E1).

Gold Substrate Fabrication. Au thin-film substrates were fabricated through Sputter Deposition (using Denton Discovery 18 Sputter System). 100mm diameter, 500 μm thick P type doped wafer (University wafer) was cleaned with isopropanol and cleanroom cloth. The sputtering RF bias is used to clean the substrate for 20 seconds and followed with 10 seconds Cr (400 W) and 120 seconds Au (300 W) sputtering with the Ar gas pressure as 2.4 mTorr. Then the wafer was diced into 1cm x 1cm size for later use.

Ag nanocubes (AgNCs) Preparation. Ag Nanocubes were synthesized via a polyol method published elsewhere.17 AgNO3 is reduced in a solution of pentanediol, CuCl2, and polyvinylpyrrolidone (PVP) (Mw=55,000). PVP serves as a selective capping agent that controls nanocube nucleation and growth. The reaction was allowed to proceed until the resulting colloidal dispersion turned an opaque yellow-green color. To remove excess reactants, the nanocube dispersion product was centrifuged (2700 rpm for 10 min) using a Thermo Scientific CL2 Centrifuge, and the resulting precipitate was redispersed and diluted in an ethanol and water mixture, and then vacuum-filtered (Millipore Durapore membranes, with 0.65 μm, 0.45 μm, then 0.22 μm pore sizes) to remove any larger, unwanted particles.

Plasmonic PDMS Stamp Fabrication. AgNCs on silicon substrate was prepared by Langmuir-Schaefer deposition, as previously described[24]. PDMS solution was prepared by mixing 10-part solution A and 1-part solution B of Sylgard 184, stirring 5 min, and degassing in vacuum desiccator for 30 min. We added few drops PDMS solution on the AgNCs supported by Si substrate and spin coated in 3 steps (500 RPMs for 15 sec, 2000 RPMs for 60 sec and 300 RPMs for 10 sec), followed by 20 hours curing at room temperature and 48 hours curing at 80°C.

PDMS NOM Fabrication. The edges of silicon supported plasmonic PDMS stamp were cut by blade, and tweezer was used to strip plasmonic PDMS stamp from the silicon substrate. Then, plasmonic PDMS stamp was slowly transferred to Au supported 2D materials and form PDMS NOM.

UV-Vis-NIR measurements. UV-Vis-NIR measurements were carried out using PerkinElmer Lambda 1050 spectrometer and Universal Reflectance Accessory and 8° reflection angle. Absorption spectra was calculated by A (%) = 100 (%) – R (%).

mSERS measurements. 785 nm illumination was provided by a Renishaw 300 mW diode laser and all Raman spectra were obtained using a Renishaw inVia confocal Raman microscope. Large-scale Raman mappings (1 mm x 1 mm mapping area, 500 μm step size, 400 data points) were taken under 785 nm excitation with 2 seconds exposure, 50% excitation power and 3 accumulations. The spectra were collected through a 20x, 0.4 NA objective. High resolution Raman mapping (500 μm x 500 μm mapping area, 50μm step size, 100 data points) was taken under 785 nm excitation with 2 seconds exposure, 5% excitation power and 3 accumulations. The spectra were collected through a 50x, 0.75 NA objective.

FDTD Simulations & Simulated EF. Electromagnetic modeling was performed with Lumerical FDTD Solutions. 90 nm AgNCs (Palik dielectric data) were modeled in 3 dimensions with an underlying 75 nm Au thin film. A 5 nm dielectric layer with n = 1.55 was added around AgNC to reflect PVP coating. Background refractive index was set to n = 1 in conventional NOM simulation and n = 1.43 in PDMS NOM. Incident light was injected normal to the substrate and polarized parallel to the (100) faces of the AgNC. A 1 nm global mesh was used. The electric field profiles were calculated in the plane parallel to Au thin film, distance to Au thin film is varied due to different gap location. An average EF for the mSERS substrate is calculated by summing $|E/Eo|^4$ at each pixel (1x1 nm) and normalizing to the cross-sectional area of each nanocubes. This calculation was carried out at discrete wavelengths over the visible range. In Graphene/h-

BN hybrid model, we used graphene surface conductivity material from Lumerical materials database to represent monolayer graphene (location is 0.2 nm above Au thin film), and modified surface conductivity material[26] (σ =10^{-13} $(\Omega \cdot m)^{-1}$) to represent monolayer h-BN (location is 0.4 nm above Au thin film). The effective gap distance was adjusted based on experimental resonance shift and field monitor was placed at 0.5 nm above Au thin film to monitor near-field enhancement. In TiN volumetric permittivity model, TiN (Palik dielectric database) with varied thickness was added above Au thin film and field monitor was placed at 0.5 nm above TiN layer.

Results and Discussion

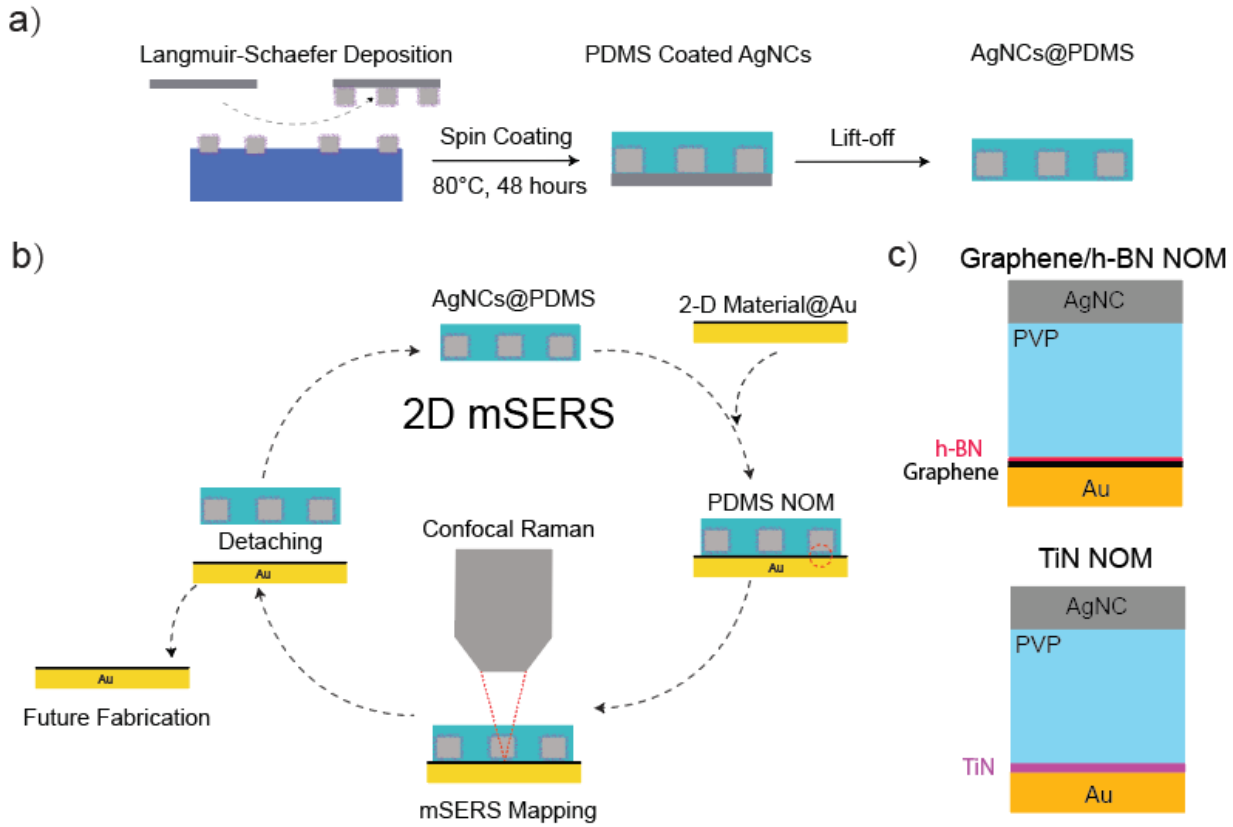

Figure 6.1 | 2D Materials characterization platform fabrication. a) Deposition and encapsulation of AgNCs in PDMS. b) Application and reusability of plasmonic PDMS stamp in scanning mSERS. c) Graphene/hBN and TiN NOM device schematics.

In Figure 6.1a, the fabrication process for silver nanocubes (AgNCs) embedded PDMS is schematically drawn. AgNCs were dispersed in chloroform and drop-cast onto an air-wafer

interface to form a monolayer. Langmuir-Schaefer deposition was used to transfer the AgNC monolayer to a bis(trimethylsilyl)amine (HMDS) functionalized Si substrate. A layer of polydimethylsiloxane (PDMS) was subsequently applied to the surface via spin coating. After curing, the PDMS was lifted off the Si substrate to yield a plasmonic PDMS stamp. Figure 6.1b shows the utilization a plasmonic PDMS stamp in our 2D mSERS (micro-surface-enhanced Raman scattering) characterization method for 2D materials on thin Au films. A plasmonic PDMS stamp is transferred onto a 2D materials on Au to form a nanoparticle-on-metal (NOM) metasurface. Next, we use a scanning confocal Raman microscope to map an area of the sample surface (1cm x 1cm) with a 500 μm step size. As a result of the ~5 nm dielectric gap between the AgNCs and the Au thin film, gap mode capacitive coupling causes strong near-field enhancement in the 2D materials and provides a strong enhancement factor (EF). After Raman mapping, the plasmonic PDMS stamp is stripped from the 2D material/Au heterostructure and reused for subsequent characterizations. Two types of 2D materials on Au thin film samples were fabricated to be used as a testbed to demonstrate the capabilities of our 2D mSERS characterization platform and each are schematically drawn in Figure 6.1c. The graphene/h-BN NOM is composed of a graphene monolayer (0.33 nm) and an h-BN monolayer (0.34 nm) on an Au thin-film. TiN film NOM samples were grown with a range of thicknesses using RF sputtering on DC-sputtered ~30 nm Au on c-sapphire substrates (Appendix E, E1).

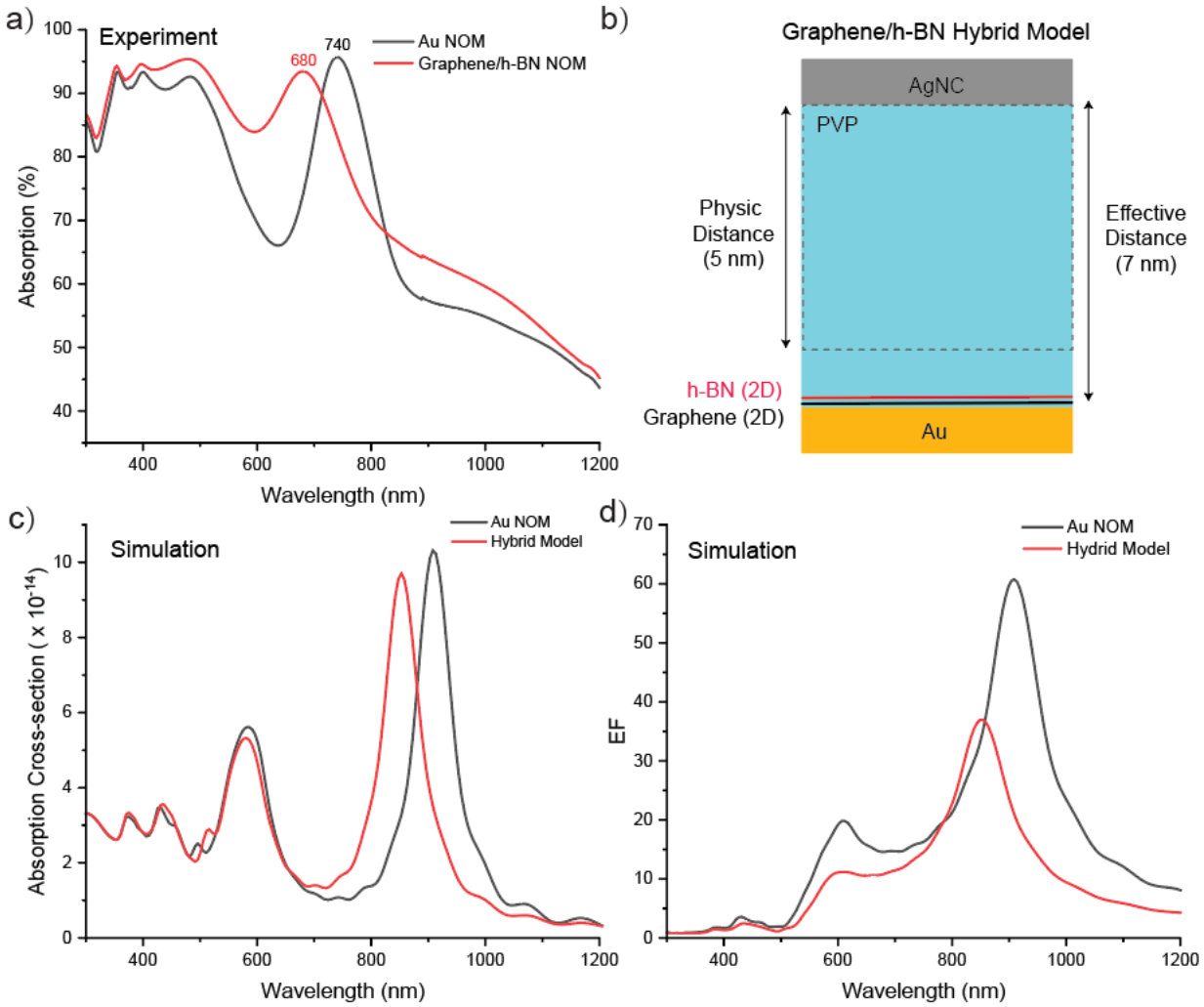

Figure 6.2 | Simulated far-field and near-field in PDMS metasurface with Graphene/h-BN heterostructure. a) Experimentally determined absorptivity of the graphene/h-BN NOM compared to a bare Au reference NOM. b) Schematic of hybrid model generated to study quantum effects in the graphene/h-BN NOM. c) Simulated far-absorption cross section comparison of a bare Au reference NOM and a graphene/h-BN NOM generated with the hybrid model. d) Simulated enhancement factor comparison of a bare Au reference NOM and a graphene/h-BN NOM generated with the hybrid model.

In Figure 6.2a, the measured absorption spectra of a Graphene/h-BN NOM is given in comparison to a reference of a bare Au NOM (e.g. not having graphene and h-BN). As a result of the screening effect contributed by either graphene's conductivity or the high-k dielectric barrier of h-BN, the graphene/h-BN NOM has a weaker coupling between the AgNCs and the Au thin film as compared to the bare Au NOM used for reference and the absorption peak blue-shifts from 740 nm to 680 nm. Because the signal intensity in SERS intensity is proportional to $(E/E_0)^4$, we used a finite-difference time-domain (FDTD) simulation to investigate effects of the near-field enhancement in the Graphene/h-BN NOM. Quantum size effects (due to the ~1/3 nm layer

thicknesses) play a significant role in these devices. In order to characterize the influences of these quantum size effects, we generated a surface conductivity model to study charge screening effects graphene, and a quantum-corrected model to study the effects arising from a dielectric barrier (Appendix E, E2). In order to study both of these effects, a surface conductivity model and quantum-corrected model were combined to create a hybrid model which is given in Figure 6.2b. In this hybrid model, we increased the effective gap distance to 7 nm and added a volumeless 2D conductor layer (material: graphene, conductivity scale = 1) to represent graphene and a volumeless 2D insulator layer (conductivity = 1 x 10^{-13} $(\Omega m)^{-1}$) to represent h-BN. In Figure 6.2c, the simulated far-field absorption spectrum of an Au NOM reference (black) is given in comparison to the hybrid model (red) for the graphene/h-BN NOM. The model shows that an Au NOM will have a moderate absorption peak at 581 nm originating from nanocube (NC) mode resonances, and a strong absorption peak at 908 nm originating from the gap mode resonance. In hybrid model, owing to a two-nanometer increase in effective gap distance, the coupling strength of the gap mode resonance decreases and results in a 55 nm blue-shift to 853 nm. Because the two-nanometer increase in effective gap distance is 3 times larger than the thickness of the graphene/h-BN bilayer (~ 0.67 nm), we believe that the dielectric barrier effect plays a significant role in the origin of the blue-shifted gap mode resonance. Simulated wavelength-dependent near-field enhancement (E/E_0) factors are shown in Figure 6.2d. At the gap mode resonance wavelength, the Au NOM has an E/E_0 of 61 and the hybrid model has an E/E_0 of just 37 meaning that the combined screening and barrier effects result in a 39.3% decrease in the near-field enhancement and a seven times decrease in the EF. Because the EF in the Au NOM is up to 10^7, a less than one order of magnitude decrease in EF is not a significant issue and suggests that these metasurfaces can be used as a SERS platform for graphene and h-BN characterization. Furthermore, although our metasurface has a moderate absorption peak from the NC mode resonance at 581 nm, E/E_0 at 581 nm is about two times lower than gap mode resonance at 908 nm. Therefore, we choose 785 nm laser excitation for all Raman measurements.

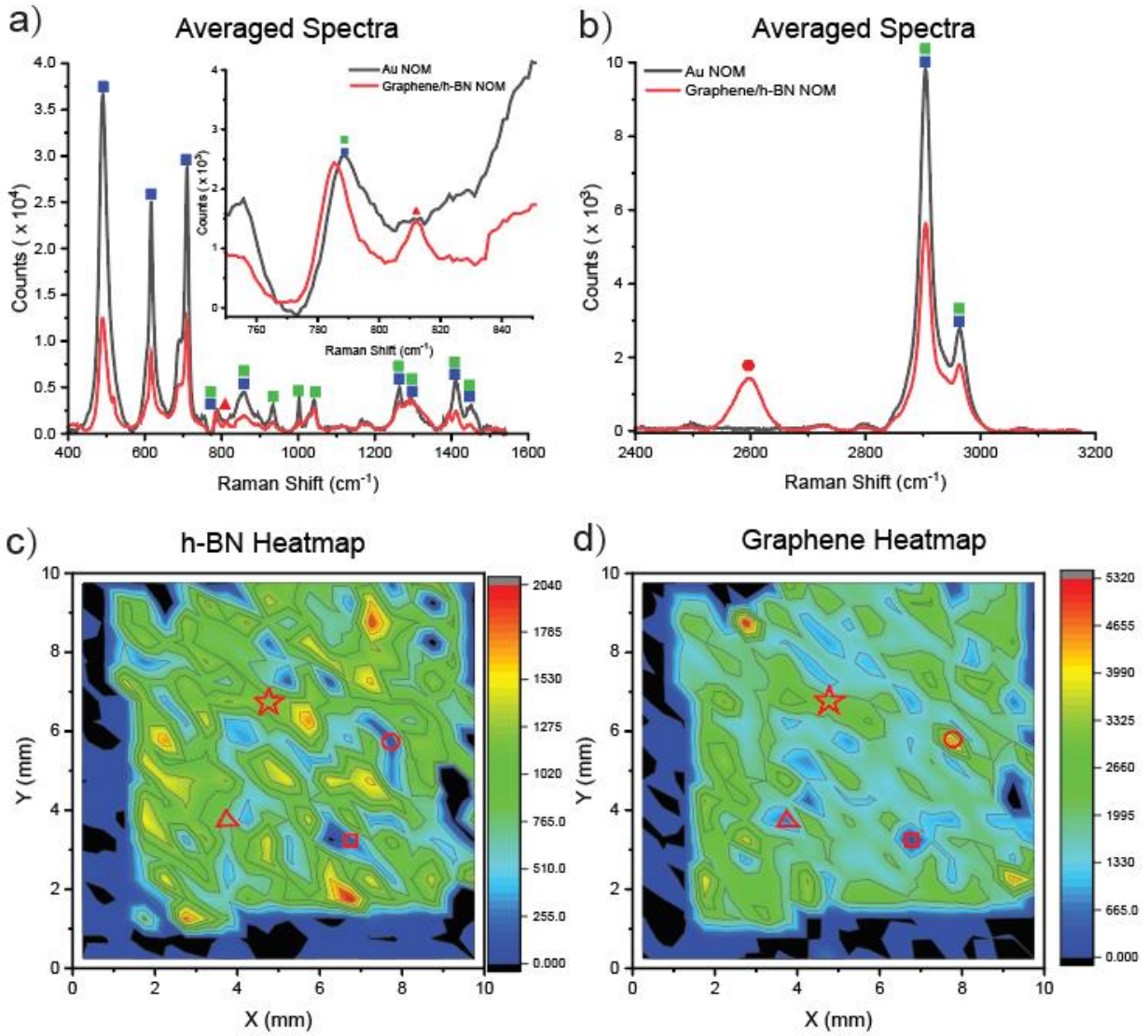

Figure 6.3 | Raman mapping of Graphene/h-BN heterostructure. (a) Averaged Raman spectra (400 points) in low wavenumber regime. (b) Averaged Raman spectra (400 points) in high wavenumber regime. (c) h-BN Raman heatmap plotted with intensity at 812 cm^{-1}. (d) Graphene Raman heatmap plotted with intensity at 2596 cm^{-1}.

To demonstrate the effectiveness of this characterization technique, we transferred a plasmonic PDMS stamp onto a 1 cm x 1 cm graphene/h-BN sample and carried out Raman mapping with a 500 μm step size over the sample surface. Figure 6.3a and Figure 6.3b show the averaged Raman spectra of graphene/h-BN NOM and the Au NOM reference in low (400 cm^{-1} to 1500 cm^{-1}), and high (2400 cm^{-1} to 3200 cm^{-1}) wavenumber regimes respectively. The strong peaks at 490 cm^{-1}, 616 cm^{-1}, and 710 cm^{-1} (blue squares) originate from the PDMS film and the moderate peaks at 934 cm^{-1}, 1002 cm^{-1}, and 1028 cm^{-1} (green squares) originate from trace

polyvinyl propylene (PVP) residue grafted onto the AgNC surfaces. The broad peaks located between 1230 cm^{-1} and 1480 cm^{-1} are attributed to C-C stretch in PVP and CH_3 deformation in PDMS, and the peaks at 2904 cm^{-1} and 2963 cm^{-1} are attributed to C-H stretching in both PVP and PDMS (blue and green squares). In FTIR spectroscopy, h-BN has two strong bands at 1370 cm^{-1} and 812 cm^{-1} which originate from B-N in-plane ring vibration modes and a B-N-B out of plane bending mode respectively.[27] In conventional Raman spectroscopy, because out of plane vibrational (ZO) mode at 812 cm^{-1} is not Raman active[28], the in-plane ring vibrational mode at 1370 cm^{-1} is the only peak which can be used for h-BN characterization and analysis.[29,30] In our graphene/h-BN NOM, owing to the small Raman cross-section and limited B-N bonds in monolayer h-BN, the peak at 1370 cm^{-1} is completely overwhelmed by background and cannot be used for h-BN characterization. However, take the advantage of strong coupling between AgNC and Au thin film, our metasurface has near-field enhancement inside the dielectric gap which is dominated by z-polarized E-field, and results an excitation of the Raman silent mode at 812 cm^{-1} (red triangle). Monolayer graphene exhibits three vibrational modes in Raman spectroscopy. The D band at 1350 cm^{-1} is attributed to defects and sp^3 sites in graphene, the G band at 1587 cm-1 is attributed to in-plane vibrational mode of sp^2 hybridized carbon, and the 2D band is attributed to two phonon lattice vibrational process. Owing to large amount of sp^2 and sp^3 carbon in PDMS and PVP, we measured 2D band in Graphene/h-BN NOM and used it for quantitative analysis. Then, we plotted the Raman heatmap of Graphene/h-BN NOM with h-BN ZO mode (Figure 6.3c, h-BN heatmap) and graphene 2D mode (Figure 6.3d, graphene heatmap). In the area without plasmonic PDMS stamp, both h-BN heatmap and graphene heatmap is completely dark due to the lack of near-field enhancement (Appendix E, E3). In the area covered by plasmonic PDMS stamp, near-field enhancement from metasurface provides us macroscopic information about the graphene/h-BN heterostructure: i) both h-BN heatmap and graphene heatmap has a bright spot at starred area (4.75 mm, 6.75 mm), indicating the presence of graphene/h-BN heterostructure, ii) h-BN heatmap has a bright spot and graphene heatmap has

a dark spot at triangled area (3.75 mm, 3.75mm), indicating the presence of graphene voids, iii) h-BN heatmap has a dark spot and graphene heatmap has a bright spot at circled area (7.75 mm, 5.75 mm), indicating the presence of h-BN voids, and iv) both h-BN heatmap and graphene heatmap have a dark spot at squared area (6.75 mm, 3.25 mm), indicating the presence of both graphene and h-BN voids (Appendix E, E4). Also, because the most frequent Raman intensity is 1020 $\pm$ 255 counts (green in Figure 6.3c) in h-BN heatmap and 2660 $\pm$ 665 counts (green in Figure 6.3d) in graphene heatmap, approximately half of the maximum intensity in each map. Therefore, we hypothesize that the red/yellow spots in h-BN heatmap originates from double layer

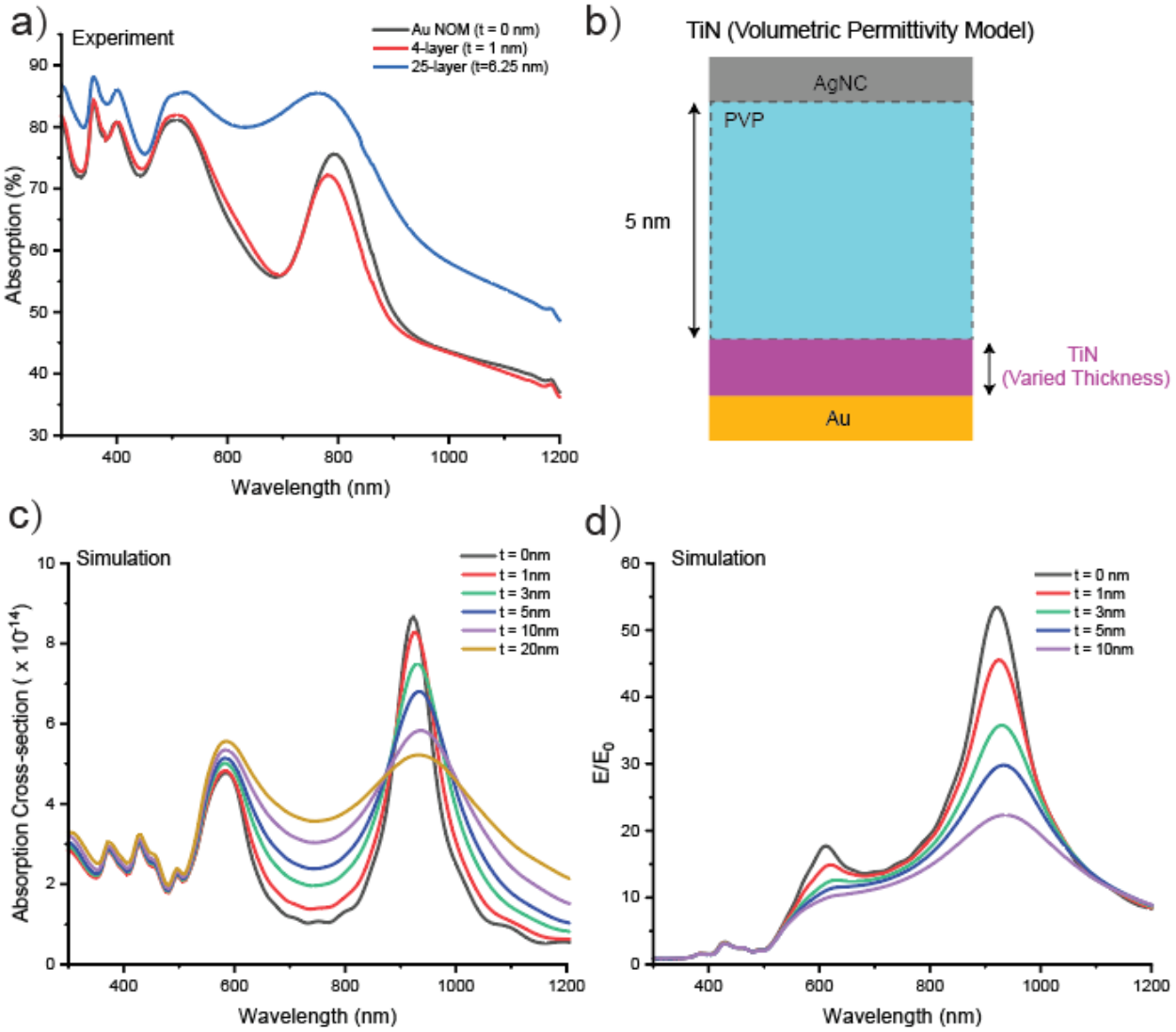

Figure 6.4 | Simulated far-field and near-field in PDMS metasurface with TiN. (a) Experimental absorption spectra of Au NOM (black), 4-layer-TiN NOM (red) and 25-layer-TiN NOM. (b) Schematic of TiN NOM simulation model. (c) Simulated absorption spectra of NOM with different TiN thickness. (d) Simulated enhancement factor of NOM with different TiN thickness.

h-BN and the red/yellow spots in graphene heatmap originates from double layer graphene (Appendix E5).

To demonstrate our metasurface platform is generally available for other 2-D materials like Mxene, we used epitaxy growth to synthesize titanium nitride with 1 nm thickness (4 layers) and 6.25 nm thickness (25 layers) on Au thin-film. Because a single layer of TiN has a thickness of approximately 0.25 nm, The NOM with 4 layers TiN (labelled 4-layer TiN-NOM) has additional 1 nm TiN inside dielectric gap and The NOM with 25 layers TiN (labelled 25-layer TiN-NOM) has additional 6.25 nm TiN inside dielectric gap. Figure 6.4a shows the experimentally determined absorption spectra of the following: Au NOM, 4-layer TiN-NOM, and 25-layer TiN-NOM. As TiN thickness increases from 0 layer to 25 layers, the gap mode resonance blue-shifted slightly from 794 nm to 764 nm because TiN has properties that are similar to gold in the visible spectral range.[31,32] It suggests that TiN does not serve as a dielectric material and instead couples plasmons between AgNCs and TiN. Also, the increased absorption peak broadness indicates a decreased quality factor[33,34] of the gap mode resonance. Figure 6.4b shows a schematic of our simulation model for TiN NOM. Here, TiN NOM is simulated with volumetric permittivity model and TiN is treated as a 3-D material with finite thickness. Figure 6.4c shows simulated absorption spectra for a range of TiN thickness. Similar to experimental spectra in Figure 6.4a, the broadness of simulated gap mode resonance increases significantly with TiN thickness. However, in contrast to blue-shifted gap mode resonance, the simulated gap mode resonance redshifted slightly from 923 nm to 938 nm. This discrepancy between experiment and simulation might originate from two factors: i) defects and surface oxidation in our experiment and ii) dielectric constant change with phase transition from 3-D bulk crystal to 2-D MXene. Figure 6.4d shows simulated near-field enhancement (E/E_0) for a range of TiN thicknesses. As TiN thickness increases from 0 nm to 10 nm, the E/E_0 ratio at the resonance wavelength decreases from 53 to 22, corresponding to a decrease in EF by a factor of 34.

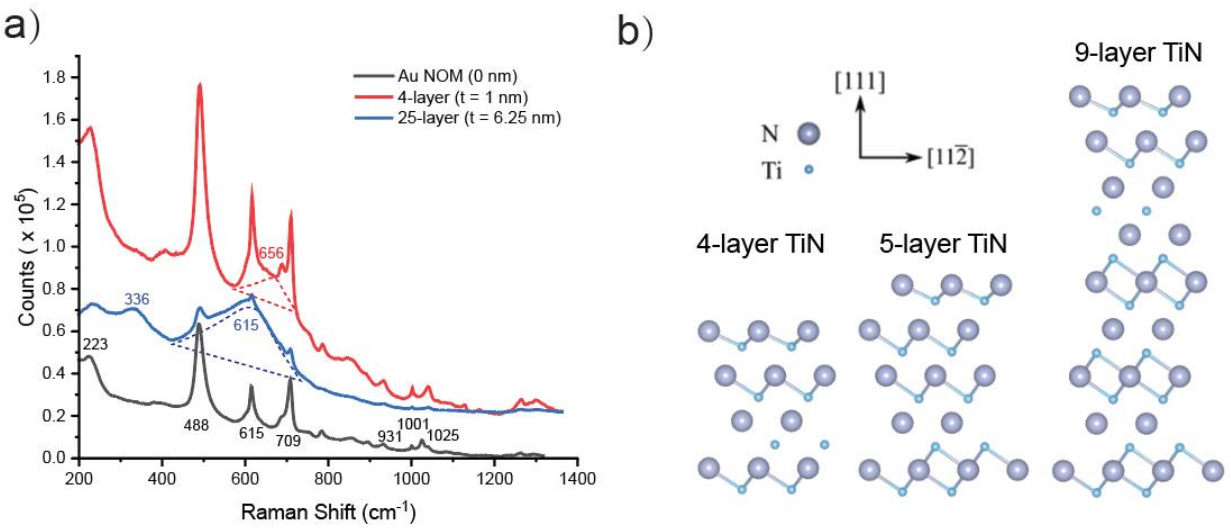

Figure 6.5 | TiN thickness dependent study. (a) Raman spectra of Au NOM (black), 4-layer-TiN NOM (red) and 25-layer-TiN NOM (blue). (b) Relaxed atomic structures of 4, 5, and 9 atomic layer slabs

Figure 6.5a shows Raman spectra of Au NOM, 4-layer-TiN NOM and 25-layer-TiN NOM. TiN has three Raman bands at 213 cm^{-1}, 305 cm^{-1} and 636 cm^{-1} and they are attributed to transverse acoustic (TA), longitudinal accounts (LA) and transverse optical (TO) modes, respectively.[35] Also, owing to strain-induced vibrational energy increase[29], decreased TiN thickness results a blue-shift in Raman modes.[35] In Au NOM, the strong peaks at 490 cm^{-1}, 616 cm^{-1}, and 710 cm^{-1} are attributed to PDMS the moderate peaks at 934 cm^{-1}, 1002 cm^{-1}, and 1028 cm^{-1} are attributed to PVP on AgNC surface. The peak at 223 cm^{-1} is attributed to surface oxidation of AgNC.[36] In 25-layer-TiN NOM, the broad peak at ~ 615 cm^{-1} (dashed blue) is attribute to TO mode and the peak at 336 cm^{-1} is attributed to LA mode. The peak at 230 cm^{-1} is attributed to overlapping of TiN TA mode and background from AgNC surface oxidation. In 4-layer-TiN NOM, TO mode blue-shifted to ~ 656 cm^{-1} (dashed red) due to the decreased thickness. However, the peak at 336 cm-1 drops significantly to background noise level, indicating that LA mode is suppressed. We hypothesize that a decrease in the LA mode originates from a kinetically dominated transition in the preferred bonding from 3-D bulk crystal regime to trans-dimensional mononitride MXene. To confirm this hypothesis, we calculated the relaxed crystal structures of (111)-oriented TiN layers on a (111)-oriented Au slab using the Vienna Ab initio Simulation

Package (VASP).[37,38] Figure 6.5b shows the results of these VASP calculations (Appendix E, E6). The calculations show that low-strain (to the 2.1175Å equilibrium bonding length of relaxed bulk rock salt TiN) interlayer bonds do not begin to form until 5 layers of TiN are deposited. Furthermore, low-strain interlayer bonds begin forming between atomic layer pairs, strongly reminiscent of the MXene regime. Furthermore, because PVP peaks in the 25-layer-TiN NOM have a much lower magnitude than the Au NOM and 4-layer-TiN NOM, we believe the 25-layer-TiN NOM has a lower EF than the 4-layer-TiN NOM which is consistent with our simulation in Figure 6.4d). This thickness dependent EF causes a challenge in TiN thickness characterization with Raman

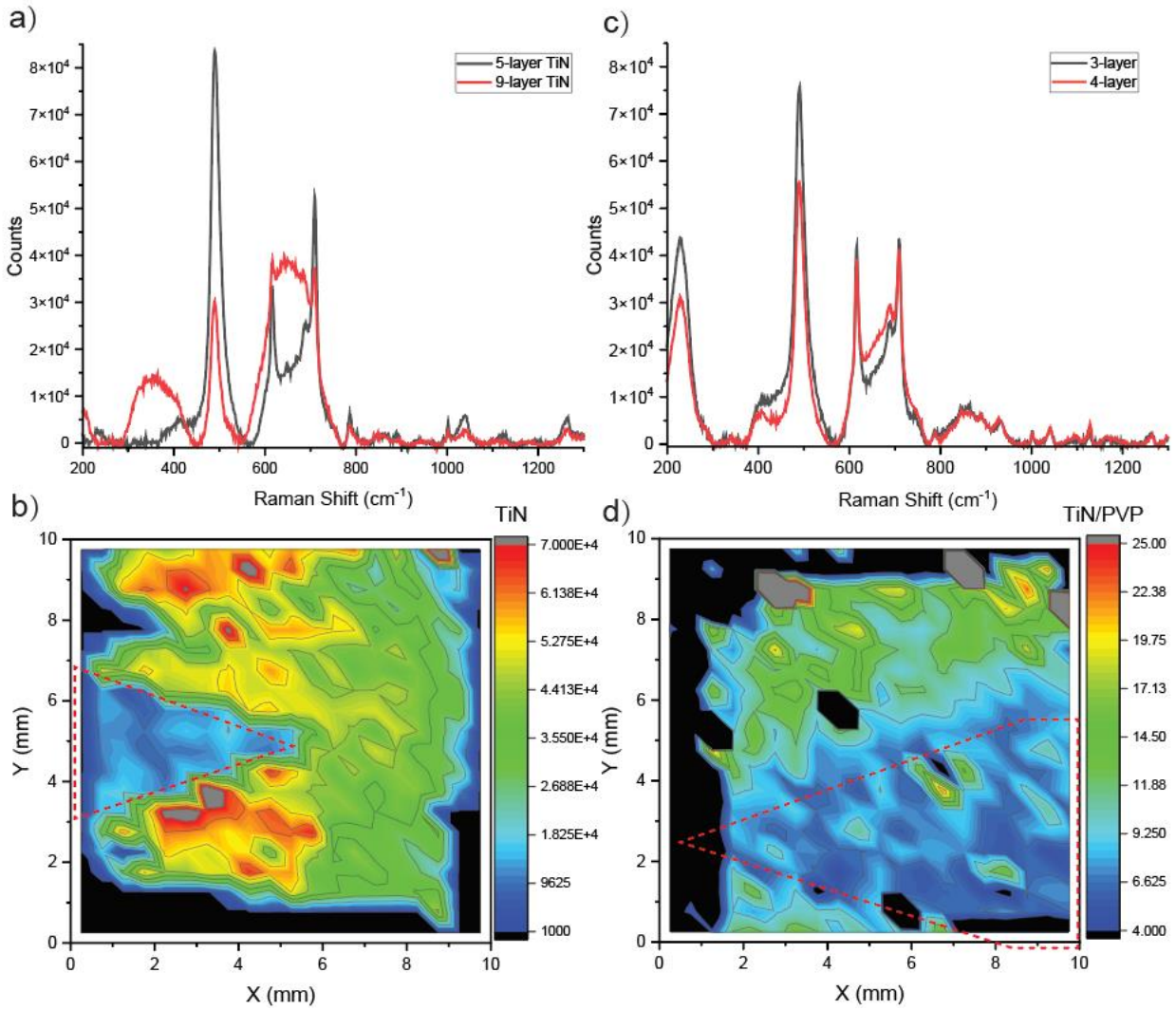

Figure 6.6 | Raman mapping of TiN with different thickness. (a) Raman spectra of 5-layer-TiN NOM and 9-layer-TiN NOM (b) Raman spectra of 3-layer-TIN NOM and 4-layer-TiN NOM. (c) Wafer-scale Raman heatmap of 5/9-layer-TiN NOM. (d) Wafer-scale Raman heatmap of 3/4-layer-TiN NOM

mapping.

To demonstrate the ability of characterizing thickness variation, we prepared two types of mask-patterned multilayers (Appendix E, E7): i) nanometer variation in thickness: we grew 5 layers TiN in mask patterned area and 9 layers TiN in non-patterned area, the thickness difference is 1 nm (labelled as 5/9-layer-TiN) and ii) monolayer variation in thickness: we grew 3 layers TiN in patterned area and 4 layers TiN in non-patterned area, the thickness difference is 1 atomic layer (labelled 3/4-layer-TiN). Figure 6.6a shows the Raman spectra of 5/9-layer-TiN NOM. In 9 layers TiN (non-patterned area), there is a strong peak at 656 cm^{-1} which is attributed to TO mode and a moderate peak at 341 cm^{-1} which is attributed to LA mode, indicating that 9 layers TiN exhibits 3-D bulk crystal structure. In 5 layers TiN (patterned area), the TO mode ~ 660 cm^{-1} has much lower intensity owing to less amount of B-N bonds. Because LA mode is not presented in 5 layers TiN area, we believe 5 layers TiN exhibits 2-D Mxene structure. Owing to significant difference in Raman intensity and line shape, we are able to use the Raman intensity at 656 cm^{-1} to plot a heatmap and identify nanometer variation in TiN thickness. Figure 6.6b shows Raman heatmap of 5/9-layer-TiN NOM which is plotted with TO mode intensity at 656 cm^{-1}. In the dashed triangle, Raman intensity is significantly lower than other plasmonic PDMS stamp covered area. It suggests that 5/9-layer-TiN NOM has 5 layers TiN in the dashed triangle and 9 layers TiN outside the dashed triangle, which is consistent with the mask patterned multilayer growth (Appendix E, E8). Also, there are some bright spots (red/yellow) next to the patterned area, it might originate from edge induced accumulation and relative thick (> 9 layers) TiN. Furthermore, based on the information from large-scale mapping, we are able to zoom into the boundary between different thickness and take a high-resolution mapping with 50 μm resolution (Appendix E, E9). Figure 6.6c shows the Raman spectra of 3/4-layer-TiN NOM. Owing to compensation between increased number of TiN bonds and decreased EF with increased thickness, Raman spectra of 3 layers TiN (patterned area) and 4 layers TiN (non-patterned area) has nearly identical line shape and similar

intensity at 656 cm^{-1} Therefore, a Raman heatmap plotted with the TO mode intensity does not have enough resolution to identify single-layer variation in TiN thickness (Appendix E, E10). To overcome this challenge, we calculated TiN/PVP ratio with TiN TO mode intensity at 656 cm^{-1} and PVP intensity at 1002 cm^{-1} and use it to plot the heatmap (Figure 6.6d). Because both TiN and PVP molecules are trapped inside the dielectric gap and near-field enhancement is nearly consistent, TiN/PVP ratio can normalize the EF difference and increase the resolution of heatmap. In the dashed triangle area, TiN/PVP ratio is smaller than other plasmonic PDMS stamp covered area. It suggests that 3/4-layer-TiN NOM has 3 layers TiN in the dashed triangle and 4 layers TiN outside the dashed triangle, which is consistent with the mask patterned multilayer growth (Appendix E, E11)

Conclusion

Overall, we proposed a novel 2-D material characterization platform based on metasurface enhanced Raman spectroscopy. Take the advantage of near-field enhancement, our mSERS platform can be used to characterize different types of 2-D materials, including graphene, h-BN, and TiN (Mxene). From the wafer-scale Raman heatmap analysis, we are able to characterize 2-D materials distribution in a graphene/h-BN heterostructure, thickness variation and phase transition in TiN (Mxene). Because our plasmonic PDMS stamp fabrication is very similar to the stamp fabrication in nanoimprint lithography (NIL), there is no significant challenge in scaling up this mSERS platform and integrating into 8-inch/12-inch production line of semiconductor industry. Also, because most 2-D materials are synthesized on single crystal Cu foil and the gap mode coupling between AgNC and Cu thin-film is nearly consistent with coupling between AgNC and Au thin-film (Appendix E, E12), we believe this platform can be used to characterize both as-synthesized 2-D materials and 2-D devices fabricated on a metal substrate. In the future, we will perform three optimizations to improve this 2-D materials characterization

platform: i) generating Raman intensity (or Raman intensity to reference peak ratio) vs. number of layers calibration curves for quantitative analysis of 2-D materials thickness, ii) using machine learning to remove background peaks from PVP and PDMS for more precise peak identification and intensity calculation, and iii) using high young's modules PDMS and substrate conformal imprint lithography (SCIL) to improve the plasmonic PDMS stamp lifetime (the expected lifetime is 100 to 1000 cycles).

Acknowledgements:

The authors would like to thank Nano3 and the San Diego Nanotechnology Infrastructure (NSF Award ECCS-2025752), the UC San Diego MRSEC (NSF Award DMR-2011924), and the NanoEngineering MRC for use of their equipment and facilities. This work was supported by NSF Awards CHE-1807891 and DMR-2011924.

Steven Bopp thanks the support of the Department of Defense (DoD) through the National Defense Science & Engineering Graduate (NDSEG) Fellowship Program. This research used resources of the National Energy Research Scientific Computing Center (NERSC), a U.S. Department of Energy Office of Science User Facility located at Lawrence Berkeley National Laboratory, operated under Contract No. DE-AC02-05CH11231 using NERSC project identifier M3047 for 2022.

Chapter 6, in part (Figure 1,2,3,4,6), is currently being prepared for submission for publication of the materials by Yuan Zeng[‡], Steven Bopp[‡], Tod Pascal, Zhaowei Liu* and Andrea R. Tao*. The dissertation author was the primary investigator and author of this paper

Chapter 6, in part (Figure 5), is currently being prepared for submission for publication of the materials by Steven Bopp[‡], Yuan Zeng[‡], Tod Pascal, Andrea R. Tao* and Zhaowei Liu*. The dissertation author was the co-author of this paper.

References

(1) Fan, F. R.; Wang, R.; Zhang, H.; Wu, W. Emerging Beyond-Graphene Elemental 2D Materials for Energy and Catalysis Applications. *Chem. Soc. Rev.* **2021**, *50* (19), 10983–11031. https://doi.org/10.1039/C9CS00821G.

(2) Kang, J.; Sangwan, V. K.; Wood, J. D.; Hersam, M. C. Solution-Based Processing of Monodisperse Two-Dimensional Nanomaterials. *Acc. Chem. Res.* **2017**, *50* (4), 943–951. https://doi.org/10.1021/ACS.ACCOUNTS.6B00643/ASSET/IMAGES/MEDIUM/AR-2016-006436_0008.GIF.

(3) Zhang, L.; Dong, J.; Ding, F. Strategies, Status, and Challenges in Wafer Scale Single Crystalline Two-Dimensional Materials Synthesis. *Chem. Rev.* **2021**, *121* (11), 6321–6372. https://doi.org/10.1021/ACS.CHEMREV.0C01191/ASSET/IMAGES/MEDIUM/CR0C01191_0048.GIF.

(4) Huang, X.; Tang, S.; Mu, X.; Dai, Y.; Chen, G.; Zhou, Z.; Ruan, F.; Yang, Z.; Zheng, N. Freestanding Palladium Nanosheets with Plasmonic and Catalytic Properties. *Nat. Nanotechnol. 2011 61* **2010**, *6* (1), 28–32. https://doi.org/10.1038/nnano.2010.235.

(5) Chen, K. S.; Balla, I.; Luu, N. S.; Hersam, M. C. Emerging Opportunities for Two-Dimensional Materials in Lithium-Ion Batteries. *ACS Energy Lett.* **2017**, *2* (9), 2026–2034. https://doi.org/10.1021/ACSENERGYLETT.7B00476/ASSET/IMAGES/MEDIUM/NZ-2017-00476B_0007.GIF.

(6) Baugher, B. W. H.; Churchill, H. O. H.; Yang, Y.; Jarillo-Herrero, P. Optoelectronic Devices Based on Electrically Tunable p–n Diodes in a Monolayer Dichalcogenide. *Nat. Nanotechnol. 2014 94* **2014**, *9* (4), 262–267. https://doi.org/10.1038/nnano.2014.25.

(7) Ross, J. S.; Klement, P.; Jones, A. M.; Ghimire, N. J.; Yan, J.; Mandrus, D. G.; Taniguchi, T.; Watanabe, K.; Kitamura, K.; Yao, W.; Cobden, D. H.; Xu, X. Electrically Tunable Excitonic Light-Emitting Diodes Based on Monolayer WSe2 p–n Junctions. *Nat. Nanotechnol. 2014 94* **2014**, *9* (4), 268–272. https://doi.org/10.1038/nnano.2014.26.

(8) Desai, S. B.; Madhvapathy, S. R.; Sachid, A. B.; Llinas, J. P.; Wang, Q.; Ahn, G. H.; Pitner, G.; Kim, M. J.; Bokor, J.; Hu, C.; Wong, H. S. P.; Javey, A. MoS2 Transistors with 1-Nanometer Gate Lengths. *Science (80-.).* **2016**, *354* (6308), 99–102. https://doi.org/10.1126/SCIENCE.AAH4698/SUPPL_FILE/DESAI-SM.PDF.

(9) Radisavljevic, B.; Radenovic, A.; Brivio, J.; Giacometti, V.; Kis, A. Single-Layer MoS2 Transistors. *Nat. Nanotechnol. 2011 63* **2011**, *6* (3), 147–150. https://doi.org/10.1038/nnano.2010.279.

(10) Li, H.; Yin, Z.; He, Q.; Li, H.; Huang, X.; Lu, G.; Fam, D. W. H.; Tok, A. I. Y.; Zhang, Q.; Zhang, H. Fabrication of Single- and Multilayer MoS2 Film-Based Field-Effect Transistors for Sensing NO at Room Temperature. *Small* **2012**, *8* (1), 63–67. https://doi.org/10.1002/SMLL.201101016.

(11) Park, J. M.; Cao, Y.; Watanabe, K.; Taniguchi, T.; Jarillo-Herrero, P. Tunable Strongly Coupled Superconductivity in Magic-Angle Twisted Trilayer Graphene. *Nat. 2021 5907845* **2021**, *590* (7845), 249–255. https://doi.org/10.1038/s41586-021-03192-0.

(12) Kang, J.; Sangwan, V. K.; Lee, H. S.; Liu, X.; Hersam, M. C. Solution-Processed Layered Gallium Telluride Thin-Film Photodetectors. *ACS Photonics* **2018**, *5* (10), 3996–4002. https://doi.org/10.1021/ACSPHOTONICS.8B01066/SUPPL_FILE/PH8B01066_SI_001.P

DF.

(13) Bellani, S.; Bartolotta, A.; Agresti, A.; Calogero, G.; Grancini, G.; Di Carlo, A.; Kymakis, E.; Bonaccorso, F. Solution-Processed Two-Dimensional Materials for next-Generation Photovoltaics. *Chem. Soc. Rev.* **2021**, *50* (21), 11870–11965. https://doi.org/10.1039/D1CS00106J.

(14) Saini, A. EU Graphene Flagship Project Aims for Technological Breakthroughs: Graphene-Flagship.Eu. *MRS Bull.* **2014**, *39* (5), 393–394. https://doi.org/10.1557/MRS.2014.107.

(15) Milana, S. The Lab-to-Fab Journey of 2D Materials. *Nat. Nanotechnol. 2019 1410* **2019**, *14* (10), 919–921. https://doi.org/10.1038/s41565-019-0554-3.

(16) Chen, T. A.; Chuu, C. P.; Tseng, C. C.; Wen, C. K.; Wong, H. S. P.; Pan, S.; Li, R.; Chao, T. A.; Chueh, W. C.; Zhang, Y.; Fu, Q.; Yakobson, B. I.; Chang, W. H.; Li, L. J. Wafer-Scale Single-Crystal Hexagonal Boron Nitride Monolayers on Cu (111). *Nat. 2020 5797798* **2020**, *579* (7798), 219–223. https://doi.org/10.1038/s41586-020-2009-2.

(17) Li, J.; Chen, M.; Samad, A.; Dong, H.; Ray, A.; Zhang, J.; Jiang, X.; Schwingenschlögl, U.; Domke, J.; Chen, C.; Han, Y.; Fritz, T.; Ruoff, R. S.; Tian, B.; Zhang, X. Wafer-Scale Single-Crystal Monolayer Graphene Grown on Sapphire Substrate. *Nat. Mater. 2022* **2022**, 1–8. https://doi.org/10.1038/s41563-021-01174-1.

(18) Li, P.; Wei, W.; Zhang, M.; Mei, Y.; Chu, P. K.; Xie, X.; Yuan, Q.; Di, Z. Wafer-Scale Growth of Single-Crystal Graphene on Vicinal Ge(001) Substrate. *Nano Today* **2020**, *34*, 100908. https://doi.org/10.1016/J.NANTOD.2020.100908.

(19) Li, H.; Lu, G.; Yin, Z.; He, Q.; Li, H.; Zhang, Q.; Zhang, H. Optical Identification of Single- and Few-Layer MoS2 Sheets. *Small* **2012**, *8* (5), 682–686. https://doi.org/10.1002/SMLL.201101958.

(20) Late, D. J.; Liu, B.; Matte, H. S. S. R.; Rao, C. N. R.; Dravid, V. P. Rapid Characterization of Ultrathin Layers of Chalcogenides on SiO2/Si Substrates. *Adv. Funct. Mater.* **2012**, *22* (9), 1894–1905. https://doi.org/10.1002/ADFM.201102913.

(21) Raja, S. S.; Cheng, C. W.; Sang, Y.; Chen, C. A.; Zhang, X. Q.; Dubey, A.; Yen, T. J.; Chang, Y. M.; Lee, Y. H.; Gwo, S. Epitaxial Aluminum Surface-Enhanced Raman Spectroscopy Substrates for Large-Scale 2D Material Characterization. *ACS Nano* **2020**, *14* (7), 8838–8845. https://doi.org/10.1021/ACSNANO.0C03462/SUPPL_FILE/NN0C03462_SI_001.PDF.

(22) Kim, C.; Yoon, M. A.; Jang, B.; Kim, H. D.; Kim, J. H.; Hoang, A. T.; Ahn, J. H.; Jung, H. J.; Lee, H. J.; Kim, K. S. Damage-Free Transfer Mechanics of 2-Dimensional Materials: Competition between Adhesion Instability and Tensile Strain. *NPG Asia Mater. 2021 131* **2021**, *13* (1), 1–11. https://doi.org/10.1038/s41427-021-00311-1.

(23) Tucher, N.; Höhn, O.; Hauser, H.; Müller, C.; Bläsi, B. Characterizing the Degradation of PDMS Stamps in Nanoimprint Lithography. *Microelectron. Eng.* **2017**, *180*, 40–44. https://doi.org/10.1016/J.MEE.2017.05.049.

(24) Zeng, Y.; Qian, H.; Rozin, M. J.; Liu, Z.; Tao, A. R. Enhanced Second Harmonic Generation in Double-Resonance Colloidal Metasurfaces. *Adv. Funct. Mater.* **2018**, *28* (51), 1803019. https://doi.org/10.1002/adfm.201803019.

(25) Splendiani, A.; Sun, L.; Zhang, Y.; Li, T.; Kim, J.; Chim, C. Y.; Galli, G.; Wang, F. Emerging Photoluminescence in Monolayer MoS2. *Nano Lett.* **2010**, *10* (4), 1271–1275.

https://doi.org/10.1021/NL903868W/ASSET/IMAGES/MEDIUM/NL-2009-03868W_0005.GIF.

(26) Momentive Performance Materials HBN Hot-Pressed Boron Nitride https://www.matweb.com/search/datasheet.aspx?matguid=8fbbb7d47809493e9afbb7778657d5bb&ckck=1 (accessed Jun 4, 2022).

(27) Gonzalez Ortiz, D.; Pochat-Bohatier, C.; Cambedouzou, J.; Bechelany, M.; Miele, P. Exfoliation of Hexagonal Boron Nitride (h-BN) in Liquide Phase by Ion Intercalation. https://doi.org/10.3390/nano8090716.

(28) Serrano, J.; Bosak, A.; Arenal, R.; Krisch, M.; Watanabe, K.; Taniguchi, T.; Kanda, H.; Rubio, A.; Wirtz, L. Vibrational Properties of Hexagonal Boron Nitride: Inelastic X-Ray Scattering and Ab Initio Calculations. *Phys. Rev. Lett.* **2007**, *98* (9), 095503. https://doi.org/10.1103/PHYSREVLETT.98.095503/FIGURES/3/MEDIUM.

(29) Gorbachev, R. V; Riaz, I.; Nair, R. R.; Jalil, R.; Britnell, L.; Belle, B. D.; Hill, E. W.; Novoselov, K. S.; Watanabe, K.; Taniguchi, T.; Geim, A. K.; Blake, P.; Gorbachev, R. V; Riaz, I.; Nair, R. R.; Jalil, R.; Britnell, L.; Belle, B. D.; Hill, E. W.; Novoselov, K. S.; Geim, A. K.; Blake, P.; Watanabe, K.; Taniguchi, T. Hunting for Monolayer Boron Nitride: Optical and Raman Signatures. *Small* **2011**, *7* (4), 465–468. https://doi.org/10.1002/SMLL.201001628.

(30) Song, L.; Ci, L.; Lu, H.; Sorokin, P. B.; Jin, C.; Ni, J.; Kvashnin, A. G.; Kvashnin, D. G.; Lou, J.; Yakobson, B. I.; Ajayan, P. M. Large Scale Growth and Characterization of Atomic Hexagonal Boron Nitride Layers. *Nano Lett.* **2010**, *10* (8), 3209–3215. https://doi.org/10.1021/NL1022139/SUPPL_FILE/NL1022139_SI_001.PDF.

(31) Kumar, M.; Umezawa, N.; Ishii, S.; Nagao, T. Examining the Performance of Refractory Conductive Ceramics as Plasmonic Materials: A Theoretical Approach. *ACS Photonics* **2016**, *3* (1), 43–50. https://doi.org/10.1021/ACSPHOTONICS.5B00409/SUPPL_FILE/PH5B00409_SI_001.PDF.

(32) Guler, U.; Boltasseva, A.; Shalaev, V. M. Refractory Plasmonics. *Science (80-.).* **2014**, *344* (6181), 263–264. https://doi.org/10.1126/SCIENCE.1252722/ASSET/E359A6F9-AFE1-4697-9827-7C665B5F7DE1/ASSETS/GRAPHIC/344_263_F1.JPEG.

(33) Cuadra, J.; Baranov, D. G.; Wersäll, M.; Verre, R.; Antosiewicz, T. J.; Shegai, T. Observation of Tunable Charged Exciton Polaritons in Hybrid Monolayer WS2-Plasmonic Nanoantenna System. *Nano Lett.* **2018**, *18* (3), 1777–1785. https://doi.org/10.1021/ACS.NANOLETT.7B04965/SUPPL_FILE/NL7B04965_SI_003.MPG.

(34) Zheng, D.; Zhang, S.; Deng, Q.; Kang, M.; Nordlander, P.; Xu, H. Manipulating Coherent Plasmon-Exciton Interaction in a Single Silver Nanorod on Monolayer WSe2. *Nano Lett.* **2017**, *17* (6), 3809–3814. https://doi.org/10.1021/ACS.NANOLETT.7B01176/SUPPL_FILE/NL7B01176_SI_001.PDF.

(35) Sousa, R. R. M. de; Sato, P. S.; Viana, B. C.; Jr., C. A.; Nishimoto, A.; Nascente, P. A. P. Cathodic Cage Plasma Deposition of TiN and TiO2 Thin Films on Silicon Substrates. *J. Vac. Sci. Technol. A Vacuum, Surfaces, Film.* **2015**, *33* (4), 041502. https://doi.org/10.1116/1.4919770.

(36) Pal, A. K.; Mohan, D. B. Fabrication of Partially Oxidized Ultra-Thin Nanocrystalline Silver Films: Effect of Surface Plasmon Resonance on Fluorescence Quenching and Surface

Enhanced Raman Scattering. *Mater. Res. Express* **2014**, *1* (2), 025014. https://doi.org/10.1088/2053-1591/1/2/025014.

(37) Gajdoš, M.; Hummer, K.; Kresse, G.; Furthmüller, J.; Bechstedt, F. Linear Optical Properties in the Projector-Augmented Wave Methodology. *Phys. Rev. B - Condens. Matter Mater. Phys.* **2006**, *73* (4), 045112. https://doi.org/10.1103/PHYSREVB.73.045112/FIGURES/1/MEDIUM.

(38) Kresse, G.; Furthmüller, J. Efficient Iterative Schemes for *Ab Initio* Total-Energy Calculations Using a Plane-Wave Basis Set. *Phys. Rev. B* **1996**, *54* (16), 11169. https://doi.org/10.1103/PhysRevB.54.11169.

Chapter 7

From Classical to Quantum: Probing Raman Enhancement for a Colloidal Metasurface in the Quantum Regime

Yuan Zeng[1,2], Andrea L. Rodarte[1], Tyler J. Dill[1], and Andrea R. Tao[1,2*]

[1]Department of NanoEngineering, University of California, San Diego, 9500 Gilman Drive MC 0448, La Jolla, California 92093-0448

[2]Materials Science and Engineering, University of California, San Diego, 9500 Gilman Drive, La Jolla, California 92093

*Email: atao@eng.ucsd.edu

Introduction

Surface plasmons are capable of confining electromagnetic fields to subwavelength scales, overcoming the classical optical diffraction limit and providing optical enhancements by orders of magnitude in the near-field.[1,2] However, as optical volumes shrink beyond this to the deep subwavelength scale (< 1 nm), a classical descriptions of surface plasmons become insufficient and quantum behaviors — such as wave-particle duality and non-local tunneling effects — start to play an important role.[3] This quantum mechanics description of surface plasmons and related light-matter interactions has opened up a new research field on quantum plasmonics, combining quantum optics with modern plasmonics research.[4,5] When plasmonic nanostructures approach the quantum regime, new phenomena such as the electrical excitation of plasmons[6–8] and optical rectification[9] are observed to occur and provides new opportunities to integrate plasmonic nanostructures for electronics[10], design sub-nanometer scale photonics for biochemical sensing and molecular spectroscopy,[11] and develop novel quantum plasmonics devices includes optical scanning tunneling microscopes, quantum optical antennas[8,12], tunneling diodes,[13] and optical rectifiers[14].

Although quantum plasmonic benefits many applications in quantum optics and nanophotonic, however, it is a major drawback in near-field dependent optical process, such as Surface Enhanced Raman Spectroscopy (SERS). SERS is a surface sensitive technique that molecular Raman scattering been enhanced after binding on the rough metal surface.[15] In electromagnetic (EM) theory, incident light excites localized surface plasmon resonance (LSPR) at resonance frequency, create hot-spots and provide a strong near-field enhancement.[16] This electric field is enhanced as E^2 at both excitation stage and emission stage, results a total enhancement of E^4.[17–19] In quantum plasmonics, tunneling current through the nanojunction causes a charge neutralization on opposite side of nanojunction and significant decrease in local

field enhances.[11] Therefore, the SERS enhancement can decrease orders of magnitude when quantum plasmonics play an important role.[20]

On the experimental side, owing to easily controlled gap distance and less plasmonic coupling with near-by structures, plasmonic dimer are widely used in quantum plasmonic study and both quantum regime and classical regime are well characterized. Duan et al. used lithography to fabricate gold nanoprism dimers with different nanojunction gap distance;[21] Scholl et al. built nanosphere dimers with ligand-free silver nanoparticles, then used an electron beam to induce nanoparticle motion and manipulate the nanojunction size.[22] Cha et al. developed an assembly method to fabricated gold nanosphere dimers where nanojunction size is controlled by ligand length.[23] Based on these studies where optical properties are measured as function of nanojunction size, three different optical regimes have been observed: a classical regime, a crossover regime, and a quantum regime.[24] In the classical regime (nanoparticle separation > 1 nm), plasmonic coupling between nanoparticles can be described by hybridized surface plasmons, include a bonding dipolar plasmon (BDP) mode at lower energy and a higher order bonding quadrupolar plasmon (BQP) mode at higher energy.[22] As interparticle spacing decreases, the BQP mode becomes dominant and both modes red-shift. In the crossover regime (nanoparticle separation 0.5-1 nm), there is a small amount of charge transfer across the plasmonic nanojunction that neutralizes the charge densities on opposing sides of the junction[11], resulting in a much lower degree of plasmon hybridization and decreased red-shift of the BDP mode. In the quantum regime (< 0.5 nm), more electrons tunnel across the nanojunction and induce a new charge transfer plasmon (CTP) mode which blue-shifts with decreasing interparticle distance.

To study SERS in quantum regime, plasmonic dimer structures have a limitation in large scale fabrication. Previous work measuring SERS intensity distribution and they found 24% of total observed SERS signal originates from 0.007% of the total analyte molecules and 61% of

analyte molecules only contribute to 4% of total SERS intensity.[25] This non-uniform distribution of enhancement causes large point to point variation and requires large amount of data points for SERS analysis. Therefore, large scale fabrication which provide more than thousands of nanojunctions with consistent gap distance and orientation is required for studying SERS in quantum regime.

Here, we designed a novel nanofabrication protocol, used PDMS stamping and alkanethiol ligand exchange to make a chip-scale colloidal metasurface with gap distance smaller than critical distance of quantum effect and consistent orientation in out-of-plane direction. This allows us to carry out independent chemical surface modification of the AgNCs and metal surface, providing a versatile method for introducing SERS analytes into the plasmonic nanojunction and for tuning the gap with sub-nanometer resoution. Unlike previous investigations of AgNC metasurfaces where the smallest gap size observed was 2-3 nm,[26] we are able to tune gap size between 0.9 - 3.2 nm, allowing us to accurately observe the onset of electron tunneling. In this manner, we are able to carry out systematic studies that measure how the optical gap-mode and corresponding SERS intensities change as a function of gap height. Because SERS intensity is proportional to enhancement factor $(E/E_0)^4$, therefore, we can qualitatively compare near-field enhancement at different gap height which significantly modified by quantum tunneling.

Experimental Methods

Gold Substrate Fabrication. Au Substrates are fabricated through Sputtering (using Denton Discovery 18 Sputter System). 500 um thick, 4 inches size silicon substrates were washed with ethanol, piranha solution, DI water and dryied with Nitrogen stream. The sputtering RF bias is used to clean the substrate for 40 seconds, and follows with Cr (400 W, 10 second) and Au film

(300 W, 115 second) sputtering with the Ar gas pressure as 2.4 mTorr. Then diced into 1cm by 1 cm pieces for later use.

Ag nanocubes (AgNCs) Synthesis. Ag nanocubes were synthesized using a modified polyol reaction as previously described.[27] Briefly, $AgNO_3$was reduced in 1,5-pentanediol heated to ~200 °C. $CuCl_2$ and PVP (55000 MW) were added to control the nucleation and growth process, as well as to passivate the nanocube surfaces after growth. In order to decrease polydispersity and remove non-cubic particles, nanocubes were vacuum filtered. Millipore Durapore membranes were used in three different sizes to remove sequentially smaller nanoparticles: 650 nm, 450 nm, and 220 nm.

Metasurface fabrication. Ag nanoparticles are repeatedly washed by centrifugation in ethanol and finally redispersed in chloroform. The nanoparticle solution is then carefully drop-cast onto a DI water sub-phase and allowed to equilibrate. Thin (150 μm) PDMS adhered to a silicon backing was then mechanically dipped through the film to transfer it to the substrate. Alkanethiols were used to displace the PVP and form SAMs on the nanoparticle surfaces. Nanoparticle coated PDMS surfaces were submerged in a 1 mM ethanolic solution of the desired alkanethiol for 1 hour. They were then rinsed copiously with ethanol, dried in N_2, and adhered immediately to an Au thin-film substrate. The Au thin film was then either treated with a 1 mM ethanolic solution of a desired thiolated molecule prior to adhesion to the Ag nanoparticle PDMS surface, or immediately adhered to form the metasurface.

Gap Height Determination. We used theoretical calculation to determine the gap distance. For bare Au substrates, we have used previously reported alkanethiol SAMs on Ag thickness measurements.[28] For PhSH, we have assumed a linear addition of the thickness PhSH SAM on Au and the alkanethiol SAMs on Ag.[29] For the gap distance of dHDT Au substrates, interdigitation was assumed to calculate gap thickness. It has been shown that opposing alkanethiol monolayers on nanoparticles will interdigitate on assembly.[30] The distance calculation was followed the equation:

$$D = 0.458 + 0.126 \times n + D\,(PhSH)$$

Where D is gap distance in nanometer, n is number of CH_2 groups in alkanethiols and D (PhSH) is thickness of thiophenol SAM (0.6 nm).[28]

UV-Vis and SERS Measurements. a Perkin-Elmer Lambda 1050 was used for all reflectance measurements. Data was collected with an 8° angle of incidence. Raman measurements were collected on a Renishaw inVia Raman microscope, either with a 633 nm HeNe laser or a 785 nm diode laser. All measurements were collected with < 1 mW with a 0.9 NA 50x objective. 100 measurements were collected at random for each substrate.

FDTD Simulation. FDTD simulations were carried out with Lumerical FDTD Solutions. AgNCs (Palik dielectric data) were modeled in 3 dimensions with a flat gold film as a substrate. A spacer of various thickness was added with index of refraction (n) = 1.4 to reflect the organic SAM spacers. Incident light was normal to the substrate with s-polarized light. A 1 nm global mesh was used with a 0.5 nm local mesh at the junction added to improve accuracy. The model was solved from 300-1500 nm. The electric field enhancements were calculated in the plane of the Ag film, in the center of the gap.

Results and Discussion

Finite difference time domain (FDTD) simulations were used to characterize the expected classical response (e.g. in the absence of tunneling) of the AgNC metasurfaces. Figure 7.1a shows the FDTD model, where a 73.6 nm edge length (*e*) AgNC with a corner radius of curvature of 17 nm is placed over a 50 nm thick (τ) Au film with a gap height, *h*. The molecular gap between the metal structures is modeled as a dielectric with a refractive index of *n*= 1.4 and a conductivity of $\sigma_T = 0$. The condition of $\sigma_T = 0$ denotes a purely insulating gap medium, where electron tunneling probability is zero regardless of *h*, consistent with a classical response.[11] The structure is illuminated from the top of silver nanocube (AgNC) with a polarized plane wave source (red

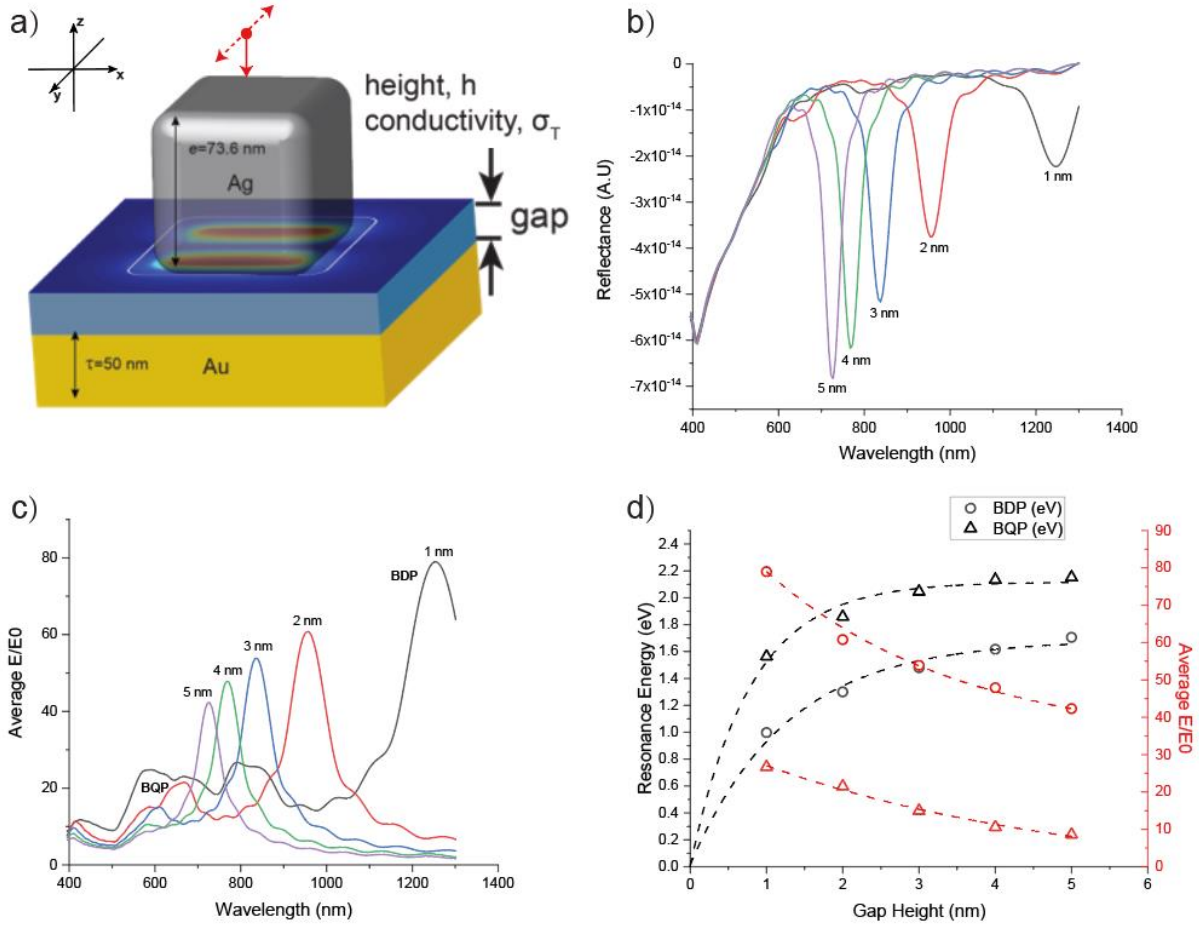

Figure 7.1 | Schematic and simulated classical model metasurface: (a Schematic for FDTD simulation of an Ag NC on an Au substrate separated by a gap of height h and conductivity σ_T=0 **(b)** Simulated reflectance spectra of metasurface for different values of h **(c)** Simulated average electric field enhancement for different gap height *h* **(d)** Gap height dependence of Resonance energy (black curve) and average near-field enhancement at resonance frequency(red curve). circle represents BDP mode and triangle represents BQP mode

dot) where the electric field is polarized in y-direction (dashed arrows) and propagate along the negative z-direction (solid arrow). At resonance frequency, strong plasmonic coupling between AgNC and Au substrate will generate a near-field hot-spot inside gap. Figure 7.1b shows simulated far-field reflectance spectra with different gap height, the dips between 650 nm and 1100 nm corresponds to bonding dipolar plasmon (BDP) mode and the dip between 400 nm and 650 nm corresponds to both band to band transition of gold and bonding quadrupolar plasmon (BQP) mode of plasmonic coupling.[31] As gap distance decreases from 5 nm to 1 nm, the coupling strength become stronger and results a redshift of BDP mode from 667 nm to 1089 nm. Figure 7.1c shows the average near-field enhancement factor (EF), an integration of $|E/E_0|$ over the

junction area, obtained for nanojunctions with varied gap heights (*h*) from 5 nm to 1 nm. The averaged peak enhancement factor increases and redshifts with BDP mode as gap distance decreasing. When gap distance smaller than 3 nm, the BQP mode appears due to the strong coupling and red shift weakly with distance decrease.[24] Figure 7.1d shows gap height dependence of resonance energy and average enhancement factor (EF). For gap height decreases from 5 nm to 1 nm, the BDP mode red-shifts from 1.86 eV to 1.14 eV and EF increases from 44-folds to 91 folds. The BQP mode also red-shifts from 2.2 eV to 1.66 eV and EF increases from 11-folds to 34-folds. When gap distance keep decreasing to 0 nm, the resonance energy of BDP mode and BQP mode will keep decreasing and eventually approach to 0 eV, which is consistent with previous theoretical and computational work examining classical model plasmonic coupling between two metallic antennas with sub-nanometer spherical gap.[11,32]

In the classical model, we used a perfect insulator as dielectric material of nanojunctions, and the calculation is consistent with experimental results in nanojunctions with few nanometers separation. However, when nanojunctions shrink to sub-nanometer scale and quantum tunneling effect starts to play an important role, this classical model deviates from the experimental observations. To model the presence of electron tunneling, time-dependent density functional theory (TDDFT)[33,34] has been used to generate a quantum-mechanical model (QM) of the optical response of plasmonic materials at fully quantum ab initio resolutions. However, this fully QM model is limited to small plasmonic structures with a few thousands of conducting electrons[24,35] and is not suitable for larger plasmonic system containing millions or billions of electrons. To overcome this challenge and simulate quantum effects in larger plasmonic system, we applied the quantum corrected model (QCM) developed by Esteban and co-workers, which used a fictitious conductive material to replace the purely insulating gap medium and mimics electron tunneling.[11] This allows quantum optical properties to be calculated within a classical electrodynamic framework[36] and has excellent agreement with fully QM calculations, indicating

that QCM can be applied to larger plasmonic systems consist of multiple metallic nanostructures with arbitrary shapes and sizes.

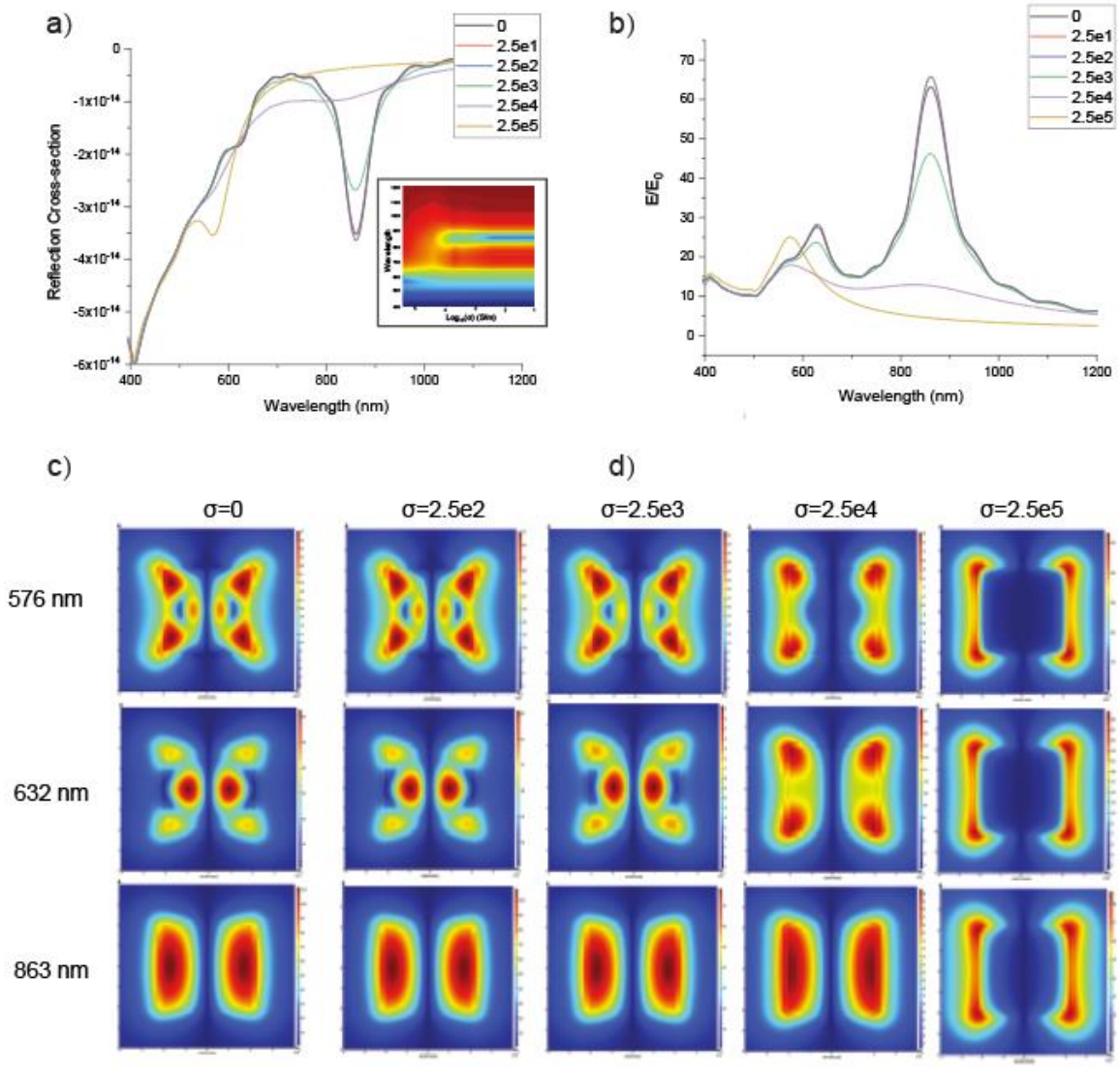

Figure 7.2 | Simulated quantum correction model metasurface: (a) Simulated reflectance spectra for metasurface with constant gap height (2 nm) and varied conductivity σ_T, insert is reflectance intensity map for metasurface with different conductivity (b) Simulated average electric field enhancements for metasurface with constant gap height (2 nm) and varied conductivity σ_T. (c) near-field distribution for metasurface with different conductivity σ_T

To apply the QCM to our FDTD simulations of a plasmonic nanojunction, we keep the gap height as a constant (2 nm) and the nanojunction gap is considered as being filled with a conductive medium with non-zero variable σ_T, effectively allowing electrons to cross the gap in the model. Figure 7.2a shows the simulated reflectance spectra of metasurface with varied gap

medium conductivity. As conductivity increased from 0 to 2.5 x 10^5 S/m, the dip intensity at 632 nm (BQP) and 863 nm (BDP) gradually decreases to 0 because the tunneling current neutralizes the induced charges at the opposite side of the junction[31]. Also, when conductivity approach to 2.5 x 10^4 S/m, there is a new dip shows up at 576 nm and increases with conductivity, which can be assigned to charge transfer plasmon (CTP) mode[11,22]. Figure 7.2b shows calculated average enhancement factor with different gap medium conductivity. For increased conductivity from 0 to 2.5 x 10^3 S/m, the maximum enhancement factor of BDP mode drops 30% from 66-folds to 46-folds and BQP mode drops 14% from 28-folds to 24-folds, also, the wavelength of maximum EF does not shift with increased conductivity. For increased conductivity from 2.5 x 10^3 S/m to 2.5 x 10^5 S/m, the BDP mode drops significantly to 5-folds and BQP mode drops to 15-folds owing to reduced electric field enhancement from charge neutralization. Figure 7.2c shows near-field distribution at 576 nm (CTP mode), 632 nm (BQP mode) and 863 nm (BDP mode) with varied gap medium conductivity. For increased conductivity from 0 to 2.5 x 10^3 S/m, there is a slightly decrease in near-field intensity but no change in the distribution of hot-spot. When conductivity keep increasing to 2.5 x 10^4 S/m, the near-field distribution start to move from the center to the edge and completely disappeared when conductivity approach to 2.5 x 10^5 S/m.

To understand how SERS mechanism performs in quantum regime, we carried out experiments using a modified fabrication of the AgNC metasurface previously described by our group.[37,38] A schematic of the PDMS stamping colloidal metasurface fabrication is shown in Figure 7.3a. Colloidal Ag nanocubes with an edge length of 74 nm were synthesized using methods previously reported (see Methods), then deposited onto a PDMS-coated support by Langmuir-Blodgett film transfer. PDMS is chosen for the stamp because it is optically transparent and provides an easily identified Raman background without signal overlapping with analyst molecules. The capping polymer (Polyvinylpyrrolidone, PVP) on the surface of the as-made AgNCs was displaced through a solution-based ligand exchange using a 1 mM ethanolic solution

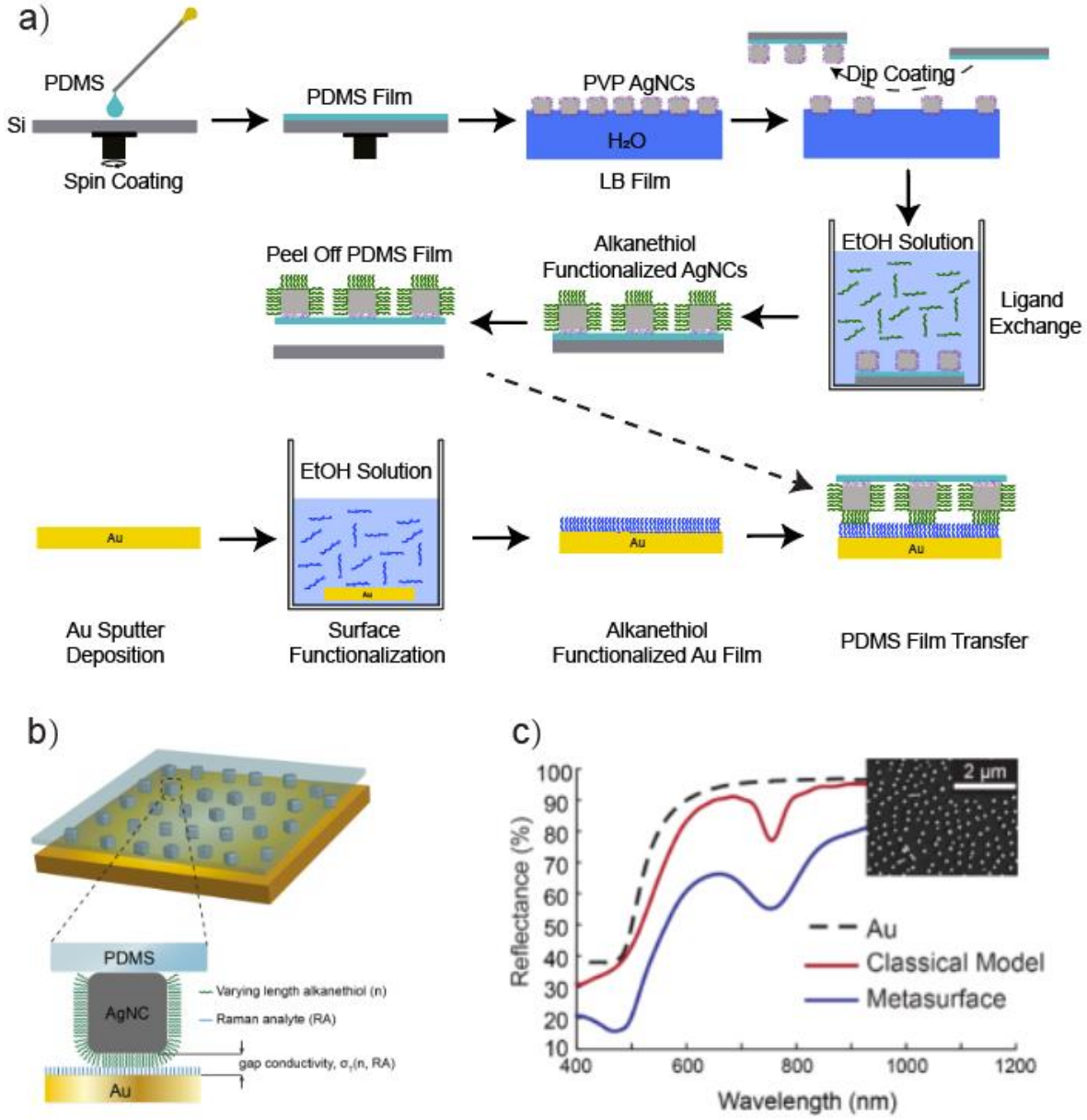

Figure 7.3 | Schematic and far field spectra of metasurface: (a) Schematic of colloidal metasurface fabrication using PDMS stamping method (b) Schematic of a single meta-atom formed by AgNC and Au thin-film and separated by a dielectric gap consist of Raman analyte (dHDT) and alkanethiol (DDT). (c) Experimental (blue) reflectance spectra for an AgNC metasurface in classical regime (d = 3.27 nm) and simulated (red) reflectance spectra with classical model (h = 3 nm, $\sigma_T = 0$). The inset shows an SEM image of AgNCs (73.6 ± 3.7 nm) deposited on PDMS prior to adhesion to an Au substrate, dashed line shows the reflectance spectra of PDMS adhered to Au with no AgNCs

of an end-terminated alkanethiol ($CH_3(CH_2)_nSH$) of variable number of carbon atoms, C_n. The flexible elastomer substrate is removed from its solid support and can be used to bring the AgNC film into contact with arbitrary flat surfaces. Figure 7.3b shows a schematic of PDMS stamping metasurface. By changing C_n of alkanethiol on AgNCs, we can maintain precise control over the

separation distance of the AgNC to Raman analyte (RA). In our experiments, we employ alkanethiols as the RA since they form a self-assembled monolayer with a known thickness. To prepare the RA films, we sputtered a 75 nm Au thin film onto a solid support and allowed the RA layer to adsorb to the Au surface from solution. The total gap height, *h* is dictated by both the thickness of the RA layer and C_n of alkanethiols on AgNCs. Figure 7.3c shows UV/Vis reflectance spectra for an AgNC metasurface with gap height in classical regime. For this metasurface, the AgNCs were functionalized with 1-dodecanethiol (DDT, C_n = *12*) and deuterated 1-hexadecanethiol (dHDT) was used as the RA. We estimate the gap size to be 3.27 nm (see Methods) based on thickness of alkanethiol self-assembled monolayer (SAM)[39] and interdigitation of absorbed thiolate groups[30]. The BDP mode is observed as a dip in the reflectance spectrum at λ_{res}=756 nm, consistent with other reports.[26,38,40] For comparison we include the simulated reflectance obtained from our classical model with *h*=3 nm. It should be noted that this spectrum differs from the plot in Figure 1b since it has been normalized to reproduce the surface density of the fabricated AgNC metasurface shown in the inset in Figure 3c. There is excellent agreement between the simulated and experimental data, indicating that for 3.27 nm gap distance, the metasurface is well within the classical regime and no electron tunneling is expected. The larger full-width half-maximum (FWHM) of the experimental data can be ascribed to the polydispersity of the AgNCs, which exhibit a size distribution of 73.6 ± 3.7 nm and corner sharpness of 17 ± 2.2 nm as observed by image analysis of scanning electron microscope (SEM) images.

We then fabricated AgNCs metasurface functionalized with different alkanethiol lengths ranging from C_n = 2 to C_n = 18. Thiophenol (PhSH) was chosen as the RA and adsorbed onto an Au film because it has large Raman cross-section and relatively small molecule size (Figure 7.4a). Figure 7.4b shows the UV/vis spectra of these AgNCs metasurface. For decreasing C_n from 18 to 6, the dip at 780 nm redshifts to 820 nm due to smaller distance and stronger BDP mode

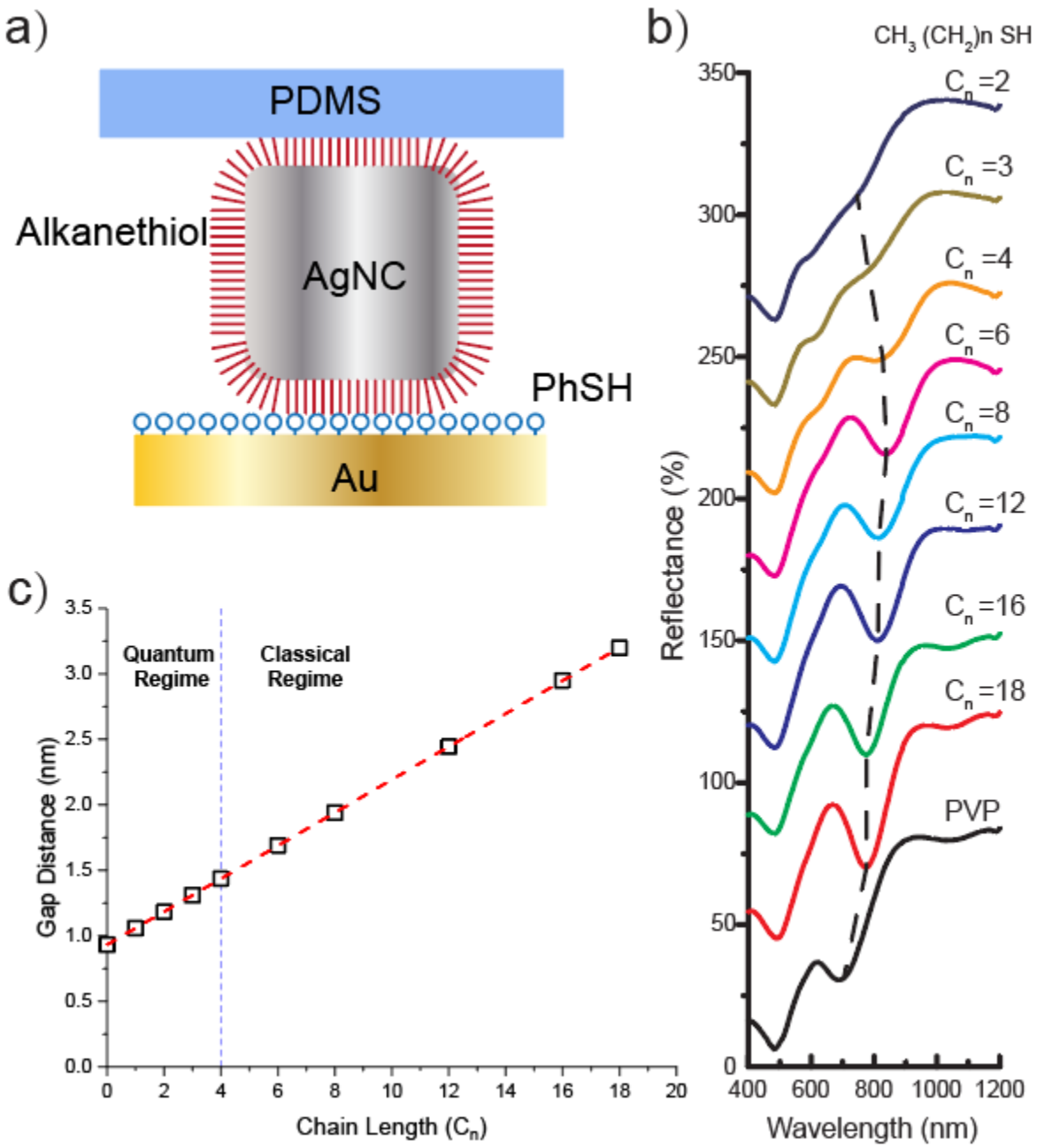

Figure 7.4 | Schematic and far field spectra of metasurface with varied gap height: (a) Schematic of a AgNCs metasurface separated by a dielectric gap consist of Raman analyte (PhSH) and alkanethiol (varied chain length). (b) Calculated gap distance for metasurface with different alkanethiol chain lengths. (c) Experimental reflectance spectra for metasurface with varied chain length

coupling. This observation is consistent with our classical model simulation in Figure 7.1b and indicates the metasurface located in classical regime. As C_n decreases from 6 to 4, the dip no longer redshift and dip wavelength stay constant at 820 nm. It means the metasurface located in crossover regime where electron begin to tunnel between AgNCs and Au substrate.[24] In this case,

the redshift induced by smaller distance compensates with blue shift induced by charge transfer and results a non-shifted overall spectrum. For decreased C_n from 4 to 2, the dip corresponds to BDP mode starts to blue-shift from 820 nm to 770 nm, indicates the metasurface is in quantum regime. This blue-shifting phenomenon has been observed in previous quantum tunneling model[41] because decrease in gap distance causes an increase in conductivity[42] and results a blue-shift in resonance frequency[43]. Also, when C_n = 4, there is another dip shows up at 610 nm and become more intensity when n decreases, this observation is consistent with our quantum correction model simulation in Figure 7.2. This peak can be assigned to higher order charge transfer plasmon (CTP') mode, which induced by charge transfer between AgNCs and Au

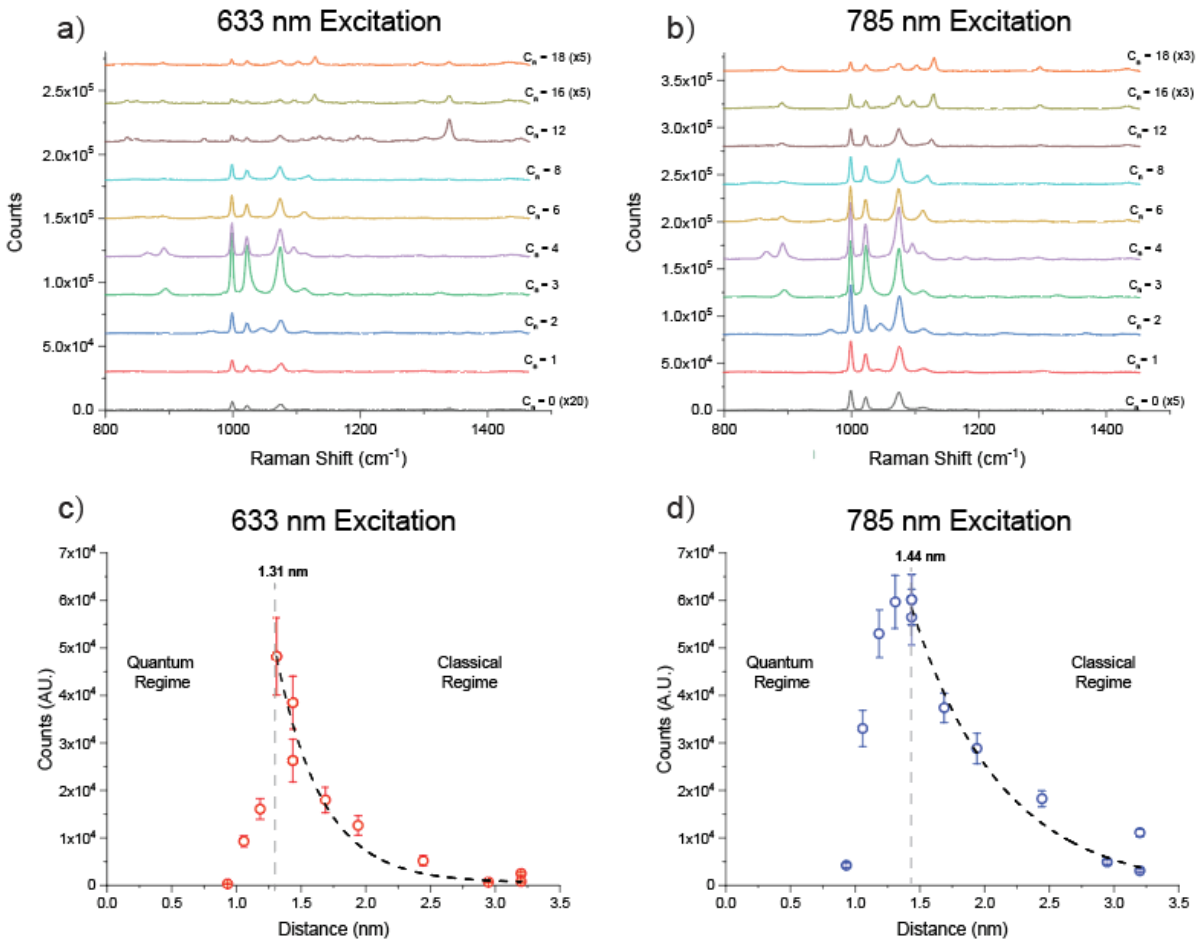

Figure 7.5 | SERS measurement and gap height dependent Raman intensity: (a) Raman spectra for metasurface separated by different chain length alkanethiol at 633 nm excitation. (b) Raman spectra for metasurface separated by different chain length alkanethiol at 785 nm excitation. (c) Gap distance dependent Raman intensity at 633 nm excitation. (d) Gap distance dependent Raman intensity at 785 nm excitation.

substrate and plays a significant role in quantum regime. Figure 7.4c shows the calculated gap distance for metasurface with different alkanethiol chain lengths. The gap distance corresponds to C_n = 4 is 1.44 nm and the gap distance corresponds to C_n = 6 is 1.69 nm, indicates that critical gap distance between quantum regime and classical regime is approximately 1.55 nm $\pm$ 0.15 nm in our metasurface.

To further investigate quantum tunneling effect in our metasurface, we performed a SERS experiment for metasurface with different gap heights. According to our quantum correction model and previous papers, we expected to observe a significant decrease in Raman intensity when the metasurface approach to quantum regime because quantum tunneling neutralizes the induced charges and decreases coupling strength and near-field intensity. It should be noted that tunneling current can also play a role in generating Raman signal and affect chemical enhancement even the near-field enhancement is the dominant factor.[35] Figure 7.5a and 7.5b shows Raman intensity at 633 nm and 785 nm laser excitation, respectively. The thiophenol (analyst) exhibits the $\beta_{CCC}(a_1)$ vibrational mode at 999cm^{-1}, $\beta_{CH}(a_1)$ vibrational mode at 1023 cm^{-1} and $\beta_{CCC}(a_1)$ vibrational mode at 1076 cm^{-1}. For decreased C_n from 18 to 3, there is an increase in Raman counts because smaller gap distance provides stronger near-field enhancement, indicates the metasurface stays in classical regime. For decreased C_n from 3 to 0, there is a significant decrease in Raman intensity, represents a large decrease in near-field enhancement because the metasurface moves into quantum regime as we predicted before. Then we used the chain length of alkanethiol and thiophenol to calculate the estimated gap distance[29,39]. Figure 7.5c shows distance dependent Raman intensity (999 cm^{-1}) under 633 nm excitation. For gap distance > 1.31 nm, the Raman intensity increases exponentially with decreased gap distance, this is consistent with exponential increase in near-field enhancement calculation in Figure 1d. For gap distance < 1.31 nm, the Raman intensity decreases dramatically with gap distance, indicates a significantly decrease in near-field enhancement owing to metasurface in quantum regime. Figure 7.5d shows distance

dependent Raman intensity under 785 nm excitation. For gap distance > 1.44 nm, the Raman intensity increases exponentially with decreased gap distance which consistent with classical model. When gap distance decreases from 1.44 nm to 1.31 nm, the Raman intensity remains nearly constant and indicates the metasurface located in a crossover regime that finite electron density is present inside the junction.[24] As distance further decreases to less than 1.31 nm, the Raman intensity starts to drop significantly, indicates the metasurface moved into quantum regime. The critical distance between quantum regime and classical regime is dependent on wavelength that 785 nm excitation has approximately 0.13 nm larger critical distance than 633 nm excitation. This is originate from wavelength dependence of critical distance that critical distance = $\ln(3q\,\lambda\alpha/2\pi)/2q$, where q is semiclassical electron tunneling wavenumber, λ is optical plasmon wavelength and α is the fine structure constant.[41] Compare to previous observation that quantum tunneling effects only become significant below two atomic lattice spacing[22] (0.8 nm for silver), the critical tunneling distance in our metasurface is approximately 0.5 nm to 0.6 nm larger. This relatively large distance (1.3 nm) tunneling has also been observed in tunneling junction between two AgNCs separated with 1,4-benzenedithiolates self-assembled monolayer.[44] At the critical distance (1.3 nm), the dielectric gap is composed of 0.6 nm thick PhSH SAM and 0.7 nm alkanethiol SAM. Owing to the conductive link through the π-orbitals[43,45], aromatic PhSH SAM has large conductivity and can be treated as a conductive layer. However, alkanethiol SAM has a large electronic energy barrier and form an insulating dielectric layer.[46] As a result, the effective tunneling distance (electronic energy barrier) is 0.7 nm, smaller than the physical critical distance of dielectric gap.

Conclusion

Overall, we designed a scalable method to fabricate colloidal metasurface with tunable gap distance at sub-nanometer scale. By changing the chain length of surface functionalized

alkanethiol, the gap distance of metasurface was precisely controlled between 0.9 nm to 3.2 nm. In this metasurface, the experimental critical distance between quantum regime and classical regime is 1.3 – 1.4 nm. For gap distance larger than 1.4 nm, the optical properties of metasurface are consistent with the classical model of plasmonic nanojunction. However, when gap distance smaller than 1.3 nm, charge transfer mechanism plays a dominant role inside nanojunction and our metasurface is more consistent with the quantum model. Owing to charge neutralization on opposite side of junctions, near-field strength decreases significantly with gap distance in quantum regime, results orders of magnitude decrease in SERS intensity. Therefore, the optimized SERS intensity is observed at the critical distance and smaller critical distance is important for further improvement of SERS enhancement. Because shorter optical plasmon wavelength has smaller critical distance, plasmonic nanojunctions with higher resonance energy has a higher limit in SERS enhancement. Also, to minimize the charge transfer across the nanojunction, replacing polymer dielectric layer with high-k materials, such as HfO_2, ZrO_2 and TiO_2, is an alternative method to decrease the critical distance and increase SERS enhancement. Furthermore, owing to easily controlled nanojunction distance and large range tunability, this metasurface has a great potential to be used as a cost-effective platform for quantum devices.

Acknowledgements

The authors would like to thank the Nano3 facility at Calit2 and NE-MRC facility at NanoEngineering for the use of their facility. We also would like to acknowledge the National Science Foundation under award number 1807891.

Chapter 7, in full, is currently being prepared for submission for publication of the materials by Yuan Zeng, Andrea L. Rodarte, Tyler J. Dill, and Andrea R. Tao*. The dissertation author was the primary investigator and author of this paper.

References

(1) Mühlschlegel, P.; Eisler, H. J.; Martin, O. J. F.; Hecht, B.; Pohl, D. W. Applied Physics: Resonant Optical Antennas. *Science (80-.).* **2005**, *308* (5728), 1607–1609. https://doi.org/10.1126/science.1111886.

(2) Maier, S. A.; Kik, P. G.; Atwater, H. A.; Meltzer, S.; Harel, E.; Koel, B. E.; Requicha, A. A. G. Local Detection of Electromagnetic Energy Transport below the Diffraction Limit in Metal Nanoparticle Plasmon Waveguides. *Nature Materials*. Nature Publishing Group April 2, 2003, pp 229–232. https://doi.org/10.1038/nmat852.

(3) Xu, D.; Xiong, X.; Wu, L.; Ren, X.-F.; Png, C. E.; Guo, G.-C.; Gong, Q.; Xiao, Y.-F. Quantum Plasmonics: New Opportunity in Fundamental and Applied Photonics. *Adv. Opt. Photonics* **2018**, *10* (4), 703. https://doi.org/10.1364/aop.10.000703.

(4) Fitzgerald, J. M.; Narang, P.; Craster, R. V.; Maier, S. A.; Giannini, V. Quantum Plasmonics. *Proceedings of the IEEE*. Institute of Electrical and Electronics Engineers Inc. December 1, 2016, pp 2307–2322. https://doi.org/10.1109/JPROC.2016.2584860.

(5) Tame, M. S.; McEnery, K. R.; Özdemir, Ş. K.; Lee, J.; Maier, S. A.; Kim, M. S. Quantum Plasmonics. *Nature Physics*. Nature Publishing Group June 3, 2013, pp 329–340. https://doi.org/10.1038/nphys2615.

(6) Lambe, J.; McCarthy, S. L. Light Emission from Inelastic Electron Tunneling. *Phys. Rev. Lett.* **1976**, *37* (14), 923–925. https://doi.org/10.1103/PhysRevLett.37.923.

(7) Bharadwaj, P.; Bouhelier, A.; Novotny, L. Electrical Excitation of Surface Plasmons. *Phys. Rev. Lett.* **2011**, *106* (22), 226802. https://doi.org/10.1103/PhysRevLett.106.226802.

(8) Qian, H.; Hsu, S. W.; Gurunatha, K.; Riley, C. T.; Zhao, J.; Lu, D.; Tao, A. R.; Liu, Z. Efficient Light Generation from Enhanced Inelastic Electron Tunnelling. *Nature Photonics*. Nature Publishing Group August 1, 2018, pp 485–488. https://doi.org/10.1038/s41566-018-0216-2.

(9) Ward, D. R.; HÜser, F.; Pauly, F.; Cuevas, J. C.; Natelson, D. Optical Rectification and Field Enhancement in a Plasmonic Nanogap. *Nat. Nanotechnol.* **2010**, *5* (10), 732–736. https://doi.org/10.1038/nnano.2010.176.

(10) Ozbay, E. Plasmonics: Merging Photonics and Electronics at Nanoscale Dimensions. *Science*. American Association for the Advancement of Science January 13, 2006, pp 189–193. https://doi.org/10.1126/science.1114849.

(11) Esteban, R.; Borisov, A. G.; Nordlander, P.; Aizpurua, J. Bridging Quantum and Classical Plasmonics with a Quantum-Corrected Model. *Nat. Commun.* **2012**, *3* (1), 1–9. https://doi.org/10.1038/ncomms1806.

(12) Merlein, J.; Kahl, M.; Zuschlag, A.; Sell, A.; Halm, A.; Boneberg, J.; Leiderer, P.; Leitenstorfer, A.; Bratschitsch, R. Nanomechanical Control of an Optical Antenna. *Nat. Photonics* **2008**, *2* (4), 230–233. https://doi.org/10.1038/nphoton.2008.27.

(13) Bowen, R. C.; Klimeck, G.; Lake, R. K.; Frensley, W. R.; Moise, T. Quantitative Simulation

of a Resonant Tunneling Diode. *J. Appl. Phys.* **1997**, *81* (7), 3207–3213. https://doi.org/10.1063/1.364151.

(14) Ward, D. R.; HÜser, F.; Pauly, F.; Cuevas, J. C.; Natelson, D. Optical Rectification and Field Enhancement in a Plasmonic Nanogap. *Nat. Nanotechnol.* **2010**, *5* (10), 732–736. https://doi.org/10.1038/nnano.2010.176.

(15) Jeanmaire, D. L.; Van Duyne, R. P. Surface Raman Spectroelectrochemistry. Part I. Heterocyclic, Aromatic, and Aliphatic Amines Adsorbed on the Anodized Silver Electrode. *J. Electroanal. Chem.* **1977**, *84* (1), 1–20. https://doi.org/10.1016/S0022-0728(77)80224-6.

(16) Schatz, G. C.; Young, M. A.; Duyne, R. P. Electromagnetic Mechanism of SERS. In *Surface-Enhanced Raman Scattering*; Springer Berlin Heidelberg, 2006; pp 19–45. https://doi.org/10.1007/3-540-33567-6_2.

(17) Moskovits, M. Surface-Enhanced Raman Spectroscopy: A Brief Perspective.

(18) Sharma, B.; Frontiera, R. R.; Henry, A. I.; Ringe, E.; Van Duyne, R. P. SERS: Materials, Applications, and the Future. *Materials Today*. Elsevier January 1, 2012, pp 16–25. https://doi.org/10.1016/S1369-7021(12)70017-2.

(19) Stiles, P. L.; Dieringer, J. A.; Shah, N. C.; Van Duyne, R. P. Surface-Enhanced Raman Spectroscopy. *Annu. Rev. Anal. Chem.* **2008**, *1* (1), 601–626. https://doi.org/10.1146/annurev.anchem.1.031207.112814.

(20) Zhu, W.; Crozier, K. B. Quantum Mechanical Limit to Plasmonic Enhancement as Observed by Surface-Enhanced Raman Scattering. *Nat. Commun. 2014 51* **2014**, *5* (1), 1–8. https://doi.org/10.1038/ncomms6228.

(21) Duan, H.; Fernández-Domínguez, A. I.; Bosman, M.; Maier, S. A.; Yang, J. K. W. Nanoplasmonics: Classical down to the Nanometer Scale. *Nano Lett.* **2012**, *12* (3), 1683–1689. https://doi.org/10.1021/nl3001309.

(22) Scholl, J. A.; García-Etxarri, A.; Koh, A. L.; Dionne, J. A. Observation of Quantum Tunneling between Two Plasmonic Nanoparticles. *Nano Lett.* **2013**, *13* (2), 564–569. https://doi.org/10.1021/nl304078v.

(23) Cha, H.; Yoon, J. H.; Yoon, S. Probing Quantum Plasmon Coupling Using Gold Nanoparticle Dimers with Tunable Interparticle Distances down to the Subnanometer Range. *ACS Nano* **2014**, *8* (8), 8554–8563. https://doi.org/10.1021/nn5032438.

(24) Zuloaga, J.; Prodan, E.; Nordlander, P. Quantum Description of the Plasmon Resonances of a Nanoparticle Dimer. *Nano Lett.* **2009**, *9* (2), 887–891. https://doi.org/10.1021/nl803811g.

(25) Fang, Y.; Seong, N. H.; Dlott, D. D. Measurement of the Distribution of Site Enhancements in Surface-Enhanced Raman Scattering. *Science (80-.).* **2008**, *321* (5887), 388–392. https://doi.org/10.1126/science.1159499.

(26) Lassiter, J. B.; McGuire, F.; Mock, J. J.; Ciracì, C.; Hill, R. T.; Wiley, B. J.; Chilkoti, A.;

Smith, D. R. Plasmonic Waveguide Modes of Film-Coupled Metallic Nanocubes. *Nano Lett.* **2013**, *13* (12), 5866–5872. https://doi.org/10.1021/nl402660s.

(27) Sun, Y.; Xia, Y. Shape-Controlled Synthesis of Gold and Silver Nanoparticles. *Science (80-.).* **2002**, *298* (5601), 2176–2179. https://doi.org/10.1126/science.1077229.

(28) Walczak, M. M.; Chung, C.; Stole, S. M.; Widrig, C. A.; Porter, M. D. *Structure and Interfacial Properties of Spontaneously Adsorbed N-Alkanethiolate Monolayers on Evaporated Silver Surfaces*; 1991; Vol. 113.

(29) Frey, S.; Stadler, V.; Heister, K.; Eck, W.; Zharnikov, M.; Grunze, M.; Zeysing, B.; Terfort, A. Structure of Thioaromatic Self-Assembled Monolayers on Gold and Silver. *Langmuir* **2001**, *17* (8), 2408–2415. https://doi.org/10.1021/la001540c.

(30) Wang, Z. L.; Harfenist, S. A.; Whetten, R. L.; Bentley, J.; Evans, N. D. Bundling and Interdigitation of Adsorbed Thiolate Groups in Self-Assembled Nanocrystal Superlattices. *J. Phys. Chem. B* **1998**, *102* (17), 3068–3072. https://doi.org/10.1021/jp980864v.

(31) Marinica, D. C.; Kazansky, A. K.; Nordlander, P.; Aizpurua, J.; Borisov, A. G. Quantum Plasmonics: Nonlinear Effects in the Field Enhancement of a Plasmonic Nanoparticle Dimer. *Nano Lett.* **2012**, *12* (3), 1333–1339. https://doi.org/10.1021/nl300269c.

(32) Esteban, R.; Aguirregabiria, G.; Borisov, A. G.; Wang, Y. M.; Nordlander, P.; Bryant, G. W.; Aizpurua, J. The Morphology of Narrow Gaps Modifies the Plasmonic Response. *ACS Photonics* **2015**, *2* (2), 295–305. https://doi.org/10.1021/ph5004016.

(33) Marques, M. A. L.; Gross, E. K. U. TIME-DEPENDENT DENSITY FUNCTIONAL THEORY. *Annu. Rev. Phys. Chem.* **2004**, *55* (1), 427–455. https://doi.org/10.1146/annurev.physchem.55.091602.094449.

(34) Stratmann, R. E.; Scuseria, G. E.; Frisch, M. J. An Efficient Implementation of Time-Dependent Density-Functional Theory for the Calculation of Excitation Energies of Large Molecules. *J. Chem. Phys.* **1998**, *109* (19), 8218–8224. https://doi.org/10.1063/1.477483.

(35) Mao, L.; Li, Z.; Wu, B.; Xu, H. Effects of Quantum Tunneling in Metal Nanogap on Surface-Enhanced Raman Scattering. *Appl. Phys. Lett.* **2009**, *94* (24), 243102. https://doi.org/10.1063/1.3155157.

(36) García de Abajo, F. J.; Howie, A. Retarded Field Calculation of Electron Energy Loss in Inhomogeneous Dielectrics. *Phys. Rev. B - Condens. Matter Mater. Phys.* **2002**, *65* (11), 1154181–11541817. https://doi.org/10.1103/PhysRevB.65.115418.

(37) Dill, T. J.; Rozin, M. J.; Brown, E. R.; Palani, S.; Tao, A. R. Investigating the Effect of Ag Nanocube Polydispersity on Gap-Mode SERS Enhancement Factors. *Analyst* **2016**, *141* (12), 3916–3924. https://doi.org/10.1039/c6an00212a.

(38) Rozin, M. J.; Rosen, D. A.; Dill, T. J.; Tao, A. R. Colloidal Metasurfaces Displaying Near-Ideal and Tunable Light Absorbance in the Infrared. *Nat. Commun.* **2015**, *6* (1), 1–7. https://doi.org/10.1038/ncomms8325.

(39) Walczak, M. M.; Chung, C.; Stole, S. M.; Widrig, C. A.; Porter, M. D. *Structure and*

Interfacial Properties of Spontaneously Adsorbed N-Alkanethiolate Monolayers on Evaporated Silver Surfaces; 1991; Vol. 113.

(40) Moreau, A.; Ciracì, C.; Mock, J. J.; Smith, D. R.; Hill, R. T.; Chilkoti, A.; Wang, Q.; Wiley, B. J. Controlled-Reflectance Surfaces with Film-Coupled Colloidal Nanoantennas. *Nature*. Nature Publishing Group December 5, 2012, pp 86–89. https://doi.org/10.1038/nature11615.

(41) Savage, K. J.; Hawkeye, M. M.; Esteban, R.; Borisov, A. G.; Aizpurua, J.; Baumberg, J. J. Revealing the Quantum Regime in Tunnelling Plasmonics. *Nature* **2012**, *491* (7425), 574–577. https://doi.org/10.1038/nature11653.

(42) Esteban, R.; Borisov, A. G.; Nordlander, P.; Aizpurua, J. *Supplementary Information Bridging Quantum and Classical Plasmonics Using a Quantum-Corrected Model*.

(43) Benz, F.; Tserkezis, C.; Herrmann, L. O.; De Nijs, B.; Sanders, A.; Sigle, D. O.; Pukenas, L.; Evans, S. D.; Aizpurua, J.; Baumberg, J. J. Nanooptics of Molecular-Shunted Plasmonic Nanojunctions. *Nano Lett.* **2015**, *15* (1), 669–674. https://doi.org/10.1021/nl5041786.

(44) Celebrano, M.; Wu, X.; Baselli, M.; Großmann, S.; Biagioni, P.; Locatelli, A.; De Angelis, C.; Cerullo, G.; Osellame, R.; Hecht, B.; Duò, L.; Ciccacci, F.; Finazzi, M. Mode Matching in Multiresonant Plasmonic Nanoantennas for Enhanced Second Harmonic Generation. *Nat. Nanotechnol.* **2015**, *10* (5), 412–417. https://doi.org/10.1038/nnano.2015.69.

(45) Bürkle, M.; Viljas, J. K.; Vonlanthen, D.; Mishchenko, A.; Schön, G.; Mayor, M.; Wandlowski, T.; Pauly, F. Conduction Mechanisms in Biphenyl Dithiol Single-Molecule Junctions. *Phys. Rev. B - Condens. Matter Mater. Phys.* **2012**, *85* (7), 075417. https://doi.org/10.1103/PhysRevB.85.075417.

(46) Vickers, E. T.; Graham, T. A.; Chowdhury, A. H.; Bahrami, B.; Dreskin, B. W.; Lindley, S.; Naghadeh, S. B.; Qiao, Q.; Zhang, J. Z. Improving Charge Carrier Delocalization in Perovskite Quantum Dots by Surface Passivation with Conductive Aromatic Ligands. *ACS Energy Lett.* **2018**, *3* (12), 2931–2939. https://doi.org/10.1021/ACSENERGYLETT.8B01754.

Chapter 8

Conclusion: The Future of Bottom-up Total Fabrication and Reverse Engineering

Yuan Zeng[1,2]

[1]Department of NanoEngineering, University of California, San Diego, 9500 Gilman Drive MC 0448, La Jolla, California 92093-0448

[2]Materials Science and Engineering, University of California, San Diego, 9500 Gilman Drive, La Jolla, California 92093

8.1 Total Fabrication and Reverse Engineering

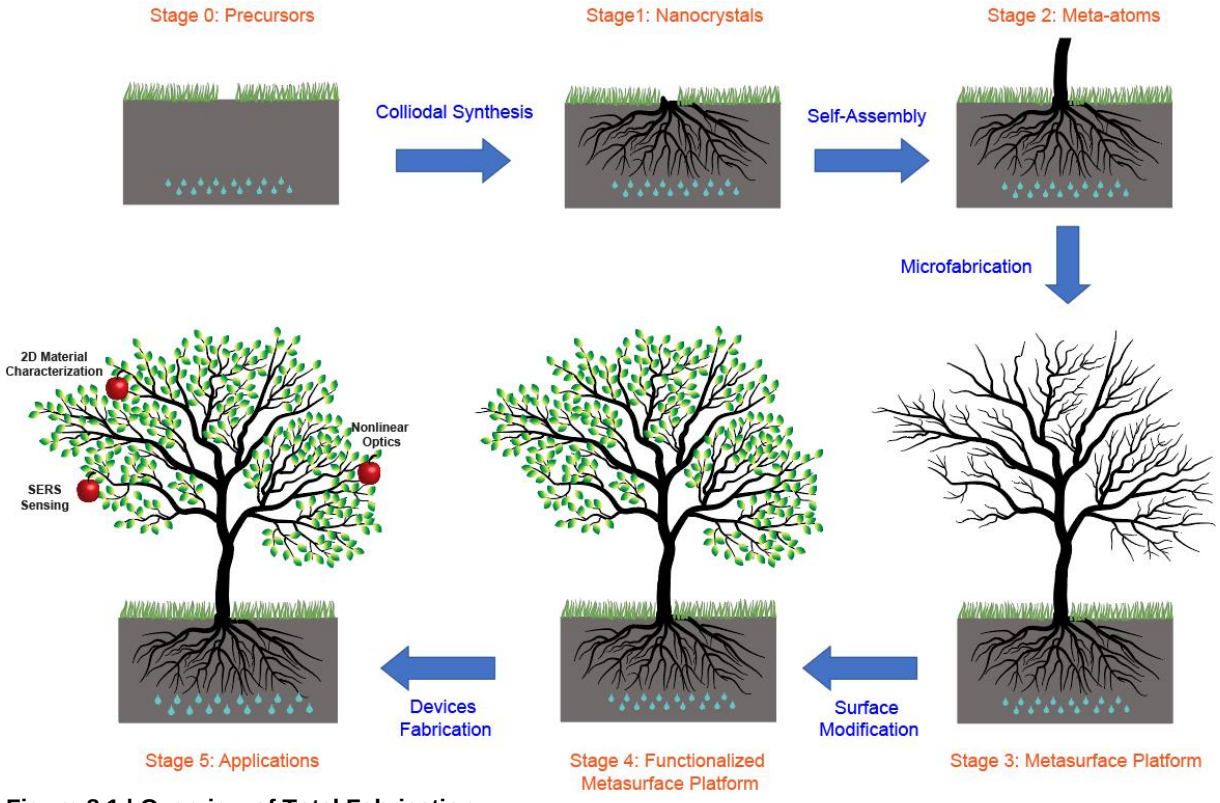

Figure 8.1 | Overview of Total Fabrication.

In this dissertation, we developed a novel bottom-up fabrication process for cost-efficient and wafer-scale plasmonic platforms, named as the “Total Fabrication” (Figure 8.1). The initial stage of Total Fabrication is commercially available molecular/atomic/ionic precursors (*stage 0*). First, colloidal synthesis is performed in wet chemistry lab to achieve nanocrystals in batch-scale (*stage 1*). Next, self-assembly and Langmuir-Schaefer deposition are performed on Langmuir-Blodgett trough to create billions of meta-atoms (*stage 2*). Then, microfabrication processes, such as soft-lithography, are performed to build the wafer-scale metasurface platform (*stage 3*). Based on the requirements of platform surface properties, such as hydrophobicity, solution-based ligand exchange is performed to selectively functionalize the metasurface platform and enables the interaction with other nanoscale materials, such as molecules (*stage 4*). Finally, device-level engineering is performed and the metasurface platform is used for different applications, including nonlinear optics, SERS sensing, and wafer-scale 2D materials characterization (*stage 5*).

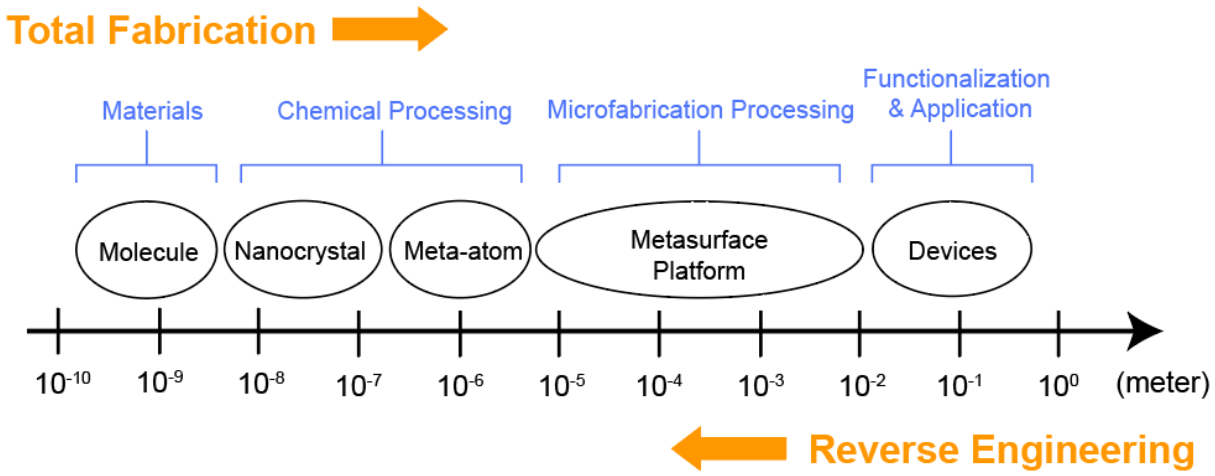

Figure 8.2 | Total Fabrication and Reverse Engineering

Owing to great tunability on each stage of Total Fabrication, we can customize this bottom-up fabrication process based on the technological applications of wafer-scale platform. Here, we proposed a reverse engineering process from stage 5 to stage 1, for efficient development of Total Fabrication (Figure 8.2). First, device level engineering is performed to guide the design of wafer-scale platform (*stage 5*). Based on requirements on surface properties, selective surface modification on metasurface platform is developed after device level engineering (*stage 4*). Next, different microfabrication processes, such as patterning, etching, nanoimprinting etc., are integrated and permutated for targeted metasurface platform (*stage 3*). Then, according to the requirements on meta-atom size, shape, orientation, and interparticle distance etc., self-assembly methods are developed (*stage 2*). Finally, to prepare nanoparticles for self-assembly, colloidal synthesis is engineered by controlling temperature, concentration, surfactant etc., to achieve desired nanoparticle size, shape, and composition (*stage 1*). In the following sections, we will focus on Total Fabrication of plasmonic metasurface platform and discuss each stage of reverse engineering.

8.2 Stage 5: Light-Matter Interaction and Device-Level Engineering

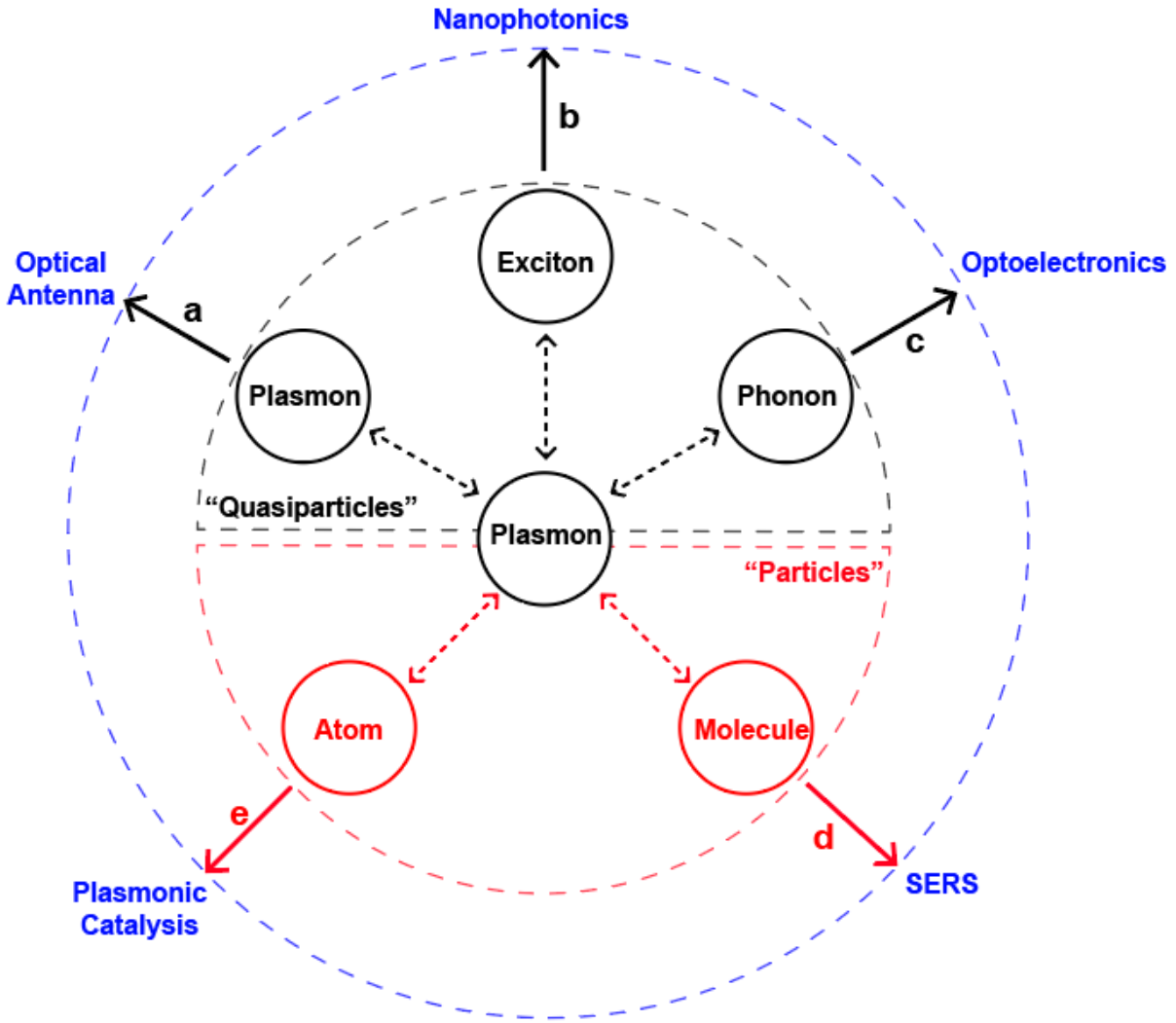

Figure 8.3 | Light-Matter interaction and device level enginnering. (a) plasmon-plasmon coupling, (b) plasmon-exciton coupling, (c) plasmon-phonon coupling, (d) plasmon-molecule interaction, (e) plasmon-atom interaction. (a)-(c) are quasiparticle-quasiparticle coupling, (d) and (e) are particle-quasiparticle interaction

Particles are the building blocks of the universe, if we consider the universe as a stage of time and space, particles are the "actors" in this stage.[1] The proton, electron, and neutron are the most fundamental building blocks of all matter around us. Owing to strong nuclear force induced attraction, atoms are composed of these three fundamental building blocks. Then, strong attractions between atoms result in chemical bonds and create more complex particles, like molecules, organic complexes, and microbials. In quantum physics, "particle-like" quantized entitles play a significant role in determining matter properties.[2] For examples, quantum of electromagnetic wave can be described as photon; quantum of vibrational mechanical energy can

be described as phonon; quantum of free carrier oscillation can be described as plasmon. Because these “particle-like” entitles are massless and have different physical properties than real particles, they are named as “quasiparticles” by Lev Landau in the 1930s.[3]

In particle physics, if two particles are connected by one of the four fundamental interactions[4]: (1) electromagnetic interactions, (2) gravitational interactions, (3) strong interactions, and (4) weak interactions, they are considered as coupled particles and the interaction between them is named as coupling. Owing to new physical phenomenal arises from particle-particle, particle-quasiparticle, quasiparticle-quasiparticle coupling, we can engineer these coupling effects and use them for different technological applications. In this section, we will focus on engineering and application of plasmon based coupling (Figure 8.3).

8.2.1 Plasmon-Plasmon Coupling

When interparticle distance between two or more plasmonic particles smaller than their dimensions, plasmon resonance of individual particles start to hybridize and result in a red-shifted resonance spectrum and significantly increased near-field intensity compared to individual particles (Figure 8.4a).[5–7] This phenomenon is called plasmon-plasmon coupling or plasmon coupling. In addition to particle size, shape, and composition, interparticle distance plays a significant role in plasmon-plasmon coupling. Figure 8.4b) shows interparticle distance dependent EM field intensity (E^2) between two face-face orientated silver nanocubes (red) and edge to edge orientated silver nanocubes. As interparticle distance increase from 2 nm to 20 nm, E^2 decreases exponentially from more than 4 orders of magnitude to around 3 orders of magnitude.[7] When interparticle distance increase to hundred nanometer scale, plasmon resonance hybridization and near-field enhancement become negligible. However, owing to far-field coupling between well-spaced plasmonic particles, the extinction spectra also redshifted with increased distance from 150 nm to 450 nm (Figure 8.4c).[8] The critical distance is about one diameter’s length, less than one diameter’s length is near-field coupling regime, and between 1-

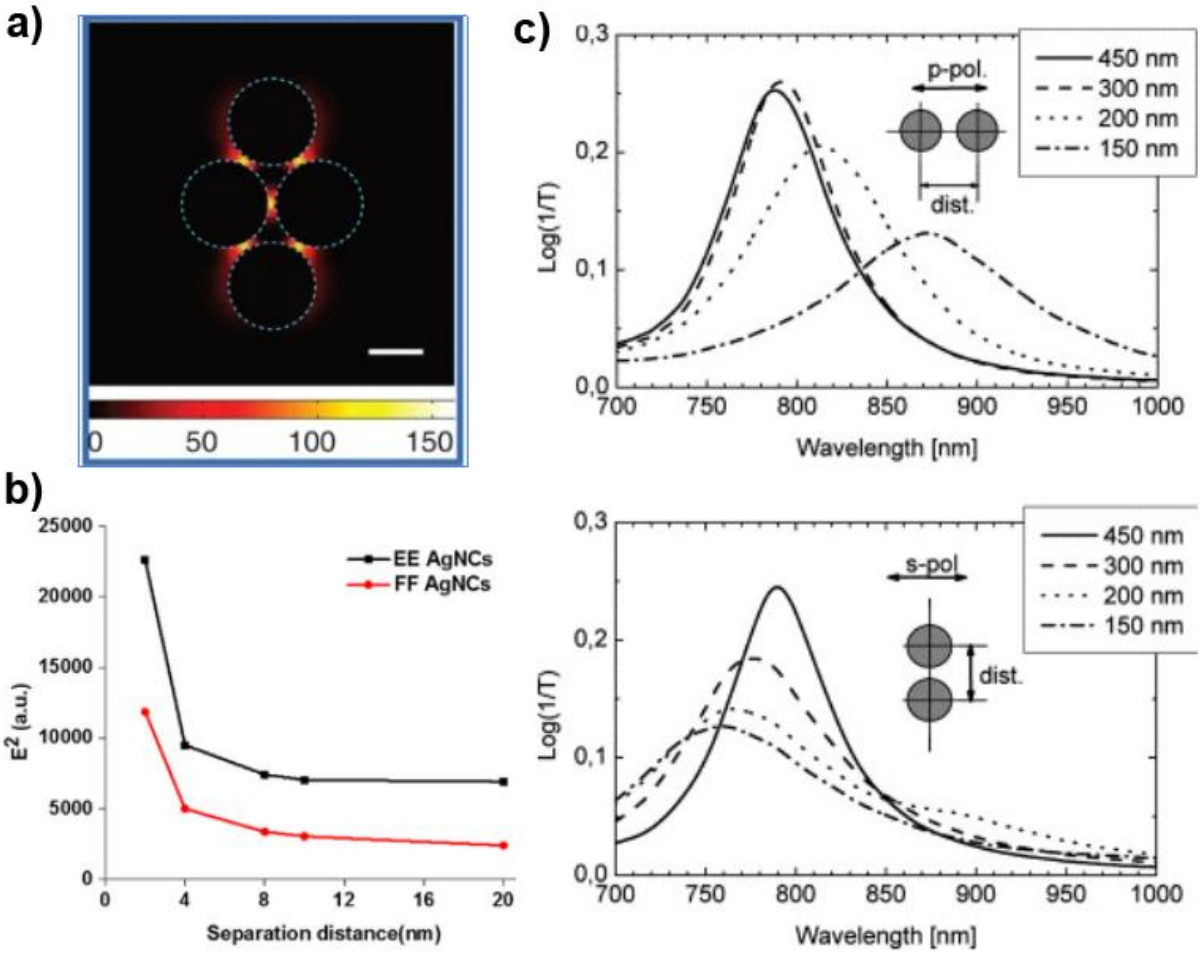

Figure 8.4 | Plasmon-Plasmon coupling. (a) Electromagnetic hotspots from plasmon-plasmon coupling. Reproduced with permission from ref 5. Copyright xx The xx. (b) Distance dependent Intensity (E^2) between coupled silver nanocubes. Reproduced with permission from ref 7. (c) Distance dependent extinction spectra for far-field coupling. Reproduced with permission from ref 8.

7 diameter's length is far-field coupling regime. There is a special case called quantum regime. When interparticle distance approach to sub-nanometer regimes, quantum effects like electron tunneling starts to play a dominant role. Tunneling electron causes charge neutralization and reduce the coupling strength, result in a blue-shifted resonance spectrum, and significantly decreased near-field enhancement.[9,10] Because plasmon-plasmon coupling has different characteristics in each regime, we are able to develop different applications by controlling interparticle distance. Take the advantage of near-field enhancement, plasmon-plasmon coupling in near-field regime can be used for enhanced nonlinear optical process[11] and SERS[5]. Owing to distance dependent spectrum shift, plasmon-plasmon coupling in far-field regime can be used for

plasmonic ruler.[6,12] Application in quantum regime has not been well-developed yet, but we believe plasmon-plasmon coupling in quantum regime has a great potential for developing quantum devices[13].

8.2.2 Plasmon-Exciton Coupling

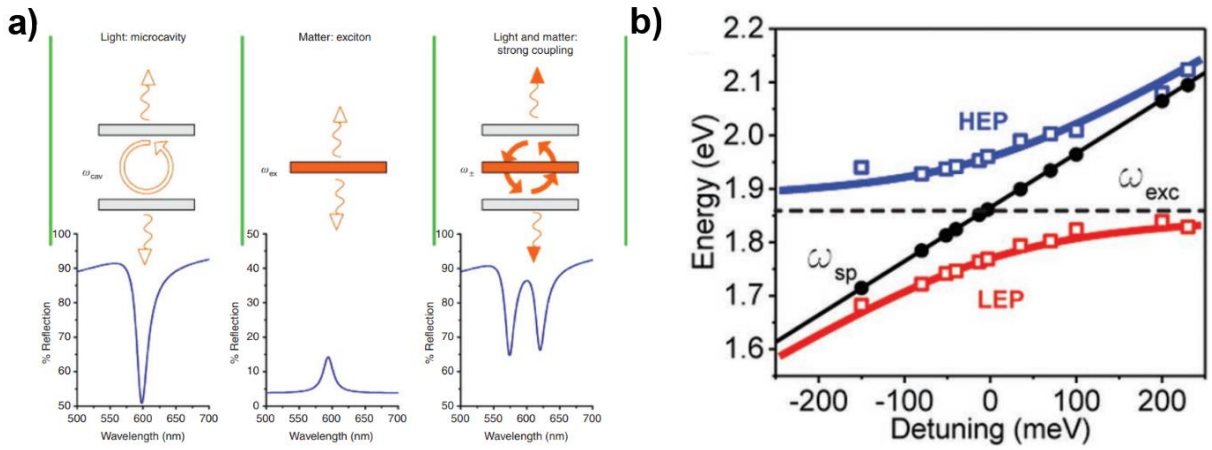

Figure 8.5 | Plasmon-Exciton coupling. (a) Sketched reflectance spectra of strong coupling of light and matter. Reproduced with permission from ref 21. (b) High energy polariton (HEP) and low energy polariton (LEP) as a function of detuning. Reproduced with permission from ref.14.

Like plasmon-plasmon coupling, plasmon-exciton coupling also has two distinct regimes: i) strong coupling regime and ii) weak coupling regime. Generally, strong plasmon-exciton coupling occurs in highly confined environment that excitonic TMDs are trapped inside a plasmonic cavity[14–18] or close to an plasmonic optical antenna[19]. Owing to strong near-field enhancement in plasmonic cavity, plasmonic resonator interact with exitonic resonator and form in a new light-matter hybridized state with brand new physical properties. To make a better description of this hybridized state, a new quasiparticle called plexciton (plasmon-exciton polariton) is used to describe the quantized entitle.[20,21] Plasmon-exciton coupling is defined by three important parameters: i) energy transfer rate between light and matter (g), ii) rate of light escape from the cavity (κ), and rate of matter loses its polarization (γ). In strong coupling regime, energy transfer rate between light and matter is faster than light escape rate and matter loss rate, and result in two new resonance frequencies in optical spectrum (Figure 8.5a).[21] When energy transfer rate slower than light escape rate and matter loss rate, plasmon-exciton coupling locate in weak coupling regime and does not affect wave functions of plasmons and excitons. Owing to

great tunability in plasmon energy, plasmon-exciton coupling can be manipulated. In Figure 8.5b), exciton energy is fixed at 1.85 eV and plasmon energy increases from 1.6 eV to 2.1 eV.[14] When detuning energy (energy difference between plasmon and exciton) is larger than 150 meV, polariton energy is similar to plasmon energy and exciton energy, indicates a weak plasmon-exciton coupling. When detuning energy approaches to 0, energy transfer rate between plasmon and exciton increases significantly, and polariton energy starts to deviate from plasmon energy and exciton energy. This clear anti-crossing behavior indicates the formation of hybridized states and strong plasmon-exciton coupling. Therefore, coupling strength can be tuned by controlling energy difference between plasmon and exciton, and we are able to build nanophotonic devices based on plasmon-exciton coupling. In strong coupling regime, plasmon-exciton coupling can be used for chemical rate modification, quantum information processing and low threshold laser. In weak coupling regime, plasmon-exciton coupling can be used for SERS, surface enhanced fluorescence, and photovoltaics.

8.2.3 Plasmon-Phonon Coupling

In quantum physics, the vibrational motion of atom or molecule lattice can be described by a quasiparticle, phonon. Acoustic phonon has transverse acoustic (TA) mode and longitudinal acoustic (LA) mode, owing to low frequency coherent movements of atom out of their equilibrium position. Similarly, optical phonon has transverse optical (TO) mode and longitudinal acoustic (LO) mode, owing to out of phase (two atoms in opposite direction) movement of neighboring atoms. Owing to strong light-matter interaction, plasmon can couple with optical phonon and form plasmon-phonon coupling.[22,23] To achieve strong coupling between plasmon and phonon, Yoo, D. et. al. developed epsilon-near-zero (ENZ) nanocavities filled with SiO_2[24]. By increase cavities diameter from 430 nm to 1120 nm, ENZ resonance is tuned from 1000 to 2500 cm^{-1}. As cavities resonance energy approaches to transverse optical (TO) and longitudinal optical (LO) phonon energy, strong coupling occurs and results in modal splitting in transmittance spectra. This ENZ nanocavities platform provides a new path to study strong plasmon-phonon coupling, which may

lead to application in optoelectronic devices and quantum sensing. Also, because phonon properties are determine by atomic lattice, plasmon-phonon coupling can be used to probe crystal structure, chemical composition and electronic properties simultaneously.[25]

8.2.4 Plasmon-Molecule Interaction

Plasmon-molecule interaction is observed when molecules are trapped in plasmonic cavities[26–28] or absorbed on plasmonic nanocrystal surface[29]. The behavior of plasmon-molecule interaction is highly dependent on organic molecules electronic structures and can be described in three constituents at resonance frequencies: i) refractive index-dependent plasmon resonance, ii) plasmon-molecule resonance coupling, and iii) plasmon enhanced fluorescence.[30] In the first case, organic molecules do not have light absorption and the interaction with plasmonic nanocrystal results in an increased refractive index of surround environment and red-shifted plasmon resonance. This type of plasmon-molecule interaction can be used for refractive index sensor. In the second case, organic molecules have strong absorption on plasmonic nanocrystal surface, lead to fast energy transfer rate between plasmonic nanocrystals and molecules, formation of hybridized state, and anti-crossing behavior. This type of plasmon-molecule interaction can be used for SERS. In the third case, organic molecules have both strong absorption and emission. Owing to near-field enhancement during excitation process and increased local density of photonic states during emission process[31], the radiative emission rate is significantly boosted, and the fluorescence lifetime is also decreased. This type of plasmon-molecule interaction can be used for biological imaging[26] and two-photon fluorescence[32,33].

8.2.5 Plasmon-Atom Interaction

In plasmonic nanostructures, there are two channels for plasmon decay: i) radiative damping by photon emission, and ii) non-radiative Landau damping by creating hot electron-hole pairs.[34] In the first 100 fs of nonradiative channel, plasmon decay via Landau damping generate “hot” electron-hole pairs. At t = 100 fs to 1 ps, electron-electron interaction leads to carrier relaxation. At t = 1- 100 ps, electron-phonon collision leads to nanoparticle heating.[35] Typically,

hot carrier production is maximized when imaginary part of the permittivity is large.[36] However, owing to small imaginary permittivity in plasmonic materials[37], the rate of hot carrier generation is limited.

To overcome this challenge, Aslam et.al. synthesized Ag-Pt core-shell nanocubes and achieved strong light absorption and large hot carrier generation spontaneously.[38] In this multi-metallic nanostructure, plasmonic Ag core plays the dominant role in photon absorption and generates localized surface plasmons. By introduce Pt shell, a fast plasmon decay channel is opened, and large friction of energy is dissipated through Pt shell via hot carrier generation. In this case, the plasmon energy transfer between Ag core and Pt shell is mediated by interaction between plasmon and Pt atoms. Recently, Zhou et, al. developed an antenna-reaction platform for photocatalysis.[39] This plasmonic photocatalyst consisting of plasmonic Cu nanoparticle "antenna" with Ru atom "reactor" sites. Because Cu nanoparticles play the dominant role in the light absorption and Ru atoms play the dominate role in catalysis, there is an energy transfer channel between Cu nanoparticles and Ru atoms, due to plasmon-atom interaction. Although the detailed energy transfer mechanism has not been well-studied yet, the experimental observation indicates that plasmon-atom interaction has a great potential in plasmonic catalysis and chemical reaction modification[40].

8.2.6 Summary

In this section, we provide a brief overview of light-matter interaction, including plasmon-quasiparticle couplings and plasmon-particle couplings, and their technological applications. Based on technological need from customer, we can select the most appropriate light-matter interaction and develop a plasmonic metasurface platform. Because coupling is determined by multiple critical factors, such as particle size, shape, composition and interparticle distance, a device-level engineering is required before Total Fabrication. Moreover, most of these coupling originate from interaction between different types of particles, for example, plasmon-exciton coupling is interaction between plasmonic particle and excitonic particle. Therefore, precise

engineering of complex heterogeneous system is critical and need to be involved in the customization of Total Fabrication.

8.3 Stage 4: Surface Modification and Ligand Exchange

Surface modification is an engineering process that brings new physical or chemical characteristics, such as roughness[41], hydrophobicity[42], surface charge[43], surface energy[44], and reactivity[45] etc., to material surface and makes it different from the original surface. Because interparticle interaction is highly dependent on the interface properties between particles, surface modification is critical for engineering plasmon-quasiparticle couplings and plasmon-particle interactions. For example, Benz et. al. developed molecular-shunted plasmonic nanojunctions using biphenyl-4-thiol (BPT) and biphenyl-4,4'-dithiol (BPDT) molecules.[46] Because BPDT molecules have two thiol groups, they form conductive linkers between plasmonic nanoparticle and planar gold film. However, owing to lack of second thiol group, BPT modified nanojunction does not form conductive linkers and has significantly lower charge transfer rate. Owing to electron transfer induced charge neutralization on opposite nanojunction[10], BPDT modified nanojunction has weaker coupling strength and blue-shifted gap mode resonance.

8.3.1 Ligand Exchange

Owing to formation of dense and uniform molecular layer on surface, Ligand exchange (or ligand substitution) is one of the most widely used surface modification method, especially for solution dispersed nanocrystals. In plasmonic nanostructures, amine, alkanoic acid, and thiolated molecules are used for surface modification because amino group and carboxylic group have strong electrostatic bonding, and thiol group has strong covalent bonding with surface metal atoms. In the surface modification of metal oxides, phosphates and phosphonates are the most studied ones.[47] For silicon-based materials (Si, SiO_2 etc.), aminosilane and silazane are used for surface modification. In general, molecules with high affinity functional groups have stronger binding with surface atoms and can be used to replace molecules with lower binding energy.

However, if two ligands have similar binding energy on surface, concentration will play an important role during ligand exchange, especially for reversible binding.

8.3.2 Specific Interaction and Non-Specific Interaction

After surface modification, plasmonic nanostructures are surrounded by organic molecules and these surface binding molecules interact with other particles in two ways: i) specific interaction (or specific binding), and ii) non-specific interaction (or non-specific binding). In specific interaction, a molecule (specific binder) interacts with its partner via a defined end state with shape complementarity and stereospecificity. In non-specific interaction, a molecule (non-specific binder) with ill-defined binding interface interacts with another molecule in multiple ways without shape complementarity and stereospecificity.[48] In Chapter 5, we designed a PBDE sensor using alkanethiol functionalized plasmonic metasurface. Because both alkanethiol and PBDE are hydrophobic, PBDE molecules are more favorable to bind on the metasurface rather than dissolve in water solution. This hydrophobic interaction between alkanethiol and PBDE is non-specific, which means other hydrophobic molecules like fluorocarbon can also bind on the alkanethiol functionalized surface. Biotin-streptavidin affinity is a well-known specific interaction system. Based on specific binding between streptavidin and biotin-labeled N-gene probe, Song et. al. developed a COVID-19 nucleic acid detection platform.[49] Therefore, surface modification provides us an appropriate way to manipulate specific interaction and non-specific interaction, and realize the technological application from device-level engineering.

8.4 Stage 3: Microfabrication

Microfabrication is the bridge between sub-micron scale meta-atoms and wafer-scale metasurface platforms. Because the Total Fabrication aims for cost-efficient and industrial-scale production of plasmonic metasurface platforms, in addition to performance in technological applications, a lot of other metrics such as cost, throughput, yield, and safety (toxicity) need to be considered and balanced. Owing to more than four decades experiences in nano-scale device

manufacturing, microfabrication processes in semiconductor industry are well-developed and ready to use. In this dissertation (Chapter 6), we used soft-imprint method inspired by nanoimprint lithography (NIL) and developed the Total Fabrication for wafer-scale plasmonic platforms. In the future, other microfabrication processes such as templating, and masking and etching can also be integrated into the Total Fabrication, lead to lower cost, higher resolution, better uniformity, and more technological applications.

8.4.1 Nanoimprint Lithography

Nanoimprint Lithography is a low cost, high resolution, high throughput microfabrication process for nanoscale patterning. In general, an inverse patterned stamp (or template) is used to mechanically deform the monomer or polymer imprint resist, followed by UV or heat curing. UV or heat induced reaction generate covalent bonds and form solid state nanostructures. After curing, stamp is released from the nanostructures and recycled for another imprinting. In soft-imprint, poly(dimethylsiloxane) (PDMS) is the most demonstrated stamp material.[50] Take the advantage of flexible elastomer, soft stamp can deform around contaminated particles and avoid damage to the stamp. The major challenge in soft stamp is limited resolution because nanometer-scale elastomer features collapse under influence of surface tension.[51,52] To replicate high resolution features below 10 nm, Kumar et. al. developed nanomould with amorphous metal.[53] The major challenge in this rigid stamp is lack of local deformation and particle contamination induced stamp damage. To make a balance between resolution and local deformation, Verschuuren developed a nanoimprint method using composite stamp, named as Substrate Conformal Imprint Lithography (SCIL).[54] In this composite stamp, high Young's modulus PDMS (X-PDMS) is used to fabricate nanometer-scale features, low Young's modulus PDMS is used for supporting layer, and 150 – 200 micron thick glass is used for substrate. Owing to balance between resolution and local deformation, SCIL stamp has demonstrated replication of nanometer-scale structures and 100 – 1000 cycles lifetime.

8.4.2 Templating, Masking and Etching

In addition to NIL, templating, masking and etching are the most widely used microfabrication processes in semiconductor industry. By integrating these processes with colloidal nanocrystal assembly, large-scale high-resolution patterns have been created.[55] Recently, Schulevitz et.al. fabricated millimeter-scale area nanodiamond array with template-assisted self-assembly method.[56] First, electron-beam lithography is used to fabricate PMMA templates with periodic holes, and then home-built apparatus is used to deposit aqueous nanodiamond dispersion and let them assemble in template. Keller et. al. developed a masking and etching process with self-assembled GdF_3 nanocrystal monolayer.[57] GdF_3 nanocrystals SAM are transferred from air-water interface to SiO_2/Si substrate and form a patterned mask. Then, CF_4/O_2 ICP RIE is used to etch SiO_2 layer between nanocrystals and Cl_2/Ar ICP RIE is used to etch underlayer Si and form patterned nanostructures. Finally, GdF_3 nanocrystals are lift-off via HF wet etch on SiO_2 layer. In the future, multi-step microfabrication process can be developed for more complex heterostructure and enable more possibilities in technological applications.

8.5 Stage 2: Programmable Assembly of Meta-Atoms

Except for plasmon-plasmon coupling, most of the plasmon-quasiparticle coupling and plasmon-particle interactions are based on two different types of nanocrystals. Therefore, heterogeneous meta-atom consisting of two particles with different composition is desired. To achieve large-scale and uniform heterogeneous meta-atoms, two programmable assembly methods have been developed: i) binary nanoparticle superlattice and ii) DNA-mediated self-assembly.

8.5.1 binary nanoparticle superlattice

In a mixture with two different sized spheres, the superlattice growth depends on the size ratio between two spheres.[58] In theoretical calculation, binary superlattice assembly can be driven by entropy alone without interparticle interactions and only a few binary superlattices are thermodynamically stable.[59,60] However, in experimental practice, Schevchenko et. al. fabricated

various superlattices using different combination of metal particles, semiconductor particles and metal oxide nanoparticles.[61] Because the packing density of these binary superlattices is lower than FCC close packing, the main driving force in assembly is not entropy. Also, because these binary superlattices have lower packing density than single component superlattices, van der Waals, steric or dipolar interactions between particles do not play an important role. In this case, opposite surface charge induced Coulomb energy difference is the driving force in binary superlattice growth and determines the stoichiometry. To achieve broad range tunability, they also demonstrated that adding surfactant molecules like carboxylic acid and alkyl-phosphine oxide can alter the surface charge and superlattice structure. Moreover, nanoparticles with different shapes, such as triangular nanoplate and spherical nanoparticles, can also be used to grow binary superlattices.

8.5.2 DNA mediated self-assembly

Owing to selective affinity and strong hydrogen in DNA hybridization, DNA mediate self-assembly can be used to build-up well-arranged nanostructures.[62] Recently, Xiong et. al. developed a molecular stamping method to transfer multiple tyles of DNA sequences on nanoparticle surface and form anisotropic patterning.[63] Taking the advantage of distinctive affinities between different DNA sequences, functionalized nanoparticles can selectively bond with quantum dots, and form complex heterogeneous nanoclusters. In general, DNA mediate self-assembly has three major advantages: i) because DNA sequence and size are programmable, interparticle interaction is selective and interparticle distance is tunable,[63,64] ii) because DNA hybridization is sensitive to temperature, self-assembled nanostructures can be dynamically controlled[65,66], iii) because DNA origami can build any desired architectures, self-assembled nanostructures have great tunability in 2D and 3D organizations.[67–69] Owing to significant progress in large-scale DNA self-assembly[70,71] and biotechnological mass production of DNA origami[72], DNA mediated self-assembly is a good fit for the Total Fabrication.

8.6 Stage 1: Colloidal Nanoparticle Synthesis

In the Total Fabrication, colloidal nanoparticle synthesis is the prerequisite of other stages. Nanoparticles size and shape play a significant role in self-assembly (stage 2), nanoparticles polydispersity affects the microfabrication process (stage 3), nanoparticles surface chemistry determines the surface modification (stage 4, and nanoparticles composition controls the function of light-matter interaction (stage 5). Therefore, a precise control on nanoparticles size, shape, uniformity, surface chemistry, and composition during colloidal synthesis is important for the success in the Total Fabrication.

8.6.1 Heterogeneous nanoparticles

Although heterogeneous meta-atoms are good candidates for light-matter interaction, owing to few nanometers thick and insulating surfactant layer, direct charge transport and energy transfer between nanoparticles are nearly negligible.[73] To achieve lower interface barrier and more efficient energy transport between different components, heterogeneous nanoparticles are focused. Core-shell nanoparticles[74] are the most well-known heterostructure in colloidal synthesis and there are three approaches to synthesize them: i) epitaxial growth method, (ii) ion exchange method, iii) multi-step method. In the epitaxial growth approach, core nanoparticles are synthesized and redispersed in a solution containing shell precursor. Then, mild reduction agent is added to reduce shell precursor and epitaxially grow on the core particles to form core-shell structure.[75] In the ion exchange approach, shell precursor and ligands are introduced to template nanoparticles consisting of core materials, Then, ligand coordination can extra core material out and shell material are more favorable to replace the vacancies to form core-shell structure. The extent of ion exchange (volumetric ratio between core and shell) is determined by ligand coordination strength and concentration.[76] Multistep approach is used for heterostructures with large lattice constant and composition difference between core and shell, such as Au/CdS core-shell nanocrystals.[73] First, epitaxial growth is used to grow Au/Ag core-shell structure. Then, sulfur-oleylamine complex is introduced and reacted with Ag shell, to form Au/Ag_2S core-shell

structure. Finally, Cd precursor is added and replace Ag atom via ion exchange, lead to Au/CdS core-shell structure. Owing to unique properties in heterogeneous nanoparticles, they have been widely used in a lot of technological applications, including plasmonic catalysis[38], photothermal therapy[77], photoluminescence[78], and biomedical applications[79].

8.6.2 Shape control and 2D materials

Owing to large surface to volume ratio, nanoparticle geometry is directly related to its properties. In plasmonic nanoparticles, the geometry determines both resonance features (frequency, linewidth, extinction cross-section etc.)[80,81] and energy transfer path[82], and impact the device level performance. Although both size and shape are the dominant factors in nanoparticles geometry and resulted properties, the shape control is more focused because size can be easily controlled via tuning reactant concentration, reaction time, and temperature. In colloidal synthesis, shape control is achieved by manipulating surface energy which is defined as the excess free energy per unit area for a particular crystallographic face and plays the dominate role in crystal growth and faceting. Owing to selective binding preference between different crystal planes, molecules such as surfactant, polymers, biomolecules, adsorbed gas, and atomic species (metal ions) can be used to control the surface energy, lead to a selective growth and shape control.[83]

In addition to mechanical exfoliation[84,85] and CVD epitaxial growth[86], colloidal synthesis of 2D materials is focused on the past decade and two synthesis methods are designed. Huang et. al. developed a surfactant directed soft-templating method to synthesis colloidal Au square sheet.[87] First, Au^{+} complexed with 1-amino-9-octadecne absorbed on graphene oxide (GO) surface and form a self-assembled organic layer. Then, Au+ are reduced to Au atom via increasing temperature, lead to the formation of 2D Au square sheet. Huang et. al. developed a CO-confined growth method to prepare colloidal palladium nanosheets.[88] Strong CO adsorption on the basal (111) plane of palladium nanosheet prevent overgrowth along [111] direction and result in the anisotropic 2D nanosheet. Owing to unique properties in 2D materials and flexible processing in colloidal solution, colloidal synthesized 2D materials can open up new avenues via

the Total fabrication. Solution-based exfoliation is an alternative method for large-scale production 2D colloidal nanomaterials.[89] However, owing to large polydispersity in size, shape, and thickness, exfoliated 2D nanomaterials have more challenges on the other stages of the Total Fabrication.

8.7 Conclusion

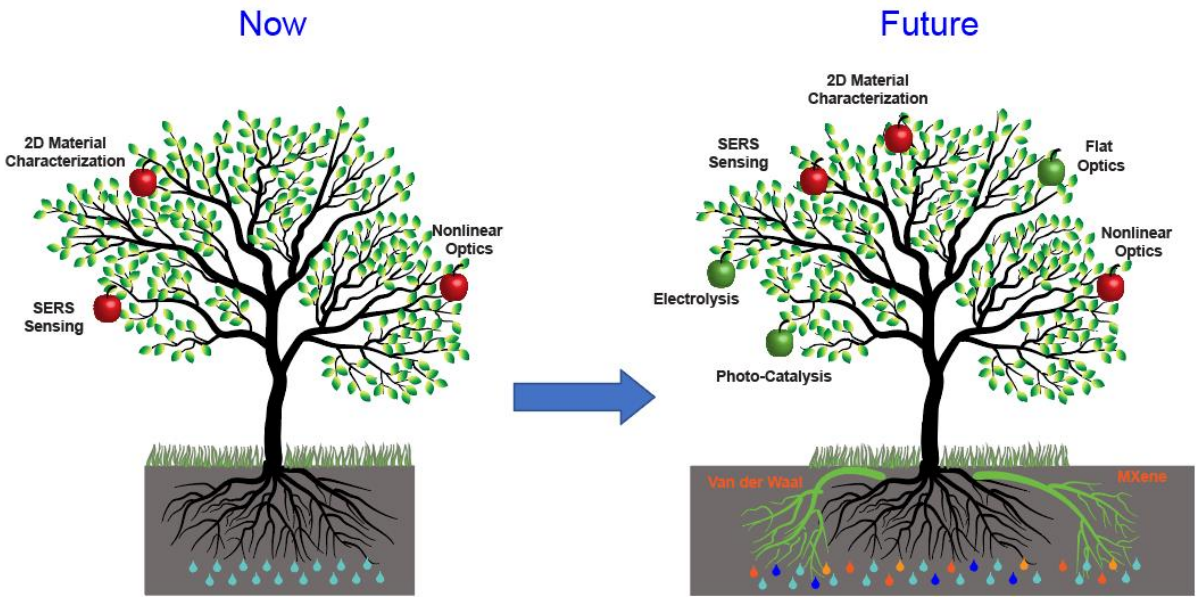

Figure 8.6 | Future possibilities in the Total Fabrication of plasmonic platforms

In conclusion, we developed a cost-efficient fabrication process to build-up wafer-scale plasmonic metasurface platforms, from simple and commercially available precursors. Because this concept is similar to the “Total Synthesis” in organic chemistry, we named it as the “Total Fabrication”. Then, we performed a device-level engineering with these plasmonic metasurface platforms and used them for different applications, including optical second harmonic generation (nonlinear optics), 2D materials characterization and SERS sensing of pollutant PBDE molecules. Owing to great tunability on each stage of Total Fabrication, we are able to customize the Total Fabrication and open up more possibility in the future, such as flat optics, plasmonic catalysis, electrolysis etc. (Figure 8.6) To improve the efficiency of Total Fabrication development, we proposed a reverse engineering process from device level (stage 5) back to precursors (stage 0). In device level engineering (stage 5), plasmon-particle and/or plasmon-quasiparticle can be

manipulated and enable different applications. In surface modification stage (stage 4), plasmonic metasurface platform can be functionalized with electrostatic binding (amine-group, carboxyl group) or covalent binding (thiol-group) molecules. By engineering interaction between surface binding molecules and external nanomaterials, such as hydrophobic interaction, biotin-streptavidin interaction etc., this plasmonic metasurface platform can meet the requirements from device level engineering. In microfabrication (stage 3), substrate conformal imprint and lithography can be used to optimize the soft-imprint method we used. Also, by integrating other microfabrication processes, such as templating, masking, and etching, uniformity and quality can be improved significantly. In self-assembly (stage 2), binary nanoparticle superlattices and DNA mediated self-assembly enable the design of complex hybrid plasmonic metasurface and open new opportunities for applications. In colloidal synthesis (stage 1), manipulation in reaction parameters (reactant, surfactant, temperature, temperature etc.) can control the size, shape, structure, and composition of nanoparticles, and provide the required nanomaterials for self-assembly. Also, owing to sub-micron scale thickness in our wafer-scale plasmonic metasurface platform, we believe hybridization of nanoparticle and 2D van der Waals materials / Mxenes is an interesting topic. Furthermore, by alternating the precursors, the Total Fabrication can be used in fields beyond plasmonic. For example, cadmium-based and chalcogenide-based precursors can be used for total fabrication of photonic device, and transition metal precursors (Pt, Pd, Ru etc.) can be used for total fabrication of catalysis devices. In the next decade, we expect the Total Fabrication can make a significant contribution in the lab-to-fab journey of nanomaterials.

References

(1) Mohapatra, R. N. Particles as Building Blocks of Matter. *Neutrino Story One Tiny Part. Gd. Role Cosm.* **2021**, 7–20. https://doi.org/10.1007/978-3-030-51846-2_2.

(2) Mühlbauer, S.; Binz, B.; Jonietz, F.; Pfleiderer, C.; Rosch, A.; Neubauer, A.; Georgii, R.; Böni, P. Skyrmion Lattice in a Chiral Magnet. *Science (80-.).* **2009**, *323* (5916), 915–919. https://doi.org/10.1126/SCIENCE.1166767/SUPPL_FILE/MUEHLBAUER.SOM.PDF.

(3) Ultracold atoms permit direct observation of quasiparticle dynamics – Physics World https://physicsworld.com/a/ultracold-atoms-permit-direct-observation-of-quasiparticle-dynamics/ (accessed May 20, 2022).

(4) Braibant, Sylvie and Giacomelli, G. and S.; Maurizio. *Particles and Fundamental Interactions: An Introduction to Particle Physics*; Springer, 2012.

(5) Zhang, Y.; Zhen, Y. R.; Neumann, O.; Day, J. K.; Nordlander, P.; Halas, N. J. Coherent Anti-Stokes Raman Scattering with Single-Molecule Sensitivity Using a Plasmonic Fano Resonance. *Nat. Commun. 2014 51* **2014**, *5* (1), 1–7. https://doi.org/10.1038/ncomms5424.

(6) Tabor, C.; Murali, R.; Mahmoud; El-Sayed, M. A. On the Use of Plasmonic Nanoparticle Pairs as a Plasmon Ruler: The Dependence of the near-Field Dipole Plasmon Coupling on Nanoparticle Size and Shape. *J. Phys. Chem. A* **2009**, *113* (10), 1946–1953. https://doi.org/10.1021/JP807904S/SUPPL_FILE/JP807904S_SI_001.PDF.

(7) Hooshmand, N.; El-Sayed, M. A. Collective Multipole Oscillations Direct the Plasmonic Coupling at the Nanojunction Interfaces. *Proc. Natl. Acad. Sci. U. S. A.* **2019**, *116* (39), 19299–19304. https://doi.org/10.1073/PNAS.1909416116.

(8) Rechberger, W.; Hohenau, A.; Leitner, A.; Krenn, J. R.; Lamprecht, B.; Aussenegg, F. R. Optical Properties of Two Interacting Gold Nanoparticles. *Opt. Commun.* **2003**, *220* (1–3), 137–141. https://doi.org/10.1016/S0030-4018(03)01357-9.

(9) Zuloaga, J.; Prodan, E.; Nordlander, P. Quantum Description of the Plasmon Resonances of a Nanoparticle Dimer. *Nano Lett.* **2009**, *9* (2), 887–891. https://doi.org/10.1021/nl803811g.

(10) Esteban, R.; Borisov, A. G.; Nordlander, P.; Aizpurua, J. Bridging Quantum and Classical Plasmonics with a Quantum-Corrected Model. *Nat. Commun.* **2012**, *3* (1), 1–9. https://doi.org/10.1038/ncomms1806.

(11) Zeng, Y.; Qian, H.; Rozin, M. J.; Liu, Z.; Tao, A. R. Enhanced Second Harmonic Generation in Double-Resonance Colloidal Metasurfaces. *Adv. Funct. Mater.* **2018**, *28* (51), 1803019. https://doi.org/10.1002/ADFM.201803019.

(12) Davis, T. J.; Hentschel, M.; Liu, N.; Giessen, H. Analytical Model of the Three-Dimensional Plasmonic Ruler. *ACS Nano* **2012**, *6* (2), 1291–1298. https://doi.org/10.1021/NN204029P/ASSET/IMAGES/NN-2011-04029P_M013.GIF.

(13) Zhou, Z. K.; Liu, J.; Bao, Y.; Wu, L.; Png, C. E.; Wang, X. H.; Qiu, C. W. Quantum Plasmonics Get Applied. *Prog. Quantum Electron.* **2019**, *65*, 1–20. https://doi.org/10.1016/J.PQUANTELEC.2019.04.002.

(14) Hou, S.; Tobing, L. Y. M.; Wang, X.; Xie, Z.; Yu, J.; Zhou, J.; Zhang, D.; Dang, C.; Coquet, P.; Tay, B. K.; Birowosuto, M. D.; Teo, E. H. T.; Wang, H. Manipulating Coherent Light–Matter Interaction: Continuous Transition between Strong Coupling and Weak Coupling in MoS2 Monolayer Coupled with Plasmonic Nanocavities. *Adv. Opt. Mater.* **2019**, *7* (22), 1900857. https://doi.org/10.1002/ADOM.201900857.

(15) Wen, J.; Wang, H.; Wang, W.; Deng, Z.; Zhuang, C.; Zhang, Y.; Liu, F.; She, J.; Chen, J.; Chen, H.; Deng, S.; Xu, N. Roomerature Strong Light-Matter Interaction with Active Control in Single Plasmonic Nanorod Coupled with Two-Dimensional Atomic Crystals. *Nano Lett.* **2017**, *17* (8), 4689–4697. https://doi.org/10.1021/ACS.NANOLETT.7B01344/ASSET/IMAGES/LARGE/NL-2017-01344E_0004.JPEG.

(16) Geisler, M.; Cui, X.; Wang, J.; Rindzevicius, T.; Gammelgaard, L.; Jessen, B. S.; Gonçalves, P. A. D.; Todisco, F.; Bøggild, P.; Boisen, A.; Wubs, M.; Mortensen, N. A.; Xiao, S.; Stenger, N. Single-Crystalline Gold Nanodisks on WS 2 Mono- and Multilayers for Strong Coupling at Room Temperature. *ACS Photonics* **2019**, *6* (4), 994–1001. https://doi.org/10.1021/ACSPHOTONICS.8B01766/ASSET/IMAGES/LARGE/PH-2018-01766G_0005.JPEG.

(17) Han, X.; Wang, K.; Xing, X.; Wang, M.; Lu, P. Rabi Splitting in a Plasmonic Nanocavity Coupled to a WS2 Monolayer at Room Temperature. *ACS Photonics* **2018**, *5* (10), 3970–3976. https://doi.org/10.1021/ACSPHOTONICS.8B00931/ASSET/IMAGES/LARGE/PH-2018-00931X_0004.JPEG.

(18) Cuadra, J.; Baranov, D. G.; Wersäll, M.; Verre, R.; Antosiewicz, T. J.; Shegai, T. Observation of Tunable Charged Exciton Polaritons in Hybrid Monolayer WS2-Plasmonic Nanoantenna System. *Nano Lett.* **2018**, *18* (3), 1777–1785. https://doi.org/10.1021/ACS.NANOLETT.7B04965/ASSET/IMAGES/MEDIUM/NL-2017-049652_M004.GIF.

(19) Stührenberg, M.; Munkhbat, B.; Baranov, D. G.; Cuadra, J.; Yankovich, A. B.; Antosiewicz, T. J.; Olsson, E.; Shegai, T. Strong Light-Matter Coupling between Plasmons in Individual Gold Bi-Pyramids and Excitons in Mono- and Multilayer WSe2. *Nano Lett.* **2018**, *18* (9), 5938–5945. https://doi.org/10.1021/ACS.NANOLETT.8B02652/ASSET/IMAGES/MEDIUM/NL-2018-026529_M006.GIF.

(20) Sun, J.; Li, Y.; Hu, H.; Chen, W.; Zheng, D.; Zhang, S.; Xu, H. Strong Plasmon–Exciton Coupling in Transition Metal Dichalcogenides and Plasmonic Nanostructures. *Nanoscale* **2021**, *13* (8), 4408–4419. https://doi.org/10.1039/D0NR08592H.

(21) Cao, E.; Lin, W.; Sun, M.; Liang, W.; Song, Y. Exciton-Plasmon Coupling Interactions: From Principle to Applications. *Nanophotonics* **2018**, *7* (1), 145–167. https://doi.org/10.1515/NANOPH-2017-0059/ASSET/GRAPHIC/J_NANOPH-2017-0059_FIG_002.JPG.

(22) Jablan, M.; Soljačić, M.; Buljan, H. Unconventional Plasmon-Phonon Coupling in Graphene. *Phys. Rev. B - Condens. Matter Mater. Phys.* **2011**, *83* (16), 161409. https://doi.org/10.1103/PHYSREVB.83.161409/FIGURES/3/MEDIUM.

(23) Kukharskii, A. A. Plasmon-Phonon Coupling in GaAs. *Solid State Commun.* **1973**, *13* (11), 1761–1765. https://doi.org/10.1016/0038-1098(73)90724-2.

(24) Yoo, D.; de León-Pérez, F.; Pelton, M.; Lee, I. H.; Mohr, D. A.; Raschke, M. B.; Caldwell, J. D.; Martín-Moreno, L.; Oh, S. H. Ultrastrong Plasmon–Phonon Coupling via Epsilon-near-Zero Nanocavities. *Nat. Photonics 2020 152* **2020**, *15* (2), 125–130.

https://doi.org/10.1038/s41566-020-00731-5.

(25) Huber, A.; Ocelic, N.; Taubner, T.; Hillenbrand, R. Nanoscale Resolved Infrared Probing of Crystal Structure and of Plasmon-Phonon Coupling. *Nano Lett.* **2006**, *6* (4), 774–778. https://doi.org/10.1021/NL060092B/ASSET/IMAGES/LARGE/NL060092BF00003.JPEG.

(26) Lakowicz, J. R. Plasmonics in Biology and Plasmon-Controlled Fluorescence. *Plasmon. 2006 11* **2006**, *1* (1), 5–33. https://doi.org/10.1007/S11468-005-9002-3.

(27) Haran, G.; Chuntonov, L. Artificial Plasmonic Molecules and Their Interaction with Real Molecules. *Chem. Rev.* **2018**, *118* (11), 5539–5580. https://doi.org/10.1021/ACS.CHEMREV.7B00647/ASSET/IMAGES/MEDIUM/CR-2017-00647X_M011.GIF.

(28) Roelli, P.; Galland, C.; Piro, N.; Kippenberg, T. J. Molecular Cavity Optomechanics as a Theory of Plasmon-Enhanced Raman Scattering. *Nat. Nanotechnol. 2015 112* **2015**, *11* (2), 164–169. https://doi.org/10.1038/nnano.2015.264.

(29) Zhao, J.; Jensen, L.; Sung, J.; Zou, S.; Schatz, G. C.; Van Duyne, R. P. Interaction of Plasmon and Molecular Resonances for Rhodamine 6G Adsorbed on Silver Nanoparticles. *J. Am. Chem. Soc.* **2007**, *129* (24), 7647–7656. https://doi.org/10.1021/JA0707106/SUPPL_FILE/JA0707106SI20070404_010259.PDF.

(30) Chen, H.; Ming, T.; Zhao, L.; Wang, F.; Sun, L.-D.; Wang, J.; Yan, C.-H. Plasmon-Molecule Interactions. *Nano Today* **2010**, *5*, 494–505. https://doi.org/10.1016/j.nantod.2010.08.009.

(31) Anger, P.; Bharadwaj, P.; Novotny, L. Enhancement and Quenching of Single-Molecule Fluorescence. *Phys. Rev. Lett.* **2006**, *96* (11), 113002. https://doi.org/10.1103/PHYSREVLETT.96.113002/FIGURES/4/MEDIUM.

(32) Kano, H.; Kawata, S. Two-Photon-Excited Fluorescence Enhanced by a Surface Plasmon. *Opt. Lett. Vol. 21, Issue 22, pp. 1848-1850* **1996**, *21* (22), 1848–1850. https://doi.org/10.1364/OL.21.001848.

(33) Wang, T.; Halaney, D.; Ho, D.; Feldman, M. D.; Milner, T. E.; Roger, V. L.; Go, A. S.; Lloyd-Jones, D. M.; Adams, R. J.; Berry, J. D.; Brown, T. M.; Carnethon, M. R.; Dai, S.; de Simone, G.; Ford, E. S.; Fox, C. S.; Fullerton, H. J.; Gillespie, C.; Greenlund, K. J.; Hailpern, S. M.; Heit, J. A.; Ho, P. M.; Howard, V. J.; Kissela, B. M.; Kittner, S. J.; Lackland, D. T.; Lichtman, J. H.; Lisabeth, L. D.; Makuc, D. M.; Marcus, G. M.; Marelli, A.; Matchar, D. B.; McDermott, M. M.; Meigs, J. B.; Moy, C. S.; Mozaffarian, D.; Mussolino, M. E.; Nichol, G.; Paynter, N. P.; Rosamond, W. D.; Sorlie, P. D.; Stafford, R. S.; Turan, T. N.; Turner, M. B.; Wong, N. D.; Wylie-Rosett, J.; Kolodgie, F. D.; Virmani, R.; Burke, A. P.; Farb, A.; Weber, D. K.; Kutys, R.; Finn, A. V; Gold, H. K.; Chaudhary, M.; Basu, A.; Bhonde, R. R.; Sastry, M.; Ji, X.; Shao, R.; Elliott, A. M.; Stafford, R. J.; Esparza-Coss, E.; Bankson, J. A.; Liang, G.; Luo, Z.; Park, K.; Markert, J. T.; Li, C.; Au, L.; Lu, X.; Li, X.; Xia, Y.; Ma, L. L.; Feldman, M. D.; Tam, J. M.; Paranjape, A. S.; Cheruku, K. K.; Larson, T. A.; Tam, J. O.; Ingram, D. R.; Paramita, V.; Villard, J. W.; Jenkins, J. T.; Wang, T.; Clarke, G. D.; Asmis, R.; Sokolov, K.; Chandrasekar, B.; Milner, T. E.; Johnston, K. P.; Mancuso, J. J.; Kazmi, S. M.; Dwelle, J.; Sapozhnikova, V.; Willsey, B.; Qiu, J.; Dunn, A. K. Two-Photon Luminescence Properties of Gold Nanorods. *Biomed. Opt. Express, Vol. 4, Issue 4, pp. 584-595* **2013**, *4* (4), 584–595. https://doi.org/10.1364/BOE.4.000584.

(34) Li, X.; Xiao, D.; Zhang, Z. Landau Damping of Quantum Plasmons in Metal Nanostructures. *New J. Phys.* **2013**, *15* (2), 023011. https://doi.org/10.1088/1367-2630/15/2/023011.

(35) Linic, S.; Chavez, S.; Elias, R. Flow and Extraction of Energy and Charge Carriers in Hybrid Plasmonic Nanostructures. *Nat. Mater. 2021 207* **2021**, *20* (7), 916–924. https://doi.org/10.1038/s41563-020-00858-4.

(36) Brongersma, M. L.; Halas, N. J.; Nordlander, P. Plasmon-Induced Hot Carrier Science and Technology. *Nat. Nanotechnol. 2015 101* **2015**, *10* (1), 25–34. https://doi.org/10.1038/nnano.2014.311.

(37) Aslam, U.; Rao, V. G.; Chavez, S.; Linic, S. Catalytic Conversion of Solar to Chemical Energy on Plasmonic Metal Nanostructures. *Nat. Catal. 2018 19* **2018**, *1* (9), 656–665. https://doi.org/10.1038/s41929-018-0138-x.

(38) Aslam, U.; Chavez, S.; Linic, S. Controlling Energy Flow in Multimetallic Nanostructures for Plasmonic Catalysis. *Nat. Nanotechnol. 2017 1210* **2017**, *12* (10), 1000–1005. https://doi.org/10.1038/nnano.2017.131.

(39) Zhou, L.; Martirez, J. M. P.; Finzel, J.; Zhang, C.; Swearer, D. F.; Tian, S.; Robatjazi, H.; Lou, M.; Dong, L.; Henderson, L.; Christopher, P.; Carter, E. A.; Nordlander, P.; Halas, N. J. Light-Driven Methane Dry Reforming with Single Atomic Site Antenna-Reactor Plasmonic Photocatalysts. *Nat. Energy 2020 51* **2020**, *5* (1), 61–70. https://doi.org/10.1038/s41560-019-0517-9.

(40) Guselnikova, O.; Audran, G.; Joly, J. P.; Trelin, A.; Tretyakov, E. V.; Svorcik, V.; Lyutakov, O.; Marque, S. R. A.; Postnikov, P. Establishing Plasmon Contribution to Chemical Reactions: Alkoxyamines as a Thermal Probe. *Chem. Sci.* **2021**, *12* (11), 4154–4161. https://doi.org/10.1039/D0SC06470J.

(41) Lapshin, R. V.; Alekhin, A. P.; Kirilenko, A. G.; Odintsov, S. L.; Krotkov, V. A. Vacuum Ultraviolet Smoothing of Nanometer-Scale Asperities of Poly(Methyl Methacrylate) Surface. *J. Surf. Investig. X-ray, Synchrotron Neutron Tech. 2010 41* **2010**, *4* (1), 1–11. https://doi.org/10.1134/S1027451010010015.

(42) Jiang, X.; Lai, Y.; Wang, W.; Jiang, W.; Zhan, J. Surface-Enhanced Raman Spectroscopy Detection of Polybrominated Diphenylethers Using a Portable Raman Spectrometer. *Talanta* **2013**, *116*, 14–17. https://doi.org/10.1016/j.talanta.2013.04.056.

(43) Bertazzo, S.; Rezwan, K. Control of α-Alumina Surface Charge with Carboxylic Acids. *Langmuir* **2010**, *26* (5), 3364–3371. https://doi.org/10.1021/LA903140K/SUPPL_FILE/LA903140K_SI_005.PDF.

(44) Vudayagiri, S.; Junker, M. D.; Skov, A. L. Factors Affecting the Surface and Release Properties of Thin Polydimethylsiloxane Films. *Polym. J. 2013 458* **2013**, *45* (8), 871–878. https://doi.org/10.1038/pj.2012.227.

(45) Fadeev, A. Y.; McCarthy, T. J. Surface Modification of Poly(Ethylene Terephthalate) to Prepare Surfaces with Silica-like Reactivity. *Langmuir* **1998**, *14* (19), 5586–5593. https://doi.org/10.1021/LA980512F/ASSET/IMAGES/LARGE/LA980512FF00004.JPEG.

(46) Benz, F.; Tserkezis, C.; Herrmann, L. O.; De Nijs, B.; Sanders, A.; Sigle, D. O.; Pukenas, L.; Evans, S. D.; Aizpurua, J.; Baumberg, J. J. Nanooptics of Molecular-Shunted Plasmonic Nanojunctions. *Nano Lett.* **2015**, *15* (1), 669–674. https://doi.org/10.1021/nl5041786.

(47) Yildirim, O.; Gang, T.; Kinge, S.; Reinhoudt, D. N.; Blank, D. H. A.; van der Wiel, W. G.; Rijnders, G.; Huskens, J. Monolayer-Directed Assembly and Magnetic Properties of FePt Nanoparticles on Patterned Aluminum Oxide. *Int. J. Mol. Sci. 2010, Vol. 11, Pages 1162-1179* **2010**, *11* (3), 1162–1179. https://doi.org/10.3390/IIJMS11031162.

(48) Frutiger, A.; Tanno, A.; Hwu, S.; Tiefenauer, R. F.; Vörös, J.; Nakatsuka, N. Nonspecific Binding - Fundamental Concepts and Consequences for Biosensing Applications. *Chem. Rev.* **2021**, *121* (13), 8095–8160. https://doi.org/10.1021/ACS.CHEMREV.1C00044/ASSET/IMAGES/MEDIUM/CR1C00044_M057.GIF.

(49) Song, Z.; Ma, Y.; Chen, M.; Ambrosi, A.; Ding, C.; Luo, X. Electrochemical Biosensor with Enhanced Antifouling Capability for COVID-19 Nucleic Acid Detection in Complex Biological Media. *Anal. Chem.* **2021**, *93* (14), 5963–5971. https://doi.org/10.1021/ACS.ANALCHEM.1C00724/ASSET/IMAGES/LARGE/AC1C00724_0006.JPEG.

(50) Xia, Y.; Whitesides, G. M. SOFT LITHOGRAPHY. *http://dx.doi.org/10.1146/annurev.matsci.28.1.153* **2003**, *28* (1), 153–184. https://doi.org/10.1146/ANNUREV.MATSCI.28.1.153.

(51) Nistor, C.; van Landuyt, J.; Barton, J. D.; Hole, D. E.; Skelland, N. D.; Townsend, P. D.; Arnold, G. W.; Battaglin, C.; Beroncello, R.; Cattaruz-za, E.; Mattei, G.; Mazzoldi, P.; Trivillin, E.; Mennig, M.; Spanhel, J.; Schmidt, H.; Betzholz, S.; Liciulli, A.; Massaro, C.; Tapfer, L.; Catalano, M.; Battaglin, G.; Meneghini, C.; Biebuyck, H.; Delamarche Schmid B Michel, E. H.; Emmanuel Delamarche, B.; Schmid, H.; Michel, B.; Biebuyck, H. Stability of Molded Polydimethylsiloxane Microstructures. *Adv. Mater.* **1997**, *9* (9), 741–746. https://doi.org/10.1002/ADMA.19970090914.

(52) Hui, C. Y.; Jagota, A.; Lin, Y. Y.; Kramer, E. J. Constraints on Microcontact Printing Imposed by Stamp Deformation. *Langmuir* **2002**, *18* (4), 1394–1407. https://doi.org/10.1021/LA0113567/ASSET/IMAGES/MEDIUM/LA0113567E00070.GIF.

(53) Kumar, G.; Tang, H. X.; Schroers, J. Nanomoulding with Amorphous Metals. *Nat. 2009 4577231* **2009**, *457* (7231), 868–872. https://doi.org/10.1038/nature07718.

(54) Substrate conformal imprint lithography for nanophotonics - NASA/ADS https://ui.adsabs.harvard.edu/abs/2010PhDT.....81V/abstract (accessed May 22, 2022).

(55) Greybush, N. J.; Saboktakin, M.; Ye, X.; Della Giovampaola, C.; Oh, S. J.; Berry, N. E.; Engheta, N.; Murray, C. B.; Kagan, C. R. Plasmon-Enhanced Upconversion Luminescence in Single Nanophosphor-Nanorod Heterodimers Formed through Template-Assisted Self-Assembly. *ACS Nano* **2014**, *8* (9), 9482–9491. https://doi.org/10.1021/NN503675A/SUPPL_FILE/NN503675A_SI_001.PDF.

(56) Shulevitz, H. J.; Huang, T. Y.; Xu, J.; Neuhaus, S. J.; Patel, R. N.; Choi, Y. C.; Bassett, L. C.; Kagan, C. R. Template-Assisted Self-Assembly of Fluorescent Nanodiamonds for

Scalable Quantum Technologies. *ACS Nano* **2022**, *16* (2), 1847–1856. https://doi.org/10.1021/ACSNANO.1C09839/SUPPL_FILE/NN1C09839_SI_001.PDF.

(57) Keller, A. W.; Marino, E.; An, D.; Neuhaus, S. J.; Elbert, K. C.; Murray, C. B.; Kagan, C. R. Sub-5 Nm Anisotropic Pattern Transfer via Colloidal Lithography of a Self-Assembled GdF3Nanocrystal Monolayer. *Nano Lett.* **2022**, *22* (5), 1992–2000. https://doi.org/10.1021/ACS.NANOLETT.1C04761/ASSET/IMAGES/LARGE/NL1C04761_0004.JPEG.

(58) Murray, M. J.; Sanders, J. V. Close-Packed Structures of Spheres of Two Different Sizes II. The Packing Densities of Likely Arrangements. *http://dx.doi.org/10.1080/01418618008239380* **2006**, *42* (6), 721–740. https://doi.org/10.1080/01418618008239380.

(59) Cottin, X.; Monson, P. A. Substitutionally Ordered Solid Solutions of Hard Spheres. *J. Chem. Phys.* **1998**, *102* (8), 3354. https://doi.org/10.1063/1.469209.

(60) Eldridge, M. D.; Madden, P. A.; Frenkel, D. Entropy-Driven Formation of a Superlattice in a Hard-Sphere Binary Mixture. *Nat. 1993 3656441* **1993**, *365* (6441), 35–37. https://doi.org/10.1038/365035a0.

(61) Shevchenko, E. V.; Talapin, D. V.; Kotov, N. A.; O'Brien, S.; Murray, C. B. Structural Diversity in Binary Nanoparticle Superlattices. *Nat. 2006 4397072* **2006**, *439* (7072), 55–59. https://doi.org/10.1038/nature04414.

(62) Sharma, A.; Vaghasiya, K.; Verma, R. K.; Yadav, A. B. DNA Nanostructures: Chemistry, Self-Assembly, and Applications. *Emerg. Appl. Nanoparticles Archit. Nanostructures Curr. Prospect. Futur. Trends* **2018**, 71–94. https://doi.org/10.1016/B978-0-323-51254-1.00003-8.

(63) Xiong, Y.; Yang, S.; Tian, Y.; Michelson, A.; Xiang, S.; Xin, H.; Gang, O. Three-Dimensional Patterning of Nanoparticles by Molecular Stamping. *ACS Nano* **2020**, *14* (6), 6823–6833. https://doi.org/10.1021/ACSNANO.0C00607/ASSET/IMAGES/MEDIUM/NN0C00607_M022.GIF.

(64) Sun, D.; Tian, Y.; Zhang, Y.; Xu, Z.; Sfeir, M. Y.; Cotlet, M.; Gang, O. Light-Harvesting Nanoparticle Core-Shell Clusters with Controllable Optical Output. *ACS Nano* **2015**, *9* (6), 5657–5665. https://doi.org/10.1021/NN507331Z/SUPPL_FILE/NN507331Z_SI_001.PDF.

(65) Maye, M. M.; Kumara, M. T.; Nykypanchuk, D.; Sherman, W. B.; Gang, O. Switching Binary States of Nanoparticle Superlattices and Dimer Clusters by DNA Strands. *Nat. Nanotechnol. 2010 52* **2009**, *5* (2), 116–120. https://doi.org/10.1038/nnano.2009.378.

(66) Nykypanchuk, D.; Maye, M. M.; Van Der Lelie, D.; Gang, O. DNA-Guided Crystallization of Colloidal Nanoparticles. *Nat. 2008 4517178* **2008**, *451* (7178), 549–552. https://doi.org/10.1038/nature06560.

(67) Tian, Y.; Wang, T.; Liu, W.; Xin, H. L.; Li, H.; Ke, Y.; Shih, W. M.; Gang, O. Prescribed Nanoparticle Cluster Architectures and Low-Dimensional Arrays Built Using Octahedral DNA Origami Frames. *Nat. Nanotechnol. 2015 107* **2015**, *10* (7), 637–644. https://doi.org/10.1038/nnano.2015.105.

(68) Kahn, J. S.; Gang, O. Designer Nanomaterials through Programmable Assembly. *Angew. Chemie* **2022**, *134* (3), e202105678. https://doi.org/10.1002/ANGE.202105678.

(69) Wu, X. R.; Wu, C. W.; Ding, F.; Tian, C.; Jiang, W.; Mao, C. De; Zhang, C. Binary Self-Assembly of Highly Symmetric DNA Nanocages via Sticky-End Engineering. *Chinese Chem. Lett.* **2017**, *28* (4), 851–856. https://doi.org/10.1016/J.CCLET.2017.01.012.

(70) Zhang, F.; Yan, H. DNA Self-Assembly Scaled Up. *Nat. 2021 5527683* **2017**, *552* (7683), 34–35. https://doi.org/10.1038/d41586-017-07690-y.

(71) Yao, G.; Zhang, F.; Wang, F.; Peng, T.; Liu, H.; Poppleton, E.; Šulc, P.; Jiang, S.; Liu, L.; Gong, C.; Jing, X.; Liu, X.; Wang, L.; Liu, Y.; Fan, C.; Yan, H. Meta-DNA Structures. *Nat. Chem. 2020 1211* **2020**, *12* (11), 1067–1075. https://doi.org/10.1038/s41557-020-0539-8.

(72) Praetorius, F.; Kick, B.; Behler, K. L.; Honemann, M. N.; Weuster-Botz, D.; Dietz, H.; Coli, P. E. Biotechnological Mass Production of DNA Origami. *Nat. 2017 5527683* **2017**, *552* (7683), 84–87. https://doi.org/10.1038/nature24650.

(73) Lambright, S.; Butaeva, E.; Razgoniaeva, N.; Hopkins, T.; Smith, B.; Perera, D.; Corbin, J.; Khon, E.; Thomas, R.; Moroz, P.; Mereshchenko, A.; Tarnovsky, A.; Zamkov, M. Enhanced Lifetime of Excitons in Nonepitaxial Au/CdS Core/Shell Nanocrystals. *ACS Nano* **2014**, *8* (1), 352–361. https://doi.org/10.1021/NN404264W/SUPPL_FILE/NN404264W_SI_001.PDF.

(74) Ghosh Chaudhuri, R.; Paria, S. Core/Shell Nanoparticles: Classes, Properties, Synthesis Mechanisms, Characterization, and Applications. *Chem. Rev.* **2012**, *112* (4), 2373–2433. https://doi.org/10.1021/CR100449N/ASSET/IMAGES/LARGE/CR-2010-00449N_0039.JPEG.

(75) Sánchez-Iglesias, A.; Carbó-Argibay, E.; Glaria, A.; Rodríguez-González, B.; Pérez-Juste, J.; Pastoriza-Santos, I.; Liz-Marzán, L. M. Rapid Epitaxial Growth of Ag on Au Nanoparticles: From Au Nanorods to Core–Shell Au@Ag Octahedrons. *Chem. – A Eur. J.* **2010**, *16* (19), 5558–5563. https://doi.org/10.1002/CHEM.201000144.

(76) Zhai, Y.; Shim, M. Cu2S/ZnS Heterostructured Nanorods: Cation Exchange vs. Solution–Liquid–Solid-like Growth. *ChemPhysChem* **2016**, *17* (5), 741–751. https://doi.org/10.1002/CPHC.201500859.

(77) Hosseini, V.; Mirrahimi, M.; Shakeri-Zadeh, A.; Koosha, F.; Ghalandari, B.; Maleki, S.; Komeili, A.; Kamrava, S. K. Multimodal Cancer Cell Therapy Using Au@Fe2O3 Core–Shell Nanoparticles in Combination with Photo-Thermo-Radiotherapy. *Photodiagnosis Photodyn. Ther.* **2018**, *24*, 129–135. https://doi.org/10.1016/J.PDPDT.2018.08.003.

(78) Bang, J.; Park, J.; Lee, J. H.; Won, N.; Nam, J.; Lim, J.; Chang, B. Y.; Lee, H. J.; Chon, B.; Shin, J.; Park, J. B.; Choi, J. H.; Cho, K.; Park, S. M.; Joo, T.; Kim, S. ZnTe/ZnSe (Core/Shell) Type-II Quantum Dots: Their Optical and Photovoltaic Properties. *Chem. Mater.* **2010**, *22* (1), 233–240. https://doi.org/10.1021/CM9027995/SUPPL_FILE/CM9027995_SI_001.PDF.

(79) Chatterjee, K.; Sarkar, S.; Jagajjanani Rao, K.; Paria, S. Core/Shell Nanoparticles in Biomedical Applications. *Adv. Colloid Interface Sci.* **2014**, *209*, 8–39.

https://doi.org/10.1016/J.CIS.2013.12.008.

(80) Langhammer, C.; Yuan, Z.; Zorić, I.; Kasemo, B. Plasmonic Properties of Supported Pt and Pd Nanostructures. *Nano Lett.* **2006**, *6* (4), 833–838. https://doi.org/10.1021/NL060219X/ASSET/IMAGES/LARGE/NL060219XF00004.JPEG.

(81) Zhuang, Y.; Liu, L.; Wu, X.; Tian, Y.; Zhou, X.; Xu, S.; Xie, Z.; Ma, Y.; Zhuang, Y.; Liu, L.; Wu, X.; Zhou, X.; Xie, Z.; Ma, Y.; Tian, Y.; Xu, S. Size and Shape Effect of Gold Nanoparticles in “Far-Field” Surface Plasmon Resonance. *Part. Part. Syst. Charact.* **2019**, *36* (1), 1800077. https://doi.org/10.1002/PPSC.201800077.

(82) Linic, S.; Chavez, S.; Elias, R. Flow and Extraction of Energy and Charge Carriers in Hybrid Plasmonic Nanostructures. *Nat. Mater. 2021 207* **2021**, *20* (7), 916–924. https://doi.org/10.1038/s41563-020-00858-4.

(83) Tao, A. R.; Habas, S.; Yang, P. Shape Control of Colloidal Metal Nanocrystals. *Small* **2008**, *4* (3), 310–325. https://doi.org/10.1002/SMLL.200701295.

(84) Yi, M.; Shen, Z. A Review on Mechanical Exfoliation for the Scalable Production of Graphene. *J. Mater. Chem. A* **2015**, *3* (22), 11700–11715. https://doi.org/10.1039/C5TA00252D.

(85) Zaretski, A. V.; Moetazedi, H.; Kong, C.; Sawyer, E. J.; Savagatrup, S.; Valle, E.; O’Connor, T. F.; Printz, A. D.; Lipomi, D. J. Metal-Assisted Exfoliation (MAE): Green, Roll-to-Roll Compatible Method for Transferring Graphene to Flexible Substrates. *Nanotechnology* **2015**, *26* (4), 045301. https://doi.org/10.1088/0957-4484/26/4/045301.

(86) Zhang, L.; Dong, J.; Ding, F. Strategies, Status, and Challenges in Wafer Scale Single Crystalline Two-Dimensional Materials Synthesis. *Chem. Rev.* **2021**, *121* (11), 6321–6372. https://doi.org/10.1021/ACS.CHEMREV.0C01191.

(87) Huang, X.; Li, S.; Huang, Y.; Wu, S.; Zhou, X.; Li, S.; Gan, C. L.; Boey, F.; Mirkin, C. A.; Zhang, H. Synthesis of Hexagonal Close-Packed Gold Nanostructures. *Nat. Commun. 2011 21* **2011**, *2* (1), 1–6. https://doi.org/10.1038/ncomms1291.

(88) Huang, X.; Tang, S.; Mu, X.; Dai, Y.; Chen, G.; Zhou, Z.; Ruan, F.; Yang, Z.; Zheng, N. Freestanding Palladium Nanosheets with Plasmonic and Catalytic Properties. *Nat. Nanotechnol. 2011 61* **2010**, *6* (1), 28–32. https://doi.org/10.1038/nnano.2010.235.

(89) Kang, J.; Sangwan, V. K.; Wood, J. D.; Hersam, M. C. Solution-Based Processing of Monodisperse Two-Dimensional Nanomaterials. *Acc. Chem. Res.* **2017**, *50* (4), 943–951. https://doi.org/10.1021/ACS.ACCOUNTS.6B00643/ASSET/IMAGES/LARGE/AR-2016-006436_0007.JPEG.

Appendix A

Supplementary Information for Chapter 2: Computation-Motivated Design of Ternary Plasmonic Copper Chalcogenide Nanocrystals

Yuan Zeng[1,2], Paul H. Joo[2], Kesong Yang[1,2], Andrea R. Tao[1,2*]

[1]Department of NanoEngineering, University of California, San Diego, 9500 Gilman Drive MC 0448, La Jolla, California 92093-0448

[2]Materials Science and Engineering, University of California, San Diego, 9500 Gilman Drive, La Jolla, California 92093

*Email: atao@eng.ucsd.edu

A1: Reaction Kinetics

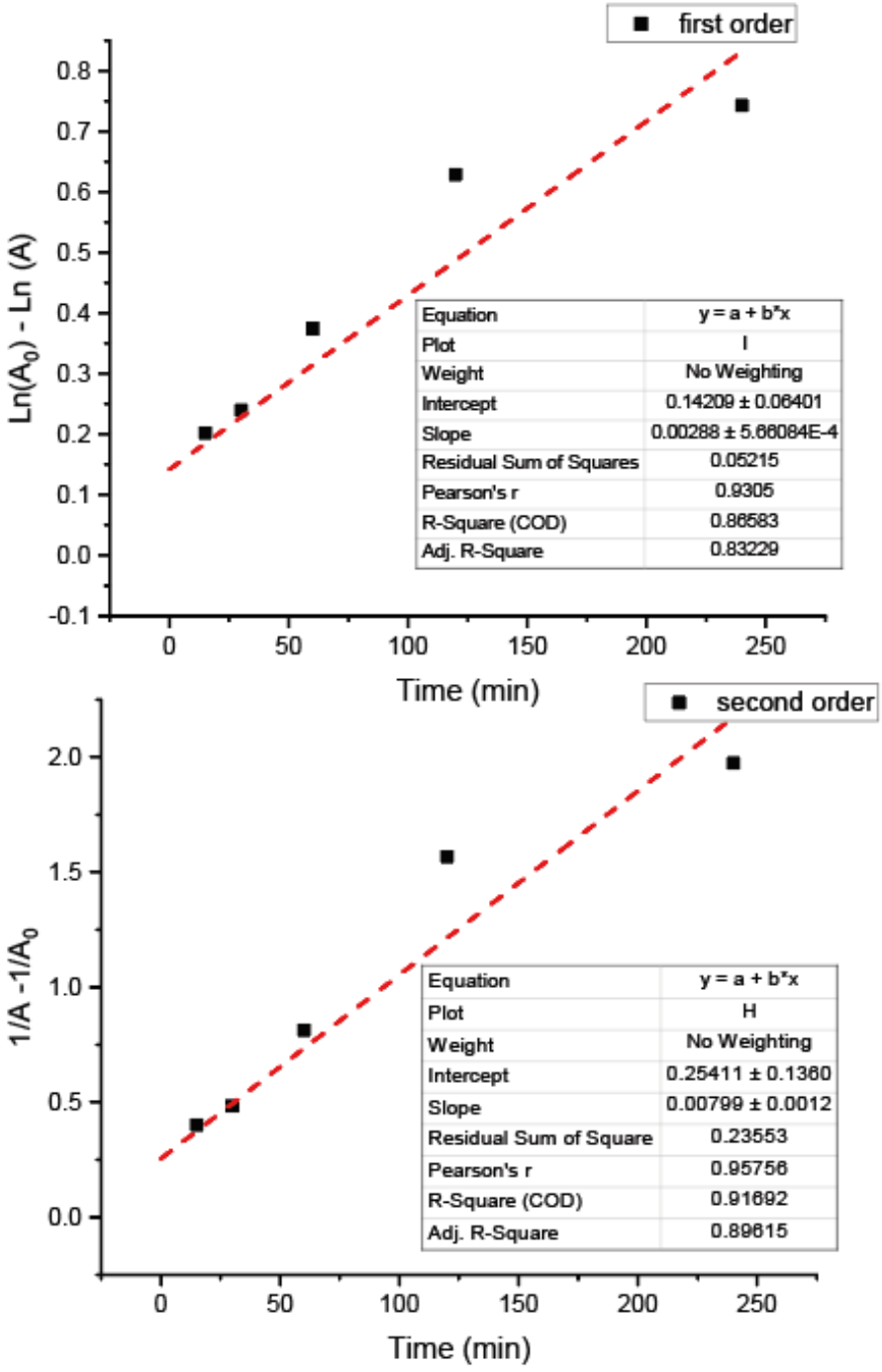

Figure A1. Reaction Kinetics

We performed linear fitting for both first order reaction ($Ln[A_0]$- Ln[A]) and second order reaction ($1/A – 1/A_0$), the R-square value is 0.866 for first order reaction and 0.917 for second order reaction. Therefore, this anion exchange should be second order reaction

A2: EDS Mapping of Anion Exchanged Alloy

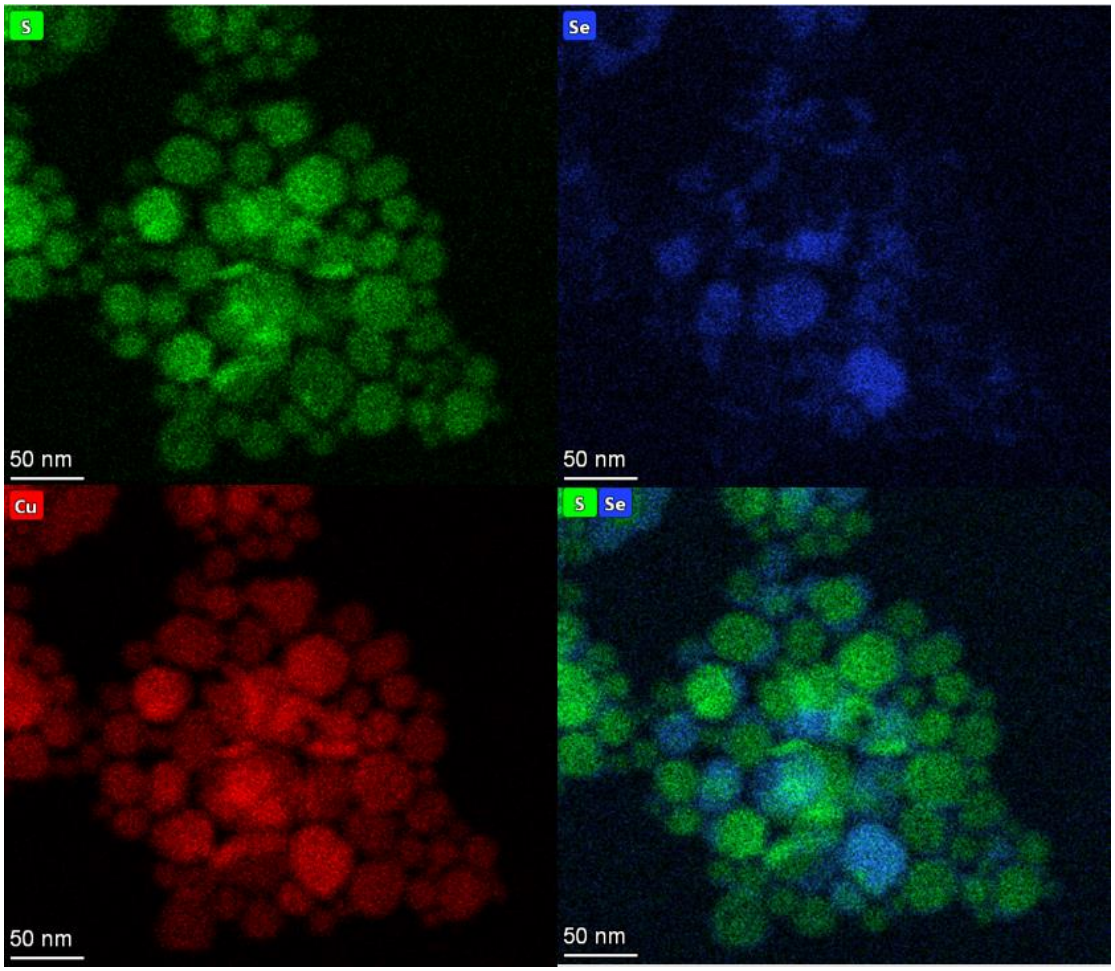

Figure A2. EDS Mapping of Anion Exchanged Alloy, green represents sulfur element, blue represents Se element and red represents Cu element

A3: Ligand Exchange Experiments

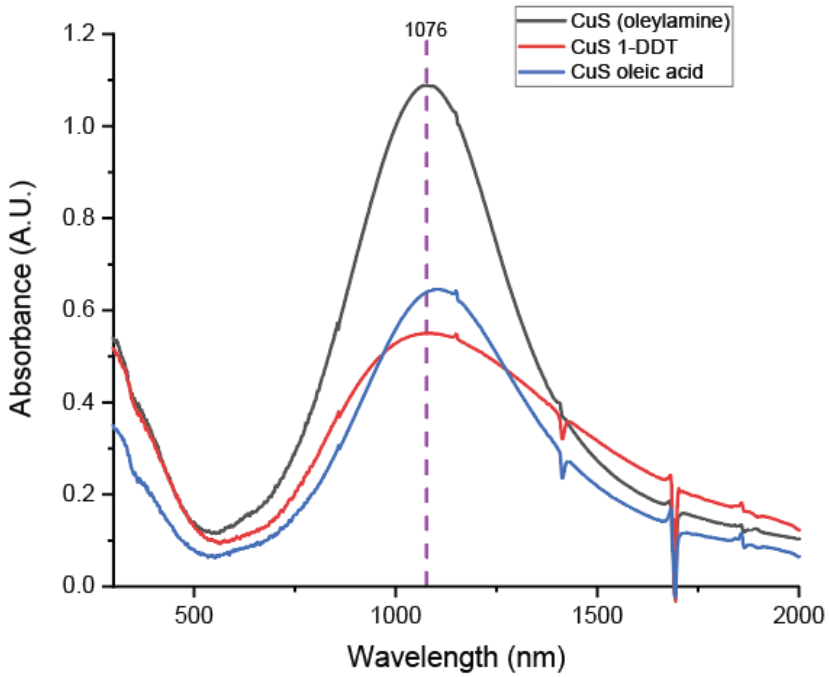

Figure A3. UV-vis absorption spectra after ligand exchange with 1-DDT and oleic acid

The ligand exchange protocol is modified from previous papers[1]. 0.5 mL CuS chloroform solution, 0.5 mL ethanol and 1 mL capping ligand were added in a 20 mL glass vial and stirring 24 hours. Then washed three time with excess chloroform/ethanol mixture, centrifuge at 6k RPM and dispersed in chloroform solution for UV/Vis Characterization.

Both oleylamine capped CuS and 1-DDT exchanged CuS has LSPR resonance at 1076 nm and oleic acid exchanged CuS has LSPR resonance at 1104 nm.

Acknowledgments

The authors would like to thank the NanoEngineering Research facility (NE-MRC), Nano3 facility of SDNI (NSF ECCS # 2025752) and Cryo-EM facility at University of California, San Diego for the use of their facility.

ART acknowledges National Science Foundation under award number CHE-1807891.

KY acknowledges the American Chemical Society Petroleum Research Fund under award number 55481-DNI6 and National Science Foundation under award number ACI-1550404. This work used the Extreme Science and Engineering Discovery Environment (XSEDE), which is supported by National Science Foundation grant number ACI-1548562.

Appendix A, in full, is a reprint of the material as it appears in Chemistry of Materials 33.1 (2020): 117-125. Yuan Zeng, Paul Hyunggyu Joo, Kesong Yang, and Andrea R. Tao. The dissertation author was the primary investigator and author of this paper.

Reference

(1) Wang, J.; Hsu, S.; Gonzalez-Pech, N.; Jhunjhunwala, A.; Chen, F.; Hariri, A.; Grassian, V.; Tao, A.; Jokerst, J. V. Copper Sulfide Nanodisks and Nanoprisms for Photoacoustic Ovarian Tumor Imaging. *Part. Part. Syst. Charact.* **2019**, *36* (8), 1900171. https://doi.org/10.1002/ppsc.201900171.

Appendix B

Supplementary Information for Chapter 3: Enhanced Second Harmonic Generation in Colloidal Metasurfaces

Yuan Zeng[1,3,‡] Haoliang Qian[2,‡] Matthew J. Rozin[1,3,‡] Zhaowei Liu[2,3] and Andrea R. Tao[1,3*]

([‡] Equal contribution)

[1]Department of NanoEngineering, University of California, San Diego, 9500 Gilman Drive MC 0448, La Jolla, California 92093-0448

[2]Department of Electrical and Computer Engineering, University of California, San Diego, 9500 Gilman Drive, La Jolla, California 92093

[3]Materials Science and Engineering, University of California, San Diego, 9500 Gilman Drive, La Jolla, California 92093

[‡]These authors contributed equally to this work.
*Email: atao@eng.ucsd.edu

Characterization:

TEM: FEI Tenia G2 Sphera running a LaB6 filament at 200 kV. A Gatan Ultrascan 1000 UHS CCD camera running Gatan Digital Micrograph was used for imaging

SEM: ZEISS SIGMA 500 Field Emission Scanning Electron Microscope

Reflection and Absorption: PerkinElmer LAMBDA 1050 UV/Vis/NIR

B1: Figure 3b Reflectance Spectrum:

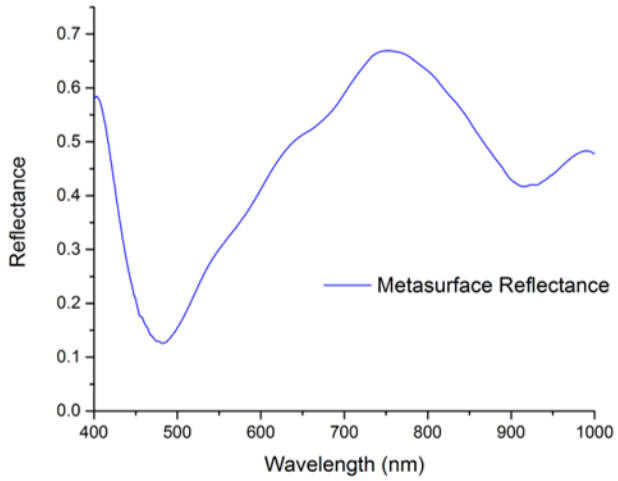

B2: Comparison between metasurface with Au substrate and Si substrate

we fabricated a colloidal metasurface with silicon substrate (Si metasurface) and compare it with metasurface with Au substrate (Au metasurface), these two metasurface has exact same cube size and cube density. Figure a) shows reflection spectrum, Au metasurface has both gap mode resonance at 920 nm and cube mode resonance at 380 nm, which is a double resonance structure. Si metasurface only has a stronger cube mode resonance at 380 nm and no gap mode resonance owing to lack coupling between AgNCs and substrate, therefore it is a single

Figure a)

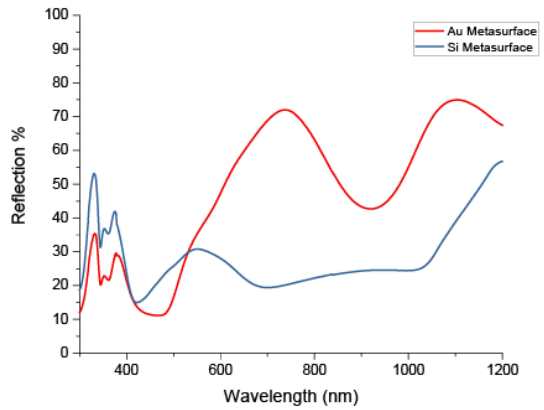

Figure b)

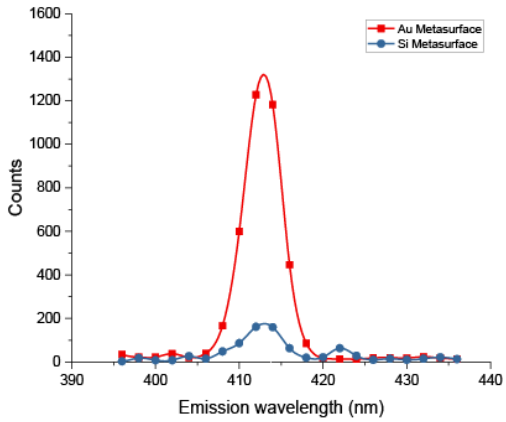

resonance structure. Because this Au metasurface has peak enhancement factor at λ_{FW}=825 nm (Supporting Information S9b), therefore we compare the efficiency of Au metasurface and Si metasurface with 825 nm excitation. Figure b) shows SHG measurement of both metasurface with 825 nm excitation, take the advantage of double resonance, the SHG efficiency of Au metasurface is one order of magnitude higher than the one in single resonance Si metasurface.

B3: Calculation:

# of photon = SHG counts per sec / Detector Efficiency

SHG power = $\#\ of\ photon\ \times\ Photon\ energy$

Active time per second = $pulse\ width\ \times\ Repetition\ Rate$

Peak Power = $\frac{Average\ Power}{Active\ time\ per\ second}$

Efficiency = $\frac{Power_{\ SHG\ peak}}{Power_{Excitation\ peak}}$

(ex. Au metasurface with 900 nm gap resonance, 800 nm excitation wavelength, 0.2 second dwell time, 2 nm detector bandwidth)

Average Excitation Power (mW)	Averaged SHG counts per 0.2 second	Detector Efficiency (counts/ photon)	# photon per second	photon energy (eV)	Average SHG Power (W)
3.91	50233	0.00594	4.23E+07	3.1	2.1E-11

Pulse width (fs)	Repetition Rate (MHz)	Active time (sec) per second	Peak Excitation Power (W)	Peak SHG Power (W)	Efficiency
1.00E+02	8.00E+01	8.00E-06	4.89E+02	2.62E-06	5.36E-09

(ex. Au metasurface with 900 nm gap resonance, 800 nm excitation wavelength, 1 second dwell time, 2 nm detector bandwidth)

Average Excitation Power (mW)	SHG counts per second	Detector Efficiency (counts/ photon)	# photon	photon energy (eV)	Average SHG Power (W)
3.91	43333	0.004752	9.12E+06	3.1	4.52E-12

Pulse width (fs)	Repetition Rate (MHz)	Active time (sec) per second	Peak Excitation Power (W)	Peak SHG Power (W)	Efficiency
1.00E+02	8.00E+01	8.00E-06	4.89E+02	5.65E-07	1.2E-09

B4: Comparison with Au antenna (2015)[1] and Bowtie aperture (2012)[2]

	Excitation power (W)	Pulse length (s)	rep. rate (Hz)	Peak excitation power (W)	Beam area (cm^2)
Metasurface	3.91E-03	1.00E-13	8.00E+07	4.89E+02	3.14E-08
Au Nanoantenna (2015)	1.20E-04	1.20E-13	8.00E+07	1.25E+01	1.54E-08
Bowtie (2012)	1.30E-03	1.50E-13	7.60E+07	1.14E+02	7.1E-08

	peak excitation intensity (W/cm^2)	SHG power(W)	SHG peak power (W)	SHG peak intensity (W/cm^2)
Metasurface	1.56E+10	2.1E-11	2.62E-06	83.44
Au Nanoantenna (2015)	8.12E+08	7.6E-13	7.92E-08	5.14
Bowtie (2012)	1.61E+09	1.7E-11	1.5E-06	21.13

	Measured Efficiency
Metasurface	5.36E-09
Au nanoantenna 2015	6.33E-09
Bowtie (2012)	1.31E-08

Note: Due to the degradation effects we mentioned in the paper, it is difficult to back calculate the efficiency and make direct comparison at same excitation intensity.

B5: Normalization (All the measurement of excitation wavelength dependent efficiency using 1 sec dwell time and 2 nm detector bandwidth)

Wavelength Dependent Beam Spot Area

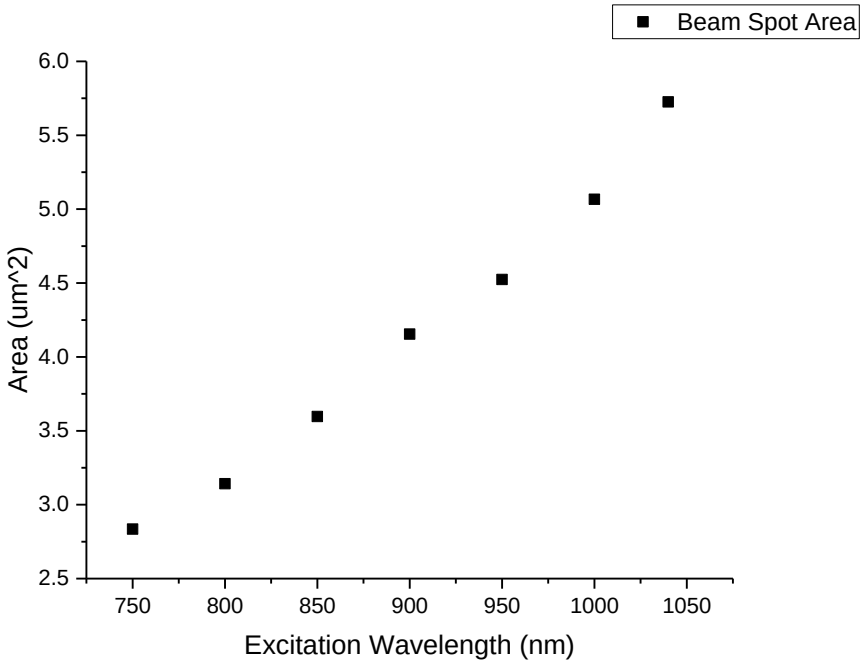

Excitation Intensity = $\frac{Peak\ Excitation\ Power}{Beam\ Spot\ Area}$

Excitation Intensity = $\frac{Peak\ SHG\ Power}{Beam\ Spot\ Area}$

SHG intensity @ 10 GW = $\frac{SHG\ Intensity}{(\frac{Excitatation\ Intensity}{10\ GW})^2}$

Follow the principle: SHG intensity is proportional to excitation intensity squared

(ex. Au metasurface with 900 nm gap resonance, 800 nm excitation wavelength, 1 second dwell time, 2 nm detector bandwidth)

Beam spot Area @ 800 nm (cm^2)	Excitation Intensity (W/cm^2)	SHG intensity (W/cm^2)	SHG intensity @ 10GW excitation (W/cm^2)	Efficiency @ 10GW Excitation (W/cm^2)
3.14E-08	1.56E+10	1.8E+01	7.4	7.4E-10

B6: Curve Fitting of SHG Excitation Scan Spectrum

For M890, Peak 1 has FWHM = 50.5 nm and Peak 2 has FWHM = 64.5 nm, Reduced Chi-Square value = 0

For M1020, Peak 1 has FWHM = 85 nm and Peak 2 has FWHM = 86.5 nm, Reduced Chi-Square value = 0

B7: Calculation of SHG enhancement factor.

Parameter:

From experiment:

A: Absorbance; A_{max}: Maximum absorbance; R: Reflectance; R_{max}: Maximum absorbance; $f(\lambda_{SH})$: Enhancement at SHG wavelength; $f(\lambda_{FW})$: Enhancement at fundamental wavelength

From simulation:

E_{SHG}: maximum near field enhancement from cube resonance; E_{FW}: maximum near field enhancement from gap resonance

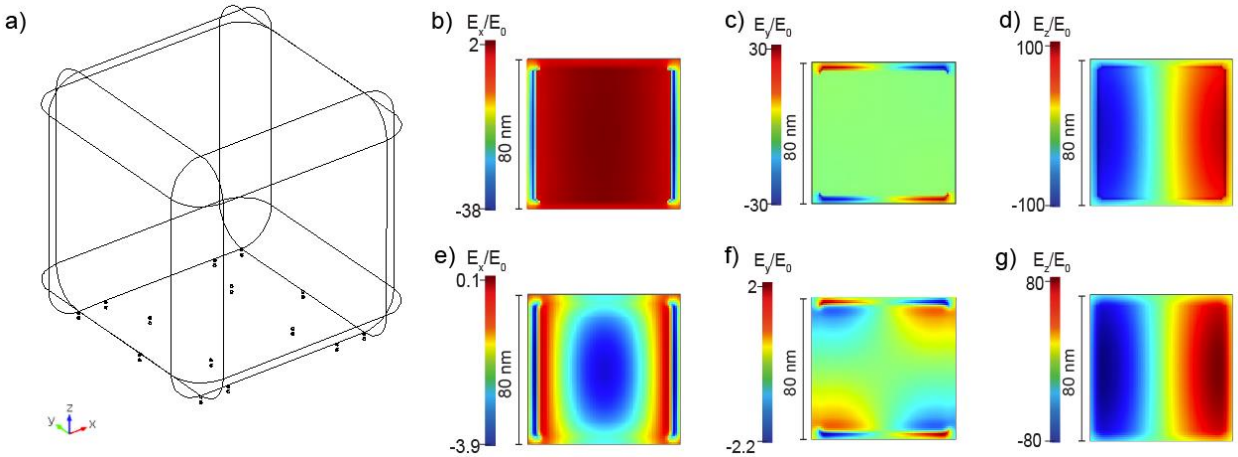

Figure S6 | *Radiation Efficiency Simulation:* (a) Location of dipoles in the simulation model. (b) x-component, (c) y-component (d) z-component of near field enhancement on bottom surface of AgNC at fundamental wavelength. (e) x-component, (f) y-component, (g) z-component of near field enhancement on top surface of gold substrate at fundamental wavelength

Because Reflectance is proportional to $f(\lambda_{SHG})^2$ and Absorbance is proportional to $f(\lambda_{FW})^2$

1: Normalization: $f(\lambda_{SH}) = \frac{\sqrt{R}}{\sqrt{R_{max}}}$

$$f(\lambda_{FW}) = \frac{\sqrt{A}}{\sqrt{A_{max}}} \times \frac{E_{FW}}{E_{SHG}}$$

2: SHG Enhancement Factor = $f(\lambda_{SHG})^2 \cdot f(\lambda_{FW})^4$

B8: Simulated Radiation Efficiency

Because SHG generated from noble metal surface, we add 14 dipole sources on bottom surface of AgNCs and 14 dipole sources on top surface of gold substrate. All these dipoles located at the hotspots, amplitude and phase of each dipole are calculated based on near field enhancement (Figure S6)**.**

B9: M920 Excitation Scan

we fabricate a new metasurface with a different batch of 90 nm AgNCs and gold substrate and take excitation scan with 25 nm data interval instead of 50 nm interval. Figure a) shows UV-VIS spectrum of this metasurface, it has cube mode resonance at 380 nm (λ_{FW}=760 nm) and gap mode resonance at λ_{FW}=920 nm. Figure b) shows wavelength dependent radiation efficiency and calculated SHG enhancement factor. The simulated radiation efficiency peak located at λ_{FW}=875 nm and calculated SHG enhancement factor peak located at λ_{FW}=813 nm. Figure c) shows wavelength dependent SHG efficiency and there are two SHG efficiency peaks. The peak at λ_{FW}=825 nm consists with SHG enhancement factor peak and the peak at λ_{FW}=875 nm consists with radiation efficiency peak. Also, these two peaks can be fitted with the gaussian function, which confirms that the peak identification and analysis we did in the manuscript is reliable.

Figure a)

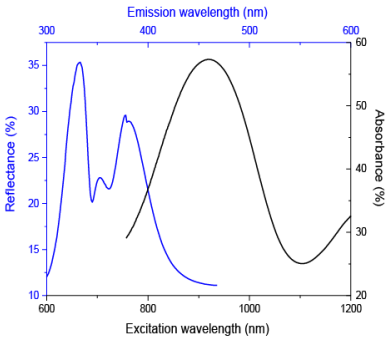

Figure b)

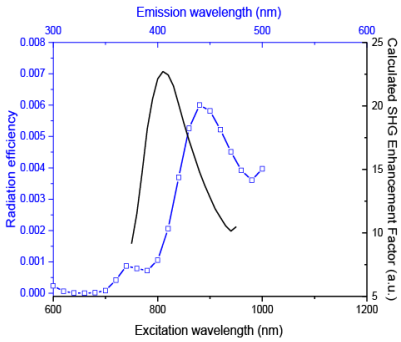

Figure c)

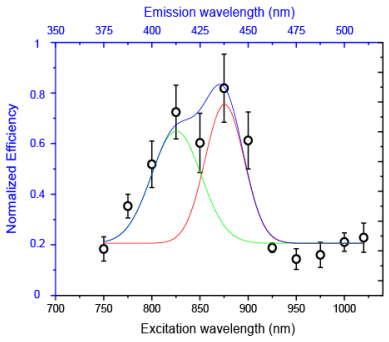

Acknowledgments

The authors would like to thank the UCSD School of Medicine Microscopy Core for the use of their facility and acknowledge its supporting grant, NS047101 and NSF CHE Award 1807891. We also would like to thank the Nano3 facility at Calit2 for the use of their facility.

Appendix B, in full, is a reprint of the material as it appears in Advanced Functional Materials 28.51 (2018): 1803019. Yuan Zeng‡, Haoliang Qian‡, Matthew J. Rozin‡, Zhaowei Liu, and Andrea R. Tao. (‡ Equal contribution). The dissertation author was the primary investigator and author of this paper.

References

1. Celebrano, M. *et al.* Mode matching in multiresonant plasmonic nanoantennas for enhanced second harmonic generation. *Nat. Nanotechnol.* **10,** 412–417 (2015).

2. Park, S., Hahn, J. W. & Lee, J. Y. Doubly resonant metallic nanostructure for high conversion efficiency of second harmonic generation. *Opt. Express* **20,** 4856 (2012).

Appendix C

Supplementary Information for Chapter 4: Metasurface-Enhanced Raman Spectroscopy (mSERS) for Oriented Molecular Sensing

Yuan Zeng[1,2], Riddhi Ananth[3], Tyler J. Dill[1], Andrea Rodarte[1], Matthew J. Rozin[1,2], Nathan Bradshaw[1], Eric R. Brown[1], and Andrea R. Tao[1,2,3*]

[1]Department of NanoEngineering, University of California, San Diego, 9500 Gilman Drive MC 0448, La Jolla, California 92093-0448

[2]Materials Science and Engineering, University of California, San Diego, 9500 Gilman Drive, La Jolla, California 92093

[3] Department of Chemistry & Biochemistry, University of California, San Diego, 9500 Gilman Drive, La Jolla, California 92093

*Email: atao@eng.ucsd.edu

C1: AFM Measurement of Au thin film

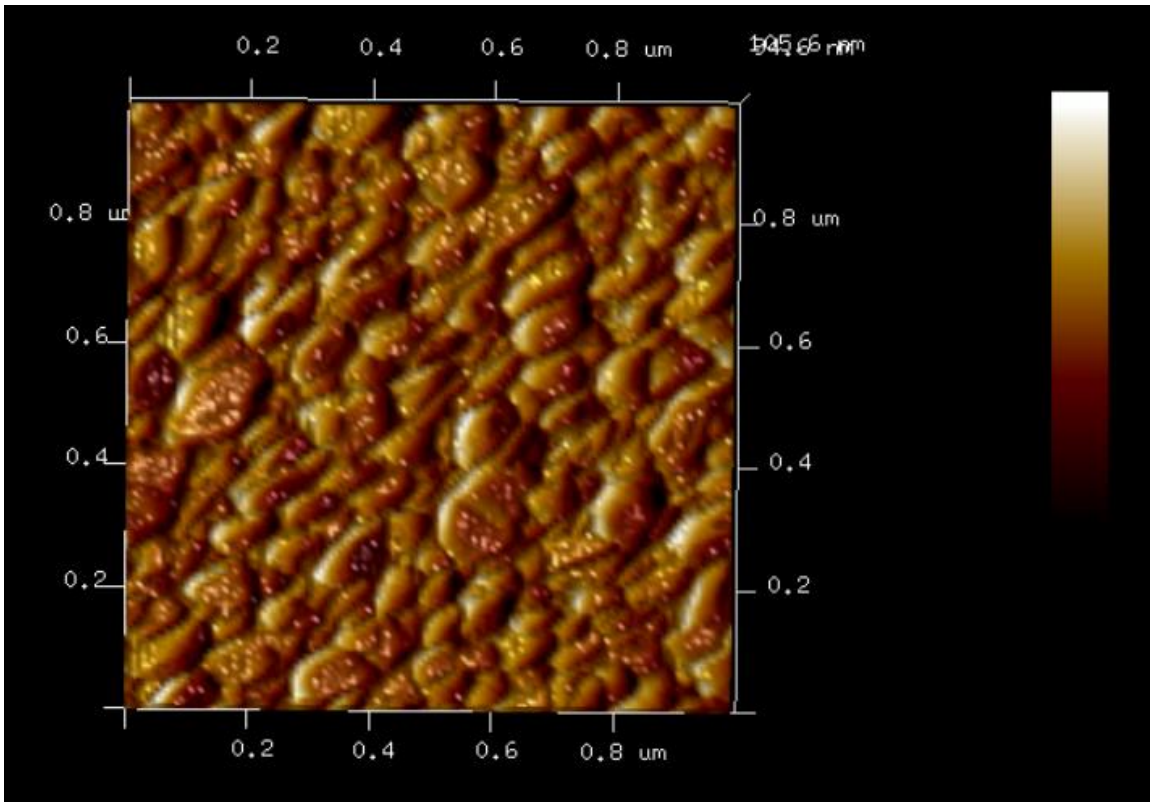

Figure C1. AFM image of Au film

Au film thickness is 94.9 nm, RMS roughness is 2.96 nm and average roughness is 2.27 nm

C2: Simulation Model

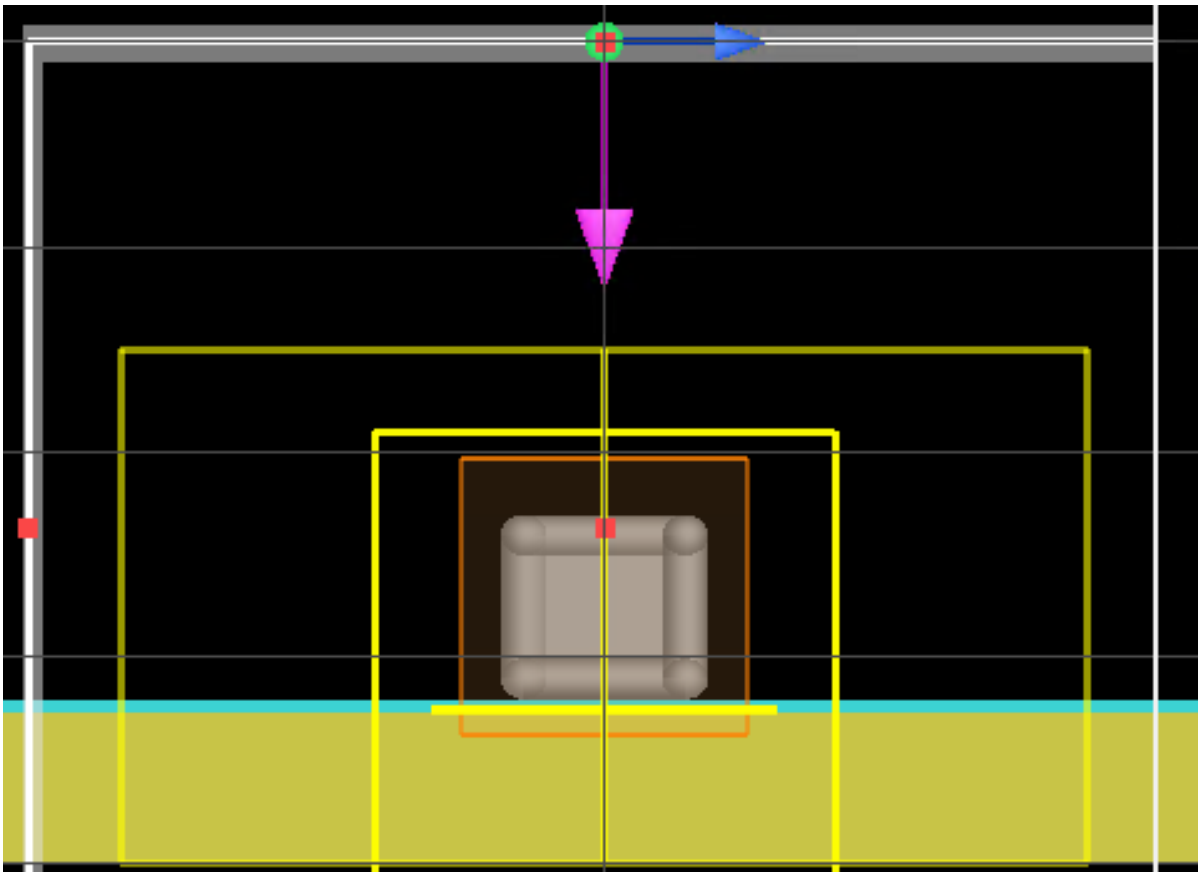

Figure C2. Simulation model of a single meta-atom, pink represents light propagation direction and blue arrow represents E-field polarization. For the excitation plane wave, propagation direction is along the z-axis and polarization is along the x-axis.

Figure S2 shows the XZ view of nanostructure model in our FDTD simulation. This nanostructure consists of 90 nm silver nanocube (AgNC) with 10 nm radius of curvature on the corners (gray), 6 nm dielectric layer (blue) and 75 nm Au (yellow). Because the analyst molecules are functionalized on Au surface, we placed the field monitor 1 nm away from the top surface of Au (yellow line). The in-plane polarized electric field components (E_x, E_y) are defined as the polarization parallel to the Au surface and out-of-plane component (E_z) is defined as the polarization perpendicular to the Au surface.

Local field (near-field) enhancement factor is defined as E/E_0, which E is the local maximum electric field and E_0 is the amplitude of input source electric field. To calculate the averaged local field EF, we used field monitor to collect the total local field EF and divided by the area of bottom surface of 90 nm AgNC (8100 nm^2).

C3: Aggregation Effect

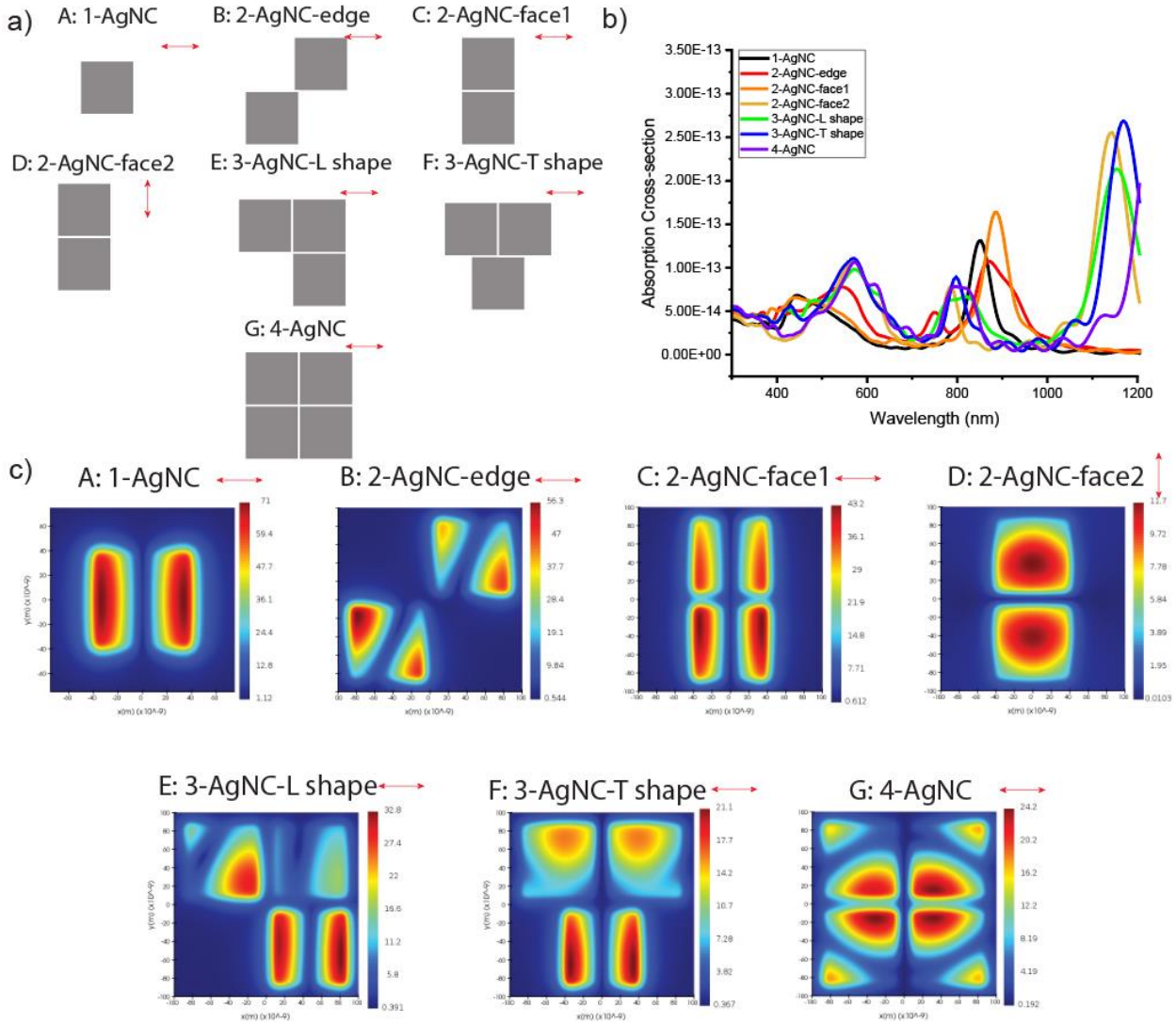

Figure C3. (a) schematic of AgNC clusters (b) far-field spectra of AgNC clusters (c) near-field distribution of AgNC clusters (at 847 nm)

Figure S3a) shows schematics of AgNC clusters made by 2/3/4 AgNCs. Owing to strong interparticle coupling, the strongest absorption peak significantly redshifted (Figure S3b) and results a decreased hotspot area and E/E_0 at gap mode resonance (Figure S3c). Because Raman intensity is proportional to hotspot area and fourth power of E/E_0, SERS intensity from well-spaced AgNCs is orders magnitude higher than AgNC clusters. Therefore, the contribution from AgNCs clusters is negligible.

C4: Peak Broadening Effect

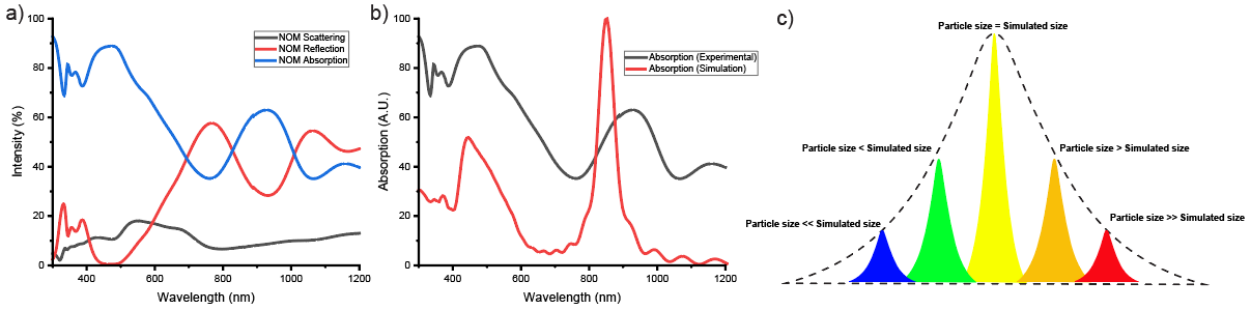

Figure C4. (a) experimental far-field of NOM metasurface (black is scattering, red is reflection, blue is absorption. (b) comparison between experimental absorption spectra and simulated absorption spectra. (c) schematic of experimental spectra broadening.

Figure S4a) shows experimental far-field spectra of our metasurface, including scattering spectra (black), absorption spectra (red) and reflection spectra (blue). At gap mode resonance (926 nm), there is a peak in absorption spectra owing to significant increase in absorption cross-section. Figure S4b) shows a comparison between experimental absorption spectra and simulated absorption spectra. The lineshapes are consistent but experimental absorption spectra is much broader. Figures S4c) shows a schematic of peak broadening. In our metasurface, the fundamental building block is meta-atom. In simulation, all the meta-atoms have consistent size and results a narrow gap mode resonance. In experiment, owing to size/shape variation in our experiment, meta-atom made by smaller AgNC has a blue-shifted spectra and meta-atom made by larger AgNC has a red-shifted spectra. Therefore, the experimental absorption spectra is much broader than simulation.

C5: Background of BT Functionalized Au thin-film and Ethanol Solution Background

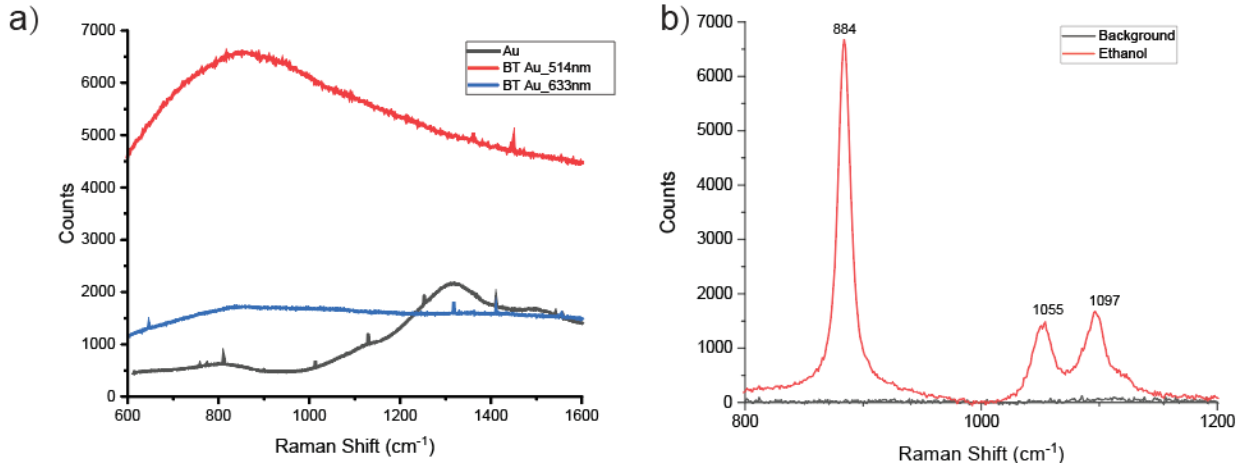

Figure C5. (a) Raman spectra of pristine Au (black), BT functionalized Au (514 nm excitation, red), BT functionalized Au (633 nm excitation, blue). (b) Raman spectra of ethanol background

We used 514 nm and 633 nm laser lines to measure the Raman spectra of a BT-functionalized Au thin-film. Figure S5a shows the corresponding Raman spectra, where no BT peak is observed even at the highest excitation power. The sharp peaks in Figure S5a are assigned to background noise (e.g. gamma rays) and are visible due to averaging.

For the BT NOM, we observe an enhancement of 10^7 at 785 nm and the BT peak is approximately 8 x 10^5 counts. Because background noise of our instrument (@ 1000 cm^{-1}) is approximately 10^2 counts, we believe the enhancement factor of BT on the Au thin-film alone is less than 10^3 and below the limit of detection. because of this, we used an isotropic solution of BT molecules as our reference spectrum. We dissolved BT molecules in ethanol to measurement the unenhanced bulk Raman intensity which we then used to calculate the enhancement factor (EF) of our BT NOM. Figure S5b shows the Raman spectra of pure ethanol as a background.

C6: Wavelength Dependent Raman Spectra of BT Ethanol Solution

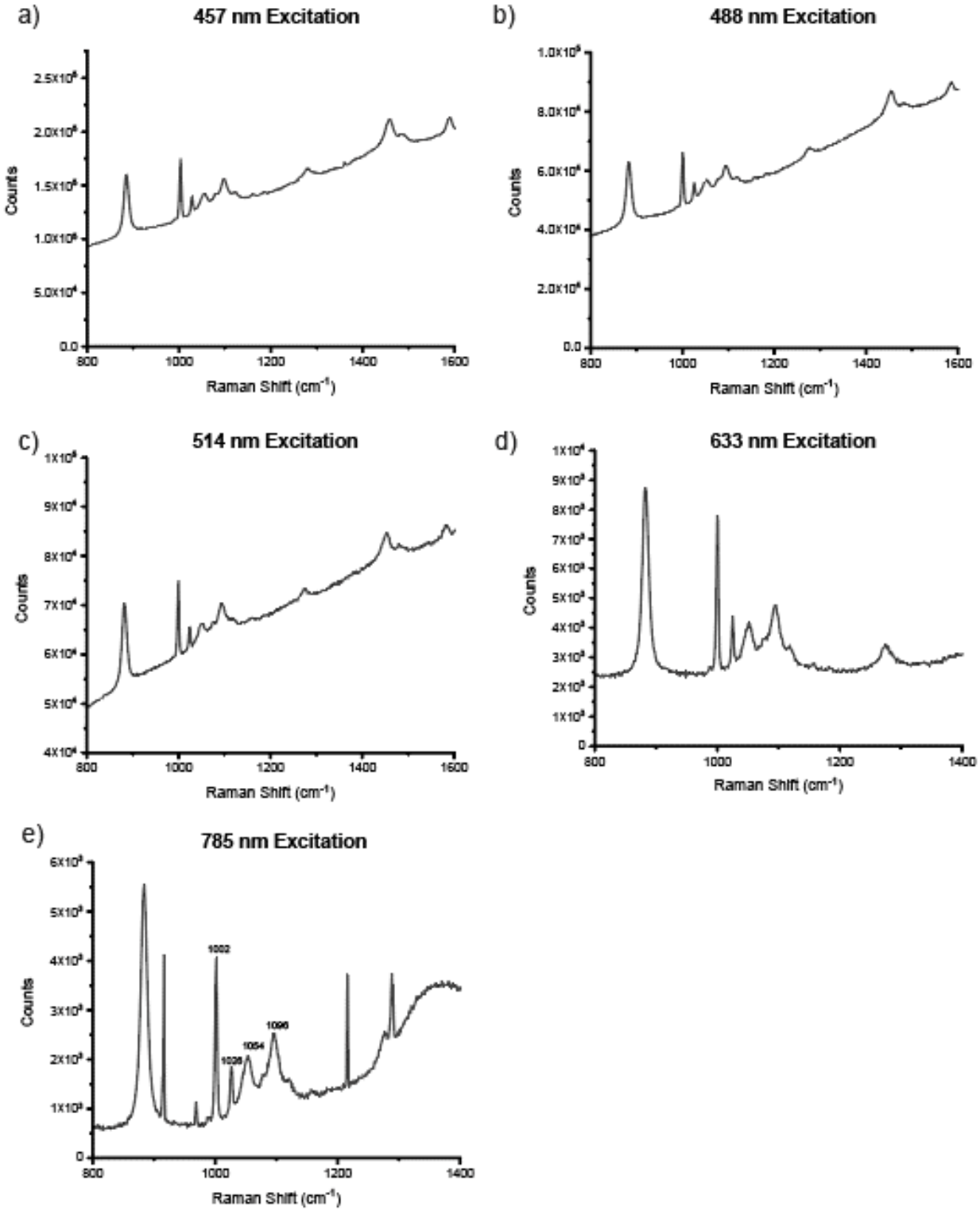

Figure C6. Raman spectra of BT in ethanol solution (I(bulk)) at different excitation wavelength. (a) 457 nm, (b) 488 nm, (c) 514 nm, (d) 633 nm, and (e) 785 nm. the sharp peaks only shown (e) are assigned to background noise (e.g. gamma rays).

C7: Wavelength Dependent Raman Spectra of Pyrene Ethanol Solution

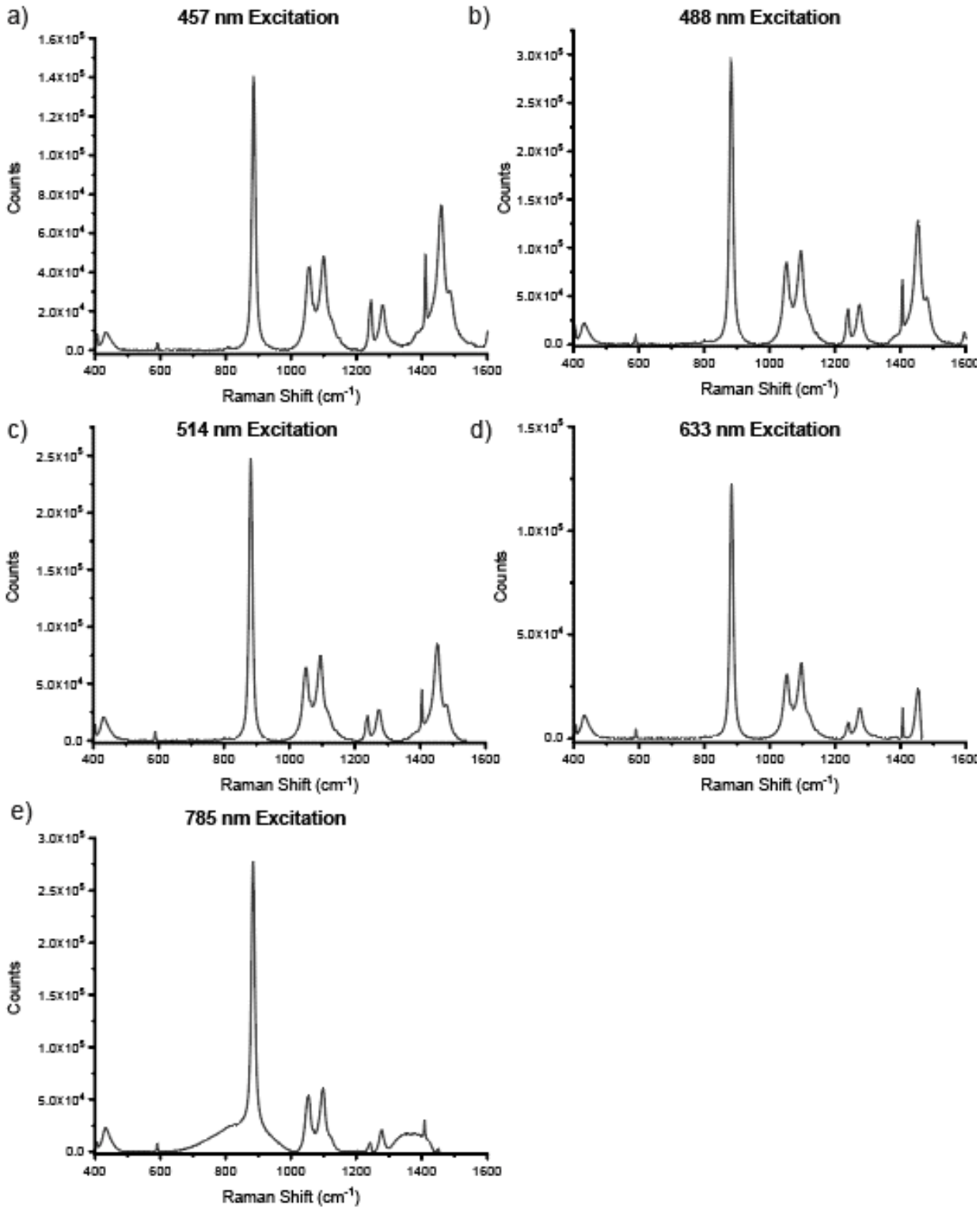

Figure C7. Raman spectra of Pyrene in ethanol solution (I(bulk)) at different excitation wavelength. (a) 457 nm, (b) 488 nm, (c) 514 nm, (d) 633 nm, and (e) 785 nm.

C8: Wavelength Dependent Raman Spectra of BT NOM and Pyrene NOM

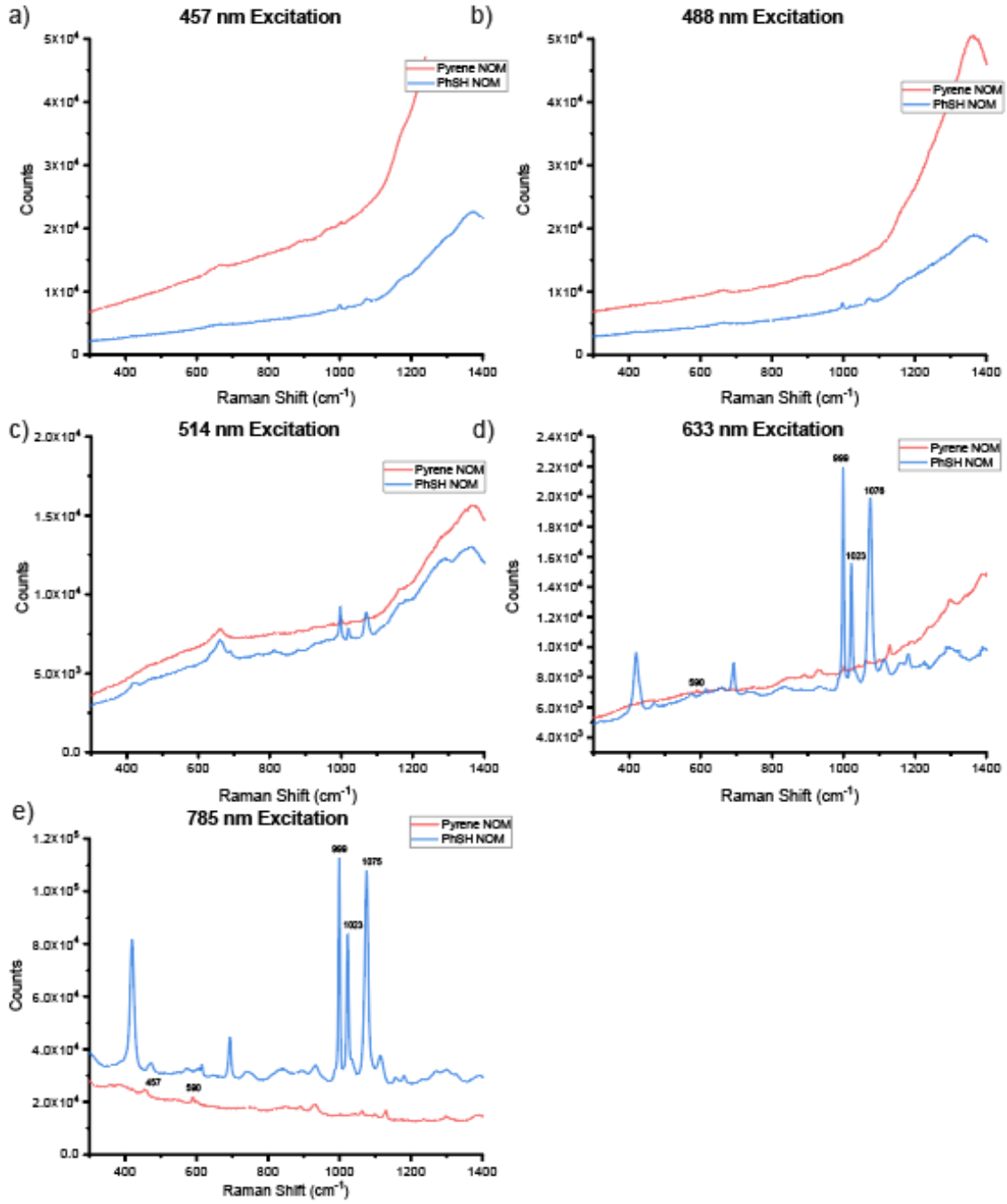

C9:

Figure C8. SERS spectra of BT NOM and pyrene NOM (I(SERS)) measurement at different excitation wavelength. (a) 457 nm, (b) 488 nm, (c) 514 nm, (d) 633 nm, and (e) 785 nm.

Raman Spectra of BDE-15 Powder

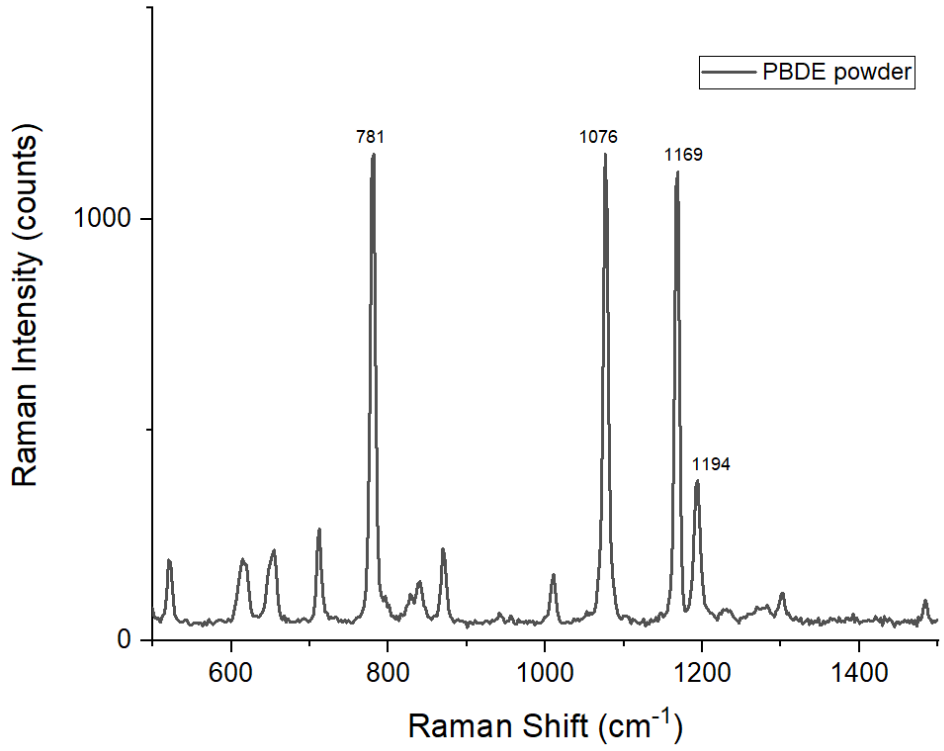

Figure C9. Raman Spectra of BDE-15 Powder

C10: SEM and UV-Vis Spectra of BDE-15 NOM

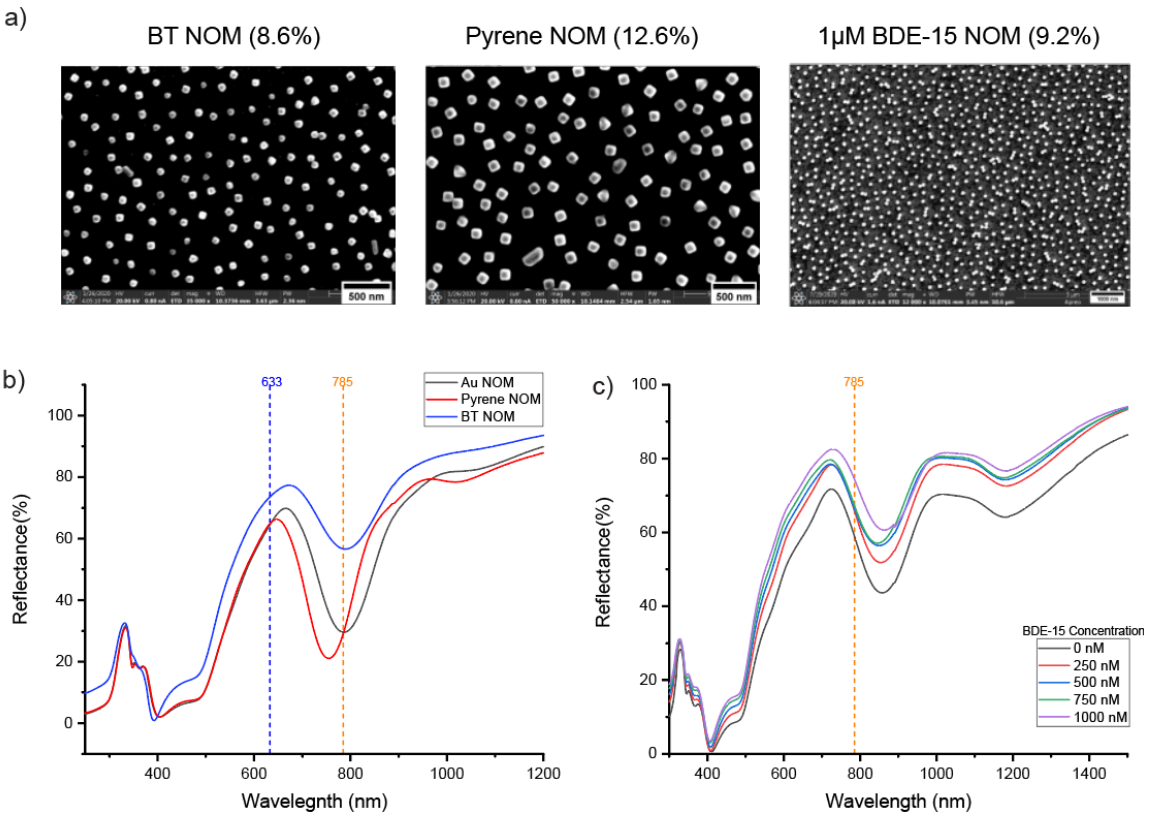

Figure C10. (a) SEM image of BT NOM (left), Pyrene NOM (middle) and BDE-15 NOM (right) (b) reflection spectra of BT NOM and Pyrene NOM (c) reflection spectra of BDE-15 NOM which incubated in different BDE-15 concentration

BDE-15 NOM is prepared with 89.2 nm AgNCs. 9.2% surface coverage density in BDE-15 NOM corresponds to 207 nm interparticle distance. BT NOM and Pyrene NOM are prepared with a different batch of AgNCs (73.4 nm). 8.6% surface coverage density in BT NOM corresponds to 177 nm averaged interparticle distance and 12.6% surface coverage density in Pyrene NOM corresponds to 133 nm averaged interparticle distance (Figure S8a). Because interparticle distance is much larger than AgNCs size, we believe interparticle coupling does not play a role in our measurements. Figure S8b) shows reflection spectra of Pyrene NOM and BT NOM, and Figure S8c) shows reflection spectra of BDE-15 NOM. Because peak wavelength and broadness is nearly consistent with Au NOM reference, we believe our simulation model can be used to predict near-field enhancement in BT NOM, Pyrene NOM and BDE-15 NOM.

C11: Enhancement Factor Calculation

Step 1: We measured wavelength dependent beam spot area and focal volume and shown in Table C1

Table C1 Optical Setup					
Wavelength (nm)	457.00	488.00	514.00	633.00	785.00
Height of focal volume (μm)	16.68	11.25	11.93	16.75	36.85
Effective beam diameter (μm)	1.26	1.66	0.89	1.20	X:1.64 Y:16.95
Effective focal area (μm^2)	0.62	1.08	0.31	0.57	27.72
Focal Volume (μm^3)	10.32	12.10	3.68	9.50	1021.61

Step 2: we measured Raman Intensity (I bulk) and # of molecules (N bulk) in the focal volume of 10% PhSH ethanol solution (Table C2) and 2.02mg/mL pyrene ethanol solution (Table C3)

Table C2 Bulk BT (10% concentration)					
Wavelength (nm)	457	488	514	633	785
density (g/mL)	0.1073	0.1073	0.1073	0.1073	0.1073
MW (g/mol)	110.18	110.18	110.18	110.18	110.18
Avogadro's	6.02E+23	6.02E+23	6.02E+23	6.02E+23	6.02E+23
molecules/μm^3	5.86E+08	5.86E+08	5.86E+08	5.86E+08	5.86E+08
# of molecules in focal volume (N(bulk))	**6.05E+09**	**7.10E+09**	**2.16E+09**	**5.57E+09**	**5.99E+11**
bulk Raman Counts (I(bulk)) @1002 cm^{-1}	**5.41E+04**	**1.76E+04**	**1.51E+04**	**5.23E+03**	**3.30E+03**
bulk Raman Counts (I(bulk)) @1026 cm^{-1}	**1.47E+04**	**4.94E+03**	**4.17E+03**	**1.60E+03**	**7.87E+02**
Exposure time (second)	1	3	3	3	3
Power (%)	50	10	10	5	0.5
Accumulations (#)	150	50	50	50	50

Table C3 Bulk Pyrene (20.2mg/10mL ethanol solution)		

Wavelength (nm)	633	785
density (g/mL)	2.02E-03	2.02E-03
MW (g/mol)	2.02E+02	2.02E+02
Avogadro's	6.02E+23	6.02E+23
molecules/μm^3	6.02E+06	6.02E+06
# of molecules in focal volume (N(bulk))	**5.72E+07**	**6.15E+09**
bulk Raman Counts (I bulk) @590 cm^{-1}	**4.30E+03**	**8.27E+03**
Exposure time (second)	3	3
Power (%)	100	100
Accumulations (#)	50	50

Step 3: we measured SERS intensity (I SERS) and # of molecules (N SERS) in focal area of BT NOM (Table C4) and pyrene NOM (Table C5). Because BT on Au is prepared by incubating Au film in BT ethanol solution, and BT binding on Au is very strong, we assume each Au atom bind with one BT molecule and use Au lattice constant to calculate BT # on Au thin film. Because Pyrene on Au film is prepared by LB transfer and hydrophobic pyrene molecule is unlikely to dissolve in water subphase, we used pyrene density on air-water interface to estimate # of pyrene molecules on Au thin film.

Table C4 BT SERS					
Wavelength (nm)	457.00	488.00	514.00	633.00	785.00
# of surface atom/ unit cell	2.00	2.00	2.00	2.00	2.00
unit cell length (nm)	0.41	0.41	0.41	0.41	0.41
#/nm^2	12.01	12.01	12.01	12.01	12.01
#/μm^2	1.20E+07	1.20E+07	1.20E+07	1.20E+07	1.20E+07
# of molecules in focal area (N(SERS))	**7.44E+06**	**1.29E+07**	**3.71E+06**	**6.82E+06**	**3.33E+08**
SERS Counts (I(SERS)) @999cm^{-1}	**8.28E+02**	**9.25E+02**	**2.12E+03**	**1.41E+04**	**7.99E+04**
SERS Counts (I(SERS)) @1023cm^{-1}	**2.23E+02**	**2.14E+02**	**6.92E+02**	**7.31E+03**	**4.91E+04**
Exposure time (second)	1.00	3.00	3.00	3.00	3.00
Power (%)	50.00	10.00	10.00	5.00	0.50
Accumulations (#)	3.00	1.00	1.00	1.00	5.00

Table C5 Pyrene SERS		
Wavelength (nm)	633	785
# of Pyrene on LB Trough	2.97725E+16	2.97725E+16

Area of LB Trough (cm^2)	30	30
#/nm^2	9.92E+00	9.92E+00
#/μm^2	9.92E+06	9.92E+06
# of molecules in focal area (N(SERS))	**5.63E+06**	**2.75E+08**
SERS Counts (I(SERS) @ 590 cm^{-1}	**1.45E+02**	**2.27E+03**

Step 4: We used $EF = \frac{I(SERS)/N(SERS)}{I(Bulk)/N(bulk)}$ to calculate the enhancement factor (parameters in this equation are bold text in the tables).

In addition, we normalized the difference from excitation power (depends on both laser source and power% in optical setting), # of accumulations and AgNCs surface coverage density on each sample.

Table C6 BT EF					
Wavelength (nm)	457.00	488.00	514.00	633.00	785.00
Relative excitation power (Ex(SERS)/Ex(bulk))	1.07	1.22	1.09	1.29	1.46
I(SERS)/I(bulk) @ 999 cm-1	0.72	2.15	6.44	104.39	166.07
I(SERS)/I(bulk) @ 1023 cm^{-1}	0.71	1.77	7.62	176.40	427.98
N(SERS)/N(bulk)	1.23E-03	1.82E-03	1.72E-03	1.22E-03	5.56E-04
AgNC coverage density	8.60E-02	8.60E-02	8.60E-02	8.60E-02	8.60E-02
EF @999cm^{-1}	**6.78E+03**	**1.38E+04**	**4.36E+04**	**9.92E+05**	**3.47E+06**
EF @1023cm^{-1}	**6.70E+03**	**1.13E+04**	**5.16E+04**	**1.68E+06**	**8.95E+06**

Table C7 Pyrene EF		
Wavelength (nm)	633.00	785.00
Relative excitation power (Ex(SERS)/Ex(bulk))	6.63E-02	1.96E-02
I(SERS)/I(bulk) @ 590 cm-1	25.48	140.01
N(SERS)/N(bulk)	0.10	0.04
AgNC coverage density	0.13	0.13
EF @ 590 cm^{-1}	**2.06E+03**	**2.49E+04**

Raman Intensity is measured from spectra shown in Figure C6 (BT solution), Figure C7 (pyrene solution), and Figure C8 (BT NOM and pyrene NOM)

Acknowledgements

The authors would like to thank Nano3 and the San Diego Nanotechnology Infrastructure (NSF Award ECCS-2025752), the UC San Diego MRSEC (NSF Award DMR-2011924), and the NanoEngineering MRC for use of their equipment and facilities, and Dr. Aliaksandr Zaretski in Grolltex, inc. for graphene sample fabrication. This work was supported by NSF Awards CHE-1807891 and DMR-2011924.

Appendix C, in full, is a reprint of the material as it appears in an under reviewed manuscript for ACS Applied Materials & Interfaces. Yuan Zeng, Riddhi Ananth, Tyler J. Dill, Andrea Rodarte, Matthew J. Rozin, Nathan Bradshaw, Eric R. Brown, and Andrea R. Tao. The dissertation author was the primary investigator and author of this paper

Reference

(1) Huang, X.; El-Sayed, M. A. Gold Nanoparticles: Optical Properties and Implementations in Cancer Diagnosis and Photothermal Therapy. *J. Adv. Res.* **2010**, *1* (1), 13–28. https://doi.org/10.1016/J.JARE.2010.02.002.

Appendix D

Supplementary Information for Chapter 5: Rapid Raman Detection of PBDEs in Water Using a Colloidal Metasurface

Yuan Zeng[1,2], Riddhi Ananth[3], Wade Shipley[1], and Andrea R. Tao[1,2,3*]

[1]Department of NanoEngineering, University of California, San Diego, 9500 Gilman Drive MC 0448, La Jolla, California 92093-0448

[2]Materials Science and Engineering, University of California, San Diego, 9500 Gilman Drive, La Jolla, California 92093

[3] Department of Chemistry & Biochemistry, University of California, San Diego, 9500 Gilman Drive, La Jolla, California 92093

*Email: atao@eng.ucsd.edu

D1：Table D1, BDE-15 Water Solution Preparation

BDE-15 Water solution concentration (M)	Volume of PBDE stock solution, in Ethanol (uL)	PBDE stock solution concentration (M)	Ethanol volume (uL)	DI water volume (mL)
2.50E-09	25	1.00E-06	75	9.9
5.00E-09	50	1.00E-06	50	9.9
1.00E-08	100	1.00E-06	0	9.9
2.50E-08	25	1.00E-05	75	9.9
5.00E-08	50	1.00E-05	50	9.9
1.00E-07	100	1.00E-05	0	9.9
2.50E-07	25	1.00E-04	75	9.9
5.00E-07	50	1.00E-04	50	9.9
7.50E-07	75	1.00E-04	25	9.9
1.00E-06	100	1.00E-04	0	9.9
2.50E-06	25	1.00E-03	75	9.9
5.00E-06	50	1.00E-03	50	9.9

BDE-15 stock solution is prepared by dissolving BDE-15 powder in ethanol solution. BDE-15 water solution is prepared by diluting stock solution in DI water, all BDE-15 water solution contains 1% ethanol.

D2：UV-Vis Reflection Spectra and Absorption Spectra

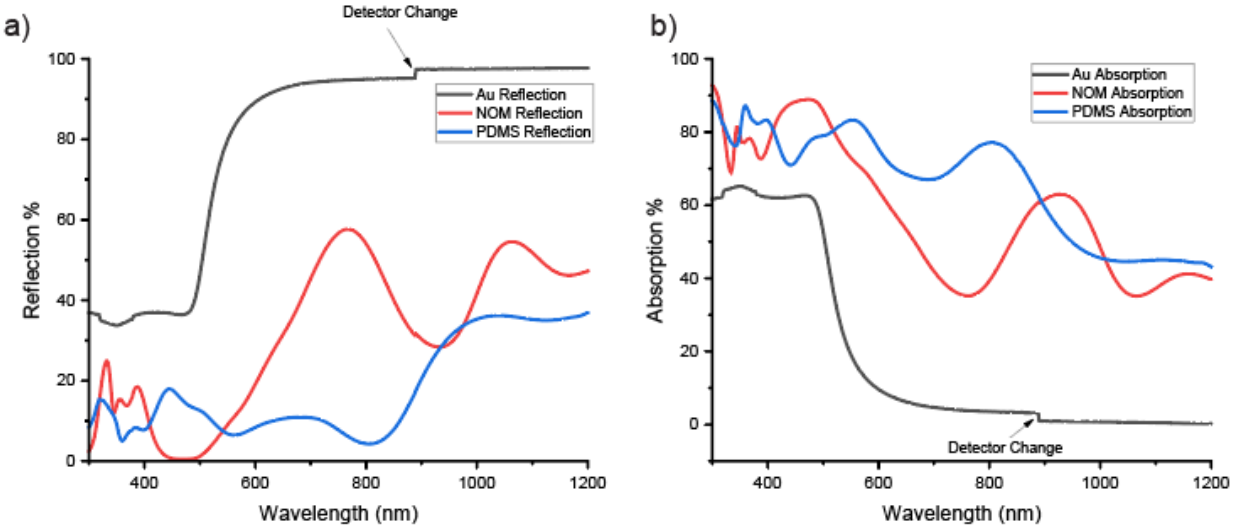

Figure D1. Reflection spectra of Au thin film (black), NOM metasurface (red) and PDMS

Scattering spectra is measured with Integrating Sphere Accessory and reflection spectra is measured with Universal Reflectance Accessory. Because our metasurface does not have transmission at visible and NIR wavelength, the absorption (%) is calculated by the following equation: A(%) = 100 (%) – R(%) – S(%)

D3：Time Dependent Study

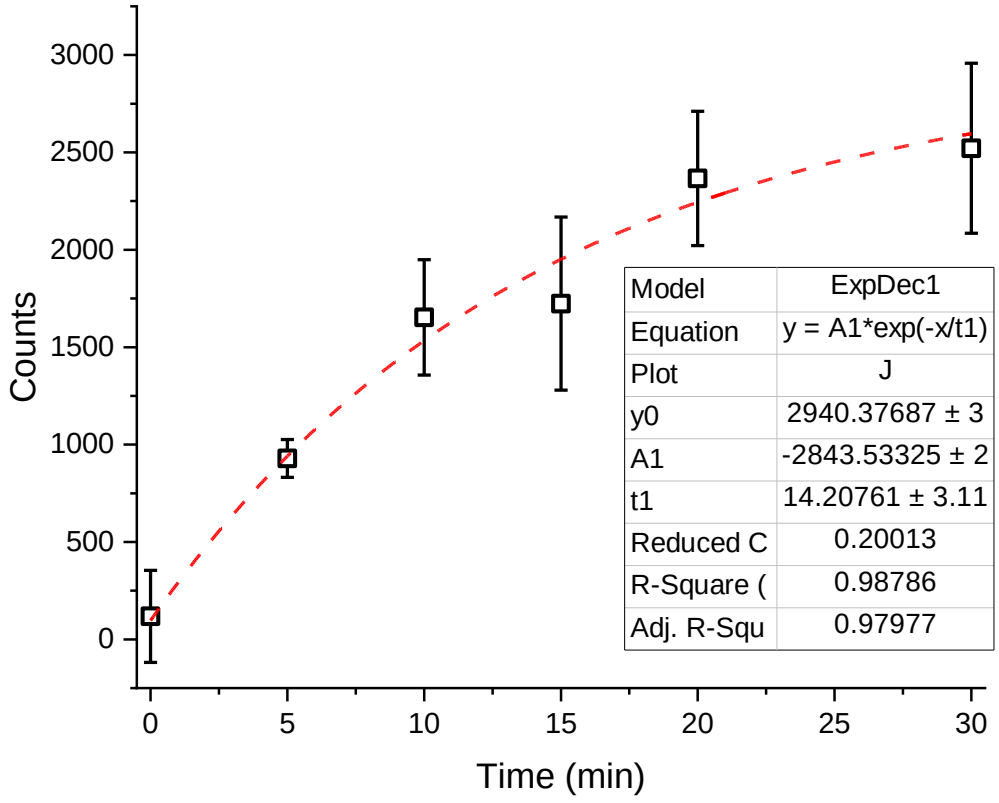

Figure D2. Time Dependent Study Curve Fitting

D4：Concentration Dependent Study

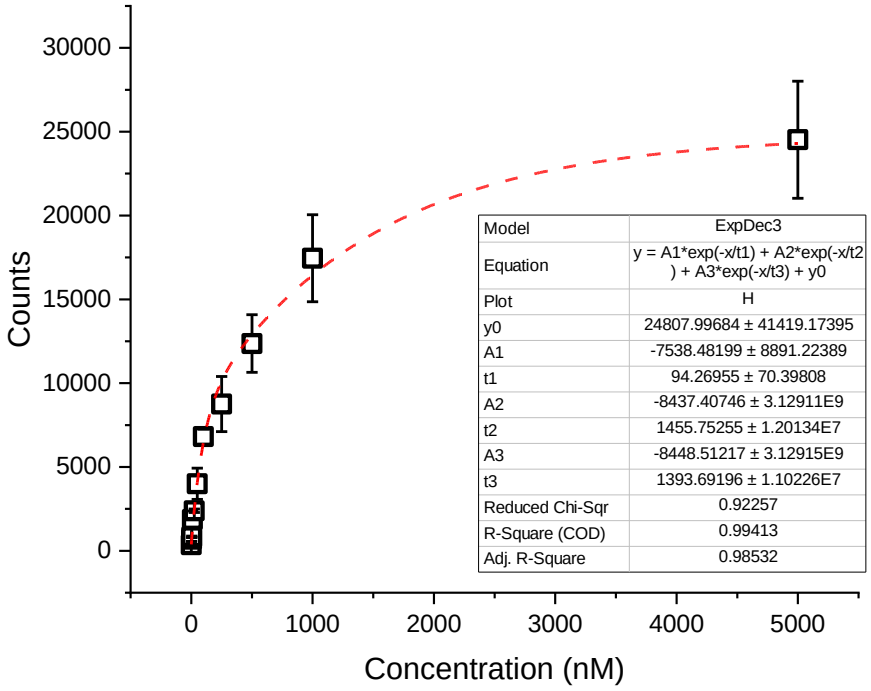

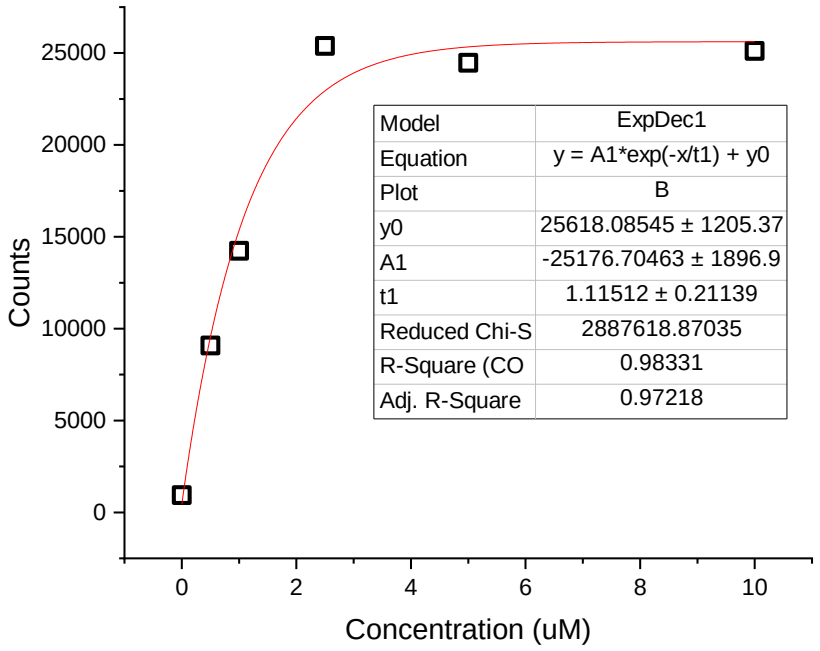

Figure D3. Concentration Dependent Study Curve fitting

D5：Gap Distance Effect on Near-field Enhancement

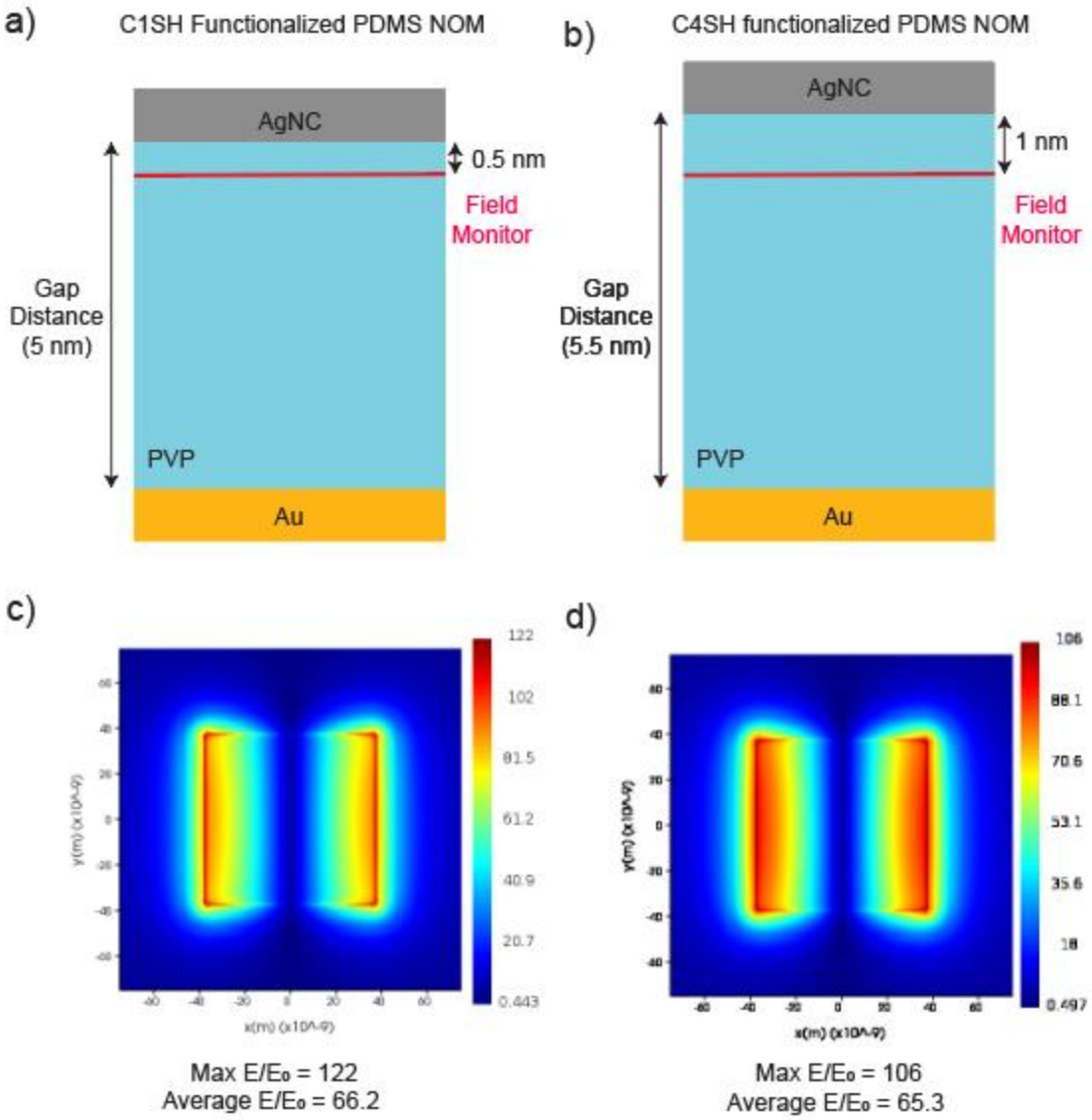

Figure D4. (a) Schematic of nanogap in C_1SH functionalized PDMS NOM. (b) Schematic of nanogap in C_4SH functionalized PDMS NOM. (c) Near-field enhancement in C_1SH functionalized PDMS NOM. (d) Near-field enhancement in C_4SH functionalized PDMS NOM.

In C_1SH functionalized PDMS NOM, we set gap distance as 5 nm and field monitor at 0.5 nm away from AgNC bottom because BDE-15 molecules bind on AgNCs and methanethiol SAM thickness is about 0.5 nm. Because butanethiol SAM thickness is 0.4 nm larger than methanethiol SAM, we set gap distance as 5.5 nm and field monitor at 1 nm away from AgNC bottom in C_4SH functionalized PDMS NOM. The maximum E/E_0 is 122 and 106 and the average E/E_0 is 66.2 and 65.3 in C_1SH functionalized PDMS NOM and C_4SH functionalized PDMS NOM, respectively.

Therefore, average enhancement factor is nearly consistent and maximum enhancement factor in C_1SH functionalized PDMS NOM is 75% higher than C_4SH functionalized PDMS NOM.

D6：Table D2, Chain Length Dependent Alkanethiol SAM Thickness

CH2(CH2)nSH	Molecule	Number of Carbon (n+1)	Alkanethiol SAM thickness (nm)
0	Methanethiol	1	0.458
1	Ethanethiol	2	0.584
2	Propanethiol	3	0.71
3	1-Butanethiol	4	0.836

The distance calculation was followed the equation:

$$D = 0.458 + 0.126 \times n$$

Where D is gap distance in nanometer, n is number of CH_2 groups in alkanethiols.[1]

Acknowledgements

The authors would like to thank Nano3 and the San Diego Nanotechnology Infrastructure (NSF Award ECCS-2025752), the UC San Diego MRSEC (NSF Award DMR-2011924), and the NanoEngineering MRC for use of their equipment and facilities. This work was supported by NSF Awards CHE-1807891 and DMR-2011924.

Appendix D, in full, is currently being prepared for submission for publication of the materials by Yuan Zeng, Riddhi Ananth, Wade Shipley, and Andrea R. Tao*. The dissertation author was the primary investigator and author of this paper.

References

(1) Walczak, M. M.; Chung, C.; Stole, S. M.; Widrig, C. A.; Porter, M. D. *Structure and Interfacial Properties of Spontaneously Adsorbed N-Alkanethiolate Monolayers on Evaporated Silver Surfaces*; 1991; Vol. 113.

Appendix E

Supplementary Information for Chapter 6: Metasurface Enhancement Raman Spectroscopy (mSERS) for Two-dimensional Materials Wafer-Scale Characterization

Yuan Zeng[1,3‡], Steven Bopp[2‡], Tod Pascal[1,4], Zhaowei Liu[2,3*] and Andrea R. Tao[1,3*]

[1]Department of NanoEngineering, University of California, San Diego, 9500 Gilman Drive MC 0448, La Jolla, California 92093-0448

[2]Department of Electrical and Computer Engineering, University of California, San Diego, 9500 Gilman Drive, La Jolla, California 92093

[3]Materials Science and Engineering Program, University of California, San Diego, 9500 Gilman Drive, La Jolla, California 92093

[4]Department of Chemical Engineering, University of California, San Diego, 9500 Gilman Drive, La Jolla, California 92093

[‡]These authors contributed equally to this work.
*Email: atao@eng.ucsd.edu, zhaowei@ucsd.edu

E1: TiN Thin-Film Synthesis and Characterization

DC Magnetron Sputtering: Thin films of Au were grown in an AJA ATC Orion DC sputtering system (vacuum pumped before growth to ~10^{-8} Torr) using a Ti adhesion layer from a ultra-high purity Au and Ti targets purchased from the Kurt J. Lesker corporation. Au films were grown with all parameters were held constant as follows: room temperature, 50 watts, 5 sccm ultra-high purity Ar, 5±0.24 mTorr growth pressure, 144 seconds, 15 minutes of pre-sputtering. Ti films were grown with all parameters were held constant as follows: room temperature, 50 watts, 5 sccm ultra-high purity Ar, 5±0.24 mTorr growth pressure, 4.5 seconds, 15 minutes of pre-sputtering. Before being introduced into the growth chamber, all samples were loaded into sputtering system's load lock and pumped down to 2.2×10^{-8} Torr or lower.

RF Magnetron Sputtering: Thin films of TiN were grown in an AJA ATC Orion 8 RF sputtering system (vacuum pumped before growth to ~10^{-8} Torr) from ultra-high purity N_2 gas and an ultra-high purity Ti target purchased from the Kurt J. Lesker corporation. TiN films were grown with the only varied parameter being time, all other parameters were held constant as follows: 350°C, 200 watts, 3 sccm Ar, 7 sccm N2, 10±0.24 mTorr growth pressure, 10 minutes of pre-sputtering. Before being introduced into the growth chamber, all samples were loaded into the load lock of the sputtering system and pumped down to 2.2×10^{-8} Torr or lower. A thick film sample of TiN was grown for 5 hours on a c-sapphire substrate to be used as a reference of the film's stoichiometry.

XRD and XRR Measurements: Structural parameters of thin films were measured with XRD and XRR in a Panalytical X'Pert X-ray Diffractometer using the in the point-source configuration and Cu-Kα radiation with a Ni Cu-Kβ filter. X-rays were generated at 45 kV and 40 mA. All X-ray measurements were carried out on a multipurpose stage where the Z-axis height of samples was carefully set for each measurement with a mechanical depth stop for consistent optimal positioning of a sample's top surface with respect to the incident X-rays. Perpendicular masks of 1- and 4-mm were used to shutter the source and to shape the X-ray beam. XRD: using

a 1° incident beam slit, samples were scanned over 2θ = 25-90° in the 2θ–ω geometry. Machine offsets were calculated by comparing substrate peak positions in the 2θ–ω and ω-scan geometries. XRR: again, using the point source configuration but this time with a 1/32° incident beam slit, and a diffracted beam slit, samples were scanned in the 2θ–ω geometry from 2θ = 0-4°. Resultant reflectograms were analyzed with GenX.[1]

RBS Measurements: The atomic composition of a reference bulk TiN thin film grown with RF magnetron sputtering for 5 hours at 350°C, 200 watts, 3 sccm Ar, 7 sccm N_2, 10±0.24 mTorr was characterized using Rutherford backscattering spectrometry (RBS). RBS was selected because of its simultaneous ability to measure heavy and light elements with high sensitivity on a substrate comprised of light elements (like sapphire). 2 MeV $^4He^{++}$ ions were incident on the samples at an 8° angle α with a spot size of approximately 1 mm^2 in a General Ionex 4117HC 1.7MV tandetron accelerator operating in the Cornell geometry. SIMNRA was used to analyze the RBS measurement data.

E2: Simulation Model of Graphene/h-BN NOM

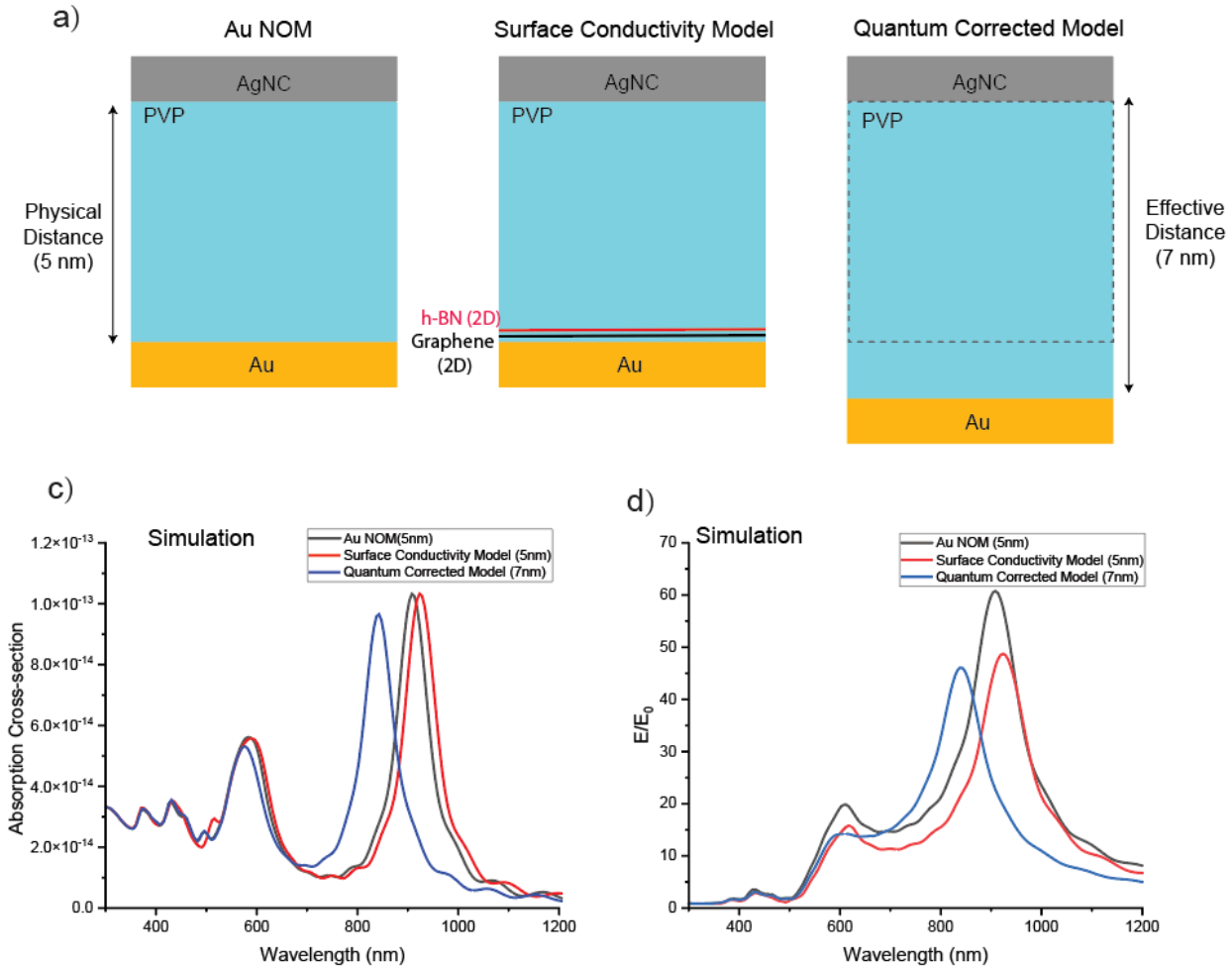

Figure E1 | Simulation model of Graphene/h-BN. (a) schematic of Au NOM (left), Surface conductivity model (middle), and Quantum-corrected model. (b) far-field absorption spectra of Au NOM (black), Surface conductivity model (red), and Quantum-corrected model (blue). (c) Wavelength dependent near-field enhancement of Au NOM, Surface conductivity model, and Quantum-corrected model.

In Au NOM reference, the dielectric gap consists of PVP and the gap distance is 5 nm. In Surface Conductivity Model, we added a volumeless 2D conductor layer (Material: Graphene, conductivity scale = 1) to represent graphene and a volumeless 2D insulator layer (conductivity = 1 x 10^{-13} $(\Omega m)^{-1}$) to represent h-BN. In Quantum Corrected Model, we increase the effective gap distance to represent the dielectric barrier effect because increased gap distance also results weaker coupling strength and blue-shifted gap mode resonance. Here, we adjusted the effective gap distance to make the blueshift in Quantum-corrected model matches with our experimental data in Figure 2a.

The simulated far-field spectra of Au NOM reference (black), surface conductive model (red) and quantum corrected model (blue) is shown in Figure S1b). Au NOM has a moderate absorption peak at 581 nm which originate from cube mode resonance and a strong absorption peak at 908 nm from gap mode resonance. In the surface conductivity model, both cube mode resonance (591 nm) and gap mode resonance (923 nm) have a slightly red-shift, indicates screening effect does not play a significant role in the blue-shifted absorption peak in Figure 2a). To mimic the dielectric barrier induced coupling strength decrease, we increase the effective gap distance to 7 nm. Because cube mode resonance is independent on the dielectric gap, the moderate absorption peak blue-shifted 5 nm to 576 nm. However, owing to decreased coupling strength, the gap mode resonance blue-shifted 66 nm to 842 nm and matches the experimental data in Figure 2a). Figure S1c) shows the wavelength dependent near-field enhancement (E/E_0). At gap mode resonance wavelength, Au NOM, surface conductivity model and quantum corrected model have 61-fold, 49-fold and 46-fold E/E_0, respectively. It means screening effect causes a 20% decrease in E/E_0 and dielectric barrier effect causes another 25% decrease in E/E_0. Finally, we integrated two models together and got a hybrid model shown in Figure 2b.

E3: Graphene/h-BN NOM Sample

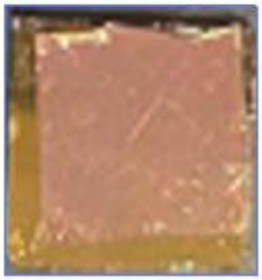

Figure E2 | Image of Graphene/h-BN NOM

E4: Individual Spectra analysis

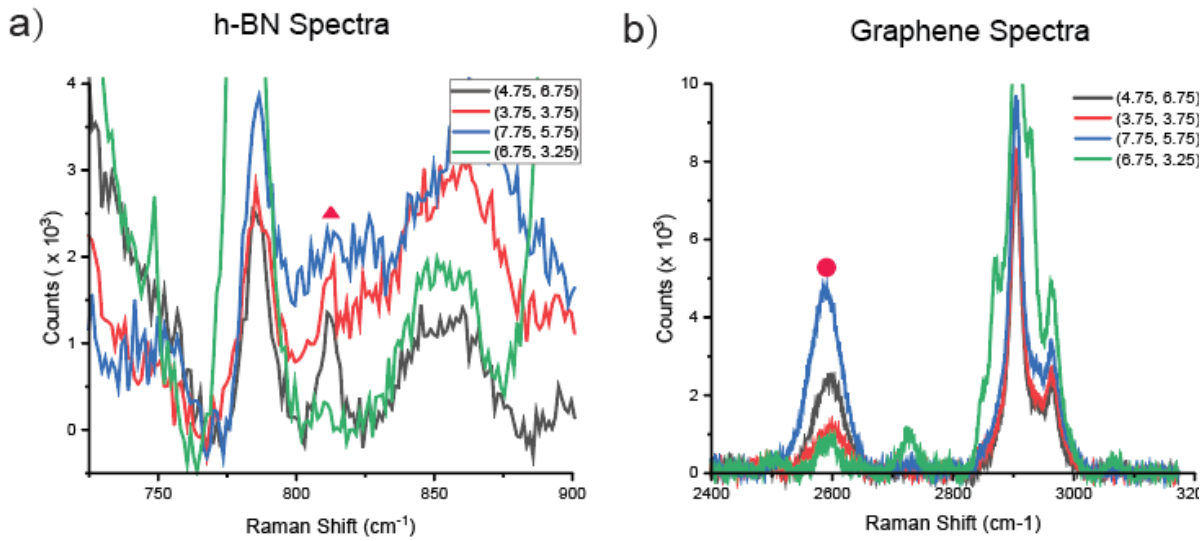

Figure E3 | Individual Raman Spectra

Figure E3a) and Figure E3b) shows Raman spectra of Graphene/h-BN NOM. Red triangle represents h-BN ZO mode and red circle represents graphene 2D mode.

E5: False positive and false negative

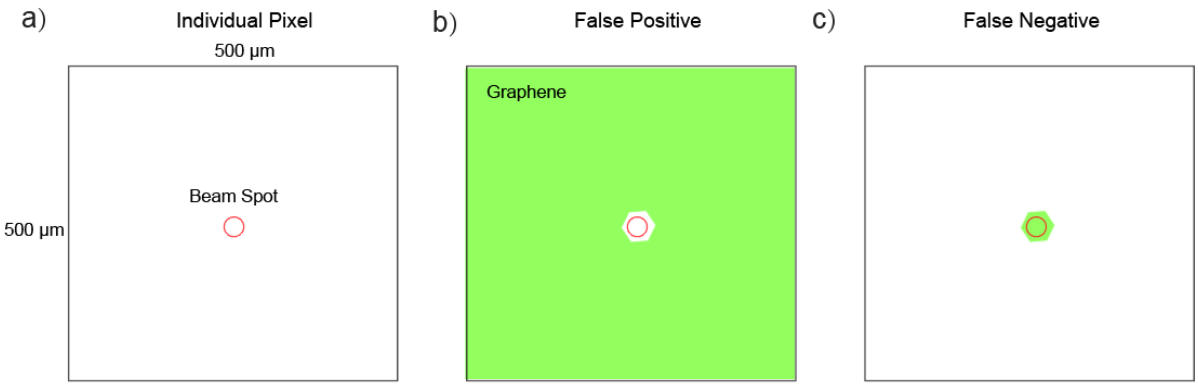

Figure E4 | False positive and false negative analysis. (a) schematic of each individual pixel in our Raman mapping. (b) false positive of graphene vacancy (c) false negative of graphene vacancy

Figure E4a) shows the schematic of an individual pixel in Raman mapping. The size of each pixel is 500 μm x 500 μm and the diameter of beam spot is only few microns. Owing to large difference (3 to 4 orders of magnitude) between Raman characterization area and pixel area, false positive and false negative are possible cases in our Raman mapping. Figure E4b shows a schematic of false positive in graphene vacancy analysis. Although most area in the pixel has graphene, there is no graphene in the beam spot area and Raman characterization result is graphene vacancy in this pixel. Figure S4c shows a schematic of false negative in graphene vacancy analysis. Although most area in this pixel does not have graphene, there is graphene in the beam spot area and Raman characterization result is no graphene vacancy in this pixel

The possibility of false positive and false negative depends on multiple factors, such as pixel size, beam spot area and uniformity of 2-D materials. Generally, smaller pixel size, larger beam spot area and higher quality (more uniform) 2-D materials has lower possibility of false positive and false negative.

Appendix E6: VASP Calculation

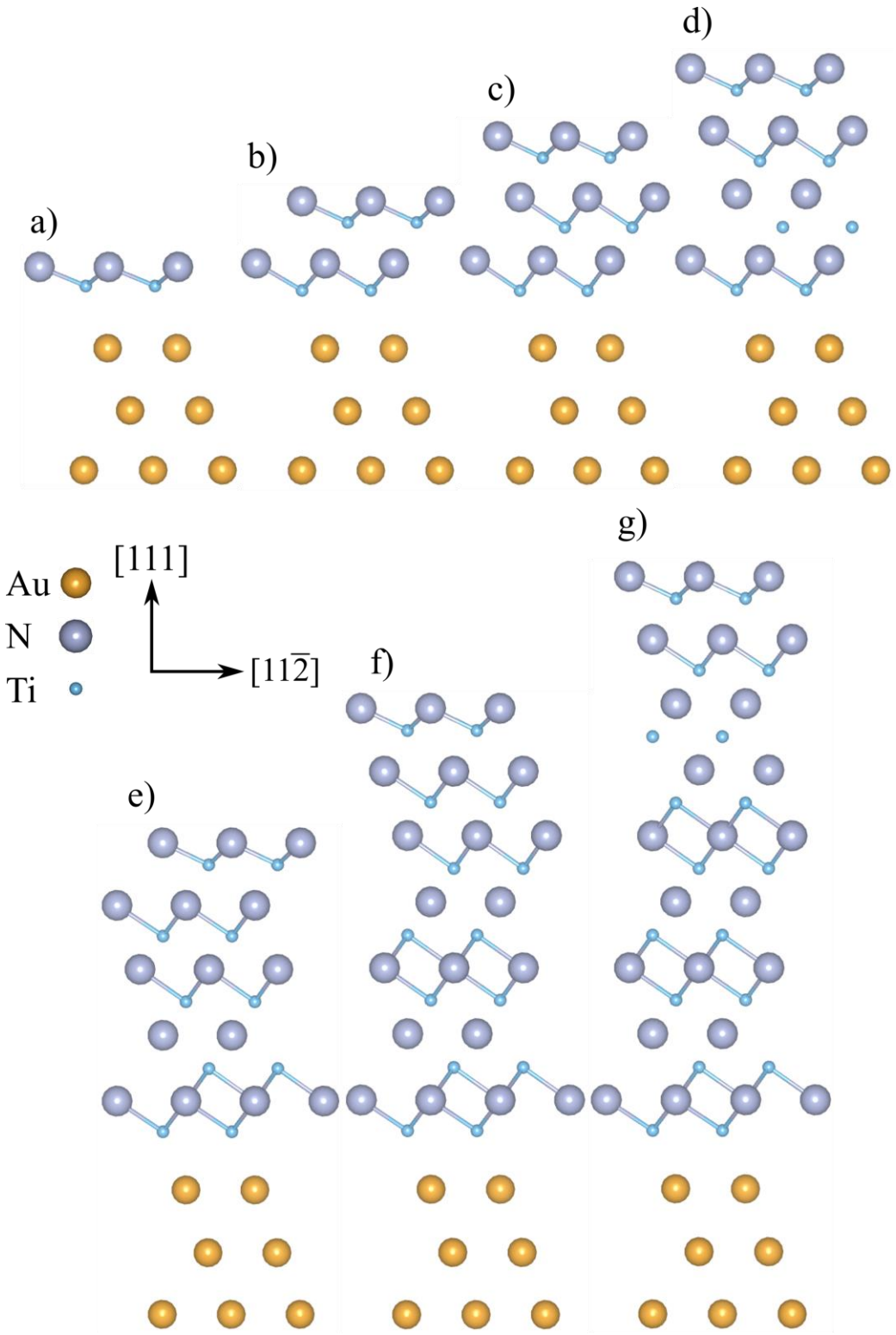

Figure E5 | Relaxed atomic structures of 1, 2, 3, 4, 5, 7, and 9 atomic layer slabs given in 5a-g respectively. All bonds are shown with a maximum length of 2.1175Å corresponding to the equilibrium bonding length in a relaxed bulk rock salt TiN crystal. Atomic layers are stacked along their respective crystal's (111) direction. Au, N, and Ti atoms are shown in yellow, gray, and cyan respectively.

VASP Calculations: Molecular files for the initial guesses of atomic arrangements in heterostructure slabs were created using Atomsk[2]. Rock salt structure Au crystal slabs with lattice petameter a_0=4.0782Å were oriented with their (111) direction parallel to the z-axis of the space; Rock salt TiN crystal slabs with lattice petameter a_0= 4.235 Å were oriented with their (111) direction parallel to the z-axis of the space. TiN crystal slabs were merged onto the Au slabs to form heterostructures. VASP calculations were carried out on an 11x11x1 k-points grid using the VASP built-in PBE pseudopotentials and a mixture of the Davidson and RMM-DIIS algorithms for energy minimization. Calculations were run on the National Energy Research Scientific Computing Center (NERSC) Cori supercomputer and were visualized with the VESTA software.[3]

Appendix E7: Masked Multilayer Growth of TiN on Ti-Seeded, Au-Buffered c-Sapphire Substrates:

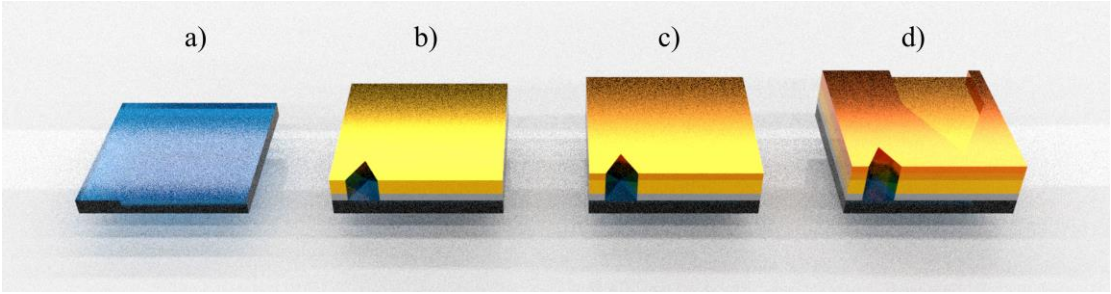

Figure E6 | Schematic of mask-patterned multilayer growth

Fabrication of the TiN mask-patterned multilayers in the nanometer and sub-nanometer regimes to demonstrate thickness characterization were carried out as shown schematically in figure S.4 a.

Appendix E8: 5/9-layer TiN NOM

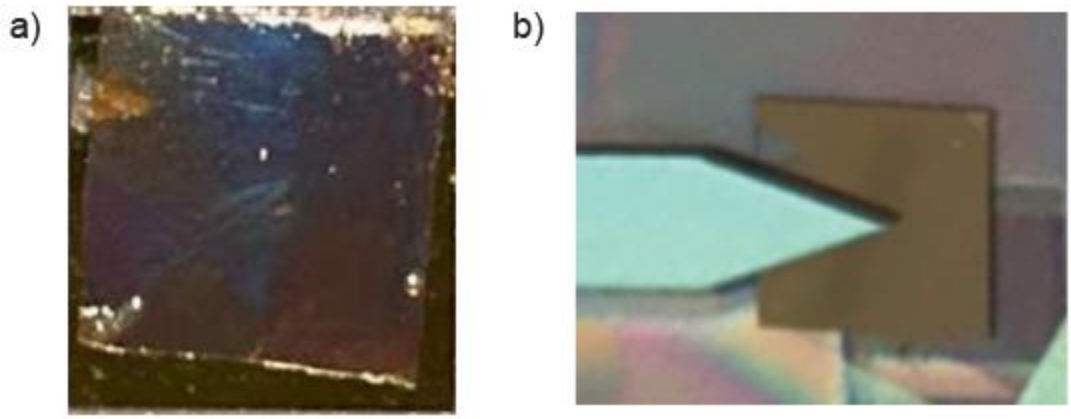

Figure E7 | 5/9-layer TiN (a) Photo image of 5/9-layer TiN NOM. (b) mask-patterned growth of 5/9-layer TiN, patterned area has 5 layers TiN and non-patterned area has 9 layers TiN

Appendix E9: High Resolution Mapping on boundary between 5 layers and 9 layers TiN

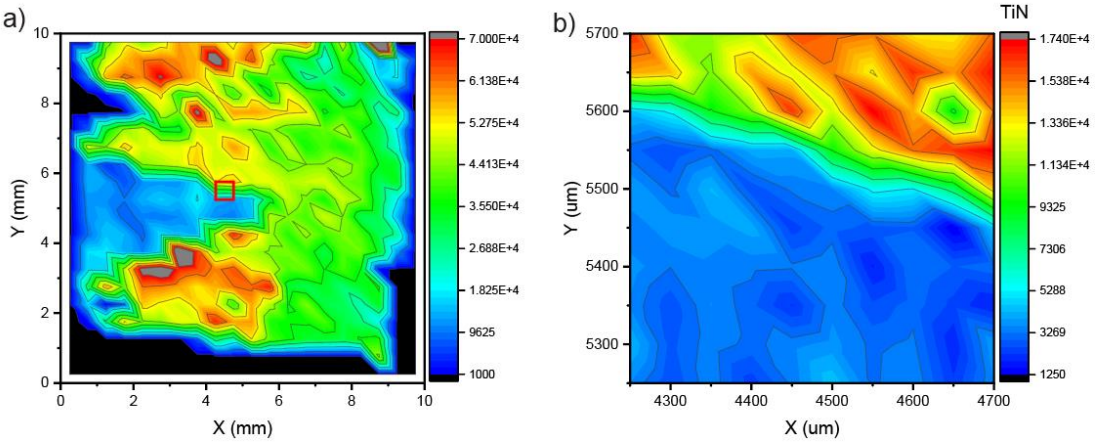

Figure E8 | High resolution mapping (a) High-resolution mapping area is represented by red square in large-scale mapping. (b) High-resolution mapping on the boundary between 5 layers TiN and 9 layers TiN

Appendix E10: Heatmap of 3/4-layer TiN NOM (plotted with TO mode intensity)

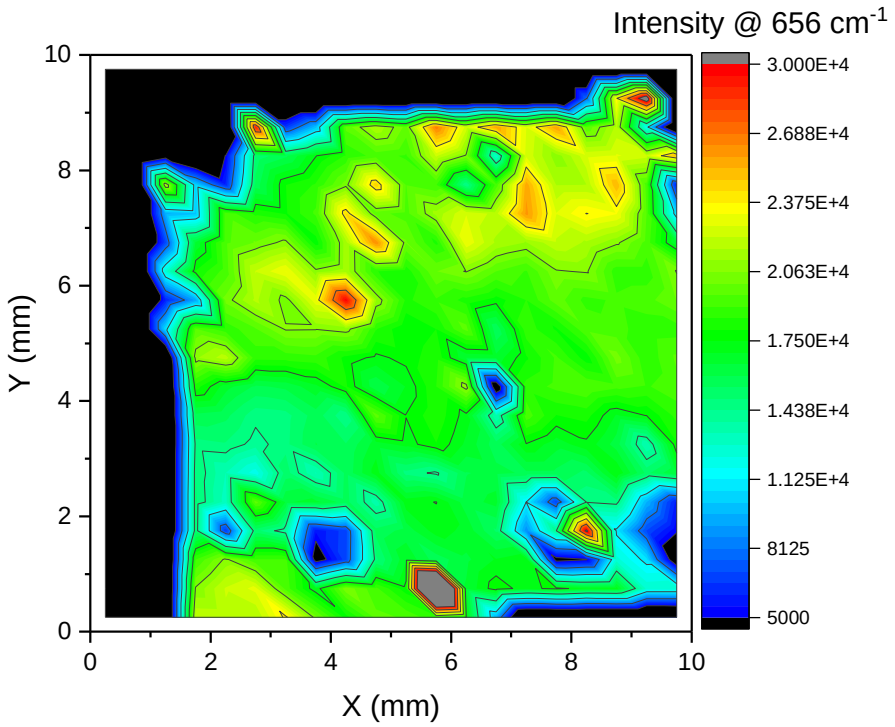

Figure E9 | Heatmap of 3/4-layer TiN NOM (plotted with TO mode intensity at 656 cm^{-1}

Appendix E11: 3/4-layer TiN NOM

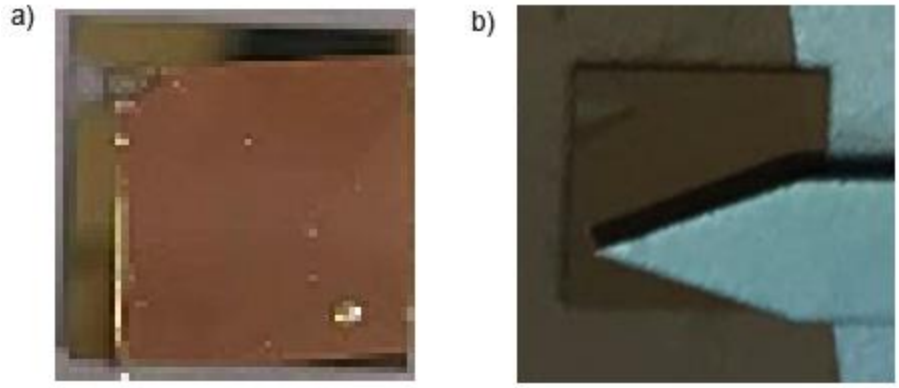

Figure E10 | 3/4-layer TiN (a) Photo image of 3/4-layer TiN NOM. (b) mask-patterned growth of 3/4-layer TiN, patterned area has 3 layers TiN and non-patterned area has 4 layers TiN

Appendix E12: Cu Thin Film Supported NOM

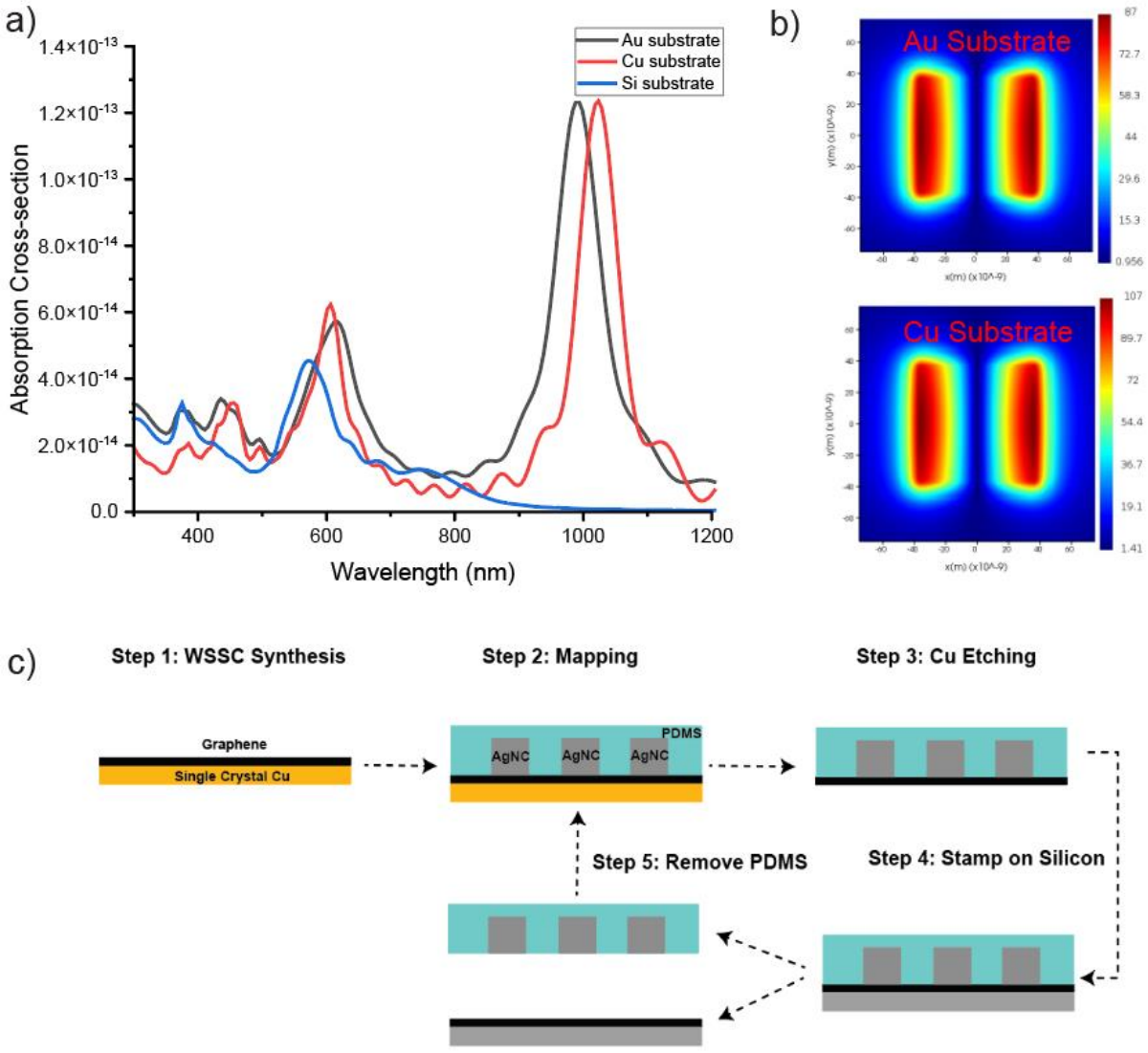

Figure E11 | Cu thin film supported NOM (a) Simulated absorption spectra of NOM supported by Au thin film (black), Cu thin film (red), and silicon thin film (black) (b) Near-field enhancement in Au thin film supported NOM (top) and Cu thin film supported NOM (bottom). (c) Proposed all-in-one characterization/transfer platform for wafer scale 2D materials.

Figure E11a) shows simulated far-field spectra of NOM supported by different substrates, including Au thin film (black), Cu thin film (red) and silicon thin film (blue). In Cu NOM, the absorption cross-section is nearly consistent with Au NOM, and the resonance wavelength slightly red shifts from 993 nm to 1023 nm. Figure E12b) shows near field enhancement in Au NOM and Cu NOM, at resonance wavelength, maximum E/E_0 is 87 and 107 in Au NOM and Cu NOM respectively, it means 2D materials on Cu thin film can be well-enhancement in our PDMS NOM

platform. Because single crystal Copper has been widely used in wafer scale single crystal 2D materials synthesis[4–6], we proposed an all-in-one characterization and transfer method in Figure E11c.

Appendix E13: Lifetime Study

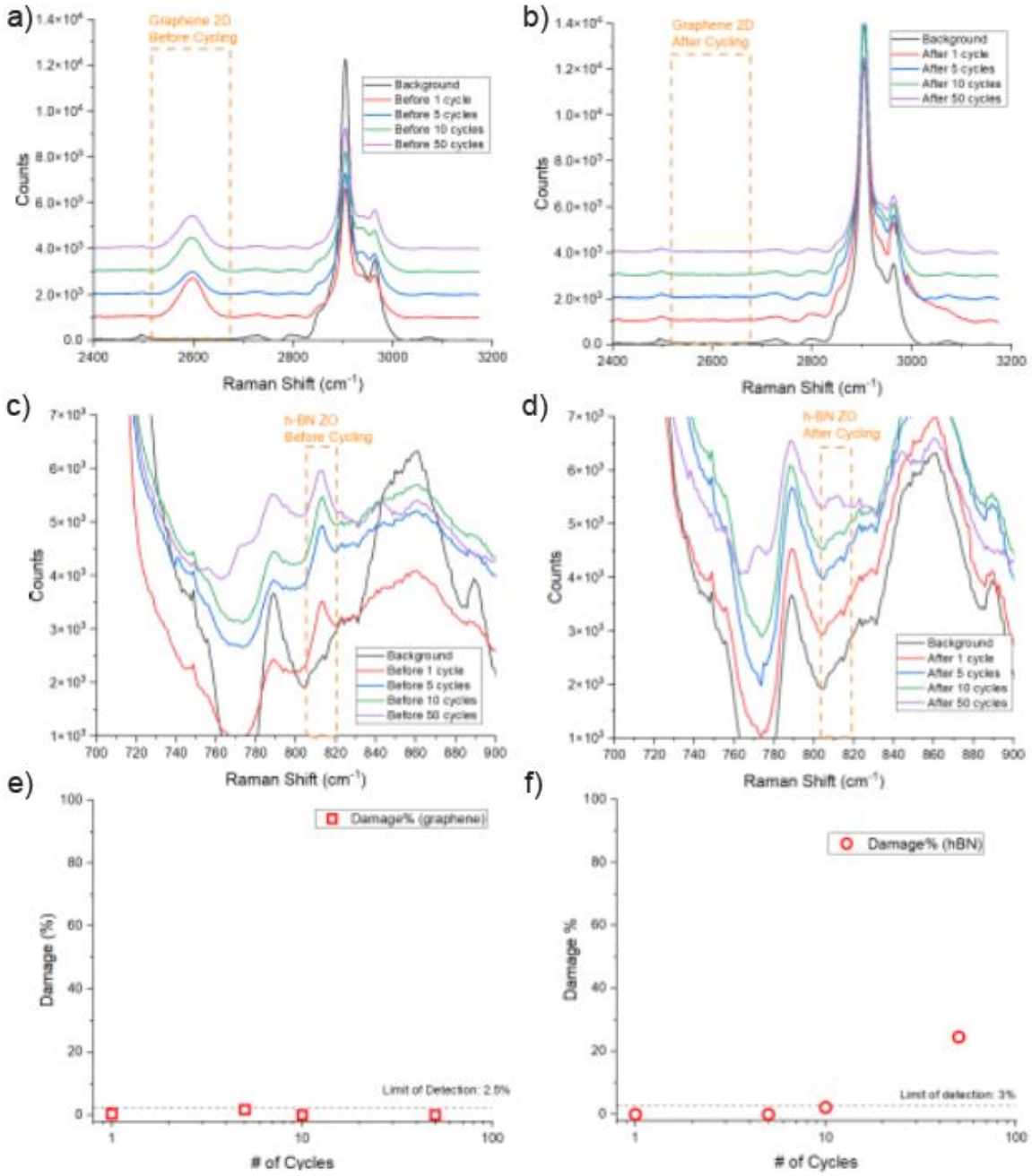

Figure E12 | Lifetime Study (a) Raman spectra of Graphene/h-BN NOM before cycling (high wavenumber regime). (b) Raman spectra of plasmonic PDMS stamp after cycling (high wavenumber regime). (c) Raman spectra of Graphene/h-BN NOM before cycling (low wavenumber regime). (d) Raman spectra of graphene 2D mode on plasmonic PDMS stamp after cycling (low wavenumber regime). (e) Damage (%) on graphene after different cycles. (f) Damage (%) on h-BN after different cycles.

There are two 2D materials damage mechanisms during the stripping process, i) instability-induced damage and ii) tensile strain-induced damage.[7] Because instability-induced damage is ubiquitous in most 2D materials and no pressure is loaded during our plasmonic PDMS

stamp transfer, tensile strain-induced damage is negligible in our platform and our lifetime study focuses on graphene and h-BN adhesion on stamp which direct relate to instability-induced damage.

In the lifetime study, we stripped plasmonic PDMS stamp from Graphene/h-BN sample and put it back repeatedly (called cycling). After cycling, we transfer the plasmonic PDMS stamp to a pristine Au thin-film to measure how many graphene and h-BN adhere on the stamp. The damage (%) is determined by the following equation: Damage (%) = (I ($After\ cycling$)) / (I ($Before\ cycling$)). I ($Before\ cycling$) is measured from Figure E12a) and Figure E12c), and I ($After\ cycling$) is measured from Figure E12b) and Figure E12d). In Figure E12e), the damage (%) on graphene has not been observed after 50 cycles because Au thin film has larger surface free energy than PDMS stamp, and h-BN layer prevent direct contact between graphene and h-BN. In Figure 12f), the damage (%) on h-BN has not been observed till 10 cycles. However, after 50 cycles, h-BN damage increase to 24% owing to relative weak van der Waals interaction between graphene and h-BN. Because most applications do not need to characterize the same sample for more than 10 times, this lifetime is acceptable at the early stage. In the future, doping[8] and surface passivation[9] of PDMS stamp, high Young's modulus PDMS[10], and robot controlled substrate conformal stamp can significantly decrease the interaction between PDMS stamp and h-BN and increase the lifetime.

Appendix E14: No AgNC contamination in Device Area

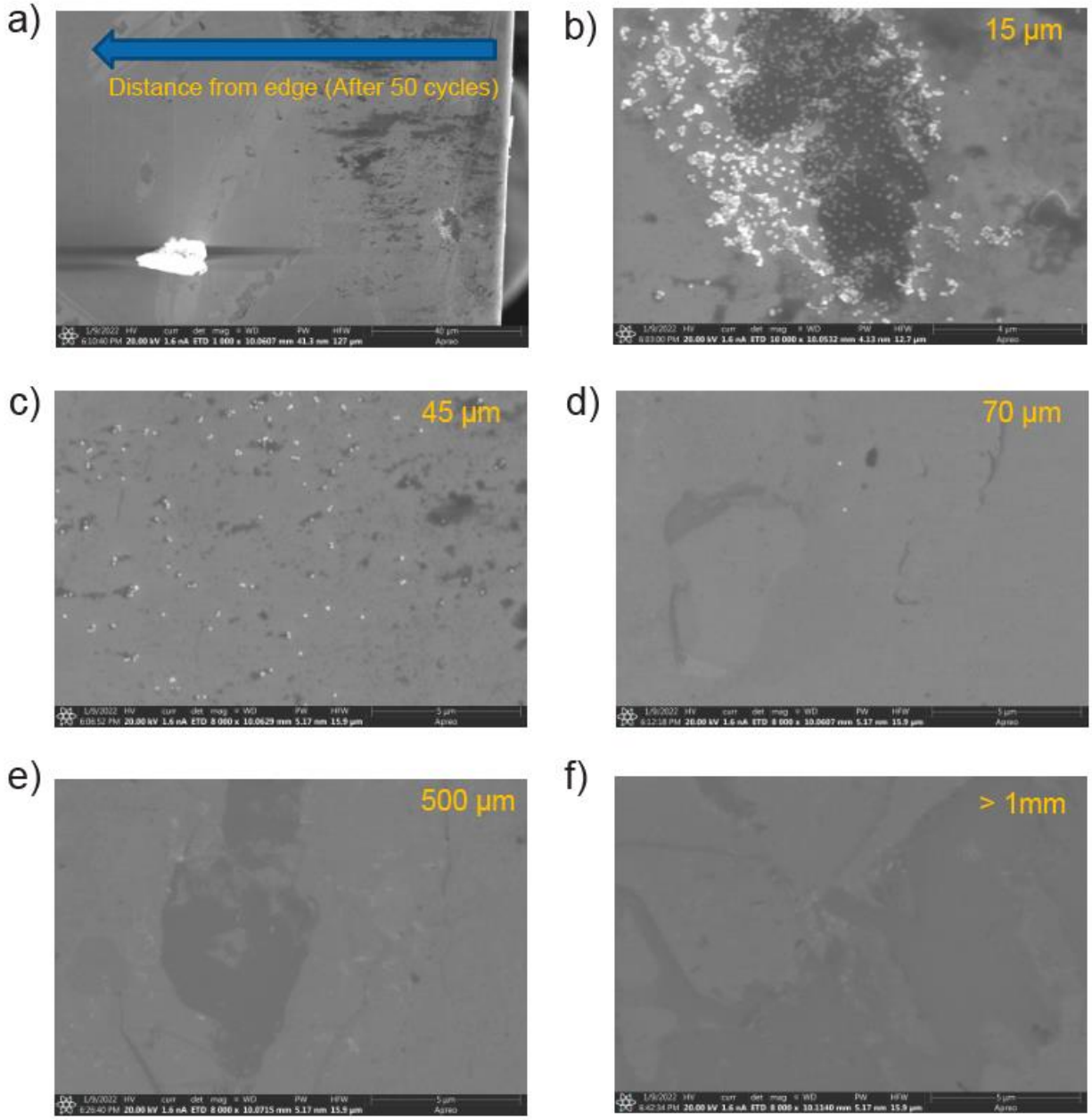

Figure E13 | SEM images of h-BN/Graphene on Au thin film after 50 cycles (a) Large Area SEM image, distance is measured from the sample edge. (b) SEM image at 15 µm away from the edge. (c) SEM image at 45 µm away from the edge. (d) SEM image at 70 µm away from the edge. (f) SEM image at 500 µm away from the edge. (b) SEM image at more than 1 mm away from the edge

To demonstrate no AgNC contamination on 2D materials, we took SEM on h-BN/Graphene sample after 50 cycles. Owing to mechanical force applied on the edge of plasmonic PDMS stamp during stripping, we have observed large amount of contamination at 15 µm away from the edge and trace amount of contamination at 70 µm away from the edge. At the locations more than 500

μm away from the edge (we imaged more than 40 different areas), we did not observe any AgNC on Graphene/h-BN sample. Because device area is at least few millimeters away from the edges of wafer in the industrial production line, AgNC contamination near the edge is acceptable.

Acknowledgements:

The authors would like to thank Nano3 and the San Diego Nanotechnology Infrastructure (NSF Award ECCS-2025752), the UC San Diego MRSEC (NSF Award DMR-2011924), and the NanoEngineering MRC for use of their equipment and facilities. This work was supported by NSF Awards CHE-1807891 and DMR-2011924.

Steven Bopp thanks the support of the Department of Defense (DoD) through the National Defense Science & Engineering Graduate (NDSEG) Fellowship Program. This research used resources of the National Energy Research Scientific Computing Center (NERSC), a U.S. Department of Energy Office of Science User Facility located at Lawrence Berkeley National Laboratory, operated under Contract No. DE-AC02-05CH11231 using NERSC project identifier M3047 for 2022.

Appendix E, in part (everything except E6 and E7), is currently being prepared for submission for publication of the materials by Yuan Zeng‡, Steven Bopp‡, Tod Pascal, Zhaowei Liu* and Andrea R. Tao*. The dissertation author was the primary investigator and author of this paper

Appendix E, in part (E1, E6 and E7), is currently being prepared for submission for publication of the materials by Steven Bopp‡, Yuan Zeng‡, Tod Pascal, Andrea R. Tao* and Zhaowei Liu*. The dissertation author was the co-author of this paper.

References

(1) Björck, M.; Andersson, G. GenX: An Extensible X-Ray Reflectivity Refinement Program

Utilizing Differential Evolution. *J. Appl. Crystallogr.* **2007**, *40* (6), 1174–1178. https://doi.org/10.1107/S0021889807045086.

(2) Hirel, P. Atomsk: A Tool for Manipulating and Converting Atomic Data Files. *Comput. Phys. Commun.* **2015**, *197*, 212–219. https://doi.org/10.1016/J.CPC.2015.07.012.

(3) Momma, K.; Izumi, F. VESTA: A Three-Dimensional Visualization System for Electronic and Structural Analysis. *urn:issn:0021-8898* **2008**, *41* (3), 653–658. https://doi.org/10.1107/S0021889808012016.

(4) Chen, T. A.; Chuu, C. P.; Tseng, C. C.; Wen, C. K.; Wong, H. S. P.; Pan, S.; Li, R.; Chao, T. A.; Chueh, W. C.; Zhang, Y.; Fu, Q.; Yakobson, B. I.; Chang, W. H.; Li, L. J. Wafer-Scale Single-Crystal Hexagonal Boron Nitride Monolayers on Cu (111). *Nat. 2020 5797798* **2020**, *579* (7798), 219–223. https://doi.org/10.1038/s41586-020-2009-2.

(5) Zhang, L.; Dong, J.; Ding, F. Strategies, Status, and Challenges in Wafer Scale Single Crystalline Two-Dimensional Materials Synthesis. *Chem. Rev.* **2021**, *121* (11), 6321–6372. https://doi.org/10.1021/ACS.CHEMREV.0C01191/ASSET/IMAGES/MEDIUM/CR0C01191_0048.GIF.

(6) Li, J.; Chen, M.; Samad, A.; Dong, H.; Ray, A.; Zhang, J.; Jiang, X.; Schwingenschlögl, U.; Domke, J.; Chen, C.; Han, Y.; Fritz, T.; Ruoff, R. S.; Tian, B.; Zhang, X. Wafer-Scale Single-Crystal Monolayer Graphene Grown on Sapphire Substrate. *Nat. Mater. 2022* **2022**, 1–8. https://doi.org/10.1038/s41563-021-01174-1.

(7) Kim, C.; Yoon, M. A.; Jang, B.; Kim, H. D.; Kim, J. H.; Hoang, A. T.; Ahn, J. H.; Jung, H. J.; Lee, H. J.; Kim, K. S. Damage-Free Transfer Mechanics of 2-Dimensional Materials: Competition between Adhesion Instability and Tensile Strain. *NPG Asia Mater. 2021 131* **2021**, *13* (1), 1–11. https://doi.org/10.1038/s41427-021-00311-1.

(8) Vudayagiri, S.; Junker, M. D.; Skov, A. L. Factors Affecting the Surface and Release Properties of Thin Polydimethylsiloxane Films. *Polym. J.* **2013**, *45*, 871–878. https://doi.org/10.1038/pj.2012.227.

(9) Zhang, X. S.; Zhu, F. Y.; Han, M. Di; Sun, X. M.; Peng, X. H.; Zhang, H. X. Self-Cleaning Poly(Dimethylsiloxane) Film with Functional Micro/Nano Hierarchical Structures. *Langmuir* **2013**, *29* (34), 10769–10775. https://doi.org/10.1021/LA4023745/SUPPL_FILE/LA4023745_SI_002.MPG.

(10) Substrate conformal imprint lithography for nanophotonics - NASA/ADS https://ui.adsabs.harvard.edu/abs/2010PhDT.....81V/abstract (accessed May 22, 2022).